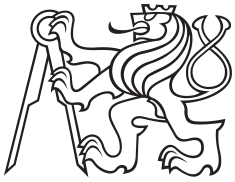

Czech
Technical
University
in Prague

F4

Faculty of Nuclear Sciences and Physical Engineering
Department of Physics

DOCTORAL THESIS

Interpretative SOLPS-ITER transport simulations of the COMPASS tokamak edge plasma

Prague 2025

Kateřina Hromasová

Bibliografický záznam

Autor	Ing. Kateřina Hromasová České vysoké učení technické v Praze, Fakulta jaderná a fyzikálně inženýrská Katedra fyziky
Název práce	Interpretativní simulace transportu v okrajovém plazmatu tokamaku COMPASS kódem SOLPS-ITER
Studijní program	Jaderné inženýrství
Školitel	Mgr. Jakub Seidl, Ph.D. Ústav fyziky plazmatu AV ČR, v. v. i., U Slovanky 2525/1a, Praha
Školitel–specialista	Mgr. Michael Komm, Ph.D. Ústav fyziky plazmatu AV ČR, v. v. i., U Slovanky 2525/1a, Prague, Czech Republic
Školitel–specialista	Dr. David Tskhakaya Ústav fyziky plazmatu AV ČR, v. v. i., U Slovanky 2525/1a, Prague, Czech Republic
Akademický rok	2025
Počet stran	212
Klíčová slova	tokamak, plazma, transport, scrape-off layer, SOLPS-ITER

Bibliographic Entry

Author	Ing. Kateřina Hromasová Czech Technical University in Prague, Faculty of Nuclear Sciences and Physical Engineering Department of Physics
Title of Dissertation	Interpretative SOLPS-ITER transport simulations of the COMPASS tokamak edge plasma
Degree Programme	Nuclear Engineering
Supervisor	Mgr. Jakub Seidl, Ph.D. Institute of Plasma Physics of the Czech Academy of Sciences, U Slovanky 2525/1a, Prague, Czech Republic
Supervisor–specialist	Mgr. Michael Komm, Ph.D. Institute of Plasma Physics of the Czech Academy of Sciences, U Slovanky 2525/1a, Praha
Supervisor–specialist	Dr. David Tskhakaya Institute of Plasma Physics of the Czech Academy of Sciences, U Slovanky 2525/1a, Praha
Academic Year	2025
Number of Pages	212
Keywords	tokamak, plasma, transport, scrape-off layer, SOLPS-ITER

Abstrakt

Tato dizertační práce zkoumá fyziku transportu v okrajovém plazmatu pomocí interpretativních simulací sedmi L-módových a H-módových výbojů v tokamaku COMPASS kódem SOLPS-ITER. SOLPS-ITER jsme použili k validaci a zlepšení rekonstrukcí magnetického ekvilibria v tokamaku a navrhujeme ho jako robustní, ač drahý způsob nalezení pozice separatrix. Probádali jsme omezování elektronového a iontového tepelného toku z hlediska teorie, 2D parametrického skenu elektronových a iontových omezovačů tepelného toku a kinetické simulace kódem BIT1, a poskytujeme vodítka, jak tyto volné parametry nastavit. Zjistili jsme, že režim transportu v L-módové SOL tokamaku COMPASS typicky podléhá vlivu stěnové vrstvy (*sheath-limited*) a pouze při nejvyšších hustotách v ní pomalu začíná převládat vedení tepla (*conduction-limited*). Závěrem konstatujeme, že kód SOLPS-ITER věrně zreprodukoval nízkohustotní a středněhustotní plazmata v L-módu a rovněž jeden H-mód, ale přesné modelování vysokohustotního L-módu pravděpodobně vyžaduje implementaci driftů a nerovného rozdělení vstupního výkonu mezi elektrony a ionty.

Abstract

This thesis explores the physics of tokamak edge plasma transport using interpretative simulations of seven L-mode and H-mode discharges of the COMPASS tokamak with the SOLPS-ITER code. SOLPS-ITER is used to validate and improve reconstructions of the tokamak magnetic equilibrium, and it is proposed as a robust if expensive mean to pinpoint the separatrix position. Electron and ion heat flux limiting is studied from the perspective of theory, a 2D heat flux limiter scan and a kinetic simulation with the BIT1 code, and guidelines are given how to use this free parameter. The SOL transport regime of COMPASS tokamak L-modes is found to be typically sheath-limited, transitioning toward conduction-limited at the highest densities. In conclusion, the SOLPS-ITER code has faithfully reproduced low- to moderate-density COMPASS L-mode plasmas as well as one H-mode, but accurate modelling of high-density L-modes likely demands the implementation of drifts and uneven electron-ion input power split.

Contents

Chapter 1

Introduction

Humanity's energy demands are rising as the average quality of life improves. Unfortunately, our chief energy source — fossil fuels — has a lasting impact on the Earth's climate and its supply is intrinsically limited. Consequently, new energy sources are sought. Among them is thermonuclear fusion.

There are several concepts of the fusion reactor, such as the tokamak, the stellarator and the inertial fusion reactor, but they all share a fundamental concern: heat exhaust. The fusion fuel, a 1:1 mixture of deuterium and tritium, burns in the plasma state at temperatures of approximately 150 million K. To achieve this temperature, the plasma is heated both externally by heating systems and internally by fusion reactions. From the conservation of energy it follows that the plasma concurrently releases the same amount of energy onto the walls of its container. This energy must be safely exhausted from the reactor without threatening the integrity of its internal components. This brings many challenges, some unique to one type of reactor, others shared. Reactors with inertially confined plasmas feature pulsed fusion power, so they must safely contain what amounts to several explosions in the reactor chamber per second. Reactors with magnetic confinement, on the other hand, face problems with heat flux localisation where the magnetic field lines connect the reactor chamber to the hot edge of the confined plasma. Ultimately, failing to resolve the problems tied to heat exhaust will shorten the reactor lifespan so drastically that building fusion power plants will not be economically feasible.

Designing and building a tokamak fusion reactor poised at the limits of material and plasma science would not be possible without predictive modelling using state-of-the-art, first-principle numerical codes. The main code which has provided us with data on plasma parameters in the edge region of the ITER fusion reactor is the SOLPS-ITER transport code (and its predecessors). [1] It is imperative to perform reliable predictive simulations of the edge plasma, so as to assess the operation windows of the reactor, prepare diagnostic systems or design operation scenarios which will not damage the machine. Predictive SOLPS-ITER simulations, however, often suffer from significant uncertainty caused by the number of free parameters in edge transport codes. For this reason, interpretative simulations of existing tokamak experiments are carried out in tandem, allowing at once investigating edge transport physics and finding optimal settings for free parameters. Predictive modelling of future fusion reactors and interpretative modelling of existing tokamak experiments thus exist in a symbiosis.

The topic of this thesis are interpretative SOLPS-ITER simulations of the COMPASS tokamak edge plasma. The COMPASS tokamak was operated by the Institute of Plasma Physics in Prague in the years 2009-2021. [2] With its small size, open divertor and limited heating power, COMPASS did not reach plasma parameters relevant to fusion reactor operation. However, its broad diagnostic coverage of the edge plasma and relatively simple Scrape-Off Layer (SOL) make it an ideal test bed for interpretative edge transport simulations. While performing interpretative simulations of COMPASS, the main purpose of this thesis is to lay the groundwork for predictive simulations

of the COMPASS Upgrade tokamak. [3] At the grand scale, this work contributes toward our understanding of the SOLPS-ITER transport code, its uncertainties and free parameters. This increases the trustworthiness of SOLPS simulations of future fusion reactors, and facilitates the timely successful addressing of the problem of tokamak reactor heat exhaust.

1.1 Heat exhaust in tokamaks

Energy and particle transport in the tokamak edge plasma is characterised by the interplay between the parallel and cross-field transport. Since charged particles can move freely along the magnetic field lines but their cross-field motion is limited, the parallel transport is orders of magnitude more efficient than the cross-field transport. As a consequence, the parallel and cross-field transport can be, to a good degree of accuracy, decoupled and solved independently. The equations of parallel and cross-field physics are naturally described using the field-aligned coordinates $[\|, r, \perp]$ rather than the usual torodial $[\phi, r, \theta]$ or cylindrical $[\phi, R, Z]$ coordinates. The parallel coordinate $\|$ points along the magnetic field lines, the radial coordinate r points away from the magnetic axis and the bi-normal coordinate $\perp$ is perpendicular both to $\|$ and r. An arbitrary flux $\mathbf{\Gamma}$ associated with charged particles will usually satisfy $\Gamma_\| \gg \Gamma_r \approx \Gamma_\perp$.

The key role of edge plasma transport in the issue of heat exhaust can be illustrated by the following simplified calculation. Consider the baseline ITER scenario with 500 MW of fusion power and 50 MW of heating power. [4] The shape of the ITER vessel may be approximated with a toroid whose major radius is $R = 6$ m and whose poloidal cross-section is an ellipse with the semi-major axis of $a = 3.5$ m and the semi-minor axis of $b = 2$ m. The area of this toroid is 663 m^2. 80 % of the fusion power is carried by neutrons, whose energy is deposited volumetrically and therefore does not contribute to the surface heat load calculation. Suppose that a third of the remaining 150 MW of power, introduced by heating systems and alpha particles, is released in the form of isotropic radiation. [4, 5] This is absorbed by the chamber surface, introducing the heat load $q = 50$ MW/663 m^2 $= 0.075$ MW.m^{-2}. The remaining 100 MW is carried predominantly by the parallel transport and deposited in a narrow strip along the strike lines. Example heat flux patterns are shown in Fig. 1.1, although COMPASS heat fluxes are not nearly as concentrated or intensive as the ITER ones. The plasma-wetted area may be estimated as [6, Sec. 6]

$$A_{wet} = 2\pi R_{sp} \lambda_q^{(OMP)} f_x, \tag{1.1}$$

where $R_{sp} \approx 6$ m is the strike point major radius, $\lambda_q^{(OMP)} \approx 3.4$ mm (predictions range from 1 mm to 6 mm) is the heat flux fall-off length for ITER H-mode at the outer midplane (OMP) [4, Sec. 3.1.2] and $f_x = 9$ is the poloidal magnetic flux expansion factor [6]. Counting both strike lines, the total plasma-wetted area is $A_{wet} = 2.31$ m^2. Dividing the total incident power

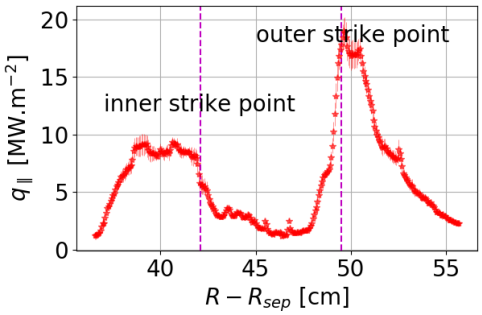

Figure 1.1: Heat flux deposition pattern along the target of the COMPASS tokamak. Measured by infrared thermography, discharge #17588.

of 100 MW by A_{wet}, we obtain the average strike line perpendicular heat load $q_\perp = 43$ MW.m^{-2}. (Divertor tile inclination is already considered by the flux expansion factor f_x.) By comparison, the heat flux density on the surface of the Sun is 63 MW.m^{-2} and the highest steady-state heat flux the ITER divertor can accommodate in the long-term is 16 MW.m^{-2}. [4]

This calculation is only estimatory. Its simplifications include neglecting $q_\parallel$ peaking near the strike points, conversion of plasma energy to neutrals and radiation and the emerging additional channels of target energy flux, power imbalance between the inner and outer target, or the shaping of the divertor tiles. A major risk to reactor divertor targets are semi-periodic H-mode instabilities called ELMs, which cause partial confinement collapse and transiently release extreme head loads on the divertor. The ITER baseline discussed above is an ELMy H-mode, so the target heat loads will also fluctuate by orders of magnitude. Rather than provide exact ITER divertor target heat load values, the calculation illustrates the basics of energy transport through the edge plasma. A fraction of the power released from the plasma crosses the separatrix in the form of charged particles, is transported to the divertor targets via edge transport and finally deposited on a small area near the divertor strike lines. One of the main goals of the edge transport research is to control this power channel and ascertain that it does not cause unacceptable damage to the divertor targets. [7]

The primary hazards which hot plasma particles pose to the divertor targets during steady-state, normal operation are recrystallisation and erosion. [4] Additionally, melting is possible under off-normal conditions such as unmitigated ELMs or disruptions, especially at leading edges of divertor tiles. [8] To minimise these risks, tungsten ($T_{melt} = 3400$ °C) was chosen as the divertor surface material for ITER. Tungsten *recrystallisation* occurs when the monoblock surface temperature rises to approximately 1300-1700 °C [9] and it results in decreased thermal shock resistance and increased brittleness. When the layer of recrystallised tungsten reaches the thickness of ~ 2 mm, the thermal stress of heating-cooling cycles causes it to crack. [10] Divertor target *erosion* is caused by prolonged periods of target sputtering, where high-energy ions knock a tungsten atom out of the target and into the plasma. The atom can be promptly ionised and, owing to Larmor rotation, redeposited

on the target, but since ion fluxes tend to be localised and tungsten Larmor radii are large, erosion patterns form along the strike lines nevertheless. Both recrystallisation and erosion are long-term processes. They will slowly occur during the steady-state reactor operation and they will be exacerbated by the presence of ELMs. To ensure sufficient divertor lifetime, these processes must be mitigated by constraining the operating space of the divertor plasma parameters.

According to [11], the divertor can be sufficiently protected from recrystallisation and erosion under the following conditions: (i) the target electron temperature T_{et} does not exceed 10 eV, and (ii) the target electron density n_{et} attains an optimal value, which is of the order $\sim 10^{21}$ m^{-3} and depends on T_{et} and the field line incidence angle α. To test if these criteria can be met in ITER, one may perform a simple calculation using the two-point model (2PM). [12, Eq. (5.4)-(5.6)] The two-point model is a simple analytic model of the Scrape-off Layer (SOL), consisting of three short equations relating plasma parameters at upstream (e.g. outer midplane, energy source region, subscript u) and downstream/target (divertor target, energy sink region, subscript t). We use the basic form of the 2PM, in which the total pressure is assumed constant along the flux tube (zero momentum losses) and all of the upstream energy is exhausted through the target sheath (zero power losses). To predict the target plasma parameters, the model requires the upstream (electron) density n_u, the parallel heat flux density $q_\parallel$ and the flux tube length L as input. SOLPS-ITER modelling of ITER H-mode indicates that the separatrix electron density is approximately $n_u = 4.1 \times 10^{19}$ m^{-3}. [13, Fig. 5a, high divertor pressure case] The parallel heat flux density can be calculated as $q_\parallel = P_{SOL}/A_\parallel$, where $P_{SOL} = 50$ MW is the power transported toward the outer target and

$$A_\parallel = 4\pi R \lambda_q^{(OMP)} \frac{B_\theta}{B} \tag{1.2}$$

is the perpendicular cross-section area of the flux tube adjacent to the separatrix. [12, Eq. (5.59)] Here $R = 8.2$ m is the outer midplane major radius, $\lambda_q^{(OMP)} = 3.4$ mm is the heat flux fall-off length [4, 14] and $B_\theta = 1.3$ T and $B = 4.2$ T [15, magnetic equilibrium used therein] are the outer midplane poloidal and total magnetic fields, respectively. This yields $A_\parallel = 0.11$ m^2 and $q_\parallel = 461$ MW.m^{-2}. The flux tube length is $L = 90$ m (beginning at the outer midplane, 0.3 mm outside the separatrix, and ending at the outer target). [15, magnetic equilibrium used therein] Inserting these values into the two-point model, one obtains the upstream (electron) temperature $T_u = 187$ eV, the target temperature $T_t = 119$ eV and the target density $n_t = 3.2 \times 10^{19}$ m^{-3}. Evidently these values are not compatible with the ITER divertor, as the temperature is much too high and the density much too low. The reason for this result is the absence of momentum and power losses in the calculation. The other simplifying assumptions, such as the absence of impurity species, $T_i = T_e$ or neglecting the flux expansion, do not impact the result nearly as heavily as the absence of losses. This calculation illustrates the key role of momentum and power losses in the edge plasma. It has been shown that only

a substantial reduction of the target plasma pressure accompanied by strong dissipation of power by radiation can usher in favourable divertor conditions in a burning plasma. [4] In the ITER baseline burning H-mode scenario, 70 % of the 100 MW power crossing the separatrix must be converted to radiation and neutrals energy in order to protect the divertor targets. [14] The key question of steady-state divertor operation in the desirable parameter window then becomes: What physics govern momentum and power losses in the edge plasma?

Experimental and modelling evidence suggest that the momentum and power loss factors,

$$f_{mom} = 1 - \frac{p_t}{p_u} \qquad (1.3) \qquad\qquad f_{pow} = 1 - \frac{q_{\parallel t} R_t}{q_{\parallel u} R_u} \qquad (1.4)$$

where p is the total pressure and the subscripts u and t denote upstream and target, respectively, are highly correlated with the target electron temperature T_{et}. [11] The evidence is especially compelling for pressure losses in cold dense plasmas, where it has been shown that the majority of the flux tube momentum is lost in a thin layer above the surface due to interaction of ions with neutral molecules. [16] This process is governed mainly by temperature and thus it is even possible to give a semi-empirical formula for $f_{mom}(T_{et})$. [17, Eq. (17)] Despite our lack of clear-cut physical understanding of *why* the losses are so dependent on T_{et}, it is certain that the target temperature is a pivotal quantity in edge momentum and power loss physics.

The coexistence of $\sim$ 150 eV upstream temperature, consistent with an H-mode pedestal needed for high fusion performance, and $\sim$ 5 eV target temperature, compatible with a long divertor life time, is the subject of study of edge transport regimes. The fundamental observation of the edge transport regimes is that the plasma ability to transport energy along the field lines is mediated mostly by electron heat conduction $q_{\parallel e} = -\chi_{\parallel e} \nabla_\parallel T_e$, and therefore it increases strongly with plasma temperature, $\chi_{\parallel e} \approx \chi_{\parallel 0} T_e^{5/2}$. (More on parallel heat conduction is given in chapter 5.) This means that in a plasma which has, on average, high temperature, a small parallel gradient of T_e will suffice to transport P_{SOL} to the target. Conversely, in a cooler plasma a large parallel gradient of T_e will form to carry the same $q_{\parallel e}$. The result of the first situation is isothermal, high-temperature SOL — the *sheath-limited regime*; the second situation will result in a SOL where upstream may be hot but the target is substantially (at least factor-of-three) cooler — the *conduction-limited regime*.[1] The loss-less example of ITER SOL given above was in the sheath-limited regime, with similar upstream and target temperatures.

[1] The regime names refer to the most prominent feature of the parallel energy transport. In the sheath-limited regime, it is the target sheath, which allows plasma cooling at the rate $q_\parallel = \gamma T_e n_e c_s$ where $\gamma \approx$ 7-11 is the total sheath heat transmission coefficient, $c_s = \sqrt{e(T_i + T_e)/m_i}$ is the sound speed and all of the quantities are measured at the sheath entrance. In the conduction-limited regime, it is the electron energy conduction with its strong dependence on the local electron temperature. This somewhat opaque nomenclature is illustrated perfectly by [18], where the total parallel heat flux is broken down into the contribution due to the sheath and due to internal transport effects, and compared for a low-

Evidently, the conduction-limited regime is more desirable in a tokamak reactor, as it allows the coexistence of high upstream and low target temperature. To transition into this regime in a given magnetic geometry, we would have to lower the overall SOL temperature. This can principally be done in three ways: increasing the upstream density (e.g. using gas puff), decreasing the upstream energy flux density (by lowering the fusion power or allowing more radiation in the core) or introducing/increasing momentum and power losses. Since the edge density is limited by turbulence [20, 21] and decreasing P_{SOL} degrades fusion performance, substantial parallel temperature gradients in the ITER SOL will be achieved by momentum and power losses. These cause the total plasma pressure to drop radically at the target compared to the upstream, and allow most of the power conducted through the SOL to be dissipated as radiation before it reaches the target. The entire power crossing the separatrix must still be exhausted from the machine divertor and first wall, but it is spread more uniformly over the divertor and first wall, easing the localised strain of the strike lines. The regime where momentum and power losses are so strong that $T_{et} < 10$ eV at the strike point and the adjacent near SOL is called *detachment*. [11]

Basic understanding of divertor detachment physics is listed in the recent review [4] as a key question regarding ITER divertor operation. Areas where further research is needed comprise not only the link between target quantities and distributed pressure/power losses, but also the precise role of volume recombination in reducing target ion flux and the behaviour of upstream density with impurity concentration. Experimentally divertor detachment has been studied on a number of machines, but diagnostic limitations, involving for instance probe measurements at temperatures below 5 eV, measurements of the neutral pressure or measurements of upstream T_i, typically allow only a certain degree of insight. For this reason, experiments are often supplemented by extensive modelling efforts. To date, the work horse of detachment modelling have been transport codes, which accurately capture the interplay between parallel and cross-field physics, atomic and molecular processes (the main cause for momentum and power losses) and the plasma-wall interaction. To further the understanding and optimise the design of the ITER divertor, the SOLPS-ITER code (described in the next section) has been developed by the ITER organisation. [1] SOLPS-ITER and other transport codes are instrumental on the way toward fusion power plants, as they predict the divertor parameters in fusion plasmas and facilitate not only understanding of the underlying physics, but also the reliable operation of the fusion power plant.

In this thesis, SOLPS-ITER is used to model the edge plasma in the COMPASS tokamak. As section 3 explains, COMPASS does not reach reactor-grade divertor target particle and heat fluxes, and it does not require routine detachment to protect the plasma-facing components. Modelling COMPASS with SOLPS-ITER is relevant to world-wide fusion research for

and high-collisionality plasma. The same effect is observed in Fokker-Planck simulations of the SOL. [19]

three main reasons. Firstly, interpretative COMPASS simulations create know-how and provide support to predictive simulations of the COMPASS Upgrade tokamak, which was designed as a DEMO-relevant device [22, 3] (more in section 3). Predictive modelling is inherently uncertain, and benefits from solid foundations built up by interpretative simulations grounded in experiment. Secondly, even if COMPASS plasmas are different from ITER plasmas, there is still "only one physics". By benchmarking SOLPS-ITER against a new tokamak[2] and against the particle-in-cell code BIT1, we contribute toward worldwide fusion reactor modelling efforts. Thirdly and finally, interpretative simulations of the COMPASS edge plasma are direct investigations of the tokamak edge plasma physics, particularly of the particle and power transport. In consequence, modelling the "compact", relatively low-parameter COMPASS with SOLPS-ITER furthers our understanding of fusion reactor plasma physics.

An integral part of this thesis is the publicly available `SOLPS-doc` documentation package [25], which records much of our technical knowledge and experience with SOLPS-ITER. It is my hope that, on top of building the foundations on which COMPASS Upgrade simulations can be performed, this thesis and `SOLPS-doc` in particular will help beginning SOLPS users around the world to understand and learn to use this complex, and sometimes incomprehensible, tokamak edge transport code.

This thesis is organised as follows. In this introduction chapter 1, I have shown the importance of reliable edge transport simulations for the tokamak heat exhaust problem. In chapter 2, I introduce transport codes, putting special emphasis on their strengths and weaknesses. In chapter 3, I describe the COMPASS and COMPASS Upgrade tokamaks. The next three "result" chapters present interpretative SOLPS-ITER simulations of the COMPASS edge plasma and investigate them in the view of a particular research question. In chapter 4, based on the L-mode discharge #17588, I gauge the impact of inaccurate magnetic equilibrium reconstruction on SOLPS-ITER simulations. I conclude that reconstruction errors can be directly quantified using interpretative SOLPS-ITER simulations and then used to perform a more accurate reconstruction. In chapter 5, based on the H-mode discharge #16908, I discuss SOL parallel heat transport and its corrections using heat flux limiters. I demonstrate that heat flux limiting enhances parallel temperature gradients and explain its knock-on effects on other plasma parameters. Emphasising the importance of sensitivity studies, I recommend optimal heat flux limiter settings for the studied simulation as well as for general edge transport modelling. In chapter 6, based on the 5-point L-mode density scan #13812-13825, I analyse the SOL transport regime of the COMPASS tokamak. I find that low-density COMPASS plasmas are sheath-limited and readily reproduced by SOLPS-ITER modelling. At high densities, however, my simulations significantly underestimate target

[2]The first simulations of the COMPASS tokamak were performed by an external collaborator [23, 24], but they focused on testing the inclusion of parallel kinetic energy among SOLPS-ITER variables rather than interpretative modelling of a tokamak experiment.

electron temperatures and place the SOL into the conduction-limited rather than transitional regime. In the concluding chapter 7, I answer the research question of this thesis:

> "How well can SOLPS-ITER model COMPASS tokamak edge plasma transport, and what can we learn from these simulations?"

Chapter 2

Edge transport codes

Tokamak edge transport codes describe the edge plasma as a mix of charged ion fluids permeated by a weightless electron fluid, confined by a static magnetic field and surrounded by boundary regions. Their variables are the velocity-space-averaged moments of the velocity distribution function $f(t, \mathbf{r}, \mathbf{v})$: particle density $n_a(t, \mathbf{r})$, temperature $T_a(t, \mathbf{r})$ and flow velocity $\mathbf{u}_a(t, \mathbf{r})$ of each particle species a at time t and position $\mathbf{r}$, as well as the plasma potential $\Phi(t, \mathbf{r})$. The spatio-temporal evolution of these variables is governed by the transport equations, which are usually a variation of the Braginskii equations [26] with various closures [27, 28]. Depending on the user input, transport codes can provide steady-state solutions of the plasma state or its temporal development. There are many different implementations of edge transport codes, from the 1D SOLF1D [29], 2D SOLEDGE2D [30] to the fully 3D EMC3 [31], and they are often supplemented with a Monte Carlo code for neutral particles modelling such as EIRENE [32]. This thesis presents simulations using the 2D edge transport code SOLPS-ITER. [1]

The main competence of edge transport codes is, as the name suggests, transport. It can be the transport of particles (pumping efficiency, sputtering intensity), energy (first wall loads, impurity radiation) or the complex interplay of both (divertor detachment). Edge transport codes are an outstanding tool for simulating the overall edge plasma state, as they offer a good compromise between the necessary physics complexity and computational time. They do, however, have limitations. Loss of information about the distribution function velocity space precludes transport codes from capturing kinetic effects. Absence of turbulence bars transport codes from self-consistent modelling of cross-field transport. This raises the question under which conditions transport codes are valid, how to expand their validity and how to test it.

The focus of this thesis are interpretative simulations, that is, simulations which reproduce experimental plasma as closely as possible. Interpretative simulations form the basis of model benchmarking and validity testing. Allowing for limitations of diagnostics, interpretative simulations facilitate direct comparison to "ground truth" experimental data and greatly facilitate code-to-code benchmarking. As the assumptions of transport codes are met to a varying degree between tokamaks, simulating each new machine aids our understanding of transport codes and increases the trustworthiness of fusion reactor predictive simulations.

A recurring topic of this thesis are transport code free parameters. Free parameters emulate physics processes which are absent from transport code equations, such as kinetic effects in parallel heat transport, or correct for known simulation errors which are difficult to remove, such as equilibrium reconstruction inaccuracy. Values of free parameters must be chosen by the modeller. In interpretative modelling, this is usually a matter of quality diagnostics and optimising the free parameters to achieve the best experiment-model match. In predictive modelling, however, free parameters become a source of uncertainty. Without experimental data to benchmark against, their values must be inferred from experimental data of other machines or another type of simulation, such as a particle-in-cell code for predicting the degree of

kinetic effects in parallel heat transport. This thesis investigates three free parameters: radial profile shifts in experiment-model matching (section 4.5), heat flux limiters $\alpha_{e,i}$ (section 5.7) and anomalous diffusion coefficients D_n (section 6.5). To better understand heat flux limiters, we show the derivation of the fluid equations and discuss their closure in the following section.

2.1 Braginskii equations

Transport equations lie at the heart of every transport code. They prescribe the plasma parameters, density n_a, temperature T_a and velocity u_a of each species a as well as the plasma potential Φ and provide formulas how to calculate all other quantities (drift velocities, heat fluxes, currents etc.) from them. Most sets of transport equations stem from the Braginskii equations [26], which describe a fully ionised plasma consisting of ions with the charge Z and electrons. The Braginskii equations were later generalised for multiple ion species. [27, 28] In this section, we follow the derivation of the fluid equations and discuss the Braginskii closure in order to grasp better the limitations of transport codes. The closure employed by SOLPS-ITER is the Balescu-Zhdanov closure [33, App. B.5], but the difference is mostly confined to specific Z_{eff}-dependent prefactors to the transport coefficients.

2.1.1 The kinetic equation

Fluid equations are derived from the kinetic equation (also called the Boltzmann equation), which describes a population of interchangeable particles, such as electrons, C^{1+} atoms or NH_3 molecules, by prescribing the time evolution of their distribution function $f(t, \mathbf{r}, \mathbf{v})$. The distribution function f has 7 variables: time t, spatial position $\mathbf{r}$ and velocity $\mathbf{v}$.[1] The differential $f(t, \mathbf{r}, \mathbf{v})\mathrm{d}\mathbf{r}\mathrm{d}\mathbf{v}$ expresses the number of particles positioned inside the infinitesimal volume $(\mathbf{r}, \mathbf{r} + \mathrm{d}\mathbf{r})$ which have velocities within the interval $(\mathbf{v}, \mathbf{v} + \mathrm{d}\mathbf{v})$ at time t.

Each species a of interchangeable particles has its own distribution function f_a and the individual distributions influence each other via elastic and inelastic collisions. Generally speaking, elastic collisions preserve the number of particles of each species (the particles only exchange momentum and the associated kinetic energy), while inelastic collisions change the internal energy of the particles and therefore convert particles of one species into another. An example of an inelastic collision is charge exchange

$$D^{*1+} + D^0 \rightarrow D^{*0} + D^{1+}, \tag{2.1}$$

where the star denotes a high-energy or excited particle. Globally, this reaction sees the "destruction" of one neutral deuterium atom in the base state, "creation" of one excited neutral deuterium atom and the loss of energy

[1] Rotational degrees of freedom, which can be important in the description of molecules, are neglected here. [26]

of a deuterium ion. The excited deuterium atoms is considered a different particle species from the deuterium atom in ground state because the two particles can be told apart, so they have distinct distribution functions $f_a(t, \mathbf{r}, \mathbf{v})$. The distribution functions of charged particles are also affected by electromagnetic fields, which can exchange momentum and energy with the particles. [34, Sec. 2.2]

The kinetic equation of species a reads [34, Eq. (2.5)]:

$$\frac{\partial f_a}{\partial t} + v_\beta \frac{\partial f_a}{\partial x_\beta} + \frac{F_{a\beta}}{m_a} \frac{\partial f_a}{\partial v_\beta} = \frac{\partial f}{\partial t}_{coll} \tag{2.2}$$

where Einstein summation is carried out over the subscript β. $\frac{\partial}{\partial x_\beta}$ is the spatial derivative in the direction β, $F_{a\beta} = F_{a\beta}(t, \mathbf{r}, \mathbf{v})$ is the force acting upon species a in the direction β, m_a is the particle mass of species a and $\frac{\partial f}{\partial t}_{coll} = \frac{\partial f}{\partial t}_{coll}(t, \mathbf{r}, \mathbf{v})$ is the collision term of species a. The particular force form depends on the species; for instance, charged particles experience the Lorentz force $q_a(\mathbf{E} + \mathbf{v} \times \mathbf{B})$ most prominently. The collision term $\frac{\partial f}{\partial t}_{coll}$ describes changes in the distribution function caused by collisions with particles of all species in the system, including species a. To sum up the meaning of the equation, the time evolution of the distribution function $\frac{\mathrm{d}f_a}{\mathrm{d}t}$ is moderated by particle collisions.

The kinetic equation is an accurate and useful mathematical description of a plasma, even if it does not capture the motion of each individual particle.[2] It can be solved numerically using kinetic codes, but this is very time-consuming due to its large 7D variable space. In many applications, the fluid description is adopted instead. The fluid approach removes 3 of the 7 variables — the velocity $\mathbf{v}$ — at the cost of losing the ability to describe phenomena stemming from the velocity distribution, such as sheath physics, non-Maxwellian parallel heat fluxes, the Landau damping or most wave-particle interactions. The fluid equations are an adequate substitute for the kinetic equations if the kinetic processes aren't expected to play a large role in the modelled plasma physics or their effect can be simulated ad hoc (using heat flux limiters, sheath boundary conditions etc.). Chapter 5 of this thesis is dedicated to one of these kinetic effects, the overestimation of the parallel heat flux often remedied by "heat flux limiting".

Fluid equations are typically derived by taking three *moments* of the kinetic equation. A moment in kinetic plasma physics is equivalent to a moment in statistics; the distribution function is multiplied by a power of one of its variables and then averaged over this variable. The three resulting equations represent the three basic laws of conservation, conservation of particles, momentum and energy, and they are the heart of transport codes.

[2] Not nearly all statistical properties of a particle system are captured by the kinetic equation. The distribution function is averaged over a large number of particles and time span comparable to the time of flight, and therefore does not capture thermal fluctuations. The terms in the kinetic equation are likewise "smoothed"; the force $\mathbf{F}_a$ doesn't contain the microfields generated when particles come into close vicinity of one another and these effects are rather moved to the collision term $\frac{\partial f}{\partial t}_{coll}$. [26]

2.1.2 Zeroth moment of the kinetic equation: the continuity equation

The zeroth moment of the distribution function, where the multiplication factor is $v^0 = 1$, is the particle conservation equation, also called the continuity equation:

$$\frac{\partial n_a}{\partial t} + \frac{\partial}{\partial x_\beta}(n_a u_{a,\beta}) = S_a, \tag{2.3}$$

where the particle density

$$n_a(t, \mathbf{r}) = \int_{\mathbb{R}^3} f_a(t, \mathbf{r}, \mathbf{v}) \mathrm{d}\mathbf{v} \tag{2.4}$$

is the zeroth moment of the distribution function in the velocity space, and the flow velocity

$$\mathbf{u}_a(t, \mathbf{r}) = \frac{1}{n_a(t, \mathbf{r})} \int_{\mathbb{R}^3} \mathbf{v} f_a(t, \mathbf{r}, \mathbf{v}) \mathrm{d}\mathbf{v} \tag{2.5}$$

is the first moment of the distribution function in the velocity space. The particle source/sink term $S_a(t, \mathbf{r})$ accounts for inelastic collisions as well as external influences (gas puff, particle recycling etc.). The continuity equation states that the local changes in density n_a can be caused by the particles flowing elsewhere as they are carried by the flow velocity $\mathbf{u}_a$, or by locally adding or removing particles of species a.

2.1.3 The need for closure

The continuity equation shows a fundamental property of the moment equations: to describe one moment of the distribution function (here n_a), knowledge of the next moment is required (here $\mathbf{u}_a$). Incidentally, the next moment is always the flux of the prior: the flow velocity $\mathbf{u}_a$ is the flux of density n_a, the pressure tensor $p_a \delta_{\alpha\beta} + \pi_{a,\alpha\beta}$ (proportionate to the energy density) is the flow of momentum $m_a \mathbf{u}_a$, the energy flux $\mathbf{q}$ is the flux of energy density etc. If one takes an infinite number of moment equations, the resulting system is equivalent to the original kinetic equation. In the fluid approach, however, usually only the first three moment equations are considered: the continuity equation (prescribes the density n_a), the equation of motion (prescribes the flow velocity $\mathbf{u}_a$) and the energy transport equation (prescribes the temperature T_a). To prescribe the third moment of the distribution function (energy flux $\mathbf{q}_a$), one does not use the third moment equation but rather an external formula which prescribes the flux in terms of n_a, $\mathbf{u}_a$, T_a and parameters such as heat conductivities or viscosities (which also depend solely on n_a, $\mathbf{u}_a$, and T_a). A set of additional assumptions and formulas which substitutes all remaining moment equations and makes the lower moment system self-sufficient is called a *closure*.

Fluid equations closures can be empirical (such as Fourier's law) or derived from the lower moment equations using particular assumptions. As seen in section 2.1.6, in the Braginskii equations, one assumes a particular *ordering of*

scales which implies that the distribution function is locally Maxwellian and its shape is fully determined by n_a, $\mathbf{u}_a$ and T_a. This allows the calculation of all the required moments and establishes n_a, $\mathbf{u}_a$ and T_a (along with the plasma potential Φ) as the principle variables of the fluid plasma description. While this is the most common type of closure, others have been proposed. Hazeltine presented two of them: a closure based on the ordering of parallel velocities [35] and a closure based on the ordering of sources [36]. These alternative closure have not received as much attention, however, as the small mean free path closure.

The fluid equations closure is one of the defining features of a transport code built upon these equations, since it ushers in further limitations to the modelled plasma physics. If, for instance, the closure assumes that electrons undergo many collisions in the SOL before they are deposited on the divertor target (their mean free path is much smaller than the connection length, the distance along the magnetic field line between the outer midplane and the divertor target), the transport code employing it will predict unphysically high parallel electron heat fluxes in low-collisionality SOL plasmas. Many closures have been published. The popular Braginskii closure, presented in [26] and summarised in section 2.1.6, is simple in containing only one, singly charged ion species. The Balescu [27] and Zhdanov [28] closures, implemented in SOLPS-ITER, elaborate the Braginskii closure in more detail. Rognlien's closure treats perpendicular transport by artificially enhancing the collisionality rather than employing anomalous diffusion. [37] Zawaideh did not stop at closing the equation system at the 2nd kinetic equation moment but continued until the 3rd moment to obtain expressions for electron and ion heat fluxes. [38] In section 2.1.6, the Braginskii equations will be discussed to gauge the limitations of the simulations presented herein. For now, let us return to the kinetic equation moments.

2.1.4 First moment of the kinetic equation: the equation of motion

(For clarity, in the rest of the chapter the subscript a will be omitted. The equations still describe solely the particles of a particular species a.)

Taking the first moment of the kinetic equation by multiplying it with $m\mathbf{u}$ and averaging over the velocity space, one obtains the momentum conservation equation, also called the equation of motion or the momentum transport equation. It is a vector equation which applies individually for each component of the momentum $m\mathbf{u}$. We write its α component:

$$mn\left(\frac{\partial}{\partial t}+u_\beta\frac{\partial}{\partial x_\beta}\right)u_\alpha=-\frac{\partial p}{\partial x_\alpha}-\frac{\pi_{\alpha\beta}}{\partial x_\beta}+qn\left(E_\alpha+(\mathbf{u}\times\mathbf{B})_\alpha\right)+R_\alpha. \quad (2.6)$$

Before we can describe the individual terms, we define the chaotic velocity component

$$\mathbf{v}'=\mathbf{v}-\mathbf{u}(t,\mathbf{r}). \quad (2.7)$$

With it, we can write the scalar pressure

$$p(t,\mathbf{r}) = \int_{\mathbb{R}^3} \frac{1}{3} m v'^2 f(t,\mathbf{r},\mathbf{v}) \mathrm{d}\mathbf{v} \tag{2.8}$$

and the stress tensor

$$\pi_{\alpha\beta}(t,\mathbf{r}) = \int_{\mathbb{R}^3} m \left(v'_\alpha v'_\beta - \frac{v'^2}{3} \right) f(t,\mathbf{r},\mathbf{v}) \mathrm{d}\mathbf{v}, \tag{2.9}$$

which are the two components of the second moment of the distribution function in the velocity space,

$$\int_{\mathbb{R}^3} m v'_\alpha v'_\beta f(t,\mathbf{r},\mathbf{v}) \mathrm{d}\mathbf{v} = p(t,\mathbf{r}) \delta_{\alpha\beta} + \pi_{\alpha\beta}(t,\mathbf{r}). \tag{2.10}$$

Finally,

$$R_\alpha(t,\mathbf{r}) = \int_{\mathbb{R}^3} m v'_\alpha \frac{\partial f}{\partial t}_{coll} (t,\mathbf{r},\mathbf{v}) \mathrm{d}\mathbf{v} + R^{ext}_\alpha(t,\mathbf{r}) \tag{2.11}$$

is the mean change of momentum due to collisions with other species and external momentum sources/sinks. Defining the local temperature as

$$T(t,\mathbf{r}) = \frac{1}{n(t,\mathbf{r})} \int_{\mathbb{R}^3} \frac{1}{3} m v'^2 f(t,\mathbf{r},\mathbf{v}) \mathrm{d}\mathbf{v}, \tag{2.12}$$

one immediately has

$$p(t,\mathbf{r}) = n(t,\mathbf{r}) T(t,\mathbf{r}), \tag{2.13}$$

the ideal gas equation. Note that, in this notation, the unit of temperature are joules and the temperature represents the mean chaotic kinetic energy per particle. The static pressure p then represents the thermal energy density in the plasma. Expressing the fluid equations using electronvolts causes T to be substituted with eT.

The meaning of the momentum conservation equation is the following. The density-weighted momentum of species a can change through five means: flows driven opposite to the scalar pressure gradient (isotropic), viscous effects (anisotropic), the external Lorentz force acting on the particles, collisions with other species and external momentum sources and sinks.

2.1.5 Second moment of the kinetic equation: the energy transport equation

Finally, taking the second moment of the kinetic equation, one arrives at the energy conservation (or transport) equation:

$$\frac{\partial}{\partial t} \left(\frac{mn}{2} u^2 + \frac{3}{2} nT \right) + \frac{\partial}{\partial x_\beta} \left\{ \left(\frac{mn}{2} u^2 + \frac{5}{2} nT \right) u_\beta + \pi_{\alpha\beta} \cdot u_\alpha + q_\beta \right\} = \\ = qn\mathbf{E} \cdot \mathbf{u} + \mathbf{R} \cdot \mathbf{u} + Q \tag{2.14}$$

Here the heat flux density

$$\mathbf{q}(t,\mathbf{r}) = \int_{\mathbb{R}^3} \frac{1}{2} m v'^2 \mathbf{v} f(t,\mathbf{r},\mathbf{v}) \mathrm{d}\mathbf{v} \tag{2.15}$$

is a component of the third moment of the distribution function f and

$$Q(t,\mathbf{r}) = \int_{\mathbb{R}^3} \frac{1}{2} m v'^2 \frac{\partial f}{\partial t}_{coll}(t,\mathbf{r},\mathbf{v})\mathrm{d}\mathbf{v} + Q^{ext}(t,\mathbf{r}) \tag{2.16}$$

is the power generated as a consequence of collisions with other species and external energy sources/sinks.

In accordance with [39, Sec. 1.2], we distinguish between the *heat flux density* and the *energy flux density*. The heat flux density denotes the flux of energy in the Lagrangean frame of reference (co-moving with the fluid). It is defined using the chaotic velocity component v' and vanishes when the distribution function is symmetrical. Conversely, the energy flux density denotes the flux of energy in the Eulerian frame of reference (laboratory). It is defined using the total velocity v and includes not only the heat flux density, but also the energy associated with the plasma movement. In literature, "heat flux" may refer to either quantity. Further complicating the matters, the correct expression for the quantity given in $\mathrm{W/m^2}$ is the heat flux *density*, while the unit of heat flux is W. This distinction is, for instance, important in SOLPS equations, which feature energy and particle fluxes in W and $\mathrm{s^{-1}}$, and before physical interpretation must be converted into flux densities using the cell face cross-section. Shortening "heat flux density" into "heat flux" and making it a synonym for "energy flux" can be confusing. In this thesis, "heat flux density" or "conductive heat flux density" refers to the quantity defined by equation (2.15) [$\mathrm{W/m^2}$], whose dominant contribution is captured by $\nabla_\parallel T$ [39, Sec. 1.2]. Conversely, the "convective energy flux density"

$$\mathbf{q}_{conv} = \frac{5}{2} T n \mathbf{u} + \frac{1}{2} m u^2 n \mathbf{u}, \tag{2.17}$$

given in $\mathrm{W/m^2}$, is the energy flux component associated with the plasma movement as a whole. Occasionally, when referring to the physical flow of energy and not a physical quantity, we will omit "density" for convenience. Lastly, we use *energy flux* and not *power flux*, as for instance [40] does, to preserve the analogy of a time-integral quantity (particles, energy, momentum) flowing somewhere.

The meaning of the energy transport equation is the following. The local energy density, composed of the kinetic energy density $\frac{mn}{2}u^2$ and the thermal energy density $\frac{3}{2}nT$ changes due to eight different processes: flux of kinetic energy $\frac{mn}{2}u^2\mathbf{u}$, flux of thermal energy $\frac{5}{2}nT\mathbf{u}$, flux of pressure energy $\overleftrightarrow{\pi}\cdot\mathbf{u}$, heat flux $\mathbf{q}$, the Joule heating $qn\mathbf{E}\cdot\mathbf{u}$, friction with other species $\mathbf{R}\cdot\mathbf{u}$, collisions with other species where kinetic or internal energy is transferred and external energy sources/sinks.

The energy transport equation is commonly taken as the last moment equation among the fluid equations. To close the equation system, it is necessary to find formulas for $\pi_{\alpha\beta}(t,\mathbf{r})$, $\mathbf{q}(t,\mathbf{r})$, $\mathbf{R}(t,\mathbf{r})$ and $Q(t,\mathbf{r})$ in terms of $n(t,\mathbf{r})$, $\mathbf{u}(t,\mathbf{r})$ and $T(t,\mathbf{r})$. In a multi-particle system, the collision terms may, of course, depend on the parameters of other species as well. This is done using the aforementioned closure. As a result, the Braginskii equations are

solved for five scalar variables in each species: the particle density $n(t, \mathbf{r})$, the three components of the flow velocity $u_\alpha(t, \mathbf{r})$ and the temperature $T(t, \mathbf{r})$.[3]

2.1.6 Braginskii closure

Braginskii derives expressions for $\pi_{\alpha\beta}(t, \mathbf{r})$, $\mathbf{q}(t, \mathbf{r})$, $\mathbf{R}(t, \mathbf{r})$ and $Q(t, \mathbf{r})$ from the kinetic equation by making several assumptions:

- The system evolves on a much slower time scale than the particle collision time.
- Its typical gradient length is much larger than the particle mean free path.
- The electron mass and inertia can be neglected compared to the ion mass and inertia.
- The only two particle species present in the plasma are singly-charged ions ($Z = 1$) and electrons (the so-called simple plasma). Accordingly, we resume the use of species symbol subscripts, with $a = e, i$ referring to electrons and hydrogen (or hydrogen isotope) ions respectively. (Generalising the Braginskii equations to multiple ion species is performed by the Balescu and later Zhdanov closure, which differ from the Braginskii closure mostly in the number of equations and parameter dependence on the effective charge Z_{eff}. [27, 28] SOLPS-ITER uses the Zhdanov closure by default.)
- The plasma is quasineutral, and therefore $n_e(t, \mathbf{r}) = n_i(t, \mathbf{r}) = n(t, \mathbf{r})$.

The first two assumptions allow for solving the kinetic equation for states close to equilibrium. In equilibrium, the distribution function $f = f_0$ is Maxwellian. In states close to equilibrium which meet the first two assumptions, $f = f_0 + \delta f$ is a perturbed Maxwellian where δf is proportional to the gradients of plasma parameters. Specifically, the full solution is:

$$f_a(t, \mathbf{r}, \mathbf{v}) = \left(\frac{m_a}{2\pi T_a(t, \mathbf{r})}\right)^{3/2} n_a(t, \mathbf{r}) \exp\left(-\frac{m_a}{2T_a(t, \mathbf{r})} - (\mathbf{v} - \mathbf{u}_a(t, \mathbf{r}))^2\right) \tag{2.18}$$

Note that the only parameters in this function are the particle density $n_a(t, \mathbf{r})$, flow velocity $\mathbf{u}_a(t, \mathbf{r})$ and temperature $T_a(t, \mathbf{r})$. This allows for eventually closing the fluid equations system.

Using perturbation analysis to find $f_a(t, \mathbf{r}, \mathbf{v})$ has the peculiar consequence that $\pi_{a,\alpha\beta}(t, \mathbf{r})$, $\mathbf{q}_a(t, \mathbf{r})$, $\mathbf{R}_a(t, \mathbf{r})$ and $Q_a(t, \mathbf{r})$ are directly proportional to the local plasma parameter gradients. [26, page 213] For instance, the ion heat flux is proportional to ∇T_i. The coefficients of proportionality are called the *transport coefficients* and their exact value depends on the type of closure one employs. All types of closure available within SOLPS-ITER (Braginskii, Balescu [27] and Zhdanov [28]) share the first two assumptions with the Braginskii closure, and thus their expressions for $\pi_{a,\alpha\beta}$, $\mathbf{q}_a$, $\mathbf{R}_a$ and Q_a share

[3] Many transport codes including SOLPS-ITER assume toroidal symmetry, which removes one component of $\mathbf{u}$, and prescribe the radial transport in terms of anomalous diffusion and drifts, removing another component of $\mathbf{u}$. This further reduces the variable number.

the same functional dependence but can differ in the value of the parallel transport coefficients. [33, Sec. B.2]

Using the ordering of temporal and spatial scales, further described in [26] and [41], separation of the perpendicular and parallel transport scales, the assumption of completely ionised hydrogen plasma ($Z = 1$) and $m_e \ll m_i$, one obtains the following expressions.[4]

The stress tensor $\pi_{a,\alpha\beta}(t, \mathbf{r})$ has the same form for electrons and ions, differing only in the viscosity coefficients η_a values. The tensor is symmetric and its 6 independent components can be written using the rate-of-strain tensor,

$$W_{a,\alpha\beta} = \frac{\partial u_{a,\alpha}}{\partial x_\beta} + \frac{\partial u_{a,\beta}}{\partial x_\alpha} - \frac{2}{3}\delta_{\alpha\beta}\nabla\mathbf{u}_a. \tag{2.19}$$

In the orthogonal Cartesian coordinate system $[x, y, z]$ where z is parallel to the magnetic field:

$$\begin{aligned}
\pi_{a,zz} &= -\eta_{a,0}W_{a,zz} \\
\pi_{a,xx} &= -\frac{1}{2}\eta_{a,0}\left(W_{a,xx} + W_{a,yy}\right) - \frac{1}{2}\eta_{a,1}\left(W_{a,xx} - W_{a,yy}\right) - \eta_{a,3}W_{a,xy} \\
\pi_{a,yy} &= -\frac{1}{2}\eta_{a,0}\left(W_{a,xx} + W_{a,yy}\right) - \frac{1}{2}\eta_{a,1}\left(W_{a,yy} - W_{a,xx}\right) + \eta_{a,3}W_{a,xy} \\
\pi_{a,xy} &= \pi_{a,yx} = -\eta_{a,1}W_{a,xy} + \frac{1}{2}\eta_{a,3}\left(W_{a,xx} - W_{a,yy}\right) \\
\pi_{a,xz} &= \pi_{a,zx} = -\eta_{a,2}W_{a,xz} - \eta_{a,4}W_{a,yz} \\
\pi_{a,yz} &= \pi_{a,zy} = -\eta_{a,2}W_{a,yz} + \eta_{a,4}W_{a,xz}
\end{aligned} \tag{2.20}$$

The ion viscosity coefficients are:

$$\begin{aligned}
\eta_{i,0} &= 0.96nT_i\tau_i & \eta_{i,1} &= \frac{3}{10}\frac{nT_i}{\omega_{ci}^2\tau_i} \\
\eta_{i,2} &= 4\eta_{i,1} & \eta_{i,3} &= \frac{1}{2}\frac{nT_i}{\omega ci} & \eta_{i,4} &= 2\eta_{i,3}
\end{aligned} \tag{2.21}$$

where the ion collision time is

$$\tau_i = 12\pi^{3/2}\frac{\varepsilon_0^2 m_i^{1/2} T_i^{3/2}}{ne^4 \ln\Lambda} \tag{2.22}$$

($\ln\Lambda$ is the Coulomb logarithm) and the ion cyclotron frequency is

$$\omega_{ci} = \frac{eB}{m_i}. \tag{2.23}$$

The electron viscosity coefficients are:

$$\begin{aligned}
\eta_{e,0} &= 0.73nT_e\tau_e & \eta_{e,1} &= 0.51\frac{nT_e}{\omega_{ce}^2\tau_e} \\
\eta_{e,2} &= 4\eta_{e,1} & \eta_{e,3} &= -\frac{1}{2}\frac{nT_e}{\omega ce} & \eta_{e,4} &= 2\eta_{e,3}
\end{aligned} \tag{2.24}$$

[4] We use formulas from [42, Sec. 2.3] instead of [26], since the former uses SI units.

where the electron collision time is

$$\tau_e = 3(2\pi)^{3/2}\frac{\varepsilon_0^2 m_e^{1/2} T_e^{3/2}}{ne^4 \ln\Lambda} \tag{2.25}$$

and the electron cyclotron frequency is

$$\omega_{ce} = \frac{eB}{m_e}. \tag{2.26}$$

The electron heat flux $\mathbf{q}_e$ consists of two contributions, the heat flux due to friction

$$\mathbf{q}_{u,e} = nT_e\left(0.71\mathbf{u}_\parallel + \frac{3}{2|\omega_{ce}|\tau_e}\mathbf{b}\times\mathbf{u}\right), \tag{2.27}$$

where $\mathbf{u} = \mathbf{u}_e - \mathbf{u}_i$ is the mutual velocity of electrons and ions and $\mathbf{b} = \mathbf{B}/B$, and the thermal heat flux

$$\mathbf{q}_{T,e} = \frac{nT_e\tau_e}{m_e}\left(-3.16\nabla_\parallel T_e - \frac{4.66}{\omega_{ce}^2\tau_e^2}\nabla_\perp T_e - \frac{5}{2|\omega_{ce}|\tau_e}\mathbf{b}\times\nabla T_e\right). \tag{2.28}$$

The ion heat flux is

$$\mathbf{q}_i = \frac{n_i T_i \tau_i}{m_i}\left(-3.9\nabla_\parallel T_i - \frac{2}{\omega_{ci}^2\tau_i^2}\nabla_\perp T_i - \frac{5}{2|\omega_{ci}|\tau_i}\mathbf{b}\times\nabla T_i\right). \tag{2.29}$$

The rate of momentum transfer from electrons to ions $\mathbf{R}_i$ is the same as the momentum transfer from ions to electrons $\mathbf{R}_e = -\mathbf{R}_i$. (External momentum sources are not considered.) Electrons and ions exchange momentum via two forces, the friction force and the thermal force. Writing $\mathbf{R}_e = \mathbf{R}_{u,e} + \mathbf{R}_{T,e}$, the friction force is

$$\mathbf{R}_{u,e} = -\frac{m_e n}{\tau_e}\left(0.51\mathbf{u}_\parallel + \mathbf{u}_\perp\right) \tag{2.30}$$

where $\mathbf{u}_\parallel$ is the projection of the relative velocity $\mathbf{u}$ along the magnetic field line and $\mathbf{u}_\perp = \mathbf{u} - \mathbf{u}_\parallel$. Using the plasma current $\mathbf{j} = en\mathbf{u}$ and the parallel and perpendicular plasma conductivity

$$\sigma_\parallel = 1.96\frac{n_e e^2\tau_e}{m_e} \tag{2.31}$$

$$\sigma_\perp = \frac{n_e e^2\tau_e}{m_e}, \tag{2.32}$$

the friction force can also be written as

$$\mathbf{R}_{u,e} = ne\left(\frac{\mathbf{j}_\parallel}{\sigma_\parallel} + \frac{\mathbf{j}_\perp}{\sigma_\perp}\right). \tag{2.33}$$

The thermal force is

$$\mathbf{R}_{T,e} = -0.71n\nabla_\parallel T_e - \frac{3}{2}\frac{n}{|\omega_{ce}|\tau_e}\mathbf{b}\times\nabla T_e. \tag{2.34}$$

Finally, the ion heat source contains the energy transfer from electrons via collisions

$$Q_i = \frac{3m_e n}{m_i\tau_e}(T_e - T_i), \tag{2.35}$$

while the electron heat source features the same term taken negatively and the Ohmic heating:

$$Q_e = -\mathbf{R}_e \cdot \mathbf{u} - Q_i = \frac{j_\parallel^2}{\sigma_\parallel} + \frac{j_\perp^2}{\sigma_\perp} + \frac{1}{ne}\mathbf{j} \cdot \mathbf{R}_{T,e} + \frac{3m_e n}{m_i \tau_e}(T_i - T_e) \tag{2.36}$$

The three conservation laws and the closure expressions form a closed equation system called the Braginskii equations. In transport codes, Braginskii equations are supplemented by the current equation $\nabla \mathbf{j} = 0$ which expresses the plasma quasineutrality. This allows the calculation of the plasma potential $\Phi(t, \mathbf{r})$, which then self-consistently yields the electric field $\mathbf{E} = -\nabla\Phi$. Solving for the magnetic field $\mathbf{B}$ usually is not in the scope of transport codes, making them electrostatic rather than electromagnetic. The magnetic field is typically taken from a magnetic equilibrium reconstruction using the Grad-Shafranov equation. [42, Sec. 3.3]

2.1.7 Boundary conditions

The Braginskii equations assume that the plasma is boundless, both in time and space. Real plasmas modelled by transport codes are, however, always bounded. Temporal boundaries are unimportant for this thesis, but spatial boundaries of the plasma remain an important consideration. Description of the edges of the computational domain is the subject of transport code *boundary conditions*.

Edge plasma transport codes such as SOLPS-ITER utilise a large number of boundary conditions. Denoting the number of ion species n_s, boundary conditions must be specified for each of its $2n_s + 3$ equations (n_s continuity equations, n_s equations of motion, 2 energy transport equations and the electric potential equation) separately at each boundary of the computational domain. In this work, default SOLPS-ITER boundary conditions were applied in nearly all cases. They are essentially simple boundary conditions, such as "the radial flux of C^{1+} ions from the plasma core into the simulated edge region is 0 s^{-1} in each cell of the computational domain". Other boundary conditions, however, correspond to sophisticated physics description of the processes occurring at the domain edge. Their impact on the simulated plasma becomes so marked that they form, *de facto*, a part of the physics system of the edge transport code. The most important boundary conditions in the context of this thesis are the ones governing plasma contact with the divertor plates: the *sheath boundary conditions*.

The sheath forms a complex interface between a plasma and a solid surface. In the tokamak, its physics is intimately involved with the plasma-wall interaction by governing the largest channel of direct energy exchange between the plasma and the divertor plasma-facing components. Sheath physics dictates the boundary conditions for particle and momentum transport equations by requiring the Bohm criterion to be met, that is, that the flow of plasma into the sheath is sonic at the ion sound speed $c_s = \sqrt{e(T_e + T_i)/m_i}$. [12, Sec 2.1] They further postulate the boundary conditions for energy transport

equations by specifying the amount of plasma thermal energy absorbed by the sheath:

$$q_{\parallel a} = \gamma_a e T_e n_e c_s \tag{2.37}$$

where γ_a is the *sheath heat transmission coefficient* of electrons or ions, and n_e and T_e are evaluated at the sheath edge. [12, Sec. 2.8] Finally, the plasma potential at the sheath entrance is determined by the biasing potential of the solid surface and the sheath potential drop, which depends most sensitively on the local electron temperature T_e. [12, Sec. 2.6] The sheath boundary conditions are significantly more complicated than the majority of SOLPS-ITER boundary conditions, precisely because much of the code's results and predictive power rests of them.

Interestingly, it is outside the scope of the Braginskii equations solver to understand why these specific boundary conditions are required, or what happens to the plasma particles, energy and momentum once it passes through the boundaries. As elaborated in the next section, often a completely different part of plasma physics than the one described in this chapter is required to explain the processes occurring at the edge plasma boundaries. They can be MHD phenomena with variable magnetic field, explaining the pedestal transport, or kinetic phenomena based in the velocity space, explaining the energy transport through the sheath. Choosing the appropriate boundary condition and/or its free parameters, such as the formula for the sheath heat transmission coefficient γ_a, is often relegated as the responsibility of the modeller, and it is the subject of intense research.

2.2 Edge transport code weaknesses

Limitations of edge transport codes generally stem from three sources: the fluid equations (loss of velocity space information), their closure (assumptions on the scale ordering) and the diffusive ansatz (simplification of radial transport). An exact list of criteria can be found in [43, Sec. 2.1.4]. As a result of these limitations, modellers of the tokamak edge often face the following challenges.

The sheath cannot be described self-consistently within a transport code. The sheath violates the spatial ordering assumption, as the plasma parameters vary greatly over a distance smaller than the mean free paths. As a result, neither the ion nor the electron velocity distribution function at the sheath edge is Maxwellian [Sec. 25.1][12] [44] and the Braginskii closure fails. This is usually overcome by modelling the sheath in a separate kinetic simulation and implementing the results as a boundary condition (for instance, [39, 45]). Essentially, the transport code knows nothing of what happens inside the sheath, only how the sheath *appears* from the outside. With regard to particle transport, the sheath is an efficient particle sink, removing all ions from the plasma as they enter it and returning approximately the same amount of neutral particles. With regard to momentum transport,

the sheath is surrounded by the pre-sheath electric field which accelerates ions toward the solid surface. With regard to energy transport, the sheath is an energy sink which cools the plasma at the rate given by equation (2.37).

Parallel transport may not be collisional enough to employ classical thermal conductivities and viscosities. This is, again, a violation of the spatial scale ordering assumption. In high-temperature or low-density tokamak SOL, the mean free path can be comparable to the connection length or the gradient size. For instance, taking the COMPASS tokamak H-mode #16908 simulation presented in section 5.1, one can calculate the electron and ion mean free path as, respectively, 2.1 m and 28 m. (Details of the calculation are given in table 5.1.) This is comparable to the connection length from the outer midplane, which is 6 m for the outer target and 12 m for the inner target. An even larger violation of spatial scales ordering is expected in the tokamak ITER, where the connection length can be 19-53x longer than the mean free path. [46] Evidently, such plasmas are not collisional enough to apply the Braginskii equations closure without reserve. The low collisionality reduces the efficiency of collision-mediated channels of energy and momentum transport, which can be expressed as the reduction of thermal conduction $\kappa\nabla_\parallel T$ and viscous momentum transfer $\eta\nabla_\parallel V_\parallel$. Using the "classical" formulas derived within the Braginskii equations may result in overestimation of heat or momentum fluxes, and even numerical instabilities in the case of unphysical viscous heating. Many paths toward correcting the fluxes have been pursued, from coupling the fluid code to a 1D kinetic code solving only the parallel heat transport [47, 48] to analytic expressions for non-Maxwellian distribution functions [49, 18]. The theory of heat flux limiting is elaborated in chapter 5.

The anomalous diffusion coefficients must be chosen. Since transport codes typically model the perpendicular transport using the diffusive ansatz, where diffusion coefficients are free input parameters, the modeller is faced with the choice which value to choose and whether to employ a radial profile. It is possible to tailor the D_n and $\chi_{e,i}$ radial profile to exactly match the experimental upstream profile [50], as well as choosing a poloidally varying diffusion coefficients to mimic the turbulent ballooning transport [51]. There are concerns, however, that this may constitute overfitting [52]. Experimental profiles are uncertain, not only in the temperature and density values, but often also in the radial coordinate thanks to inaccuracies in the magnetic equilibrium reconstruction. In transport codes, a common practice is to choose a spatially constant value of D_n and $\chi_{e,i}$ in L-mode and to employ a simplified profile in the shape of a transport barrier in H-mode. [53, 51] This problem is explored in section 6.5.

Steep gradients might develop in front of the divertor targets. As [43, Sec. 2.1.4] describes, low target temperatures (e.g. divertor detachment) may induce gradient lengths which violate the spatial scales ordering and cause code instability. The instability can be alleviated by increasing the grid resolution, but the breakdown of Braginskii equations usually requires solving the problem of plasma transport with another method, usually a kinetic simulation.

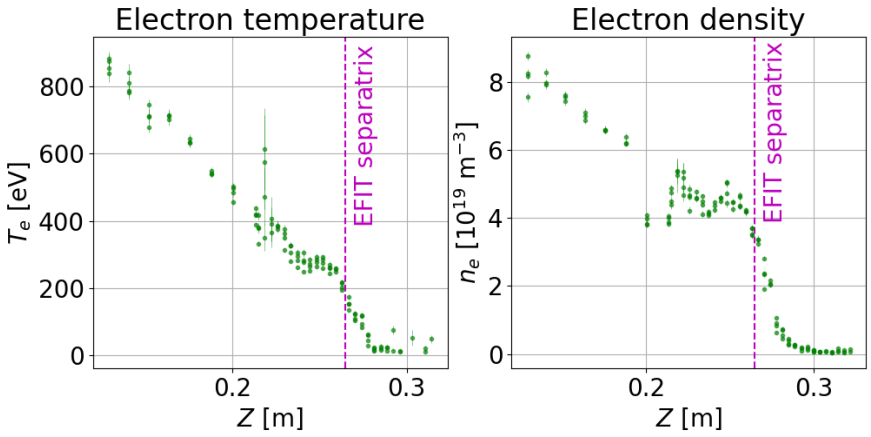

Figure 2.1: Radial profiles of the electron temperature and density measured during the period $t = 1120$-1150 ms during the COMPASS H-mode discharge #16908 (all measurements are inter-ELM). In magenta, the separatrix position as reconstructed by EFIT in this discharge is plotted. The separatrix lies near the top of the pedestal, which is obviously incorrect.

The magnetic equilibrium reconstruction underlying the transport code grid may be inaccurate. This problem does not stem from the Braginskii equations as much as their implementation on grids constructed atop a magnetic equilibrium reconstruction. Inaccuracies in the reconstruction, and particularly errors in the separatrix position, will complicate matching simulated plasma parameters to their experimental counterparts in interpretative simulations. Let us take as example the simulation of COMPASS H-mode #16908 presented in section 5.1. Plotting in figure 2.1 the upstream electron temperature T_e profile measured at the top of the plasma by the Thomson scattering diagnostic during the period $t = 1120$-1150 ms (each measurement is inter-ELM), we observe that the EFIT++ magnetic equilibrium reconstruction at $t = 1130$ ms places the separatrix on top of the pedestal, where $T_{e,u} = 200$ eV. Compare this to the peak target electron temperature measured by the combined divertor probe array during the same period, $T_{e,t} = 70$ eV. Notwithstanding that placing the separatrix on top of the pedestal is obviously wrong, matching these upstream and target parameters *simultaneously* in a SOLPS-ITER simulation is difficult. A common solution in such a situation is to introduce an arbitrary mutual spatial shift between the simulation and experimental profiles, "correcting" the equilibrium reconstruction just enough that simulation-experiment match can be achieved. Such profile shifts constitute, in effect, another free input parameter of the transport simulation. Chapter 4 is dedicated to exploring this problem.

These limitations are relatively well-explored, owing to the long history and popularity of transport codes. (The first predecessor of SOLPS-ITER, B2, was published in 1982 [54].) It remains an open question, however, to what extent they affect simulations of different tokamaks in different edge transport regimes. In a high-density discharge, for example, parallel transport may be collisional enough to employ classical thermal conductivities without

reserve. Values of perpendicular transport coefficients may change poloidally, between devices and plasma regimes (such as the density shoulder observed at ASDEX-Upgrade [55]). Equilibrium reconstructions may be more or less accurate. Chapters 5, 6.5 and 4 are dedicated to exploring the latter three problems in turn, as applied to SOLPS-ITER simulations of the COMPASS tokamak edge plasma.

2.3 Interpretative edge transport code modelling

Interpretative transport modelling of the tokamak edge plasma is a cornerstone of understanding the complex interplay of the hot confined plasma, cold SOL plasma, neutrals, impurities and the plasma-facing components. Due to diagnostic limitations, all of these actors are difficult to untangle in experiment. Edge transport modelling provides a first-principles insight into the transport and atomic processes occurring in the plasma edge, and allows a degree of predictive control unchallenged by other types of codes.

An interpretative simulation is one which was set up to match a chosen experiment as closely as possible. In the case of the steady-state tokamak edge plasma, the modelled plasma usually represents a stable part of a tokamak discharge. The modeller acquires as many diagnostic measurements as possible, and tries to match them all in the interpretative simulation. In particular, our simulations have been defined by *matching upstream and target plasma parameters at once*. This effort is marked with trade-off and compromise. In our simulations, we have aimed for the level of match within a factor of two from all experimental measurements. This may seem lenient, but the uncertainties and systematic errors of diagnostic measurements are often no better. Some simulation outputs (e.g. divertor target electron density n_e) are extremely sensitive to the simulation input, while others (e.g. upstream separatrix electron temperature T_e) are difficult to stir at all. Combined with the number of SOLPS-ITER input parameters and physical phenomena left out of its equations (e.g. electric drifts), and striving for exact quantitative agreement becomes futile.

Our "canary in the coal mine", the most useful sensitive parameter, has been the peak outer target electron temperature $T_e^{(OT,peak)}$. $T_e^{(OT,peak)}$ is an important plasma parameter in simulations of fusion reactors, as it determines the long-term target erosion and, by governing power and pressure losses, target energy fluxes. Inner target peak T_e is usually lower, so it plays a lesser role. In interpretative simulations of COMPASS, $T_e^{(OT,peak)}$ is a well-diagnosed quantity with only moderate uncertainties. Contrast this to the peak outer target electron density $n_e^{OT,peak}$. $n_e^{OT,peak}$ also determines fusion reactor target sputtering and energy fluxes, and it is also sensitive to simulation input. However, its experimental measurements are significantly more uncertain, which led us to use the ion saturated current density $j_{sat} \propto n_e T_e^{3/2}$ for matching experimental and simulation data rather than the target n_e. Additionally, the ratio of the upstream separatrix $T_{e,sep}$ and $T_e^{(OT,peak)}$

is intimately tied to the amount of power and pressure losses along the field line, as well as the SOL regime, while $n_e^{(OT,peak)}$ is not directly related to $n_{e,sep}$. Compared to upstream separatrix plasma parameters, peak target parameters are more sensitive to simulation input and they do not suffer from the separatrix position uncertainty. Finally, $T_e^{(OT,peak)} < 10$ eV is one of the definitions of detachment discussed in this thesis. On the whole, $T_e^{(OT,peak)}$ is more relevant to edge plasma physics, it is better diagnosed, and it offers immediate insights into the SOL transport regime. This is why we consider the peak outer target electron temperature $T_e^{(OT,peak)}$ perhaps the most important plasma parameters in experiment-model matching.

While matching experimental and simulation data in this thesis, we shall furthermore put more emphasis on the near SOL (approx. the first 5 mm of SOL at the outer midplane, 2 heat flux fall-off lengths $\lambda_q \approx 2.5$ mm) than the far SOL. This is because the near SOL carries most of the parallel heat flux and determines the most important transport parameters of the simulation: the amount of charged particle power converted to radiation and neutral energy (power balance), the sputtering intensity and therefore intrinsic impurity concentration, the peak target energy fluxes etc. The far SOL will be relatively neglected, both in efforts to match experimental and simulation data and in their discussion.

Chapter 3

The COMPASS and COMPASS Upgrade tokamaks

This chapter gives a brief introduction of the COMPASS and COMPASS Upgrade tokamaks. Special attention will be given to the COMPASS diagnostics used for interpretative SOLPS-ITER simulations, and to the applicability of COMPASS interpretative transport simulations to COMPASS Upgrade predictive transport simulations.

3.1 COMPASS

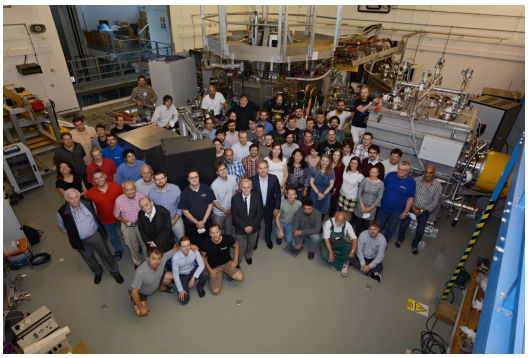

(a) : The COMPASS tokamak and its team, September 2021.

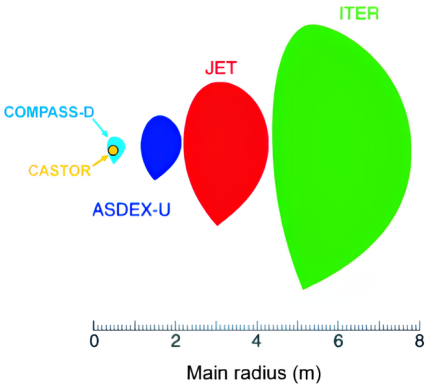

(b) : Size comparison of tokamaks CASTOR, COMPASS, ASDEX Upgrade, JET and ITER. Reprinted from [56].

Figure 3.1: The COMPASS tokamak.

The COMPASS (COMPact ASSembly) tokamak, shown in figure 3.1, was a compact machine operated at the Institute of Plasma Physics, Prague, between 2009 and 2021. [57, 58, 2] It was disassembled two years ago to make space for its successor, the COMPASS Upgrade tokamak. COMPASS had ITER-like geometry in the scale 1:10[1]; major radius $R = 0.56$ m, minor radius $a = 0.23$ m, elongation up to 1.8, plasma current $I_p < 400$ kA, toroidal magnetic field at the magnetic axis $B_t = 0.9 - 1.6$ T and pulse duration $t < 0.4$ s. During its final campaign with an additional neutral beam injector, it reached central electron temperatures of $T_e \leq 2$ keV and densities of $n_e \leq 1.5 \times 10^{20}$ m^{-3}. Its additional heating systems comprised three NBI beams, which facilitated NBI-assisted H-mode, but purely ohmic H-mode was also possible. It was equipped with a broad set of diagnostics [59, 60], including high-resolution Thomson scattering [61, 62], lithium beam emission spectroscopy [63, 64], two divertor probe arrays [65, 66], infrared thermography [67] and four reciprocating probes [60]. Its first wall was made of stainless steel and its limiters and divertor were made of carbon.

The COMPASS scientific program encompassed many areas. [68] Most prominent was edge plasma physics, concerning H-mode [58, 69, 70, 71],

[1] In practise, the plasma shape could be quite different. Typical COMPASS triangularity was, for example, much smaller than the one envisioned for the ITER baseline scenario.

pedestal width [72, 73, 74], L-H power threshold and isotope effects [75], ELMs and their control by resonant magnetic perturbations and vertical kicks [76, 77, 78], zonal flows [79, 80], transport in the edge plasma [81, 82, 83, 84] including detachment studies [85, 86], and edge plasma turbulence [87, 88, 89, 90]. Experiments with liquid lithium target were conducted. [6, 91, 92] Additional COMPASS research areas were MHD equilibrium and instabilities [93], plasma-wall interaction [94, 95, 96] and physics of runaways and disruptions [97, 98, 99, 100, 101, 102]. An overview of major COMPASS results is given in [2].

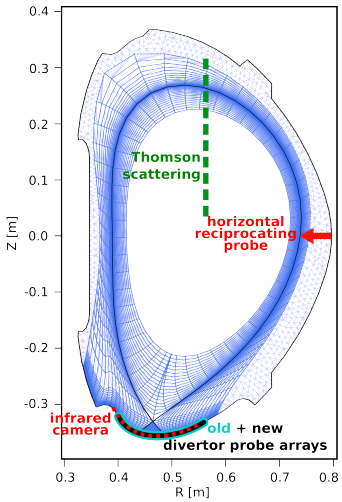

(a) : Diagnostic measurement locations of the Thomson scattering diagnostic, the horizontal reciprocating probe, the combined and swept divertor array, and the divertor infrared camera.

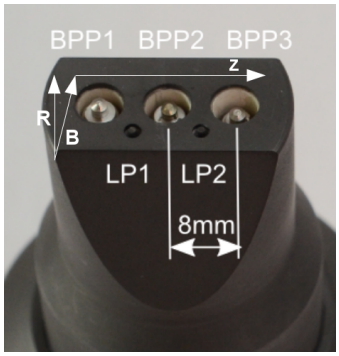

(b) : The probe head installed on the horizontal reciprocating probe in COMPASS discharges #13812-#13825, carrying three ball-pen probes (BPP1,2,3) and two Langmuir probes (LP1,2). Reprinted from [70].

Figure 3.2: Diagnostics of the COMPASS tokamak.

The following diagnostics were used in this work for direct comparison of experimental data and interpretative COMPASS SOLPS-ITER modelling results: the Thomson scattering (TS) diagnostic, the horizontal reciprocating probe (HRCP), the combined divertor array, the swept divertor array, and the divertor infrared (IR) camera. Figure 3.2a depicts schematically their measurement locations. Additionally, many diagnostics were used indirectly, such as bolometric measurements (power radiated in the confined plasma), magnetic measurements (magnetic equilibrium reconstruction with the EFIT++ code), or basic tokamak diagnostics of the plasma current I_p and loop voltage U_l (ohmic heating power). The following sections are dedicated to the directly used diagnostics. Their limitations, uncertainties and data processing details play an important role in interpretative simulations.

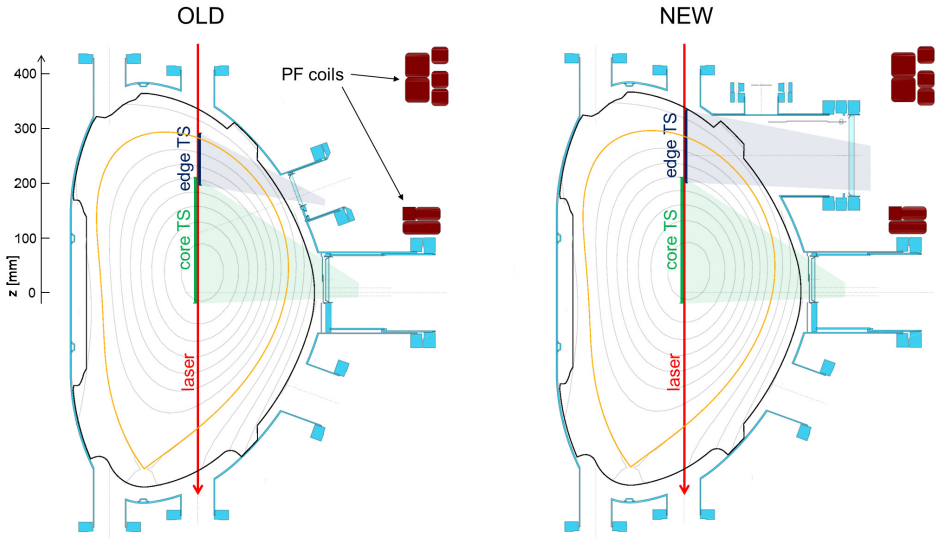

Figure 3.3: Scheme of the Thomson scattering (TS) diagnostic system, before and after the upgrade described in [62]. Reprinted from [62].

3.1.1 The Thomson scattering diagnostic

The Thomson scattering (TS) diagnostic measures the electron temperature T_e and density n_e on the plasma top by the means of Thomson scattering of laser light on electrons. It operates by periodically shining a short (~ 7 ns) laser pulse through the plasma from one of the tokamak vessel top ports, see figure 3.3. The vertical laser path is observed as it cuts approximately radially through the top half of the plasma, by two separate sets of viewing optics: one belonging to the core TS diagnostic system and one belonging to the edge TS diagnostic system. The laser light scattered by electrons into the viewing optics is collected and its spectrum is analysed and fitted to reconstruct T_e and n_e along the laser chord.

Designed and built during the COMPASS tokamak installation [61, 58], the Thomson scattering diagnostic has undergone constant improvement and development [103, 104, 105, 62] and become a routine, highly trustworthy measurement of the core and edge electron parameters with the ultimate repetition rate 120 Hz. In interpretative modelling of the COMPASS tokamak, we use the edge Thomson scattering system as a source of upstream (plasma top) T_e and n_e.

Data processing and error bars. Raw data collected by the optics of the Thomson scattering diagnostic systems was processed by the TS group of the COMPASS team. The resulting T_e, n_e and their error bars were saved into the COMPASS experimental database. Each laser blip results in one T_e and n_e profile with error bars representative of the data point uncertainty. [106] Since

the laser blip is very short, the individual profiles reflect the current state of turbulence in the plasma. To reduce the impact of plasma fluctuations, we used several consecutive profiles whenever possible. In L-mode, data collected over the entire steady-state phase of the discharge was employed. In H-mode, we used consecutive measurements which fell into the inter-ELM period and here global plasma parameters remained constant. We discarded data points with an error bar larger than 50 %, as well as obviously incorrect outliers (e.g. $T_e > 200$ eV in the SOL). These values occasionally occur when the TS data processing algorithm cannot fit the scattered light spectrum properly. The same occurs when the plasma density is very low, which is why data points with $n_e < 10^{18}$ m^3 (and their simultaneously measured T_e counterparts) were discarded from the analysis. In this work, SOLPS-ITER data is matched with discrete T_e and n_e *data points*, but in the future a *profile* fitting routine could be used in H-mode. [72]

Unique features and caveats. In the final years of the Thomson scattering diagnostic operation, it was discovered that light scattered from the steel vacuum vessel considerably impacted the measurements. Subtraction of the stray light became routine in discharges from #20366 and less accurate corrections were applied retroactively on demand. [107] All the data used in this thesis have been corrected for stray light, and it was observed that the correction improved the edge plasma profiles significantly, reducing scatter and error bars. In this work, interpretative simulation uncertainty is reduced by comparing experimental data to simulation results directly at the place of the experimental measurement. The only exception are TS measurements in section 6.1, where they are mapped to the outer midplane to facilitate simultaneous comparison to horizontal reciprocating probe results. This introduces the uncertainty of inaccurate equilibrium reconstruction. It was found, however, that the TS profiles generally needed little to radial position correction ($-$1-5 mm in 4/5 cases). This suggests that, in the discharges investigated in section 6.1, the equilibrium reconstruction is quite accurate at the plasma top.

3.1.2 The horizontal reciprocating probe

The horizontal reciprocating probe (HRCP) provided this work with measurements of the plasma potential Φ, electron temperature T_e and electron density n_e at the outer midplane of the COMPASS tokamak using several electric probes mounted on a reciprocating probe head. The HRCP reciprocation comprises of a fast movement in and out of the plasma, stops approximately at the separatrix, and lasts approximately 150 ms altogether. The probe pins installed on the probe head interact with charged plasma particles along the way, and their resulting voltages and currents can be processed and combined to reconstruct Φ, T_e and n_e.

The horizontal reciprocating probe, consisting of a removable probe head and a reciprocating manipulator, was first installed on the COMPASS tokamak during its commissioning. [59, 58] Many probe heads have been designed

and installed during the years, including the "high heat flux" probe head with large Langmuir probes [108] and the "Reynolds stress" probe head with radially spaced pins [90, 75]. In discharges #13812-#13825, modelled in this thesis, the reciprocating manipulator carried a probe head with 3 ball-pen probes and 2 Langmuir probes, shown in figure 3.2b. Langmuir probes are a traditional edge plasma diagnostics [12, Sec. 2.7] while ball-pen probes [109, 110, 111, 112] are a relatively novel design, similar to the ion-sensitive probe [113, 114, 115] or the Katsumata probe [116, 117]. One of the Langmuir probes (LP1) was electrically floating (insulated from the ground, zero passing current), with its floating potential determined by the plasma potential Φ and the electron temperature T_e [70]:

$$V_{LP} = \Phi + 2.8T_e. \tag{3.1}$$

The other Langmuir probe (LP2) was biased to the large negative voltage $V_{bias} = -250$ eV, so it repelled all electrons and collected only the ion saturation current [12, Eq. (2.74)]

$$I_{sat} = \frac{1}{2} e A_{probe} n_e c_s, \tag{3.2}$$

where $A_{probe} = 4.9$ mm^2 is the collecting area of the pin, equal to the pin surface area. [118, p. 2.1.2] The ball-pen probes BPP1,2,3 were operated in the floating regime. Their collector pin is shielded from electrons, so their floating potential V_{BPP} is closer to the plasma potential than V_{LP}: [119]

$$V_{BPP} = \Phi + (0.6 \pm 0.3)\, T_e \tag{3.3}$$

The time traces of the two floating voltages and the ion saturation current collected with the sampling frequency 5 MHz were stored in the COMPASS experimental database.

The HRCP probe head was installed in the tokamak vessel so that its ball-pen probes were spaced poloidally, allowing the measurement of the poloidal electric field

$$E_p = \frac{V_{BPP,1} - V_{BPP,2}}{d} \tag{3.4}$$

where $d = 8$ mm is the distance between the probes. This yields results in the order $E_p \sim$ kV.m^{-1}, with fluctuation levels in the hundreds of V.m^{-1}. The poloidal electric field in the SOLPS-ITER simulation is, however, $E_p \sim$ V.m^{-1}. This may be the result of SOLPS neglecting plasma turbulence, since it operates on a larger temporal and spatial scale. In reality, poloidal electric field E_p is formed by the interaction of shear flows and turbulent structures in the plasma edge via Reynolds stress. [75] This physics is entirely absent from SOLPS. Conversely, turbulence simulations of the COMPASS tokamak edge plasma with the ESEL code have shown E_p fluctuation levels in the lower hundreds of V.m^{-1}. [120] We conclude that SOLPS E_p is not realistic in our simulations, and we do not use HRCP E_p for experiment-model matching.

The probes installed on the HRCP also allow the measurement of the parallel energy flux density,

$$q_{\parallel} = \gamma \frac{I_{sat}}{A_{probe}} T_e, \tag{3.5}$$

where T_e is given in eV, $q_{\parallel}$ is given in W.m^{-2} and the classical value of the heat flux transmission factor $\gamma = 7$ is used. [12, Eq. (2.95)] However, this parallel energy flux did not match the simulation either — it was 2-4× higher than the SOLPS-ITER energy flux at the outer midplane. A thought experiment explains the discrepancy. Let us say we measure plasma parameters with a reciprocating probe at the SOLPS-ITER stagnation point. This is the poloidal location, usually between the outer midplane and the plasma top, where the parallel velocity $u_{\parallel}$ and the parallel energy flux $q_{\parallel}$ are zero as they switch from positive (toward the outer target) to negative (toward the inner target). At the stagnation point, the plasma has finite T_e and n_e, resulting in relatively high $q_{\parallel}$ measured by the probe using equation (3.5), but $q_{\parallel} = 0$ in the SOLPS-ITER simulation. An explanation may be that the probe does not really measure the energy flux travelling along the field lines; it measures the energy flux impinging onto the *probe*. Inserted into a plasma which does not flow anywhere with a perfectly symmetric Maxwellian distribution function (total energy flux is zero), the probe would still measure finite $q_{\parallel}$ thanks to the sheath forming around it. A possible avenue would be to implement $q_{\parallel}$ on the SOLPS side as an "artificial diagnostic", by replicating equation (2.37) with $\gamma = 7$. This can be done in future work. In this thesis, matching T_e and n_e is considered as sufficient proof that thus constructed $q_{\parallel}$ would match as well, and HRCP $q_{\parallel}$ is not used for experiment-model matching.

Data processing and error bars. The time traces of floating potentials $V_{BPP,LP}$ and the ion saturation current I_{sat} were collected during a period where global plasma parameters were approximately constant and the probe was moving inward. Their offset from zero, introduced by effects in the electronics, was removed and they were combined according to equations (3.1)-(3.3) to yield the plasma potential Φ, electron temperature T_e and electron density n_e. The data is plotted at the original sampling frequency of 5 MHz, their uncertainty being represented directly by the signal fluctuations. Additional uncertainty arises from the uncertainty of the probe head position, approximately $\Delta R = \pm 1$ mm.

Unique features and caveats. When the HRCP penetrates deep enough into the plasma, usually at the velocity shear layer where the plasma potential Φ peaks, it can begin cooling the edge plasma as a whole. The effect can be observed by Thomson scattering diagnostic and by the divertor probe array. Care was taken not to use TS or divertor data during such times. The reciprocating probe data was, conversely, retained with the understanding that inside the velocity shear layer, the measured plasma parameters may be lower than in the absence of the probe. The possibility that the probe may cool the plasma immediately near it and thus produce unrealistic measurements at all times is unavoidable and intrinsic to reciprocating probe measurement.

Moving on, the ratio of ion and electron temperature is unknown in experiment and $T_e = T_i$ must be assumed. This affects the calculation of the electron temperature $T_e = (V_{BPP} - V_{LP})/2.2$, as the prefactor 2.8 in equation (3.1) was calculated assuming $T_e = T_i$ and no secondary electron emission. [70] It also affects the calculation of the electron density $n_e = 2I_{sat}/eA_{probe}c_s$ where $c_s = \sqrt{e(T_e + T_i/m_i)}$. Ideally, the measurements of LP1, LP2 and BPP2 would be performed at the same spot, and the distances between them may introduce uncertainties. If the Langmuir probe biasing potential V_{bias} is not sufficiently lower than the Langmuir probe floating potential V_{fl}, the ion saturated current can become desaturated (decreased with regard to the ideal I_{sat} value). This can be corrected for using a simultaneous V_{fl} and T_e measurement as

$$I_{sat} = \frac{I_{sat}^{(desaturated)}}{1 - \exp\left(\frac{V_{bias} - V_{fl}}{T_e}\right)}. \tag{3.6}$$

The perhaps largest uncertainty in HRCP measurement is the Langmuir probe effective collecting area $A_{probe} = 4.9$ mm^2. Particle-in-cell simulations have shown that depending on the ion Larmor radius $r_L = \sqrt{2m_iT_i}/B$ (T_i [eV], [42, Eq. 14.7.2]), electron temperature T_e and density n_e, the effective collecting area can vary between 4-8 mm^2. [121] As ion temperature and its spatial variation is unknown in the experiment, it is quite impossible to capture the temporal/spatial variation of A_{probe} during HRCP measurement. Adding to this that the graphite Langmuir probe pin may have been eroded by the plasma since its manufacturing, it appears that n_e accuracy may be no better than ±50 %. It is possible to scale HRCP n_e measurements so that a match with the lithium beam emission spectroscopy (Li-BES) [63] is achieved, but this was not done for this thesis.

3.1.3 The combined divertor array

The combined divertor array, shown in figure 3.4a, comprises 56 ball-pen and 2×55 Langmuir probes embedded into a special divertor tile. Since its installment [60], it provided routine measurements of the divertor electron temperature T_e, electron density n_e and parallel energy flux $q_\parallel$. The principles of its measurement are similar to the horizontal reciprocating probe, with three quantitative and one qualitative distinctions. Firstly, the prefactor of Langmuir probe floating potential,

$$V_{LP}^{(divertor)} = \Phi + (2.0 \pm 0.1)\, T_e, \tag{3.7}$$

is different due to different Langmuir probe design. [70] Secondly, for the same reason, the effective collection area is $A_{probe} = 2.8$ mm^2. Particle-in-cell simulations have verified that this A_{probe}, originally estimated as the area projected perpendicular to the magnetic field lines [70], equals to the real effective collection area and does not vary much with flux expansion. [122] Thirdly, as the probe surface represents the same boundary condition for the plasma as the divertor target, energy flux densities evaluated with equation

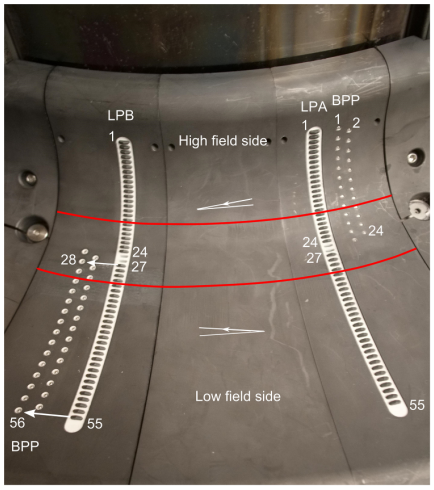

(a) : Combined divertor probe array. Four rows of probes are pointed out: two rows of ball-pen probes (BPP1-24 and BPP28-56) and two rows of Langmuir probes (LPA and LPB). Reprinted from [70].

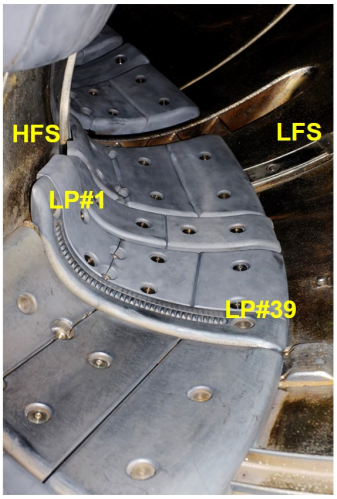

(b) : Swept divertor probe array. The single row of 39 Langmuir probes (LP1-39) is pointed out. Courtesy of M. Dimitrova.

Figure 3.4: Divertor probe arrays of the COMPASS tokamak.

(3.5) can be directly matched to energy flux densities in the SOLPS-ITER simulation. Fourthly and finally, since the divertor is grounded and not floating, the heat flux transmission factor γ value is affected by the non-ambipolar currents flowing into the divertor tiles. Comparisons of divertor infrared camera data to the combined divertor array data have shown good agreement for $\gamma = 11$ [123, Sec. 8.2.1] but also for $\gamma = 7$ [70]. While matching experimental and simulation data, we employ a formula which accounts for the non-ambipolar currents as well as the potential ionisation energy flux [124]:

$$q_{\parallel} = \frac{I_{sat}}{A_{probe}} \left[2.5T_e + \Phi + 2T_e . \min\left(7, \mathrm{e}^{-V_{fl}/T_e}\right) + 14.6 \text{ eV} \right] \tag{3.8}$$

The first two terms in the square brackets constitute the ion energy flux (assuming $T_i = T_e$), the third term corresponds to the electron energy flux, and the final term represents the potential ionisation energy flux, which brings 14.6 eV to the target per every impinging ion. This is the energy which heats the target when an ion recombines with a target electron and the electron falls into ground state. It is composed of the deuterium ionisation energy 13.6 eV and the surface binding energy 1 eV. [85] Equation (3.8) accounts for all the main energy flux channels carried by charged particles, but it cannot account for energy fluxes of neutrals and radiation. These can become significant in detached conditions, requiring the use of the infrared camera for energy flux measurement rather than probes.

Data processing and error bars. The time traces of floating potentials $V_{BPP,LP}$ and the ion saturation current I_{sat} were collected during a period where divertor plasma parameters were approximately constant. In L-mode,

this meant a part of the steady-state discharge phase when the horizontal reciprocating probe was not cooling the edge plasma. In H-mode, it meant the inter-ELM period $t = 1127$-1131 ms surrounding the modelled time $t = 1130$ ms. Error bars represent the data fluctuation levels (standard deviation).

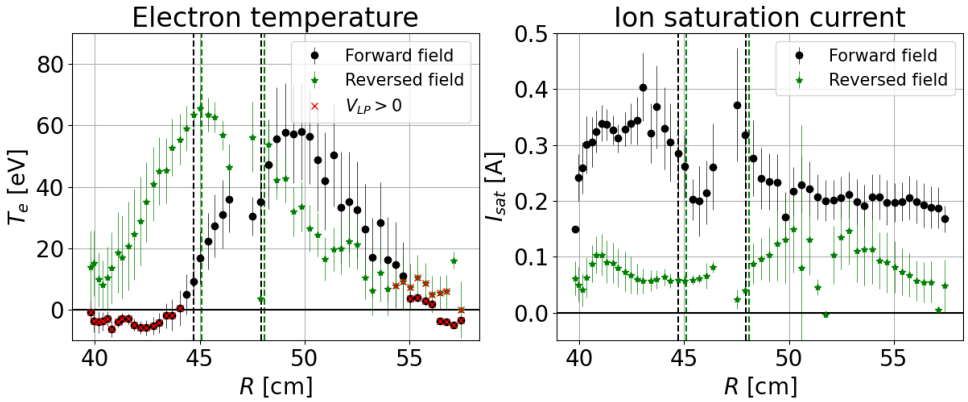

Figure 3.5: Radial profiles of the electron temperature T_e and ion saturation current $Isat$ measured by the combined divertor array in discharges #15975 (forward field) and #20914 (reversed field). Data points where the floating potential of the Langmuir probe is positive ($V_{LP} > 0$) have been crossed out, and they are not used in this thesis.

Unique features and caveats. Probes located on the high-field side (HFS, inner target) consistently measure nonsensical values of $T_e < 0$ ($V_{BPP} < V_{LP}$). This phenomenon can likely be linked to the magnetic field configuration and/or SOL drifts and currents, as it is affected by toroidal magnetic and electric field reversal. [125] Examine figure 3.5, which shows the divertor profiles of T_e and I_{sat} for two similar COMPASS discharges: #15965 (forward field) and #20914 (reversed field). This phenomenon is thought to be connected to magnetic shadowing, but it is impossible to fix. We follow the advise of a careful analysis of the combined divertor probe array data, and discard all combined divertor array measurements where the Langmuir probe floating potential $V_{LP} > 0$ (crossed out in figure 3.5). This eliminates nearly all measurements taken at the inner target. Similarly to the HRCP, $T_e = T_i$ was assumed in calculating T_e and n_e and may lead to systematic errors.

3.1.4 The swept divertor array

The swept divertor probe array, shown in figure 3.4b, consists of 39 Langmuir probes and provides measurements of the electron temperature T_e, electron density n_e and the target energy flux $q_{\parallel}$. It was in operation in the COMPASS tokamak divertor since before it was transferred to the Institute of Plasma Physics in Prague. [66, 59] Its primary mode of operation was voltage sweeping, where the probe bias is periodically varied over a large voltage span and the dependence of the collected current I on the biasing voltage V_{bias} is analysed as the I-V characteristic. This analysis was performed by M. Dimitrova using the 3-parameter fit, as the biasing voltage range was

insufficient for the 4-parameter fit to yield correct results. [122]

Data processing and error bars. Several I-V characteristics (half-periods of a complete biasing voltage sweep) were supplied to the 4-parameter fit to reduce random statistic error. Unlike in the combined divertor array, spatially varying sheath heat transmission coefficient γ was used, calculated according to [126, Eq. (1)] using the current flowing into a grounded divertor as an additional parameter. The resulting γ is between 7 and 17, peaking at the outer strike point.

Unique features and caveats. The data presented in this thesis suggest that, in attached plasmas, the swept divertor probe array measures systematically lower target electron temperatures than the combined divertor probe array.[2] I have observed this previously in my Master's thesis [118, figures 3.35 and 3.36], where $T_e^{(combined)}/T_e^{(swept)} \approx 3$ at the strike point of the low-density L-mode COMPASS discharge #13812, and $T_e^{(combined)}/T_e^{(swept)} \approx 1$ across the SOL of a high-density L-mode COMPASS discharge #15941. The swept divertor array data in that work were analysed using the first derivative probe technique, which allows for a double Maxwellian electron distribution function. While an electron velocity distribution diverging from the Maxwellian has been observed in particle-in-cell simulations of the COMPASS H-mode #16908 at the inner target [127], the first derivative probe technique is somewhat controversial. It has been argued to have advantages over the 3- and 4-parameter fit [128], but its validity has been challenged. [129, 130]. This thesis uses only swept divertor array data processed with the less controversial 4-parameter fit. This does not, however, eradicate the factor-of-three difference in temperatures. Problems with electronics, which are rather outdated in the swept divertor array, have been implicated to impair its measurements. [131] In contrast, the combined divertor probe array data has been systematically compared against 3- and 4-parameter fits of a swept Langmuir probe from the combined divertor array, and the data was found to match, confirming high strike point electron temperatures $T_e \approx 50$ eV, which are rarely obtained from the swept divertor array. Tentatively, we may conclude that the swept divertor array data is possibly inferior to the combined divertor array data.

Despite this conclusion, swept divertor array data is still used in this thesis. The reason is that any available data, even of relatively low quality, is useful input in the ill-conditioned problem that is optimising SOLPS-ITER input parameters. The discrepancy in target energy fluxes $q_\parallel$ is not as high as in the target electron temperatures T_e, which may possibly be caused by the more sophisticated formula for γ calculation. The combined divertor probe array provides nearly no useful data at the inner target, so the swept divertor array is our only source of T_e and n_e in this exceptionally sensitive location. Finally, although SOLPS-ITER results are matched primarily to the combined divertor array data, the comparison of both divertor arrays

[2] The situation is different under detached conditions. Swept Langmuir probes are known to have difficulties measuring $T_e < 5$ eV [12, Sec. 16.3], while the method combining ball-pen and Langmuir probes does not seem to have such limitations. [85]

against SOLPS-ITER simulations is an interesting addition to the discussion on the previous paragraph. More information may be found in [118, Sec. 2.1].

3.1.5 The divertor infrared camera

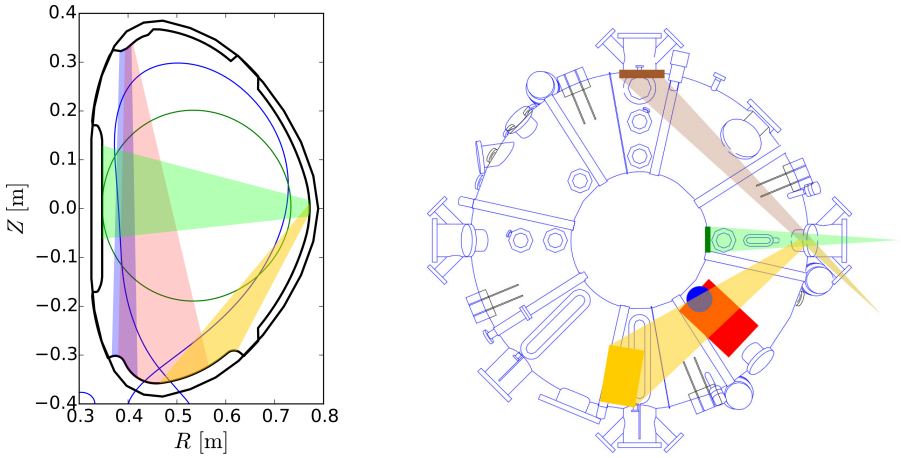

(a) : Poloidal cross-section **(b) :** Top view

Figure 3.6: Fields of view of five COMPASS infrared cameras. The divertor infrared camera is plotted in red. Reprinted from [67].

The divertor infrared (IR) camera was one of the several infrared cameras observing the inside of the experimental chamber of COMPASS, measuring the infrared radiation of a special divertor tile and delivering, after an analysis of heat transfer through the tile, the perpendicular target energy flux $q_\perp$. Since its installation [67, 123], it has been delivering high-quality, finely spatially and temporally resolved data of the target energy flux.

Data processing and error bars. The raw data was processed by P. Vondracek and the resulting perpendicular target energy flux $q_\perp$ with the sampling frequency 44 kHz was saved into the COMPASS experimental database. The data was converted to parallel energy flux using the magnetic field line impact angle at the measurement location, taking into account the 3-degree tile inclination. The data was averaged over the same time windows as the combined divertor array. The error bars represent the standard deviation of the raw data fluctuation.

Unique features and caveats. The equilibrium reconstruction of discharge #16908 misplaces the inner strike point by about 1 cm. As a result, the impact angles calculated by the reconstruction do not match the real impact angles. The impact angle is, however, small compared to the measuring divertor tile inclination of 3 degrees, so the overall error is expected to be ~ 10 % at the inner strike point. Even with this uncertainty, the IR camera is the most accurate inner strike point diagnostic we have.

3.2 COMPASS Upgrade

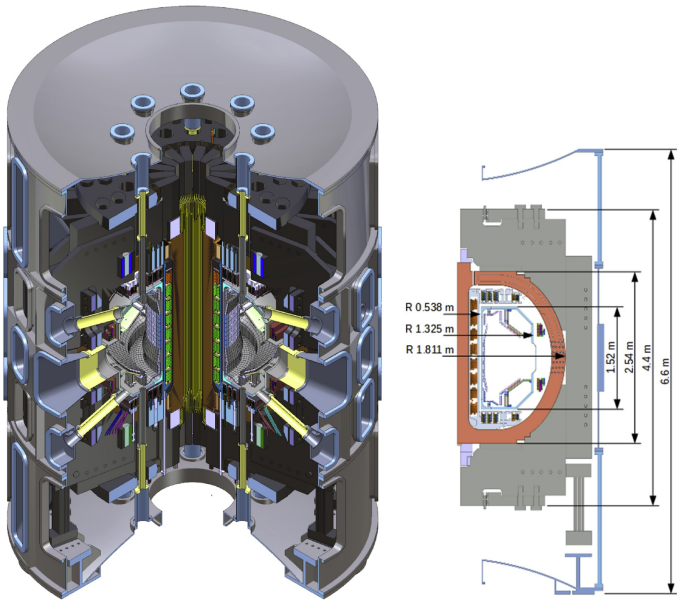

Figure 3.7: The COMPASS Upgrade tokamak. Reprinted from [3].

The COMPASS Upgrade tokamak, shown in figure 3.7, is the next machine to be operated by the Institute of Plasma Physics in Prague after COMPASS. It features new hardware infrastructure (vacuum vessel, toroidal and poloidal coils, power supplies etc.) and partially adopts the existing diagnostics systems and software infrastructure. [22, 3] At the time of writing, the experimental hall is nearly finished and several systems are being manufactured or installed (power supplies, coils) while others are still under design (diagnostics, heating systems).

COMPASS-U will be larger than COMPASS (major radius $R = 0.894$ m, minor radius $a = 0.28$ m) with a substantially higher magnetic field ($B_t \leq 5$ T, $I_p \leq 2$ MA). Its toroidal field coils won't be superconducting, however; they will be copper, cooled by liquid nitrogen to reduce their resistivity. The large magnetic field density will allow ITER- and DEMO-relevant experiments which are not possible on other currently operating tokamaks. In this sense, COMPASS-U will continue in the footsteps for the decommissioned Alcator C-mod tokamak, which was exceptional among other tokamaks for its high electron densities and high magnetic field. [132] COMPASS-U will reach central electron temperatures of $T_e = 4.5$ keV and densities up to $n_e = 8 \times 10^{20}$ m^{-3}, though its nominal H-mode n_e will be lower. This is partly because COMPASS-U will be equipped with different additional heating systems than Alcator C-mod. Where C-mod used ICRH, COMPASS-U will be equipped with 4-6 MW of NBI power and 2 MW of ECRH power, both of which require lower plasma density to remain efficient. COMPASS-U divertor will be closed more fully (C-mod divertor was not toroidally continuous, and

the gaps caused melting at high incident heat fluxes and neutral leakage) and it will be equipped with cryopumps, allowing for better control of the plasma density. Finally, a key feature of COMPASS-U will be first wall and divertor operation at the temperature at 500 °C, mitigating first wall recycling, lowering impurity content and further improving density control.

The main difference between COMPASS and COMPASS Upgrade in terms of edge plasma physics is the typical SOL transport regime. Approximating the COMPASS Upgrade edge plasma parameters with Alcator C-mod discharges, in L-mode, the outer target will likely be in the conduction-limited regime while the inner target will be partially detached. [133] In H-mode, the outer target will likely remain conduction-limited while the inner target will fully detach. [134] Preliminary SOLPS-ITER simulations of the COMPASS Upgrade tokamak indicate partial or full detachment within a large range of input parameters. Our analysis, in contrast, suggests that the COMPASS tokamak struggles to enter the outer target conduction-limited regime without impurity seeding (section 6.4). This means that COMPASS and COMPASS Upgrade edge plasma physics may evince qualitative differences, such as the sensitivity of target plasma parameters to upstream conditions, divertor target and first wall heat load patterns or the importance of radiative and neutral interaction processes in the divertor.

One of the key research topics of COMPASS-U will be divertor physics. Owing to its exchangeable divertor design, it will achieve not only the lower single null configuration but also the upper single null, double null and snowflake configuration. The small predicted heat flux fall-off length $\lambda_q^{(OMP)} \approx 1$ mm [6] will cause large power densities on the strike points, similar to fusion reactors such as ITER, so divertor detachment studies will be crucial. Additionally, COMPASS-U will explore liquid divertor target operation. On the whole, COMPASS-U is a project of international importance which will facilitate studies in hitherto unexplored physics of high magnetic field, high power flux plasmas.

SOLPS-ITER simulations, both predictive and interpretative, are the perfect complement to the COMPASS Upgrade research program. Predictive simulations of the edge plasma can contribute, for instance, toward the design of the divertor baffles and its impact on the neutral pressures in the main chamber and the divertor volume. Neutral pressures at the outer midplane will be important for neutral beam injection, as high neutral pressure in the midplane port beam duct could dissipate the beam energy before it can reach the plasma. This may essentially eliminate neutral beam heating in high-density plasmas and bar access to H-mode. Divertor neutral pressure, on the other hand, impacts the cryopump efficiency and dictates how responsive the plasma will be to density and impurity content control. Studies of detachment are going to be of utmost importance on COMPASS Upgrade, and knowing the edge plasma response to confined plasma parameters in advance will contribute toward discharge scenario design. After COMPASS Upgrade is commissioned, SOLPS-ITER will help interpret its experimental data and gain insight into its edge plasma physics. On the whole, the COMPASS

Upgrade research program can benefit greatly if we learn to use SOLPS-ITER reliably and efficiently.

How do interpretative simulations of the COMPASS tokamak contribute toward COMPASS Upgrade design and physics program? Primarily through the development of infrastructure and know-how. Partly due to the 2020-2022 COVID-19 pandemic, it has been difficult to learn using SOLPS-ITER from other SOLPS research groups, such as the one based at the Institute of Plasma Physics, Garching, Germany. While we are thankful for their help and advice, we have largely learned by performing interpretative simulations of COMPASS. COMPASS simulations are faster and more stable than COMPASS Upgrade simulations, as the machine is smaller and the open divertor lessens the role of atomic physics, and they are readily verified against experimental data. COMPASS has, therefore, served a test bed teaching us how model COMPASS Upgrade.

The particular contributions of my PhD research toward COMPASS Upgrade are the following. In summer 2023, I became the leader of the IPP Prague SOLPS group, coordinating common SOLPS research projects and representing the group as a whole. I am the main author of the SOLPS-doc documentation package [25], which teaches beginning modellers how to use SOLPS-ITER. I contribute toward the SOLPS-postproc package [135], developed by the IPP Prague Data Management Systems group, which is becoming our primary tool of SOLPS output data processing. Finally, many results of this thesis can be directly applied to COMPASS Upgrade. Discussion of the needs of matching experimental and modelling data informs the design of COMPASS Upgrade diagnostics and facilitates its future interpretative simulations. The finding that heat flux limiters enhance existing parallel temperature gradients appears to be universal (chapter 5), and will improve the accuracy of predictive COMPASS Upgrade simulations. In summary, my research has built up infrastructure and know-how necessary to perform high-quality SOLPS simulations of the COMPASS Upgrade tokamak, even though I perform simulations of the now decommissioned COMPASS.

Chapter 4

Magnetic equilibrium reconstruction inaccuracy

This chapter is structured around an interpretative SOLPS-ITER simulation of the COMPASS tokamak L-mode discharge #17588. This discharge represents a typical L-mode plasma at tokamak COMPASS; sheath-limited with moderate plasma density and high target electron temperatures. Using its SOLPS-ITER simulations, I explore the effect of inaccurate magnetic equilibrium reconstructions on simulation quality. In section 4.1, I introduce errors in equilibrium reconstructions as a wide-spread issue in edge plasma physics and I outline common approaches toward their correction. In section 4.2, I compare five reconstruction variants of magnetic equilibrium in COMPASS discharge #17588 at $t = 1100$ ms. In section 4.3, I propose that the outer midplane velocity shear layer forms a few millimetres outside the separatrix, providing a useful experimental gauge of the separatrix position. In section 4.4, I discuss two approaches to correcting the separatrix position in SOLPS-ITER simulations: the intuitive approach and the systematic approach; and show the former is inaccurate and the latter is time-consuming. In section 4.5, I use SOLPS-ITER to validate two variants of the #17588 equilibrium reconstructions, find the accurate separatrix position at the plasma top, and use it to produce an improved equilibrium reconstruction. Finally, in section 4.6, I use this reconstruction for an interpretative simulation of discharge #17588, crowning the process of using SOLPS-ITER to validate and improve reconstructions of the tokamak magnetic equilibrium.

Some of the results presented in this chapter have been publicized in a proceedings contribution of the 47th EPS Conference on Plasma Physics, 2021, which is attached in appendix A.4. Validation of magnetic equilibrium reconstructions using SOLPS-ITER simulations was the topic of a follow-up Master's thesis under my supervision [136], defended in 2024.

4.1 Magnetic equilibrium reconstructions and their accuracy in the edge plasma

Assuming that the tokamak plasma is toroidally symmetric, the principal two directions in the Braginskii equations (section 2.1) are the parallel $\parallel$ direction and the binormal $\perp$ direction, which is perpendicular both to the toroidal and the parallel coordinate. This captures the observation that parallel and perpendicular transports occur on such different temporal and spatial scales that they can be decoupled and solved independently. Accordingly, the two coordinates of the 2D plasma solver B2.5 are the poloidal coordinate x, projection of the parallel coordinate using the magnetic field pitch B_x/B, and the radial coordinate y, perpendicular both to the poloidal and toroidal coordinate.[1] To construct the B2.5 grid, one therefore requires knowledge of the local magnetic field direction in the edge plasma; in other words, a *magnetic equilibrium reconstruction*.

Magnetic equilibrium reconstructions are a basic tool of tokamak research.

[1] The y coordinate is not always binormal. In the divertor region, y transitions from being locally perpendicular to x to being aligned with the divertor target.

They are used during tokamak operation, while performing and interpreting diagnostic measurements, while processing experimental data and while setting up plasma simulations. They are typically performed by fitting a solution of the Grad-Shafranov equation to multiple magnetic measurements inside and around the vacuum vessel. The COMPASS tokamak routinely used the EFIT++ code to capture snapshots of the temporally evolving equilibrium during its discharges. [137, 138] The reconstructions were saved into the COMPASS experimental database (CDB), and they are referred to in this thesis as the *standard CDB reconstructions*.

It is known that equilibrium reconstructions based on the Grad-Shafranov equation can be inaccurate, which is mainly due to simplifying assumptions (parabolic plasma pressure profile) or few or lower quality reconstruction constraints. [139, 140, 141] An example was given in section 2.2, where the standard CDB reconstruction of the H-mode discharge #16908 at $t = 1130$ ms placed the separatrix near the top of the pedestal, where $T_e = 200$ eV and $n_e = 3.5 \times 10^{19}$ m^{-3}. The real separatrix should be somewhere near the foot of the pedestal, 1-2 cm outward of the reconstructed position, where the electron temperature is similar to the outer target peak electron temperature $T_e = 70$ eV. Such local reconstruction errors are usually a sign of global inaccuracy, which negatively impacts consequent analysis. In edge plasma physics, for example, 1 cm uncertainty in the separatrix position translates into 50% and larger uncertainties in the separatrix plasma parameters, most importantly $n_{e,sep}$ and $T_{e,sep}$. [142] The separatrix $n_{e,sep}$, $T_{e,sep}$ and $T_{i,sep}$ constitute primary input parameters of both core and SOL models, such as the SOL particle-in-cell code BIT1 [45] or the core transport code METIS [143]. Their uncertainty propagates through the code results, limiting their credibility, lowering their predictive capability and necessitating *ad hoc* corrections to the separatrix position.

A common solution to equilibrium reconstruction inaccuracy is to make a small, case-dependent correction, based on assumptions which sometimes remain implicit. For example, one might assume the following.

1. $T_{e,u} = T_{e,t}$ in the far SOL. This appears circular at first glance, but the key is that the *far* SOL tends to remain attached, sheath-limited and isothermal even at high collisionalities ν^* (5.6).[2] If the total pressure p is measured with sufficient accuracy, it may be used instead of T_e.
2. The upstream and divertor spacing of magnetic surfaces is regular and not affected by the reconstruction error (separately for upstream and divertor).
3. The strike point location is known, either because the reconstruction is considered accurate at the divertor or because the target energy flux forms a distinct, attached peak.

[2] This runs counter-intuitive to the basic two-point model, which predicts that the parallel T_e gradient is driven solely by the upstream collisionality ν^*. Figure 5.5, however, shows that this is not always the case. In SOLPS-ITER simulations of COMPASS L-mode, far SOL $\nu^* \approx 15$, and yet the flux tube is nearly isothermal. This indicates that assumptions of the two-point model are grossly violated in the far SOL. For example, $T_i \gg T_e$ due to faster parallel losses of T_e, where the basic two-point model posits $T_e = T_i$.

Under these assumptions, it is possible to map the divertor measurements onto the upstream measurements using the erroneous reconstruction, correct the mapping by aligning the far SOL T_e (or p) profiles, and then identify the separatrix with the mapped strike point location.

The result of such an operation is shown in figure 4.1a. The divertor T_e profile aligns neatly with the upstream profile, producing $T_{e,sep} = (40 \pm 10)$ eV by shifting the separatrix outward by 14 mm. Although the shifted separatrix position (dotted vertical line) is more plausible than the original reconstructed separatrix position (dashed vertical line), the alignment cannot be more precise than to several millimetres owing to uncertainties in the experimental measurements.

The search for similar corrections has a rich history which, interestingly, often concerns traditions in particular machines. In DIII-D, Porter et al introduced a method which relates the separatrix to the area of profile steepening in the plasma edge. [144] This technique has been referred to as the "standard DIII-D method" [145] and it is still routinely applied. [146, 147, 148] In ASDEX-Upgrade, calculating the separatrix temperature using the power balance in the two-point model has seen considerable popularity. [140, 149, 150, 151] In COMPASS, the separatrix has been identified with or related to the velocity shear layer, where the poloidal plasma rotation changes direction. [152, 153, 80] An interesting take on the subject was introduced at the JFT-2M tokamak, where a peculiar Langmuir probe design was put forth specifically for separatrix detection [154] and it was suggested that the geodesic acoustic eigenmode (GAEM) amplitude falls to zero at the separatrix in L-mode. [155, 156] It would be interesting to see a rigorous analysis, providing sound theoretical, modelling and experimental evidence for all of these corrections, as some may be directly applicable to other machines and may offer new insights into edge plasma physics.

Case-dependent corrections of static equilibrium reconstructions are simple and fast, given sufficient diagnostics coverage and trust in the physics assumed to underlie the process. However, they have their flaws. The corrections are only local; where no measurements are available, no correction can be made.[3] They are different for every discharge, location and time. Unless integrated diagnostic data analysis is employed, such as ASDEX-U IDA [157] or JET Minerva [158], they may also differ for every quantity and diagnostic. In summary, case-by-case equilibrium corrections are not efficient in the long run and open the door to inconsistencies in complex analyses.

[3] Applying *local* reconstruction corrections causes an interesting conundrum in interpretative SOLPS-ITER simulations. Upon measuring and simulating radial profiles of the same quantity, a modeller will shift these profiles relatively to one another to facilitate a match at the separatrix. Is this shifting the simulated data to match the experiment, or shifting the experimental data to match the simulation? Shifting the simulated profile assumes that the geometric location of diagnostic measurements is well known and thus anchors the simulation results in the $[R, Z]$ plane, but implies local distortions to the flux-surface-aligned simulation grid. Shifting experimental profiles preserves the grid integrity, but only allows locating the profiles relative to the separatrix, wherever that actually is in the vessel. The distinction appears to be a matter of taste. I prefer the former interpretation, my supervisor J. Seidl prefers the latter.

A more rigorous but demanding alternative to case-dependent corrections of equilibrium reconstruction is to find the inaccuracy root in the reconstruction algorithm. Many Grad-Shafranov equilibrium solvers, for example, assume that the plasma pressure profile is parabolic, which is not the case especially in H-mode. [159] During transients, the assumption of steady state may be violated. [160] The magnetic field measurements can be performed on adjacent flux surfaces or be few in number, failing to properly constrict the solution. The random error in constraining measurements may hamper reconstruction convergence. [161] Redressing at least some of these uncertainty sources is possible. Improvements have been made, for example, to equilibrium reconstruction of the JET tokamak, where adding motional Stark effect (MSE) data as a reconstruction constraint provided more accurate field distributions in the core region. [162] Furthermore, optimisation of magnetic diagnostic inputs and implementation of a realistic plasma pressure profile has significantly increased the separatrix reconstruction accuracy while maintaining a high level of convergence. [141] Due to large differences between tokamaks, however, progress on one machine usually cannot be easily transferred to another. As a result, uncertainties of equilibrium reconstructions have been a mainstay of edge plasma research. [144, 163, 145]

4.2 Equilibrium reconstruction accuracy at COMPASS

The COMPASS tokamak was not exempt from problems of inaccurate magnetic equilibrium reconstructions. In 2015, EFIT++ reconstructions were compared favourably with the free-boundary equilibrium code FREEBIE [164] and the plasma boundary reconstruction code VacTH [165]. [166] In the mature years of COMPASS operation, however, it was discovered that its 16 inner partial Rogowski coils (IPR coils), which provided the primary constraint for its equilibrium reconstructions, were misaligned with regard to their design installation position. [161] It was further found that flux loops and divertor Mirnov coils could provide valuable additional constraint to the reconstruction, impacting the reconstruction especially in the divertor region. However, the Mirnov coil signal quality had been poor in previous COMPASS discharges due to analog-to-digital converter settings. This prevented the retroactive adoption of flux loop and Mirnov coil signals in the reconstructions stored in the COMPASS database. Reconstruction quality was repeatedly called into question, for example in the unpublished work by J. Cavalier et al, where the upper LFS limiter radiation indicated that its clearance to the sepatrix was much smaller than suggested by the standard CDB reconstruction. Several reconstruction variants have been proposed; however, systematic testing of their quality has been limited and none succeeded the standard CDB reconstruction.

In this section, we compare five variants of equilibrium reconstruction in COMPASS L-mode discharge #17588 at $t = 1100$ ms. This discharge is, as

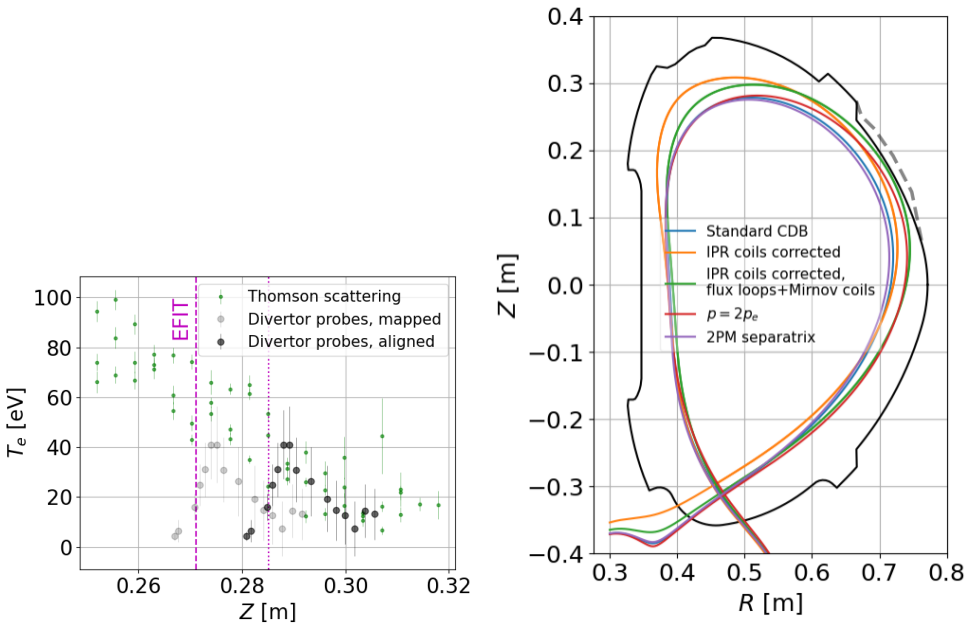

(a) : Correcting the standard CDB reconstruction separatrix position at the plasma top. The dashed magenta line denotes the standard CDB reconstruction separatrix position, the dotted magenta line is the proposed separatrix position.

(b) : Separatrix outlines of 5 equilibrium reconstructions; see the list on page 50. The dashed grey line shows where the limiter was moved away to allow for wider SOL in the SOLPS-ITER simulation presented in section 4.5.

Figure 4.1: Magnetic equilibrium reconstruction uncertainty in the COMPASS tokamak L-mode discharge #17588 at $t = 1100$ ms.

shown in section 4.6, representative of a typical COMPASS L-mode plasma at a moderate density. The variants are:

1. The standard CDB reconstruction. This is the default variant, which one would refer to without further knowledge.
2. A reconstruction with corrected IPR coils positions. [161] This variant was taken from the COMPASS experimental database under the name `V4_std_0`.
3. A reconstruction with corrected IPR coils positions, further constrained with data from flux loops and divertor Mirnov coils. [161] This variant was created using O. Kovanda's modified EFIT script.
4. A reconstruction with a realistic plasma pressure profile, calculated as $p = 2en_eT_e$ from Thomson scattering n_e and T_e. This variant was created using M. Komm's modified EFIT script.
5. A reconstruction with the additional constraint on the separatrix position at the plasma top, calculated with the two-point model. This variant was created by M. Šos and M. Komm, and it is explained in the following paragraph.

The separatrix position Z_{sep} at the plasma top, along the vertical mea-

surement chord of the Thomson scattering diagnostic, can be calculated as follows. According to the basic two-point model [12, Eq. (5.5)], the electron temperatures at the upstream (u) and target (t) end of a flux tube are related as

$$T_{e,u}^{7/2} = T_{e,t}^{7/2} + \frac{7}{2}\frac{q_{\parallel} L}{\kappa_{0e}}, \tag{4.1}$$

where the electron temperatures are given in eV, the total parallel energy flux density $q_{\parallel}$ is given in W.m^{-2}, the parallel connection length L is given in m, and the approximate electron thermal conductivity is $\kappa_{0e} = 2000$. This equation allows for calculating the upstream separatrix temperature $T_{e,u}$, given that all the other variables are known. At COMPASS, the strike point temperature can be approximated by the peak T_e at the outer target. The parallel energy flux density $q_{\parallel}$ can be estimated as $P_{SOL}/A_{\parallel}$, where the power crossing the separatrix P_{SOL} is calculated from the global power balance and the flux tube parallel cross-section $A_{\parallel}$ is calculated with equation (1.1). Finally, the connection length L is taken from a flux tube near the separatrix in the standard CDB equilibrium reconstruction. Having thus calculated the upstream separatrix $T_{e,u}$, an automatic algorithm smooths the upstream T_e profile measured by the Thomson scattering diagnostic and finds the place along it where $T_{e,u}$ is measured. This is the separatrix location Z_{sep}, calculated with the two-point model.

At the ASDEX Upgrade tokamak, where this method is particularly popular, the $T_{e,t}^{7/2}$ term is typically assumed negligible compared to the heat conduction term (conduction-limited regime), so estimating the upstream separatrix position does not require any target measurements. [167, 151, 168] Conversely, COMPASS target temperatures are typically high, between 20 eV and 60 eV. [122] SOLPS-ITER modelling presented in section 6.1 suggests that for low to moderate COMPASS densities in L-mode, the heat conduction term can be neglected compared to the $T_{e,t}^{7/2}$ term and equation (4.1) can be simplified to $T_{e,u} \approx T_{e,t}$. This streamlines the calculation as well, as it avoids the estimation of $q_{\parallel}$ and requires only routine measurements of the upstream and target temperature profiles, which in COMPASS are available from the Thomson scattering diagnostic and the combined divertor probe array. Thus it appears that in COMPASS conditions the two-point model can often be neglected, and peak outer target T_e can be taken as a proxy for separatrix T_e.

The five variants of discharge #17588 equilibrium reconstructions are shown in figure 4.1b. A large difference is observed between the standard CDB reconstruction (1, blue) and the rest. Correcting the IPR coils positions (2, orange) tends to push the separatrix outward and places the inner strike point further to the HFS. Including flux loops and Mirnov coils as reconstruction constraint (3, green) moves the inner strike point back into position, but causes very small separatrix clearance with the upper LFS limiter. Implementing a more realistic pressure $p = 2p_e$ profile (4, red) moves the separatrix outward only at the outer midplane. Finally, the two-point model reconstruction (5, purple) is nearly identical to the standard CDB reconstruction. Considering that 1 cm is a considerable radial distance in the edge plasma, the five

reconstruction variants provide very different results.

Before we discuss which reconstruction may the the best, let us show why reconstruction (5) with separatrix position constrained by the two-point model does not yield different results than the standard CDB reconstruction. Intermediate results stored in the COMPASS database indicate that $T_{e,u} = 50$ eV calculated with equation (4.1) is realistic, given that $T_{e,t} = 40$ eV. However, the corresponding $Z_{sep} = 0.266$ m is incorrect. As figure 4.1a shows, such Z_{sep} is radially inside the standard CDB separatrix, where $T_e = (70 \pm 10)$ eV. This suggests that the automatic algorithm failed to find the correct Z_{sep} along the smoothed upstream T_e profile. Given $Z_{sep} = 0.266$ m as constraint, reconstruction (5) correctly moved the separatrix at the plasma top inward. It appears that placing a constraint on the separatrix position works as expected, but that the calculation of Z_{sep} is prone to error.

Which of the five reconstruction variants is the best? To begin with, one can approach the answer using diagnostic data alone. For example, measurements of inner divertor target $q_{\parallel}$ (see figure 4.9) show that reconstruction (2) locates the inner strike point incorrectly. A detailed analysis will not be carried out here, as the diagnostic instrumental for this comparison, the horizontal reciprocating probe at the outer midplane, did not operate in discharge #17588. However, in the Master's thesis under my supervision [136], these five reconstruction variants were evaluated rigorously against experimental data of the well-diagnosed COMPASS L-mode discharge #17692. My student concluded that the reconstruction with a realistic plasma pressure profile, $p = 2p_e$, was the most accurate. We additionally note that a realistic plasma pressure profile was also instrumental in improving equilibrium reconstructions at the JET tokamak. [141] It may well be that the assumption of parabolic p profile, made in standard CDB reconstructions, is a source of error which would be rewarding to redress in COMPASS reconstructions and avoid in COMPASS Upgrade reconstructions.

Such an equilibrium reconstruction analysis has a drawback: it is only a case study. Over 20 000 discharges were recorded in the COMPASS experimental database, and it is rather uncertain if the conclusions drawn for two L-mode discharges, typical though they may be, can be applied indiscriminately to all COMPASS plasmas. To this end, I have performed a systematic analysis of experimental data and published it as *K. Jirakova*[4] *et al, Systematic errors in tokamak magnetic equilibrium reconstruction: a study of EFIT++ at tokamak COMPASS, Journal of Instrumentation* ***14*** *(2019).* [142] The article appears in appendix A.3 of this thesis. In nearly 400 L-mode discharges, I compared the outer midplane EFIT separatrix position (standard CDB reconstruction) to the measurements of the horizontal reciprocating probe. I found that the relative distance of the velocity shear layer (VSL) to the reconstructed separatrix varied systematically depending on the plasma geometry. The strongest predictors were the lower triangularity, correlated with $R_{VSL} - R_{sep}$ at 87 %, and the radial coordinate of the magnetic axis R_{mag_axis}. Recalculating the equilibrium reconstructions with corrected IPR

[4] My maiden name.

coils positions, performed by the principal co-author O. Kovanda, significantly suppressed the dependence of $R_{VSL} - R_{sep}$ on plasma geometry. Using the reconstruction with corrected IPR coils positions, the velocity shear layer tended to form 1-2 cm outside the separatrix. This is an interesting conclusion, which will be advanced upon in section 4.3.

Taking for granted that results of a magnetic equilibrium reconstruction should not systematically depend on the equilibrium itself, my article significantly increases the credibility of the IPR coils positions correction. This is despite the fact that reconstructions using this correction did not perform well in the case study conducted by me nor by my student, and significantly misplaced the inner strike point in both cases. I would conjecture that their significant scatter and low convergence rate stem not from the quality of the correction, but from want for optimisation. EFIT reconstructions have multiple input parameters which have been tuned to provide the best possible results for the standard CDB reconstructions. Changing the positions and angles of several IPR coils may have upset this optimisation and resulted in the poor performance seen in the two case studies. One may, again, recall the recent JET study [141] and note that alongside implementing a realistic pressure profile, magnetic measurements already in use were recalibrated and new ones were introduced. In summary, O. Kovanda's work toward correcting the equilibrium reconstructions may not provide reliable results at the moment, but it is a step in the right direction and should be expanded upon in future upgrades of COMPASS reconstructions and learned from in COMPASS Upgrade reconstructions.

4.3 Velocity shear layer position

The experimental result that the velocity shear layer (VSL) forms 1-2 cm outside the separatrix at the COMPASS outer midplane in diverted plasmas [142] is interesting because it provides a direct proxy for the separatrix position. Thanks to the ball-pen probes installed on the COMPASS horizontal and vertical reciprocating manipulator, upstream SOL plasma potential Φ measurements were abundant on the COMPASS tokamak. Historically, the VSL position has been assumed to lie *at* the separatrix. [80] Such results have been observed in tokamak experiment [169], torsatron experiment [170] and tokamak simulations [171, 172]. However, there has also been evidence that the VSL forms inside the separatrix [173, 174, 175] or outside the separatrix [176, 177, 178, 179, 180, 181, 182, 13]. It is evident that the VSL is bound to the separatrix in some way.

There are essentially two explanations why the VSL would form near the outer midplane separatrix. The first explanation deals with mean flows in the edge plasma. [142] Due to radial force balance, the plasma potential Φ rises with the radial coordinate r in the confined plasma. In the sheath-limited, low-resistivity SOL, upstream Φ falls with r due to electrical contact with the divertor target sheath. The result is a Φ peak near the separatrix. The consequent radial electric field $E_r = -\mathrm{d}\Phi/\mathrm{d}r$ field creates shearing poloidal

flows via the $\mathbf{E} \times \mathbf{B}$ drift. The second explanation of the VSL-separatrix relation comes from the predator-prey model of plasma turbulence. [75] Turbulent structures, which are formed at the outer midplane due to the interchange instability, pass their energy to poloidal flows via Reynolds stress. These flows have a shearing pattern, constituting the VSL, and they appear in the region where high radial gradients drive the most turbulence, at the separatrix. Since turbulence contributes toward mean flows and mean flows regulate turbulence, it is not *a priori* clear if either of these phenomena can create a VSL on its own, or if both are needed in conjunction.

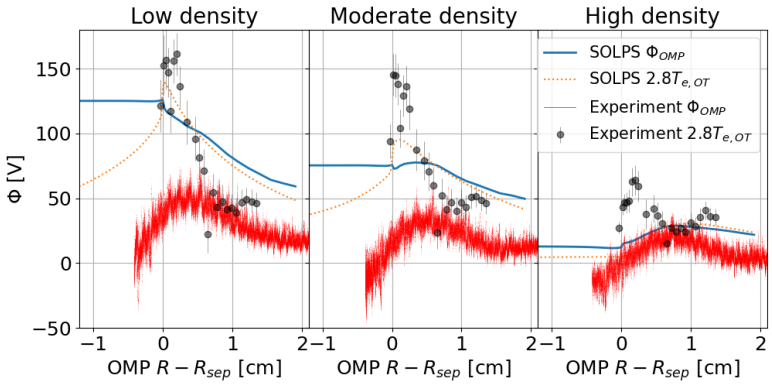

Figure 4.2: Plasma potential Φ in the low-density (#13812), moderate-density (#13820) and high-density (#13825) discharge in the density scan presented in section 6.1.

Results presented in section 6.1 of this thesis show that the SOLPS-ITER transport code, based on the mean flows approach, actually reproduces the experimental VSL in interpretative COMPASS simulations at high densities. Figure 4.2 shows the outer midplane (OMP) profiles of the plasma potential Φ as modelled by SOLPS-ITER and as measured by the horizontal reciprocating probe. The experimental data were shifted radially by the same amount as in these interpretative simulations. Both modelled and measured Φ decrease with rising plasma density, due to increasing resistivity. In the SOL, SOLPS Φ approximately follows the outer target sheath potential density drop $2.8T_e$ (for deuterium plasma [142]), while the experimental T_e profile is more peaked. In the confined region, the SOLPS model does not describe the plasma potential adequately due to exclusion of realistic drifts and currents, such as the Pfirsch-Schlütter current. In spite of this significant fault, at high density the Φ peak forms at the correct place, about 0.5 cm outside the separatrix, and has the correct magnitude, about 25 V. In the same vein, ongoing simulations of COMPASS using the GBS turbulence code [183] have formed an L-mode VSL 0.4 cm outside the OMP separatrix, even though turbulence has not yet developed in the plasma solution. [184] This suggests that the mean flows approach can be sufficient to create a VSL even without the contribution of turbulence, or even drifts.

Finally, let us note that in all five simulations presented in this thesis where outer midplane Φ measurements were available, matching OMP T_e and n_e

profiles to SOLPS data yielded the VSL about 0.5 cm outside the separatrix. In the work of my student, which modelled the COMPASS L-mode discharge #17692, the VSL appeared 0.3 cm outside the OMP separatrix. [136] This supports the claim that the VSL forms at least a few mm outside the separatrix, not at the separatrix as previously assumed at the COMPASS tokamak. Unfortunately, this statement must be supplemented with two important hedgings. Section 4.4 suggests I may have placed the separatrix a few mm too inward in the aforementioned SOLPS-ITER simulations. Furthermore, ongoing SOLPS-ITER simulations of the COMPASS tokamak performed by J. Hecko show that enabling drifts in SOLPS-ITER moves the VSL inward, directly on top of the separatrix. Further work is needed to increase the accuracy of optimised COMPASS equilibrium reconstructions and remove the possible bias from SOLPS-ITER interpretative simulations, before the VSL-separatrix relation can be claimed with certainty higher than several mm.

4.4 Correcting inaccurate equilibrium reconstructions in SOLPS-ITER simulations

Since reconstructions of the magnetic equilibrium inform the shape of the SOLPS-ITER grid, their inaccuracies are immediately evident when matching simulation results to experimental data in interpretative modelling. Separatrix plasma parameters may be unrealistic and individual diagnostics may provide contradictory data (in the absence of integrated diagnostic data analysis, mentioned previously). A common solution to this problem are *ad hoc* corrections of the separatrix position. It is so common, in fact, that it is often barely mentioned. An extensive report on ITER and JET modelling with B2-EIRENE, for example, states only: [185]

"In analysing the mid-plane profiles it has to be taken into account, that the error of the reconstruction of magnetic equilibrium (position of separatrix) can reach ± 1 *cm. The experimental profiles were shifted by* ≤ 1.0 *cm to account for uncertainties in the reconstructed magnetic equilibrium. Applying such a shift, it is always possible to get a good match outside the separatrix."*

When I was performing my first interpretative SOLPS-ITER simulations, I was fascinated by the ambiguity and arbitrariness of correcting the separatrix position. When performing an interpretative simulation "by hand", iteratively adjusting input parameters to achieve an experiment-model match, separatrix shifts essentially act as another simulation input. Qualitatively, separatrix corrections are similar to anomalous diffusion coefficients. Their magnitude is approximately known, but their exact value is chosen *ad libitum* in the pursuit of a good match between experimental and simulation data. It is questionable whether intuition can be trusted to guide the process, even if the resulting interpretative simulation reproduces experimental measurements. In this section, three approaches to the problem will be outlined: the intuitive approach and observations marked from its usage, the systematic approach where several separatrix corrections are tested, and the approach directed at

the root cause: the equilibrium reconstruction itself.

In the *intuitive approach* to correcting the separatrix position, one follows the process of launching a simulation, gauging the result, adjusting the input parameters and re-launching the simulation. During such "manual tuning", I have leaned on the following empirical rules of thumb:

- The hallmark of optimal separatrix placement is the simultaneous match of upstream $T_{e,sep}$, upstream $n_{e,sep}$ and strike point $T_{e,t}^{(peak)}$.
- It is straightforward and nearly independent of other simulation inputs to obtain a desired value of upstream $n_{e,sep}$ using simple boundary conditions (innermost flux surface $n_{i,core}$ and diffusion coefficient D_n).
- As to upstream $T_{e,sep}$, its most important driver is $n_{e,sep}$. If $n_{e,sep}$ is set higher, $T_{e,sep}$ falls, and vice versa. $T_{e,sep}$ rises only weakly with the input power P_{SOL}.
- Adjusting P_{SOL} within the uncertainties of experimental power balance can be used to match the target peak $q_{\parallel}$ without a large effect on other simulation results.
- Outer target $T_{e,t}^{(peak)}$ tends to be only slightly smaller than upstream $T_{e,sep}$ under normal COMPASS conditions (sheath-limited LFS SOL). This gives a solid estimate of the upstream separatrix position.
- If upstream measurements of plasma potential Φ are available and if the simulated Φ forms a peaked structure (velocity shear layer, VSL), aligning the experimental and simulation VSL provides a separatrix position consistent with the previous rules.

Results of a simulation of the #17588 COMPASS L-mode, conducted in line with these rules of thumb, are shown in figure 4.6. Its main inputs are specified in table 4.2. I determined the optimal correction of the separatrix position at the plasma top as $Z_{shift} = -1.4$ cm (outward of the standard CDB reconstruction Z_{sep}). Going by intuition alone, I would estimate the uncertainty of such a correction as ± 2 mm. The main challenge is typically to maximise upstream $T_{e,sep}$, which means placing the separatrix neither too outward (low experimental $T_{e,sep}$ values) nor too inward (low simulation $T_{e,sep}$ values). Intuition is, however, no great guarantee. To verify these rules of thumb, I have conducted a systematic analysis of the separatrix position correction for discharge #17588. All simulation parameters not specified in this section are identical to those listed in section 4.6.

The *systematic approach* to finding the ideal separatrix position correction lies in independently performing simulations for several corrections and choosing the best one. During the work on this thesis, Zito et al [55] published a nearly identical process, which is automatised and more sophisticated, but arguably leaves out one important consideration. The common process begins by identifying a possible range of separatrix positions and performing an interpretative SOLPS-ITER simulation for each of them. In each case, the correct $n_{e,sep}$ (corresponding to experimental data at the presumed separatrix position, plotted with bold green circles in the left part of figure 4.3) is obtained by varying the density boundary condition $n_{i,core}$ and the diffusion coefficient D_n. In my simpler analysis, a constant D_n was found manually,

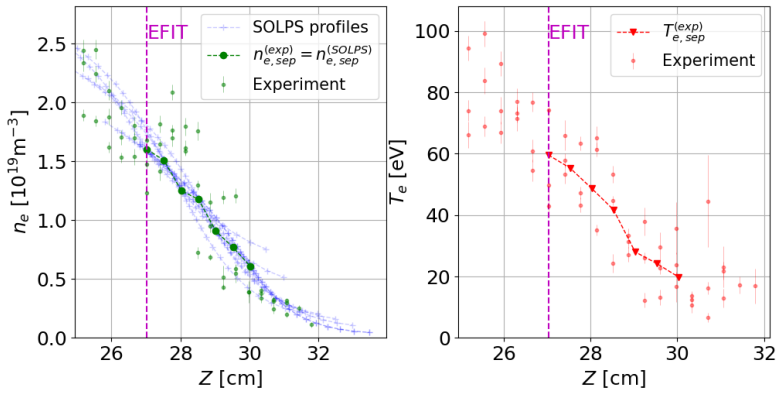

Figure 4.3: Upstream profiles of electron density n_e and temperature T_e in the COMPASS L-mode discharge #17588. On the left, SOLPS profiles of the Z_{shift} scan are plotted in blue and their respective $n_{e,sep}$ is plotted in bold green circles. On the right, averaged experimental $T_{e,sep}$ is plotted in red triangles.

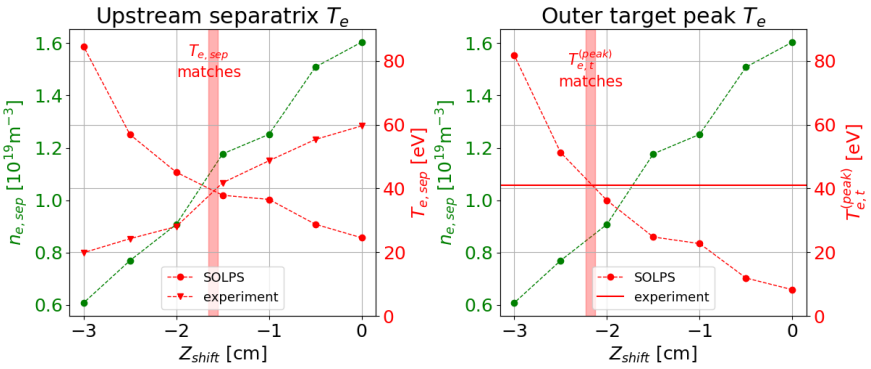

Figure 4.4: Choosing optimal separatrix correction Z_{shift} in COMPASS L-mode discharge #17588. Left: based on the upstream separatrix $T_{e,sep}$, right: based on the outer target $T_{e,peak}$.

while in Zito's analysis, a radial profile of D_n was found in an automated process of matching the local n_e profile slope. Matching the experimental $n_{e,sep}$ at a given P_{SOL} results in a particular simulation $T_{e,sep}$. This can be compared to experimental $T_{e,sep}$ at the initially chosen separatrix position (plotted with red triangles on the right of figure 4.3). The separatrix correction which yields identical simulation and experimental $T_{e,sep}$ is deemed optimal.

The results of this process are plotted in figure 4.4. Its left part shows the dependence of upstream $n_{e,sep}$ (experimental = simulation), experimental $T_{e,sep}$ and simulation $T_{e,sep}$ on the separatrix correction Z_{shift} along the vertical line of sight of the Thomson scattering diagnostic. Experimental $T_{e,sep}$ grows with experimental $n_{e,sep}$ as the separatrix is shifted inward. In contrast, SOLPS $T_{e,sep}$ falls as the separatrix is shifted inward. This agrees with the previously stated intuition that $n_{e,sep}$ and $T_{e,sep}$ are anti-correlated in SOLPS-ITER. The simulation and experimental $T_{e,sep}$ matches at $Z_{shift} = -1.7$ cm. Zito et al find the same qualitative result: SOLPS $T_{e,sep}$ falls with $n_{e,sep}$ while

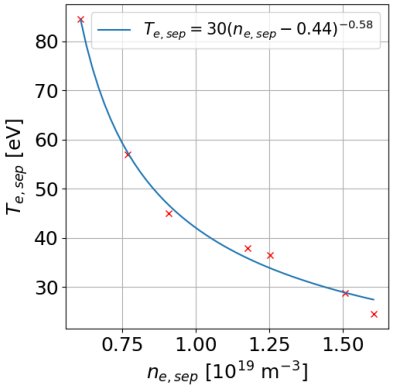

Figure 4.5: Inverse relationship between SOLPS simulation outer midplane separatrix electron temperature $T_{e,sep}$ and density $n_{e,sep}$, fitted with a power law. The data come from the Z_{shift} scan presented in this chapter.

experimental $T_{e,sep}$ rises, so there is a well-defined optimum where SOLPS matches experimental upstream density and temperature at the same time.

Let us briefly verify the relationship between $T_{e,sep}$ and $n_{e,sep}$ using this systematic scan in Z_{shift} at fixed input power P_{SOL}. Figure 4.5 shows that

$$T_{e,sep} = 30(n_{e,sep} - 0.44)^{-0.58},$$

where $n_{e,sep}$ is given in 10^{19} m^{-3}, with the coefficient of determination $R^2 = 0.99$. Using another set of simulations (variations of the density scan presented in chapter 6.1) with the same geometry and P_{SOL} varying within ± 10 %, one arrives at a result which is quantitatively nearly the same. This proves the intuitive claim that upstream $n_{e,sep}$ and $T_{e,sep}$ are anti-correlated in SOLPS-ITER simulations. However, we have no explanation for why a quantity like $T_{e,sep}(n_{e,sep} - n_{e,sep,min})^{0.6}$ should be preserved. The extended two-point model, for example, yields that in the transition between sheath- and conduction-limited regime, $T_u \propto n_u^{0.5}$. [12, Eq. (5.112)]

The work of Zito et al [55], while more advanced than our analysis, has an important drawback: it only seeks matching the *upstream* profiles while finding the optimal separatrix position. Ideally, one should make use of all available data and aim for simultaneous matching of target plasma parameters as well. I have focused on the outer target peak electron temperature $T_{e,t}^{(peak)}$, which is most readily available in COMPASS experiments. The right part of figure 4.4 shows a variation on the Z_{shift} scan analysis, this time comparing experimental and simulated outer target $T_{e,t}^{(peak)}$. SOLPS $T_{e,t}^{(peak)}$ falls as the separatrix is shifted radially inward, similarly to $T_{e,sep}$ but more steeply. On the other hand, the experimental outer target $T_{e,t}^{(peak)}$ is not affected by upstream separatrix corrections, so it is constant with Z_{shift}. The separatrix correction where outer target $T_{e,t}^{(peak)}$ matches in experiment and simulation is $Z_{shift} = -2.2$ cm.

The following table summarises the results of the three methods for finding the optimal separatrix position.

	Intuitive	Systematic (upstream)	Systematic (target)
Z_{shift}	-1.4 cm	-1.7 cm	-2.2 cm
Z_{sep}	0.285 m	0.288 m	0.293 m
Exp. $T_{e,sep}$	41 eV	38 eV	26 eV
SOLPS $T_{e,sep}$	37 eV	40 eV	49 eV
Exp. $T_{e,t}^{(peak)}$	41 eV	41 eV	41 eV
SOLPS $T_{e,t}^{(peak)}$	24 eV	29 eV	42 eV

Table 4.1: Outer midplane separatrix and outer target peak T_e depending on the upstream separatrix correction.

Comparing experimental and simulated T_e values, we observe a trade-off between matching upstream and target T_e. Matching upstream $T_{e,sep}$ leaves a discrepancy on the target, while matching target $T_{e,t}^{(peak)}$ leaves a discrepancy at upstream. Interestingly, the upstream-centric systematic correction constitutes a better compromise than the intuitive correction. Their Z_{shift} difference is not within my estimated uncertainty ± 2 mm, which may indicate a systematic error in the intuitive approach. If my intuition truly places the separatrix a few millimetres too inward, the conclusion of section 4.3 (the velocity shear layer forms approximately 0.5 cm outside the separatrix) may be weakened as well. What is more, the interpretative simulations presented in chapters 5 and 6 are all based on the intuitive approach, which may be an additional source of uncertainty. Performing a Z_{shift} scan for each of them is simply too time-consuming, which highlights the automated nature of Zito's algorithm. I do not believe that the separatrix position uncertainty is large enough to affect the results qualitatively, but it would certainly be desirable to reach a better quantitative agreement using a more sophisticated tool.

A promising tool for systematically identifying the optimal separatrix position has been prototyped in a recent Master's thesis. [186] In collaboration with the IPP SOLPS group, the student has implemented an automatised framework using Bayesian processes to find optimal SOLPS inputs in an interpretative COMPASS simulation. This approach naturally accommodates both additional diagnostics and uncertainties. Upon further development, the tool would significantly simplify making interpretative simulations of L-mode discharges and allow straightforward quantification of confidence intervals.[5]

Having thoroughly discussed the intuitive and systematic approach to correcting the separatrix position in interpretative SOLPS simulations, one

[5]The tool does not accommodate H-mode simulations as readily because the H-mode transport barrier typically demands a profile of anomalous diffusion coefficients, increasing the number of simulation input parameters. In simple L-mode simulations, the number of free parameters is 5-6: core density boundary condition $n_{i,core}$, input power P_{SOL}, particle diffusion coefficient D_n, thermal diffusion coefficients $\chi_e = \chi_i$, and 1-2 upstream separatrix position corrections. A typical transport barrier requires 5 additional parameters for particle diffusion (core value, well value, SOL value, 2 well boundaries) and 5 more for thermal diffusion, tripling the number of parameters to be optimised.

last method remains: to address the root cause and optimise the magnetic equilibrium reconstruction itself. The next section is focused on this approach. It should be noted, however, that not every SOLPS modeller has the knowledge or external support to correct their equilibrium reconstructions. Locally correcting the separatrix position is likely to remain the primary avenue to facilitate interpretative edge transport simulations. This section has shown that intuitive corrections of the separatrix position are not entirely arbitrary, and though the uncertainty is larger than one would believe, in the absence of more sophisticated tools it is a reasonable fix for inaccurate equilibrium reconstructions.

4.5 Improving equilibrium reconstructions using SOLPS-ITER simulations

In this thesis, I propose a new approach to validating and improving tokamak magnetic equilibrium reconstructions: using SOLPS-ITER simulations. The first part, validation, helps to assess a reconstruction quality and choose between variants of the same reconstruction. It consists of making an interpretative SOLPS-ITER simulation on top of different equilibria and gauging how large separatrix shifts need to be employed to facilitate experiment-model match. The reconstruction which requires the least amount of shifting is deemed the most accurate. The second part, improvement, leverages the optimal separatrix position found in the previous step by providing it to a Grad-Shafranov equilibrium solver as constraint.

Let us demonstrate reconstruction validation by comparing three SOLPS-ITER simulations of the COMPASS L-mode discharge #17588 at $t = 1100$ ms:

1. A simulation based on the standard CDB reconstruction with the intuitive separatrix shift $Z_{shift} = -1.4$ cm (outward).
2. A simulation based on the standard CDB reconstruction with no separatrix shift.
3. A simulation based on the reconstruction with optimised IPR coils positions and constrained by flux loop and Mirnov coil data, with no separatrix shift. This is reconstruction (3) in section 4.2, green in figure 4.1b. To allow for a sufficiently wide computational region [187], part of the limiter outline was withdrawn as shown in figure 4.1b.[6]

In each of the three cases, simulation inputs were tuned individually to achieve the best possible experiment-model match. They are listed in table 4.2.

Results of the three simulations are shown in figure 4.6. Simulations (1,

[6]As currently ongoing COMPASS Upgrade simulations show, a narrow SOL grid causes a multitude of problems. The proximity of the far SOL particle and energy sink lowers the fraction of input power which arrives at the divertor targets. Diagnostics measurements cannot be exploited fully and tightly spaced cells may drive numerical instabilities. After consulting [52], it was decided to side-step the issue by moving the offending limiter part out of the way. As a consequence, SOLPS-ITER will not capture the effect such low clearance would have on the SOL plasma.

	Standard CDB reconstruction		Corrected reconstruction
Z_{shift}	−1.4 cm	0 cm	0 cm
P_{SOL}	110 kW	110 kW	110 kW
$n_{i,core}$	2.1×10^{19} m^{-3}	2.4×10^{19} m^{-3}	1.8×10^{19} m^{-3}
D_n	0.15 m^{2}s^{-1}	0.4 m^{2}s^{-1}	0.15 m^{2}s^{-1}
$\chi_i = \chi_e$	3 m^{2}s^{-1}	1 m^{2}s^{-1}	3 m^{2}s^{-1}

Table 4.2: Input parameters of the SOLPS-ITER simulations listed on page 60: separatrix correction along the Thomson scattering vertical laser path Z_{shift}, core density boundary condition for D^{1+} $n_{i,core}$, anomalous particle diffusion coefficient D_n and electron and ion anomalous thermal diffusion coefficients χ_e and χ_i.

blue) and (3, green) yield similarly good results, while simulation (2, orange) underestimates the upstream $T_{e,sep}$ and consequently fails to reproduce outer target $T_{e,t}^{peak}$. As outlined in the previous chapter, the low $T_{e,sep}$ is primarily caused by a $n_{e,sep}$ which is much too high. The upstream SOL collisionality (5.6), $\nu^* = 17$ to the outer target and $\nu^* = 33$ to the inner target, is subsequently so high that both the targets partially detach ($p_t/p_u \approx 0.5$ in the 3rd SOL flux tube) in simulation (2).

We can draw several conclusions from this comparison.

- Starting from a considerably inaccurate equilibrium reconstruction, it is not possible to achieve good experiment-model match without shifting the separatrix. This means that a modeller who cannot procure a better reconstruction has no other recourse than to use separatrix shifting.
- Starting from an accurate equilibrium reconstruction, separatrix shifting is not needed. In other words, if the reconstruction didn't require any separatrix shifting in an interpretative SOLPS simulation, it must have been accurate (within experimental data uncertainties).
- Allowing for an intuitive correction of the separatrix position, it is possible to arrive at the same simulation results as those based on an accurate equilibrium reconstruction. This justifies the practise of separatrix shifting in interpretative modelling.

These findings are encouraging, as they lessen the impact of inaccurate magnetic reconstructions on edge plasma transport simulations. Let us not, however, walk away with the impression that an any equilibrium reconstruction will do for SOLPS-ITER. Shifting the separatrix is a source of uncertainty which can be avoided. If the reconstruction is too inaccurate, for instance placing the strike point on a baffle instead of a divertor target, no amount of shifting will save it. Most importantly, many diagnostic measurements used for interpretative simulations require an accurate equilibrium reconstruction for interpretation in the first place. The Thomson scattering system in the COMPASS tokamak cuts radially across flux surfaces, so a radial shift of the separatrix is sufficient to facilitate interpretative simulations. In contrast, the equivalent edge LIDAR diagnostic in the JET tokamak measures along

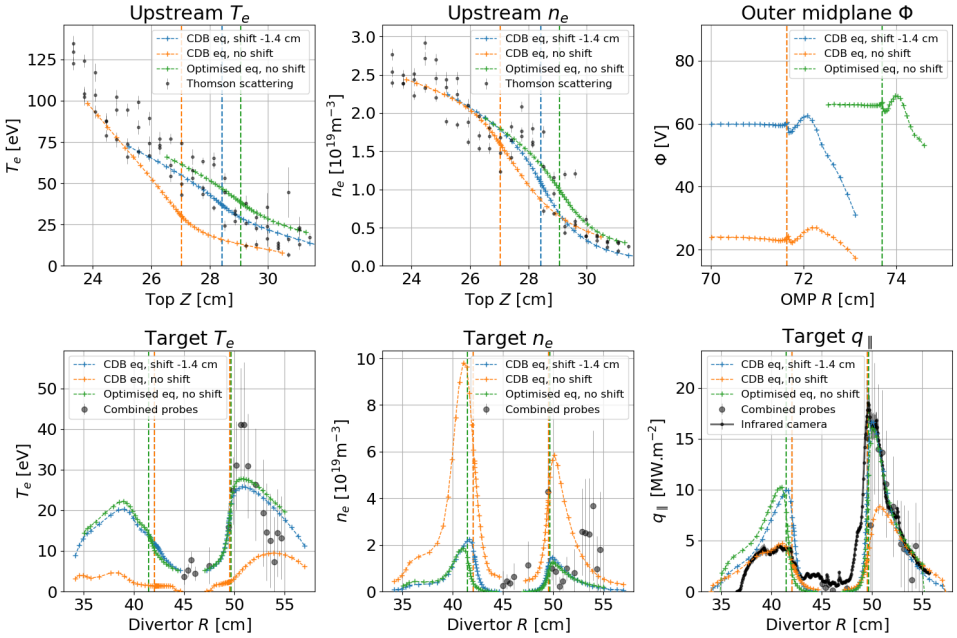

Figure 4.6: Three variants of interpretative SOLPS-ITER simulation of the COMPASS L-mode discharge #17588 at $t = 1100$ ms, listed on page 60. Experimental data is plotted in black, simulation data in colour. Vertical dashed lines denote the corresponding separatrix position.

an oblique laser path which cuts across flux surfaces at an angle. [158, 188] Such experimental data can be compared against SOLPS results directly by interpolating the simulation results along the laser path, but if the underlying equilibrium reconstruction is inaccurate, this path will not intersect the appropriate flux surfaces. In such a case, compensating for reconstruction errors is more complicated than simply shifting by some amount. In conclusion, using inaccurate reconstructions as basis for SOLPS-ITER modelling is acceptable if a better reconstruction is inaccessible and the errors are straightforward to correct for; otherwise a better reconstruction should be sought.

Now that we have shown how to validate magnetic equilibria with SOLPS-ITER simulations, let us discuss how to *improve* them. An output of a well-tuned interpretative simulation are corrected separatrix positions in one or more locations inside the vacuum vessel. In this chapter, it is the separatrix position along the Thomson scattering vertical laser path at $R = 0.557$ m. M. Komm has graciously adjusted his reconstruction script mentioned in section 4.2 to accept an arbitrary $[R, Z]$ separatrix location at time t as constraint. Passing [0.557 m, 0.285 m] (intuitive separatrix correction) at $t = 1100$ ms in discharge #17588 results in the pink equilibrium reconstruction shown in figure 4.7. The separatrix position at the top has moved to $Z = 0.284$ m and 1.5 cm outward at the outer midplane, which are good results. Additionally, the HFS separatrix as well as both strike points have moved roughly 0.4 cm to the LFS, which is not a desired effect on the divertor target, where the strike points were already well localised. In future work, adjusting the weights

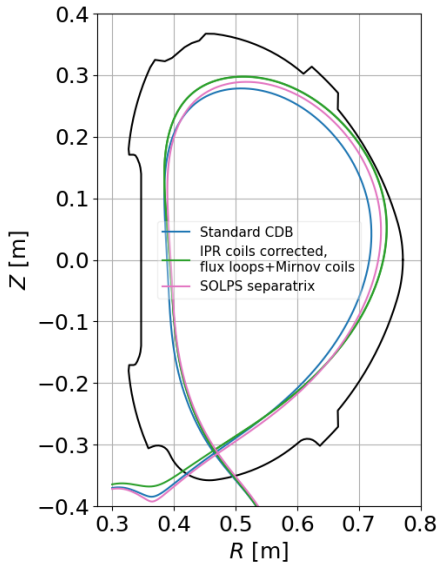

Figure 4.7: Separatrix outlines of 3 equilibrium reconstruction variants in the COMPASS discharge #17588 at $t = 1100$ ms: standard CDB reconstruction, reconstruction with corrected IPR coil positions and with additional Mirnov coils and flux loops constraints, and a reconstruction where the upstream separatrix position was set to $[R, Z] = [0.557 \text{ m}, 0.285 \text{ m}]$ according to interpretative SOLPS-ITER modelling.

of individual constraints would be desirable for the optimal result.

What is the benefit of calculating the separatrix position with SOLPS-ITER, rather than the incomparably faster two-point model? First and foremost, its SOL model is more complex. Even the extended two-point model [12, Sec. 5.4], which can accommodate SOL pressure and power losses, provides no quantitative prediction of the momentum and power loss factors $1 - f_{mom}$ (1.3) and $1 - f_{pow}$ (1.4). Using equation (4.1) (the basic two-point model), one implicitly assumes that loss factors are negligible. This may be the case in the sheath-limited regime, but it can already be questionable in the conduction-limited regime (significant power losses, see section 6.4 for examples), not to mention detachment (significant power and pressure losses). A SOLPS-ITER simulation, in contrast, solves for pressure and power losses self-consistently. Secondly, a SOLPS-ITER simulation is informed by multiple diagnostics, upstream, target, line-integrated and so forth. This lends it more credibility compared to the two-point model or nebulous assumptions about the edge plasma, such as those in section 4.1. The main drawback of using SOLPS-ITER is human time and computational resources necessary to create a simulation. In the future, these may be alleviated using SOLPS run automatisation. [186] At this stage, however, the validation process is time-intensive and only suitable for case studies where exceptionally high quality of equilibrium reconstruction is required.

The following procedure (localised to the COMPASS tokamak) can be followed to reduce the equilibrium reconstruction error:

1. In choosing a discharge to model, give preference to discharges with the divertor infrared camera, which provides accurate strike point localisation in attached plasma, and the horizontal reciprocating probe, which localises the separatrix at the outer midplane.
2. Perform several equilibrium reconstructions for the chosen discharge at the chosen time. Instructions are given in SOLPS-doc, tutorial *Creating an equilibrium reconstruction.* [25] Try as many variants as possible.
3. For each variant, compare the outer target $T_{e,t}^{(peak)}$ to the upstream $T_{e,sep}$. In COMPASS conditions, they should be rather near one another, certainly no further than a factor of two.
4. Compare the inner and outer strike point location to the peaks in the target energy flux density, measured by the divertor infrared camera. Unless the discharge is detached, their positions should coincide. The spatial resolution of the divertor probe arrays data is too low for this task, but they may provide validation.
5. Compare the outer midplane separatrix position to the velocity shear layer (VSL) position measured by the horizontal reciprocating probe. The VSL should be outside the separatrix, probably no more than 1 cm.
6. Pick the most promising equilibrium reconstruction and build a SOLPS-ITER grid on top of it. Ideally, do this for several reconstructions to gauge the uncertainty.
7. Perform the interpretative SOLPS-ITER simulations. Unless the plasma is exotic (e.g. strong impurity seeding), a simple deuterium simulation without drifts should suffice.
8. Extract the optimal separatrix positions at the plasma top, outer midplane and both strike points, and use them as constraint for a new equilibrium reconstruction.
9. Validate the new reconstruction using experimental data and a simple SOLPS-ITER simulation.

This procedure was tested in a recent Master's thesis under my supervision. [136] A well-diagnosed discharge #17692 was chosen from the COMPASS experimental database, with infrared camera measurements of divertor $q_{\parallel}$ and horizontal reciprocating probe measurements of the outer midplane VSL. Of the five reconstruction variants investigated (same as here), the variant with a realistic profile of plasma pressure was found the most accurate. Subsequent SOLPS-ITER simulations, which were performed in pure deuterium, without drifts, and with boundary conditions analogous to those used in this chapter, led to three conclusions. One, SOLPS simulations based on different equilibria but with identical inputs yield the same simulation results within uncertainties. Two, shifting the separatrix in these simulations to match experimental data yields the same optimal separatrix position. This would seem a trivial consequence of the first result, but it is made salient by the range of necessary corrections — at the plasma top, from 2.2 cm inward to 0.8 cm outward. Finally, as long as an equilibrium reconstruction is not qualitatively wrong, shifting the separatrix position is a robust process whose uncertainties are comparable to the uncertainties of diagnostics and the simulation itself. A

qualitatively wrong reconstruction is, for example, one which has such a low separatrix-limiter clearance that the equilibrium becomes limited and not diverted. These three conclusions support the conclusion of this chapter, that shifting the separatrix is an acceptable practice during interpretative SOLPS-ITER modelling.

4.6 Interpretative SOLPS-ITER simulation of the COMPASS L-mode discharge #17588

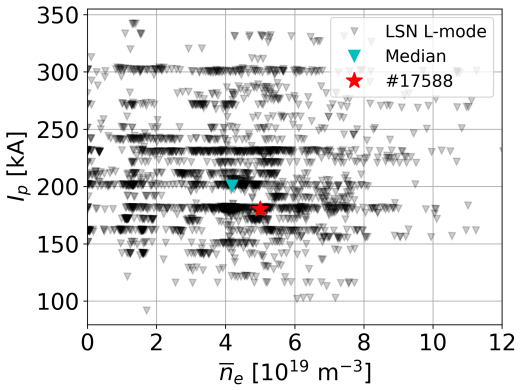

(a) : Operational space of COMPASS tokamak lower single null L-mode discharges #5985-#16521. Median line-averaged density $\overline{n}_e$ and plasma current I_p are plotted in cyan.

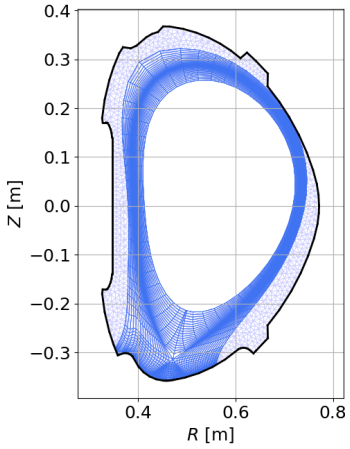

(b) : B2.5 (dark) and EIRENE (light) meshes, built using the pink equilibrium reconstruction from figure 4.7 (with SOLPS separatrix constraint).

Figure 4.8: Parameters of the COMPASS L-mode discharge #17588.

Discharge description. COMPASS discharge #17588 is a typical L-mode discharge in the lower single null (LSN) divertor configuration. It was performed in deuterium without extrinsic impurities, neutral beam heating was off at the simulated time, resonant magnetic perturbations were not applied and no particularly disruptive diagnostic (such as a reciprocating probe) was measuring. With the line-averaged density $\overline{n}_e = 5 \times 10^{19}$ m^{-3} and plasma current $I_p = 180$ kA, discharge #17588 lies near the middle of the COMPASS LSN L-mode parameter space (see figure 4.8a). The toroidal magnetic field is $B_t = -1.38$ T at the magnetic axis (forward field), the edge safety factor is $q_{95} = 4.2$ and the ion grad-B drift is directed toward the divertor. The modelled time instance is $t = 1100$ ms. At this time, the ohmic heating power was $P_{ohmic} = 200$ kW, of which $P_{rad} = 65$ kW was radiated in the core according to bolometer measurements.

Available diagnostics. The diagnostics coverage included the Thomson scattering diagnostic, the combined divertor probe array and the divertor infrared camera. Neither the horizontal reciprocating probe nor the swept divertor array were measuring. This is sufficient for an interpretative simulation,

though not entirely ideal.

Simulation details. The SOLPS-ITER mesh (figure 4.8b) was constructed using the new equilibrium reconstruction from the previous section, where the upstream separatrix position was constrained according to previous SOLPS results. The anomalous diffusion coefficients were $D_n = 0.15$ m^{2}s^{-1} for particles and $\chi_e = \chi_i = 3$ m^{2}s^{-1} for ion and electron energy. The power balance was maintained by the core energy boundary condition $P_{SOL,i} = P_{SOL,e} = 55$ kW and particle fueling was maintained by the core density boundary condition $n_{D^{1+}} = 1.8 \times 10^{19}$ m^{-3}. Heat flux limiters were set to $\alpha_e = \alpha_i = 0.3$. The main ion species was deuterium and additional carbon impurities were sputtered physically and chemically from the targets (chemical sputtering yield $\gamma_{chem} = 0.01$). The simulation was run at time step d$t = 10^{-4}$ s until converged. To avoid numerical instabilities, stemming from large acceleration forces on low-density impurity ion species and consequent high viscous heating and supra-luminal velocities, the minimum ion density was raised to 10^8 m^{-3}. Drifts were turned off. The SOLPS-ITER version was `3.0.9-27-g614fb016`.

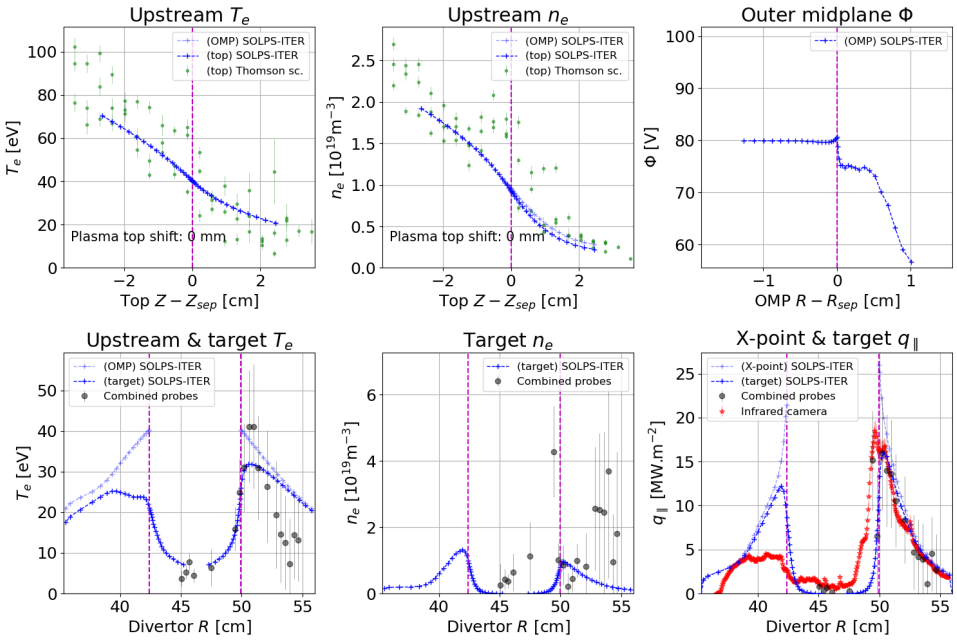

Figure 4.9: Comparison of COMPASS L-mode discharge #17588, $t = 1100$ ms, to its interpretative SOLPS-ITER simulation.

Upstream. The top part of figure 4.9 shows that the equilibrium reconstruction correction was successful — mutual shift of experimental and simulated profiles is no longer needed within experimental uncertainties. The bump on separatrix n_e is thought to be a Thomson scattering measurement artifact rather than a physical feature. The outer midplane potential profile is similar to a velocity shear layer outside the separatrix, but the Φ peak is not clearly resolved.

Target. Outer target $T_{e,peak}$ is well reproduced, although the experimental

target T_e profile is more peaked than SOLPS simulation data or upstream experimental T_e profile. This may be the effect of drifts acting on the target n_e and T_e. Strong thermoelectric and Pfirsch-Schlütter currents in the hot, low-resistivity COMPASS divertor plasma cause the build-up of electric fields, which redistribute plasma particles via the $\mathbf{E} \times \mathbf{B}$ drift. [189, 190] According to the local current direction, drifts can cause local n_e decrease or increase. T_e then adjusts in the opposite direction to compensate the total pressure. [191] As figure 3.5 as well as previous studies show [192, 2, 193], in forward field at the outer target, this results in near SOL T_e enhancement and n_e suppression, and vice versa in the far SOL. This is consistent with the observed steepening of the target T_e profile. This mutual compensation of n_e and T_e is the reason why the total target energy flux density, $q_{\parallel t} \propto n_e T_e^{3/2}$ is relatively unaffected by drifts, and its outer target profile shape is matched well by our drift-less SOLPS simulation. The location of both strike points in the equilibrium reconstruction is shifted to the LFS by a few mm, as noted in the previous section. SOLPS-ITER overestimates the inner target peak energy flux density $q_{\parallel}$ by more than a factor of two. Redistribution of outer-inner target heat load has been noted among the effects of including drifts in SOLPS simulations as well. [13] Overall, the agreement is worse than at upstream, but generally within acceptable boundaries.

Transport regime. We calculate the momentum and power loss factors f_{mom} and f_{pow} in the 3rd SOL flux tube according to section 6.4. Toward the outer target, the parallel temperature is $T_{e,u}/T_{e,t} = 1.3$, the momentum loss factor is $1 - f_{mom} = 1.1$ and the power loss factor is $1 - f_{pow} = 0.7$. This is the sheath-limited regime. Toward the inner target, the parallel temperature is $T_{e,u}/T_{e,t} = 1.7$, the momentum loss factor is $1 - f_{mom} = 1.1$ and the power loss factor is $1 - f_{pow} = 0.6$. This is the transition from sheath-limited to conduction-limited regime.

Comments. The interpretative simulation of COMPASS L-mode discharge #17588 was reasonably successful. Correction of the underlying equilibrium reconstruction using previous SOLPS-ITER simulations removed the necessity for ad-hoc upstream profile shifts, which is a good result. The disagreement in target profiles can be attributed to divertor drift effects. The transport regime, sheath-limited toward the outer target and transitional toward the inner target, agrees with previous findings. [6, 194]

Chapter 5

Heat flux limiting

This chapter investigates kinetic effects in SOL parallel heat transport on the example of an interpretative SOLPS-ITER simulation of the COMPASS H-mode discharge #16908. Physics stemming from the velocity space of the particle distribution function is dropped during the Braginskii closure (section 2.1.6), although it prominently affects heat conduction along SOL magnetic field lines. These kinetic effects are emulated in SOLPS-ITER using *heat flux limiting*, which reduces the classical (Spitzer-Härm) conductive heat flux density using a harmonic average with a fraction of the free-streaming heat flux density. The fraction is a free parameter called the *heat flux limiter* α, and its value approximates the impact of kinetic effects on parallel heat conduction. A basic question of mimicking kinetic effects in edge transport simulations is: What value should the electron and ion heat flux limiter have in the SOL?

This chapter is organised as follows. In section 5.1, I present an interpretative simulation of the COMPASS H-mode #16908. In section 5.2, I recapitulate basic properties of the classical heat flux: its locality and its strong dependence on temperature. In section 5.3, I discuss three definitions of SOL collisionality: temporal, spatial and based on the two-point model. In section 5.4, I review historical approaches to correcting the classical heat flux. In section 5.5, I gauge heat flux limiter values appropriate for COMPASS SOLPS-ITER modelling from the theoretical point of view. In section 5.6, I show how the harmonic average works and demonstrate that electron and ion heat flux limiting were not created equal. In section 5.7, I present a 2D SOLPS parameter scan in α_e and α_i, and argue that the primary effects of heat flux limiting are reducing conductive heat fluxes $q_{\parallel cond}$ and enhancing parallel temperature gradients. Finally, in section 5.8, I compare SOLPS results to a BIT1 kinetic simulation performed by D. Tskhakaya and summarize the theoretical, historical, fluid and kinetic insights into recommendations for setting heat flux limiters. In the investigated COMPASS H-mode #16908 simulation, electron heat flux limiters can be chosen arbitrarily above 0.2, while ion heat flux limiters should be adjusted in conjunction with the electron-ion input power split to obtain realistic upstream $T_{i,sep}$ values. Generally, I encourage a more holistic treatment of heat flux limiting, which does not focus so much on specific α and $q_{\parallel cond}$ values as on sensitivity ranges and knock-on effects of heat flux limiting.

Some of the results presented in this chapter have been publicized in the proceedings of the 49th EPS Conference on Plasma Physics, 2023, which are attached in appendix A.5.

5.1 COMPASS H-mode discharge #16908

Discharge description. COMPASS discharge #16908 is an H-mode discharge in the lower single null divertor configuration. It was performed in deuterium without extrinsic impurities, neutral beam heating was on at the simulated time, resonant magnetic perturbations were not applied and no particularly disruptive diagnostic (such as a reciprocating probe) was mea-

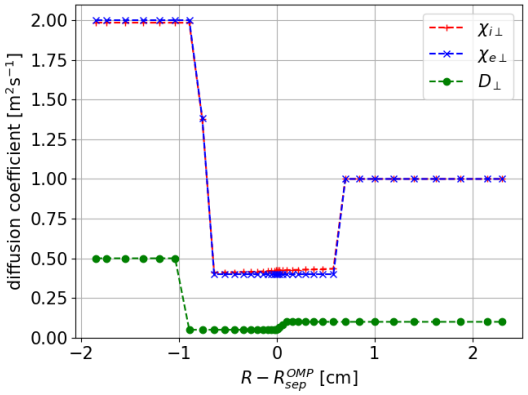

(a) : Profiles of the ion and electron anomalous thermal diffusion coefficient $\chi_{e,i}$ and the anomalous particle diffusion coefficient D_n.

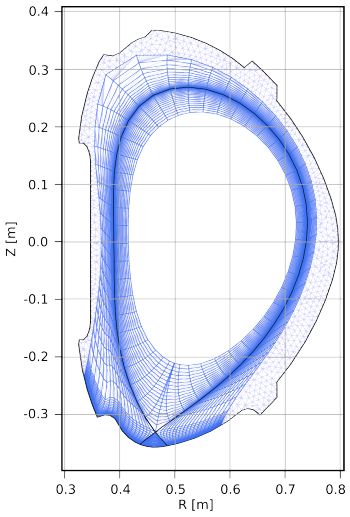

(b) : B2.5 (dark) and EIRENE (light) meshes, built using the standard CDB equilibrium reconstruction at $t = 1130$ ms.

Figure 5.1: SOLPS-ITER simulation parameters of the COMPASS H-mode discharge #16908.

suring. The line-averaged density was $\overline{n}_e = 6.5 \times 10^{19}$ m^{-3} and the plasma current was $I_p = 240$ kA. The toroidal magnetic field was $B_t = -1.15$ T at the magnetic axis (forward field), the edge safety factor was $q_{95} = 2.8$ and the ion grad-B drift was directed toward the divertor. The modelled time instance is $t = 1130$ ms, in the inter-ELM period. At this time, 90 kW of power was crossing the separatrix according to power balance taking into account ohmic heating, the energy stored in the plasma, and power radiated in the core according to bolometer measurements. Additionally, the NBI power absorbed by the plasma was 240 kW. The total power crossing the separatrix was, therefore, $P_{SOL} = 330$ kW.

Available diagnostics. The diagnostics coverage included the Thomson scattering diagnostic, the combined divertor probe array, the swept divertor array, and the divertor infrared camera.

Simulation details. The standard EFIT++ equilibrium reconstruction at $t = 1130$ ms was used to construct the SOLPS-ITER mesh (figure 5.1b). The anomalous diffusion coefficients profiles in the shape of a transport barrier, figure 5.1a, were tuned manually and iteratively to match the experimental upstream profiles shape. The power balance was maintained by the core energy boundary condition $P_{SOL,i} = P_{SOL,e} = 165$ kW and particle balance was maintained by the core density boundary condition $n_{D^{1+}} = 4.2 \times 10^{19}$ m^{-3}. Heat flux limiters were set to $\alpha_e = \alpha_i = 0.3$. The main ion species was deuterium and additional carbon impurities were sputtered physically and chemically from the targets (chemical sputtering yield $\gamma_{chem} = 0.01$). The simulation was run at time step $\mathrm{d}t = 10^{-4}$ s until converged, and

then a smoothing run at $\mathrm{d}t = 10^{-5}$ s was performed. To avoid numerical instabilities, stemming from large acceleration forces on low-density impurity ion species and consequent high viscous heating and supra-luminal velocities, the minimum ion density was raised to 10^8 m^{-3}. Drifts were turned off. The SOLPS-ITER version was `3.0.9-27-g614fb016`.

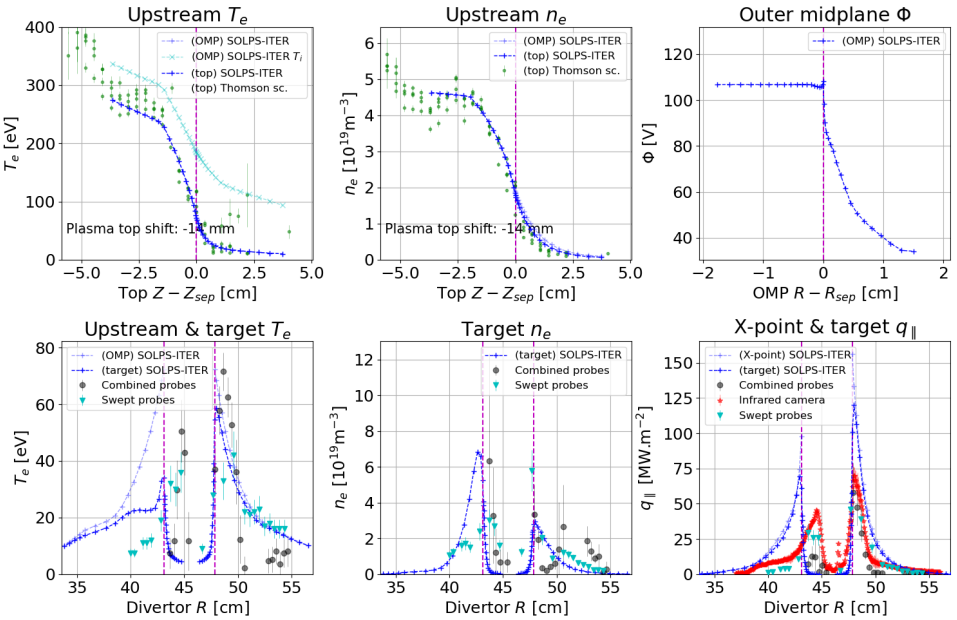

Figure 5.2: Comparison of COMPASS H-mode discharge #16908, $t = 1130$ ms, to its interpretative SOLPS-ITER simulation. The Thomson scattering data was shifted by $Z_{shift} = -14$ mm to correct for equilibrium reconstruction inaccuracy at the plasma top.

Upstream. The top part of figure 5.2 matches the SOLPS output to the Thomson scattering diagnostic. The SOLPS profiles were shifted by 14 mm to the right (radially outward) to correct for inaccurate equilibrium reconstruction. Thanks to the manual tuning of the diffusion coefficient profiles, SOLPS results follow the experimental profiles closely.

Target. The bottom part of figure 5.2 matches the SOLPS output to the combined divertor probe array, the swept divertor probe array and the divertor infrared camera. The T_e profile is highly peaked, matching the combined probe array in some parts and the swept probe array in other. The target electron density profile is of similar magnitude to that of the two probe arrays. SOLPS-ITER overestimates the parallel energy flux density at both strike points. Decreasing the input power from $P_{SOL} = 330$ kW to $P_{SOL} = 260$ kW will lower both strike point heat loads by 25 %, but it also necessitates retuning the thermal diffusivity $\chi_{e,i}$ profiles. Its impact on the simulation is not great, so it was decided to forego the weeks of effort and accept overestimated outer target $q_\parallel$. The reconstructed inner strike point position is clearly erroneous. Performing the equilibrium reconstruction with corrected IPR coils position and flux loops and Mirnov coils constraint, the inner strike points moves 1 cm to the low-field side, partially compensating

for the error. The reconstruction, however, does not move the separatrix outward at the plasma top, which is our primary concern, so it was not used as basis for the grid construction.

Transport regime. We calculate the momentum and power loss factors f_{mom} and f_{pow} in the 3rd SOL flux tube according to section 6.4. Toward the outer target, the parallel temperature gradient is $T_{e,u}/T_{e,t} = 1.1$, the momentum loss factor is $1 - f_{mom} = 1.2$ and the power loss factor is $1 - f_{pow} = 1.0$. This is the sheath-limited regime. Toward the inner target, the parallel temperature gradient is $T_{e,u}/T_{e,t} = 2.4$, the momentum loss factor is $1 - f_{mom} = 1.5$ and the power loss factor is $1 - f_{pow} = 1.0$. This is the transitional regime between sheath- and conduction-limited.

Comments. The interpretative simulation of COMPASS H-mode discharge #16908 was reasonably successful, accepting that the outer target peak energy flux density was overestimated by a factor of 2. Large T_e and n_e gradients around the separatrix have made striking a balance between $T_{e,sep}$ and $n_{e,sep}$ difficult and time-consuming. Admittedly, there is still space for optimisation; however, this is I drew the line between reaching a reasonable agreement and overfitting. In future H-mode simulations, it would be advisable to adopt an automatised algorithm to iteratively fit the diffusion coefficient profiles. [55, 186] Four months of human and computational time can be put to better use.

5.2 Classical heat flux

The "classical" (or "Spitzer-Härm", after the seminal work of Spitzer and Härm [195]) heat flux density is the conductive part of the total energy flux density appearing in equations (2.28) and (2.29) in the Braginskii closure:

$$q_{\parallel e,cond} = -\kappa_e \nabla_\parallel T_e = -3.16 \frac{e^2 n_e T_e \tau_e}{m_e} \nabla_\parallel T_e \tag{5.1}$$

for electrons and

$$q_{\parallel i,cond} = -\kappa_i \nabla_\parallel T_i = -3.9 \frac{e^2 n_i T_i \tau_i}{m_i} \nabla_\parallel T_i \tag{5.2}$$

for ions. Here $\kappa_{e,i}$ is the parallel thermal conductivity and $\tau_{e,i}$ is the collision time, given by equations (2.25) and (2.22) in the Braginskii closure. The e^2 factor accounts for different units: Braginskii equations give the temperature in joules, while this chapter works with temperature in electronvolts. The prefactor 3.16 for electrons and 3.9 for ions is specific to the Braginskii closure; in SOLPS-ITER it is modified by the Zhdanov closure to include the effects of the effective ion charge Z_{eff}. [33, Sec. B.5] The exact value of the prefactor is unimportant to the following discussion.

To reiterate section 2.1.4, the term "heat flux" is short for conductive energy flux, which stems from asymmetries in the velocity distribution function. The unit of heat flux is W, and it will be differentiated from heat flux density q [W.m^{-2}] as appropriate.

The classical heat flux has two defining features. It is *local* and it strongly depends on the temperature.

The classical heat flux being "local" means that heat flux density at position $\mathbf{r}$ can be expressed solely in terms of densities n_a, velocities $\mathbf{u}_a$ and temperatures T_a at the position $\mathbf{r}$. As [36] comments, this only makes sense under the assumption that mean free paths are much smaller than the gradient or system size. Locality is an advantage for transport codes as well as for theoretical work, as it makes the fluxes straightforward to calculate. It also makes the system proof to thermodynamic instabilities such as negative entropy production. [196]

Let us illustrate the difference between locality and non-locality in parallel SOL transport. We consider a conduction-limited flux tube, where upstream $T_e = 80$ eV and downstream $T_e = 15$ eV.

Positing for a moment that transport is purely local in this system, heat flow through the divertor plasma is not at all affected by the upstream plasma. The target plasma is shielded by the many collisions particles must undergo while travelling there from the upstream plasma, so the target velocity distribution is nearly Maxwellian and contains no information of the upstream parameters. (We neglect sheath effects, which strongly distort both the electron and ion velocity distributions. [39, Fig. 3]) The total energy flux through the sheath can be expressed locally as

$$q_\parallel(\mathbf{r}) = \gamma(\mathbf{r}) n_e(\mathbf{r}) T_e(\mathbf{r}) c_s(\mathbf{r}),$$

where the sheath heat transmission coefficient $\gamma \approx$ 7-8 is, to a good degree, determined by the classical formula.[1] [12, Sec. 2.8]

Let us allow for non-local effects now. The high-energy particles originating from the upstream velocity distribution are significantly less collisional than thermal upstream particles (20-30x for the so-called heat carrying electrons [197]). They travel to the target with little or no energy losses, and become a high-velocity tail on the distribution function. These hot particles are not nearly as many as the thermal target particles, so they do not affect the lower moments of the distribution function, density, velocity and temperature. But, as distribution function distortions become more apparent at higher moments, the suprathermal particles do increase heat flux. This can be formulated as the increase of the effective thermal conductivity $\kappa_a^{(eff)} = -q_{\parallel a}/\nabla_\parallel T_a$ and the effective sheath heat transmission coefficient $\gamma^{(eff)} = q_\parallel / n_e T_e c_s$ relative to classical values. [48] Since the parallel heat flux density is no longer given by local plasma parameters, such effective transport coefficient lose much of their physical meaning and can vary wildly in space and time. In a transport code, this effect cannot be inferred from target plasma parameters as it depends on plasma parameters elsewhere; it is, therefore, non-local.

Non-locality of SOL parallel heat transport is a headache for both theoreticians and transport modellers. It has been shown that even in a moderately

[1] For divertor target energy flux measurements at the COMPASS tokamak, $\gamma = 11$ has been used instead. [123] The exact value of γ is unimportant to the discussion at hand, and so the classical value is used for simplicity.

collisional plasma ($\nu^* = 26$, equation (5.6)), 21 % of the total heat flux is carried by hot electrons. [198] In a collisionless plasma ($\nu^* = 0.01$), the ratio grows to 65 %. Gauging and accounting for non-local effects is an important part of setting up a SOL transport simulation.

The other defining feature of the classical (or Spitzer-Härm) heat flux is that it depends strongly on the species temperature T_a. The higher the temperature, the higher the typical velocity of the particle chaotic thermal movement, the weaker Coulomb interaction between them, and the longer the collision time. In total, one obtains $\kappa_a \propto T_a^{5/2}$. This is the only functional dependence of κ_a retained in the approximation popularised by P. Stangeby [12, Eq. (4.83)],

$$q_{\parallel a} = -\kappa_0 T^{5/2} \nabla_\parallel T_a, \tag{5.3}$$

where $\kappa_0 = 2000$ for electrons, $\kappa_0 = 60$ for ions, and T_a must be given in eV to obtain the heat flux density in W.m^{-2}.

This strong dependence means that strongly collisional, hot plasma is extremely efficient at conducting energy. Electron thermal conductivity calculated with equation (5.3) for $T_e = 60$ eV is $\kappa_e = 4800$ Wm^{-1}K^{-1} and ion thermal conductivity for $T_i = 60$ eV is $\kappa_i = 140$ Wm^{-1}K^{-1}. By comparison, the thermal conductivity of gold is approximately 300 Wm^{-1}K^{-1} [199] and the thermal conductivity of graphene is approximately 2000 Wm^{-1}K^{-1} [200]. Strongly collisional, hot plasma is easily one of the best thermal conductors we know.

Another way to express thermal conductivity κ_a is as proportional to the mean free path λ_a. [12, Eq. (26.2)] and [201, Eq. (5)] give the expression for electron thermal conductivity

$$\kappa_e = 1.31 k_B n_e v_{th,e} \lambda_e, \tag{5.4}$$

where $v_{th,e} = \sqrt{eT_e/m_e}$ is the electron thermal velocity. In a collisionless plasma ($\lambda_e \to \infty$), therefore, thermal conductivity approaches infinity. This is not necessarily an unphysical result. Provided that temperature gradients vanish with increasing thermal conductivity, heat flux density $q_a = -\kappa_a \nabla T_a$ can remain finite even at long mean free paths. The calculation does, however, become impractical. This leads Hazeltine to formulate his collisionless plasma transport theory in terms of particle and energy sources rather than gradients. [36] The situation is similar to the *self-limiting* heat flux scenario analysed in [39], where the plasma is hot, mean free paths are long and the conductive heat flux is saturated on the free-streaming heat flux value, $q_{FS,a} = e n_a T_a v_{th,a}$.

5.3 SOL collisionality

What exactly do we mean by "collisional" plasma? In the Braginskii closure, section 2.1.6, high collisionality was required in two aspects: temporal (time evolution scales are larger than the collision time) and spatial (gradient scales are larger than the mean free path). In this thesis, we give plasma collisionality as the ratio "large scale/small scale", or as the inverse Knudsen number $1/K$

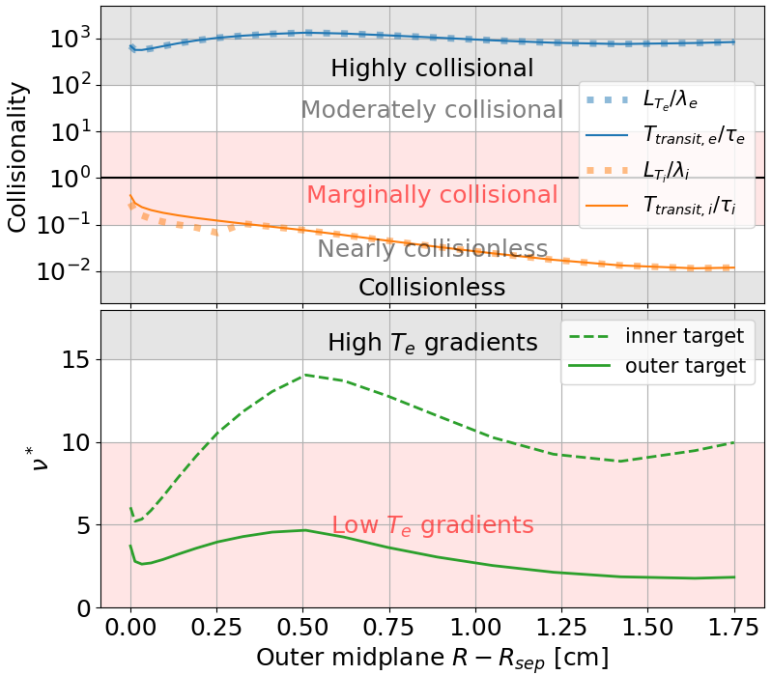

Figure 5.3: Radial profiles of upstream SOL collisionalities, calculated from the SOLPS-ITER simulation of the COMPASS H-mode #16908. Top figure: spatial collisionality (ratio of the gradient size or system size L_{T_a} to the mean free path λ_a) and temporal collisionality (ratio of the transit time $T_{transit,a}$ to the collisional time τ_a). Bottom figure: the collisionality parameter ν^*, equation (5.6). [12, Sec. 4.10.2]

[39]. The terms "collisionless", "marginally collisional" and "highly collisional" for collisionality ranges are illustrated in the upper part of figure 5.3.

In the following paragraphs, we calculate the temporal and spatial characteristics of 3rd SOL flux tube of the COMPASS H-mode #16908 simulation, which was presented in section 5.1. This flux tube is often used for SOL transport analysis, as it is near enough the separatrix to carry substantial heat fluxes, but does not suffer radial losses into the private flux region. Some of these characteristics are listed in table 5.1. As we shall see, spatial and temporal collisionality are mostly interchangeable in the SOL, which is why only the spatial scale ordering is discussed in the literature.

The time evolution scale appropriate to the SOL is the electron and ion transit time $T_{transit,a} = L/v_{th,a}$, that is, the time a particle travelling at thermal velocity from the outer midplane will take to reach a divertor target. [45] As evidenced by particle-in-cell simulations of the tokamak SOL, ions travel from the source region to the wall, where they are accelerated inside the sheath and lost to the divertor target. [202, 49] The appropriate length to travel, is therefore, the connection length to the closer outer target, which is $L = 6$ m for the analysed flux tube. Taking the thermal velocity listed in table 5.1, the ion transit time is then $T_{transit,i} = 65$ μs. The travelled distance of electrons must first be adjusted for bouncing between the divertor targets,

Electrons	upstream temperature $T_e = 63$ eV
	mass $m_e = 9.1 \times 10^{-31}$ kg
	thermal velocity $v_{th} = \sqrt{eT_e/m_e} = 3300$ km.s^{-1}
	upstream density $n_e = 1.6 \times 10^{19}$ m^{-3}
	Coulomb logarithm $\ln \Lambda = 17$
	collision time $\tau_e = 3.45 \times 10^{11} \dfrac{T_e^{3/2}}{n_e \ln \Lambda} = 0.63$ μs
	mean free path $\lambda_e = v_{th,e}\tau_e = 2.1$ m
Ions	upstream temperature $T_i = 180$ eV
	mass (deuteron) $m_i = 3.3 \times 10^{-27}$ kg
	thermal velocity $v_{th,i} = \sqrt{eT_i/m_i} = 93$ km.s^{-1}
	upstream density $n_i = 1.4 \times 10^{19}$ m^{-3}
	Coulomb logarithm $\ln \Lambda_i = 1.1 \ln \Lambda = 18.7$
	proton mass $m_p = 1.7 \times 10^{-27}$ kg
	collision time $\tau_i = 2.08 \times 10^{13} \dfrac{m_i}{m_p} \dfrac{T_i^{3/2}}{n_i \ln \Lambda_i} = 370$ μs
	mean free path $\lambda_i = v_{th,i}\tau_i = 34$ m

Table 5.1: Quantities relevant to upstream SOL collisionality in the 3rd SOL flux tube of the COMPASS H-mode #16908 simulation. Formulas were taken from [42, App. 14.6] and converted to T [eV].

as thermal electrons are reflected from the electric potential of the sheath and return to the upstream SOL. [202] Electrons typically bounce 60 times before finally impinging on the target. [203] Consequently, their travelled distance is approximately 60 times the total flux tube length, $L = 60 \cdot 18$ m $= 1080$ m, and the electron transit time is $T_{transit,e} = 330$ μs.

The "small" counterpart to the transit time are the electron and ion collision times, calculated in table 5.1 as $\tau_e = 0.63$ μs and $\tau_i = 370$ μs. Electrons are therefore highly collisional in the temporal aspect ($T_{transit,e}/\tau_e = 510$), while ions are marginally collisional ($T_{transit,i}/\tau_i = 0.18$).

In the Braginskii spatial scale ordering, the "large" scale is either the temperature gradient size or the system size, whichever is smaller (with an important caveat explained in the following paragraph). The gradient size is defined as

$$L_{T_a} = \frac{T_a}{\left|\nabla_\parallel T_a\right|}. \tag{5.5}$$

An alternative definition can be "distance along the magnetic field line over which the temperature T_a falls to $1/e \approx 38\%$ of its original value".

We note a peculiar feature here: in the absence of strong particle and power sources and sinks, the temperature gradient size L_{T_a} actually tends to *scale* with the mean free path λ_a. This phenomenon was recently stumbled upon in 1D fluid simulations of the ITER SOL. [46] The authors attempted

to predict kinetic effects using the ratio of the electron mean free path λ_e to the gradient size, but met with little success. A much better predictor turned out to be the ratio of the mean free path λ_a to the *system size*. This was explained analytically using simplified fluid equations, where the maximum T_e gradient size achieved along a flux tube was found proportional to the electron mean free path λ_e. In reality, the theoretical description of this problem is given in the well-known review by Fundamenski. [39, Sec. 2.1] It is actually quite intuitive that any features smaller than the mean free path λ_a in the temperature profile will be washed out within one collision time τ_a, as the distance can be easily travelled by thermal particles, $\lambda_a = \tau_a v_{th,a}$.

It should be stressed that the gradient size is proportional to λ_a *only in the absence of strong particle and power sources and sinks*. These are not only sources and sinks due to plasma-neutral interaction, which become important in low-temperature or highly impure plasma, but also the sheath itself. In a tokamak SOL, which is either highly affected by the plasma-neutral interaction (high-recycling regime and detachment) or by the sheath (sheath-limited regime), it is not clear *a priori* how well the gradient size will scale with the mean free path. In this section, SOL spatial collisionality will usually be gauged by comparing λ_a to the system size, as the temperature parallel profiles are rather flat. Let us keep in mind the possibility of $\lambda_a \propto L_{T_a}$.

In the 3rd SOL flux tube of the investigated simulation, ion temperature drops from its upstream value of $T_i = 180$ eV to 38 % of this value, 68 eV, within 5.5 m on the way toward the outer target. The ion spatial scale is, therefore, $L_{T_i} = 5.5$ m. The electron temperature T_e, on the other hand, only drops by 13 % from the outer midplane to the outer target and by 57 % toward the inner target. The appropriate length scale, therefore, is the system size. Considering that electrons bounce circa 60 times between the divertor targets before impinging on a divertor target, the "large" electron spatial scale is proportional to the flux tube length, $L_{T_e} = 60 \cdot 18$ m $= 1080$ m.

The "small" spatial scale in the edge plasma are the electron and ion mean free paths, that is, the typical distance over which small Coulomb collisions will add up to a total deflection angle 90 °. [195] As table 5.1 shows, the electron mean free path is $\lambda_e = 2.1$ m and the ion mean free path is $\lambda_i = 34$ m. The result is that electrons are highly collisional ($L_{T_e}/\lambda_e = 510$) and ions are marginally collisional ($L_{T_i}/\lambda_i = 0.16$).

The similarity between the conclusions of the temporal and spatial scale ordering examination follows from the fact that characteristic spatial scales are proportional to the characteristic time scales through the thermal velocity $v_{th,a}$ in table 5.1 and its source [42, App. 14.6]. In fact, if the parallel temperature gradient is small and L_{T_a} is taken as the system size, the temporal and spatial collisionality are exactly equal. In the top part of figure 5.3, we plot the temporal and spatial collisionalities for ions and electrons across the upstream SOL of the investigated simulation. Electron spatial and temporal collisionalities coincide. As shown later in figure 5.12, T_i only has substantial gradients in the near SOL. In the far SOL, ions are nearly

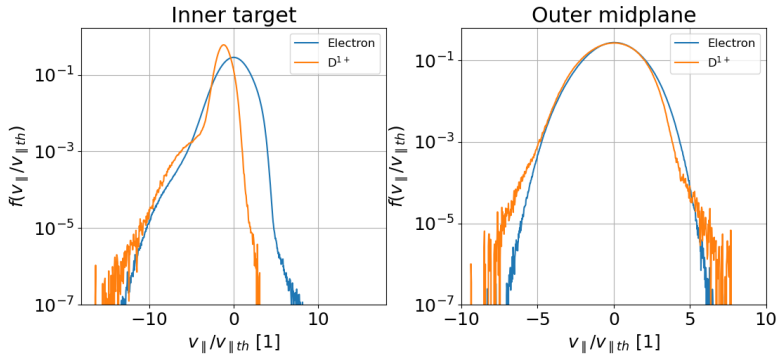

Figure 5.4: Parallel velocity $v_\parallel$ distribution functions of electrons and deuterium ions at the inner target and outer midplane of the BIT1 simulation presented in section 5.8. Parallel velocity is normalised to the thermal velocity, $v_{\parallel th,a} = \sqrt{T_a/m_a}$, where T_a [J] is calculated with (2.12).

isothermal and the outer target connection length replaces the gradient size as the "large" spatial scale. This causes the temporal and spatial collisionality criteria for ions to coincide. Across the modelled SOL, electrons are highly collisional while ions are marginally collisional or nearly collisionless. This corresponds to the results of particle-in-cell modelling of the investigated SOL by D. Tskhakaya, presented in section 5.8. As shown on the right of figure 5.4, upstream electron velocity distribution functions are more Maxwellian than deuterium ions.

A caveat of this collisionality analysis is that it pertains to thermal particles only. Hot, or suprathermal, particles are much less collisional. It is often quoted based on [19, Fig. 2] that most electron heat flux is carried by electrons with velocities 3-5$v_{th,e}$, whose collisionality is approximately 200 times lower than that of thermal electrons. More precise calculations indicate that the so-called heat carrying electrons are 20-30 times less collisional than thermal electrons. [197] In our case, this leaves the hot electrons moderately collisional and the hot ions collisionless.

Another caveat is that electron bouncing is usually not considered in the literature when calculating the system size. Were the calculation redone with the connection length to the outer target as the system size, both thermal and hot electrons would be marginally collisional ($L_{T_e}/\lambda_e = 0.1$-30).

In addition to quantifying the scale ordering requirement of the Braginskii closure, SOL collisionality is often understood to denote the dimensionless quantity defined by Stangeby, [12, Eq. (4.105)],

$$\nu^* = 10^{-16}\frac{n_e L}{T_e^2}. \tag{5.6}$$

Here the electron density n_e [m^{-3}] and temperature T_e [eV] are evaluated at upstream (usually the outer midplane separatrix) and L [m] refers to the connection length to either target, which distinguishes inner and outer target collisionality (see figure 5.3, bottom part). As [12, Sec. 4.10.2] shows, this parameter corresponds to the upstream SOL electron collisionality, where

several approximations have been made to simplify the calculation. In the analytical analysis using the basic two-point model, ν^* is found to be the principle driver of the parallel electron temperature gradient. If $\nu^* < 10$ (low collisionality), the SOL develops small parallel T_e gradients and high target T_e, and therefore small power and pressure losses. (As discussed in the introduction of this thesis, SOL plasma loses energy primarily through interaction with neutrals in the divertor region, and high plasma temperatures near the targets means low neutral density and low pressure and power losses.) If, on the other hand, the collisionality parameter is high, $\nu^* > 15$, substantial parallel T_e gradients are expected to appear.

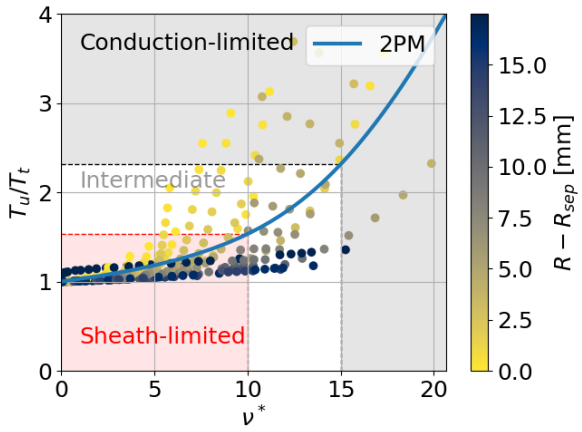

Figure 5.5: Dependence of the parallel temperature drop $T_{e,u}/T_{e,t}$ on the upstream SOL collisionality ν^*. Circles denote flux tubes in SOLPS-ITER simulations, blue line denotes the dependence derived from the basic two-point model.

In practice, the upstream SOL collisionality ν^* does not always correspond to the parallel T_e gradient. Figure 5.5 shows the parallel temperature drop $T_{e,u}/T_{e,t}$ as dependent on ν^* in a SOLPS-ITER code experiment. The points represent individual flux tubes in a density scan based on an interpretative simulation of the COMPASS #17588 L-mode discharge (section 4.6) in pure deuterium. The core density boundary condition $n_{i,core}$ was varied to approximate the range of plasma densities achieved at the COMPASS tokamak. The blue line, conversely, marks the dependence of $T_{e,u}/T_{e,t}$ on ν^* as derived from the basic two-point model. [12, Fig. 4.19] We observe that flux tubes near the separatrix (yellow points) can develop substantial T_e gradient even at low collisionalities, while the far SOL flux tubes (blue points) are isothermal even at high collisionalities. Let us, therefore, take the ν^* value with a grain of salt, remembering that it is based on the basic two-point model with its rather stringent assumptions on SOL transport.

In the literature, the term "collisionality" sometimes refers to the ν^* parameter, other times to the ratio of the T_e gradient size to the electron mean free path, rarely to their ion equivalents. The former two definitions mostly overlap. One usually considers three broad categories: the collisionless plasma ($\nu^* < 1$, $\lambda_e \gg L_{T_e}$), the highly collisional plasma ($\nu^* \gg 1$, $\lambda_e \ll L_{T_e}$), and

the intermediate state of marginally collisional plasma ($\nu^* \sim 1$, $\lambda_e \sim L_{T_e}$). In a collisionless plasma, analytical kinetic theories and velocity-space-based models can be applied with ease as the collision term in the kinetic equation (2.2) can be set to zero. In a highly collisional plasma, the fluid approximation including the classical heat flux yields good results. The marginally collisional case is the least tractable. [197]

The upstream SOL collisionality ν^* is associated with electron heat transport and with T_e gradients. There is no equivalent parameter in common use related to T_i gradients. Ion heat transport is relatively neglected for two reasons. Owing to the high electron thermal conductivity, electron conduction usually dominates the parallel heat transport, and therefore the total divertor target heat loads. [204, 205] Almost as importantly, electron temperature is much easier to measure in experiment. Even this thesis concludes that heat flux limiting lowers and raises ion temperature by a factor of two in SOLPS-ITER simulations, but that we are unable to validate it against experimental data for lack of T_i measurements. Unless a work focuses explicitly on ion heat transport, such as [206, 207], ion collisionality is usually not discussed at all.

As shown in figure 5.3, in the 3rd flux tube of the COMPASS H-mode #16908 simulation, the collisionality parameter is $\nu^* = 2.5$ toward the outer target and $\nu^* = 5.3$ toward the inner target. Indeed, we do observe smaller electron temperature gradients toward the outer target (13 % drop) than toward the inner target (57 % drop) in the simulation. The ion temperature drop, which is by 87 % toward the outer target and by 92 % toward the outer target, is not predicted by ν^*.

Finally, let us highlight that ν^* as used to quantify transport regimes is calculated from upstream plasma parameters (temperature, density, mean free path etc.). Real plasma collisionality varies across the SOL, and can be different upstream and downstream, in the near SOL and in the far SOL. In some applications, such as detachment studies, divertor collisionality may be more pertinent.

5.4 Correcting the classical heat flux

The failure of classical electron heat flux was first observed in laser plasmas, where the presence of a heat front violated the space ordering assumption with its strong gradients. [208] A similar effect was observed in solar plasmas. [201] The problem was that, taking the measured temperature profile and calculating the heat flux density flowing over it, equation (5.1) for the classical electron heat flux overpredicted the real heat flux by an order of magnitude. [209] As early as 1988, we encounter statements such as: *"It is well known that this type of solution may result in electron energy flux which is physically large (the classical electron conduction become infinite for collisionless plasma), and, in particular, inconsistent with the results of weakly collisional plasma experiments."* [38] Equation (5.1) captures the fact that highly collisional plasma is very efficient at conducting heat flux, as conduction is mediated by collisions. In a less collisional plasma, however, conduction down a given

temperature gradient becomes less effective (thermal conductivity κ_a falls). The situation is further complicated by distortions of the distribution function, as low-collisional suprathermal particles leave the hot plasma (lowering its thermal conductivity) and form a hot tail in the cold plasma (increasing its thermal conductivity). [19] These initial findings were followed by a long and rich history of attempts to correct or replace the classical heat flux in transport theory and simulations. To gain perspective on the practice of heat flux limiting, we shall go through some of it.

There is a substantial body of theoretical work searching for better analytical expressions for the parallel (or unmagnetised) heat flux density. To name a few, Rognlien and Ryutov proposed a new set of equations, an equivalent of the Braginskii equations but with more self-consistent radial transport. [37] Hazeltine and Catto derived Braginskii-like equations for the tokamak edge using the assumption of velocity ordering. [35] Zawaideh and Kim proposed heat flux expressions based on the 3rd moment of the kinetic equation (counting from zero for the continuity equation) and the assumption that the ion velocity distribution function is bi-Maxwellian and the electron velocity distribution function is Maxwellian. [38] Hazeltine derived expressions for heat and particle flux valid for both collisional and collisionless plasma, where fluxes are not driven by gradients (profile shape) but rather directly heat and particle sources. [36] Radford used 13 moments of the kinetic equation to model the JET tokamak SOL plasma and found a significant increase of the upstream ion temperature and limiting of the ion heat flux, while electron heat flux was less affected. [210, 211] More references can be found within [39] and [48].

As this thesis is concerned with SOL transport modelling, we are particularly interested in the approach where fluid codes are compared to or coupled with kinetic codes. [212, 18, 213, 48, 214, 207] The idea is to model the same plasma using two branches of plasma physics, and adopt correction factors into the fluid code which help reproduce the kinetic results. This was taken to the extreme in the KIPP code, a 1D2V Fokker-Planck kinetic code coupled to 1D SOLPS. [48, 44, 215] KIPP-SOLPS alternates between solving a kinetic simulation, which locally adjusts its sources and sinks to a perfect agreement to the previous fluid solution, and a fluid simulation, which receives as input "kinetic factors": electron heat conduction coefficient c_e, thermal force coefficient $k_\parallel$, sheath potential drop $\Delta\Phi$ and electron sheath heat transmission coefficient γ_e, calculated from the previous kinetic solution. Many such coupled codes or comparisons have reached the conclusion that the classical heat flux overestimates hot upstream parallel heat fluxes and underestimates cold target parallel heat fluxes. [216, 197, 212, 40, 204, 217] Effects on other plasma parameters, such as T_e or T_i, vary. [215, 218, 206, 39] This is presumably because details of the fluid simulation, such as whether one fixes the input power or the core temperature in the energy transport equation, affect which plasma parameters and where the kinetic corrections can affect.

Given this body of work, it is somewhat stunning that the default treatment

of correcting the classical heat flux in the SOLPS-ITER code is one of the first ever proposed: *heat flux limiting* with a harmonic average.

The rationale behind heat flux limiting is that unphysically high values of the classical heat flux can be prevented by reducing the heat flux density so it cannot exceed a certain limit. A natural limit for particle a heat flux density is some fraction of the free-streaming heat flux density,

$$q_{FS,a} = en_a T_a v_{th,a}, \tag{5.7}$$

where $v_{th,a} = \sqrt{eT_a/m_a}$ is the thermal velocity. [39] The free-streaming heat flux density can be obtained by integrating the heat carried by the left half of the Maxwellian distribution. [39] It can also be obtained by theoretical considerations of the maximum plasma heat flow which carries no current (and thus does not generate electric fields which would slow it down) and whose velocity distribution function is resistant to instabilities. [201] Limiting the classical heat flux density with a α-fraction of the free-streaming heat flux density could be implemented with a hard limit,

$$q_{\|a}^{(lim)} = \min\left\{q_{\|a}, \alpha_a . q_{FS,a}\right\}, \tag{5.8}$$

but it is more often done using the harmonic average

$$q_{\|a}^{(lim)} = \left(q_{\|a}^{-1} + \left(\alpha_a . q_{FS,a}\right)^{-1}\right)^{-1}. \tag{5.9}$$

The parameter $\alpha_a \sim 1$ is called the *heat flux limiter* of species a. It can be defined as the ratio between the real heat flux density $q_{\|a}^{(real)}$ and the free-streaming heat flux density $q_{FS,a}$ in the limit of long mean free paths λ_a: [219]

$$\alpha_a = \lim_{\lambda_a \to \infty} \frac{q_{\|a}^{(real)}}{q_{FS,a}} \tag{5.10}$$

In edge transport modelling, heat flux limiter values usually lie between 0.05 and 3. [39]

Like the anomalous diffusion coefficient, the heat flux limiter is an *ad hoc* number lacking any physical meaning, and it has been thoroughly criticised ever since it was conceived. [220, 47, 212, 46, 38] Sources of frustration include:

1. A single heat flux limiter value, no matter how well it is chosen, will not reproduce the steady-state plasma parameter profile calculated with more sophisticated means. [47, 212, 46, 207, 217, 198, 48]
2. Similarly, no single value of the heat flux limiter will reproduce realistic plasma parameters during ELM modelling. [221, 205, 222]
3. Heat flux limiting seeks to capture non-local effects, but it is still *local*. [197, 218]
4. The harmonic average is "an arbitrary interpolation". [220]
5. Appropriate heat flux limiter values will change between SOL collisionality and tokamaks. [39, 220, 219, 45, 214]

6. In a cold divertor plasma, kinetic/non-local effects cause heat flux enhancement beyond the classical value, which cannot be implemented using any value of the heat flux limiter. [40, 212, 197, 204]
7. Heat flux limiting can cause numerical instabilities at very low α. [12, Ch. 26][220]
8. Ion heat flux limiting has stronger effect on plasma parameters than electron heat flux limiting using the same α value, yet it is less explored due to the relative neglect of ion heat transport. [40, 39, 204]

To summarise, it has been well established that heat flux limiting is not adept at capturing heat fluxes calculated by kinetic simulations. It is not even entirely clear if it is always preferable over the classical heat flux. [39] In spite of this, heat flux limiting with a harmonic average has remained a vital part of edge transport codes. It is used by EDGE2D [40, 39], SOLEDGE2D [18], UEDGE [223, 207] and SONIC [206], and it is on by default in SOLPS-ITER, with the default heat flux limiter values $\alpha_e = \alpha_i = 0.15$. It isn't that no better alternative exists. There have been numerous proof-of-principle efforts to describe the parallel heat flux using coupling with a kinetic code [48, 204, 47, 213], an advanced local formula (usually based on more moments of the kinetic equation) [40, 224, 217, 210] or a non-local formula [18, 46]. None of these, however, have seen wide-spread adoption. Official recommendations for ITER and DEMO modelling still specify a value of the heat flux limiter: $\alpha_e = \alpha_i = 0.1$-$0.3$ for DEMO [218, Ch. 7.4] and $\alpha_e = 0.2$ and $\alpha_i = +\infty$ (ion heat flux limiting off) for ITER [225, Sec. 3.2.1]. Controlling the parallel heat flux density with heat flux limiting is a current and living practice, despite its drawbacks.

Given the 40-year-long history of heat flux density corrections and the abundance of alternatives, it is interesting to ask why heat flux limiting is used so widely. As the literature offers no discussions on this point, we indulge in a bit of historical speculation.

Works of the twentieth century, which could not rely on the computational capacities available today, leaned toward the analytical approach and 1D simulations in simplified geometry. This is the time when Luciani and Mora wrote their well-known work on calculating the parallel heat flux density non-locally as the average of heat fluxes in the mean-free-path vicinity [226], laying the foundation for many later theoretical and modelling works. [227, 218, 228, 18] It is also the time of theoretical works using self-similar variables by Krasheninnikov [229] or Grad's 21-moment approach by Igitkhanov [224], although neither seems to have been adopted in larger scale modelling works. [217] We cannot leave out the seminal work by Chodura [19], where electron kinetic effects were laid out for future generations to discuss and dissect. [197, 230, 44]

The turn of the millennium saw the rise of 2D transport codes. The B2 code, in existence since 1987 [231], was updated to the B2.5 code in 1996 [232] and coupled to the Monte Carlo neutral solver EIRENE [51]. This is the line of codes which would eventually peak in the SOLPS-ITER code. [1, 233] Since the very first version of B2, electron heat flux limiting with $\alpha_e = 0.12$

was employed. Ion heat flux limiting with $\alpha_i = 0.1$ followed suit in B2.5. During these times, two lines of research were pursued. On the one side, 2D transport simulations explored edge plasma physics while not delving into the details heat flux limiting, often not mentioning it at all. On the other side, research continued to find a better alternative to heat flux limiting which could be employed in a transport code.

The time of writing this thesis is a time of prototyping 1D codes which compromise between the speed of transport codes and the accuracy of kinetic codes. The KIPP-SOLPS code, described earlier, provides its transport code with 4 local kinetic factors to emulate kinetic effects in the parallel transport. [48, 215, 44, 197, 40, 204] The SOL-KiT code is mostly fluid, but has the option to switch to a kinetic treatment of electrons and self-consistently compare fluid and kinetic results. [198, 205, 213] A non-local, Luciani-like expression for the electron heat flux has been implemented in SOLEDGE2D. [18] All of these simulations are, so far, 1D. The reason is poignantly summarised by [46]:

"In theory, the Ji-Held model could be incorporated into any 2D (e.g. SOLPS, UEDGE, EDGE2D) or 3D (e.g. GBS, HERMES, STORM, TOKAM3X) by replacing the relevant term for the parallel electron thermal conduction in the pressure/energy equation with the Ji-Held model (or other nonlocal thermal transport models). However, the factor > 10 *increase in simulation time to run the Ji-Held model over the Spitzer/flux-limiters found in this study limit the model's application to 2D/3D codes, which have already long computational time demands, and may cause problems in keeping simulations running in a reasonable timeframe."*

Computational resources continue to grow, while the question of power exhaust remains at the forefront of fusion reactor research. Tokamak SOL parallel transport sets the SOL fall-off lengths in competition with radial transport, influencing the sputtering load of the first wall through λ_n and the concentration of heat load of the divertor through λ_q. [12, Ch. 21] The kinetic effects of suprathermal particles affect the divertor target sheath, influencing the sheath potential drop, heat loads and sputtering rates. [218] It is possible that in the near future, the necessity to model such effects faithfully will finally make heat flux limiting go out of fashion. My personal hope lies in the KIPP code, which was developed to complement the most widely used edge transport code SOLPS and which has already implemented the framework for 2D modelling. In the meantime, however, heat flux limiting is here to stay and we must learn working with it.

To use heat flux limiting, or not to use heat flux limiting? Which values of heat flux limiters to use? Is a common value sufficient for ions and electrons, or do they need to be different? What are the main effects of heat flux limiting on a transport simulation? How sensitive are these effects to heat flux limiter values? Are there significant differences between tokamaks, or even between plasmas in a single tokamak? This chapter is dedicated to answering these questions. We shall consider the theory of heat transport in COMPASS-like plasmas, study the inner workings of heat flux limiting, investigate a 2D scan

in electron and ion heat flux limiters, and finally compare SOLPS results to a kinetic simulation with the BIT1 code, performed by D. Tskhakaya. The aim is to produce recommendations for heat flux limiter values in SOLPS-ITER simulations of the COMPASS tokamak, and outline to what happens if we get their values wrong.

5.5 Heat flux limiting in interpretative simulations of the COMPASS tokamak

In this section, we shall leverage the theoretical and modelling works presented in the previous section to gain theoretical insight into heat flux limiting at the COMPASS tokamak. The point of departure will be the 2005 heat flux limiting review by Fundamenski. [39]

Based on the reliability of classical heat fluxes (5.1) and (5.2), edge plasma transport regimes may be sorted into three categories, similar to Stangeby's "sheath-limited, conduction-limited, detachment", but not identical to them.

1. **The hot, isothermal SOL**. This is a plasma where the upstream electron temperature is high ($T_e \gtrsim 50$ eV) and which suffers little power and pressure losses. It can be achieved in a high-power, low-density discharge with a small impurity content, with an open divertor, and especially toward the outer target. Its electron mean free path is long, collisionality is low and parallel T_e gradients are small. High strike point temperatures cause a large sheath potential drop and enhanced sputtering and erosion, as well as highly localised target heat fluxes.
2. **The cold, highly collisional SOL**. This is a plasma which is so dense and/or cold that its electron mean free paths are shorter than the gradient size along the entire SOL. It can be achieved in a low-power, high-density discharge with a large impurity content, with a closed divertor, and especially toward the inner target. The divertor targets are almost necessarily detached, as electron temperature dropping below 10 eV brings on plasma-neutral interaction causing significant energy and power losses. [4] The target is protected from large heat fluxes and sputtering alike, but the upstream temperature is so low that such a SOL cannot coexist with the hot confined region of a fusion reactor.
3. **The SOL with large parallel T_e gradients**. This is a plasma whose upstream electron temperatures are high, but where significant pressure and power losses cause T_e to drop toward the divertor target. It can be achieved in a high-power discharge with a large impurity content, with a closed divertor, and especially toward the inner target. The electron mean free path varies along the magnetic field line, very long at upstream and very short at downstream. The divertor target is either in the high recycling regime or at least partially detached, which protects it against heat and particle fluxes. This SOL is compatible both with a hot tokamak core and with long divertor lifetime, perfect for a tokamak fusion reactor.

Let us consider how well the classical heat flux will describe parallel heat transport in each of these plasmas. In other words, how important are kinetic effects and how much can we expect the distribution function to deviate from the Maxwellian?

The cold, highly collisional SOL evidently fulfils the requirements of the Braginskii closure. Its mean free paths are smaller than both the system size and the gradient size, so its distribution functions will be nearly perfectly Maxwellian, kinetic effects will play a small role and the classical heat flux will capture real heat fluxes well. It is a question if such a SOL would be stable against radiative instabilities, given its low temperature and high impurity content. However, experimental feasibility is not our foremost concern at the moment. The cold, highly collisional SOL is the high-collisionality limit where all heat flux prescriptions, non-local, employing more moments of the kinetic equation, kinetic, or classical, should yield the same results. [39, 219, 206, 207, 38, 36]

The SOL with large parallel gradients is a ground ripe with kinetic effects. The hot particle population at upstream streams freely toward the target, where it creates a suprathermal velocity distribution tail, raising heat conduction through the divertor plasma and through the sheath itself beyond classical values (increase in the thermal conductivity κ_e and sheath heat transmission coefficient γ, see the previous section). This is often called *heat flux enhancement* in the literature. Conversely, upstream collisionality is so low that the scale ordering assumptions are not met, and the real upstream heat flux is lower than classical values (heat flux limiting in the broad sense). This double whammy has been reported repeatedly, especially in detached divertor plasmas, though the exact magnitude of the heat flux enhancement/limiting varies from a few percent to two orders of magnitude. [212, 216, 197, 40, 204, 217, 127] This case is relevant to fusion power plants, since high separatrix temperatures are instrumental for good confinement and low strike point temperatures are imperative for divertor protection. The range of effects is so wide that it is doubtful whether anything but first-principles kinetic simulations can properly resolve the parallel heat flux. [203]

The hot, isothermal SOL is the case most pertinent to COMPASS plasmas, where strike point temperatures are commonly $T_e > 40$ eV and whose divertor is open. It is also, in my biased opinion, the most interesting case. Fundamenski outlines two archetypes of heat transport which may play a role in the hot, isothermal SOL: transport in an infinite, unbounded plasma with small sources and sinks, and transport in a plasma strongly affected by the sheath.

In an infinite, unbounded plasma with small sources and sinks, all plasma parameters will vary over lengths the order of the mean free path (see section 5.3). Fundamenski calls the heat fluxes in such a plasma *self-limiting*. We shall paraphrase his reasoning behind this term, as it is pertinent to setting the optimal value of heat flux limiters in COMPASS plasmas.

Assuming that the gradient size $L_{T_a} = T_a/\nabla_\parallel T_a$ is proportional to the

mean free path λ_a, we may substitute

$$\nabla_\parallel T_a = \frac{T_a}{L_{T_a}} \sim \frac{T_a}{\lambda_a}$$

into the classical heat flux

$$q_{\parallel a} = -\kappa_a \nabla_\parallel T_a \sim -\kappa_a \frac{T_a}{\lambda_a}. \tag{5.11}$$

We write the classical heat conductivity, equations (5.1) and (5.2), as

$$\kappa_a = c_a \frac{e^2 n_a T_a \tau_a}{m_a},$$

where c_a is the closure-dependent prefactor, $c_e = 3.16$ for electrons and $c_i = 3.9$ for ions in the Braginskii closure. The factor e^2 comes from giving the temperature in electronvolts. We convert the collision time τ_a into the mean free path, $\tau_a = \lambda_a / v_{th,a}$ and write the thermal velocity as $v_{th,a} = \sqrt{eT_a/m_a}$.

$$\kappa_a = c_a e n_a \lambda_a \frac{eT_a}{m_a} \sqrt{\frac{m_a}{eT_a}} = c_a e n_a \lambda_a v_{th,a}$$

This is the familiar result that thermal conductivity grows with the mean free path λ_a. We substitute this into equation (5.11) to receive our final goal:

$$q_{\parallel a} \sim c_a e n_a T_a v_{th,a} \tag{5.12}$$

Two things are noteworthy about this result. One, in an infinite, unbounded plasma with weak sinks and sources, the heat flux is a "fraction" (c_a = 3-4) of the free-streaming heat flux, lending some credibility to the practice of heat flux limiting. Two, this heat flux does not depend on the mean free path λ_a and it is valid for all collisionalities. Since equation (5.12) is nothing but the classical heat flux plus a little math (with the important ingredient being $L_{T_a} \sim \lambda_a$), it can be said that in an infinite, unbounded plasma with weak sinks and sources the classical heat flux is finite, constant and correct at any collisionality. The parallel gradient $\sim 1/\lambda_a$ flattens out just enough to compensate the thermal conductivity $\sim \lambda_a$, decreasing the conductive heat flux value to a "fraction" of the free-streaming heat flux. This is what Fundamenski calls *self-limiting*.

The other SOL archetype relevant to the hot, isothermal SOL is the SOL strongly affected by the sheath. Again, we paraphrase and summarise Fundamenski's reflections. The two major effects of the sheath on the plasma is the Bohm criterion (Mach number $M = u_{\parallel i}/c_s \geq 1$ at the sheath entrance) and the distortion of electron and ion velocity distribution functions, leading to different sheath heat transmission coefficients for electrons and ions at the sheath entrance:

$$\gamma_e = \frac{q_{\parallel e}}{e n_e T_e c_s} = 4.5\text{-}5.5 \qquad \gamma_i = \frac{q_{\parallel i}}{e n_i T_i c_s} = 2\text{-}3 \tag{5.13}$$

(Notice that γ_e and γ_i are defined in relation to electron and ion plasma parameters, respectively, while the total sheath heat transmission coefficient γ is defined relative to electron plasma parameters. Thus $q_\parallel = q_{\parallel e} + q_{\parallel i}$, but $\gamma \neq \gamma_e + \gamma_i$.)

Inserting $M = 1$, $\gamma_e = 5$ and $\gamma_i = 2.5$ into the expressions for heat fluxes at the sheath entrance, one obtains a number of interesting results which have important consequences for heat flux limiting in the SOL strongly affected by the sheath. Let us address the sheath's effect on the electron and ion heat transport in turn.

At the sheath entrance, the electron energy flux is split equally between convection and conduction, while $\lambda_e/L_{T_e} \approx 0.022$, a small but finite value denoting that electrons are highly collisional at the sheath entrance, regardless of the upstream electron collisionality. Using the relative atomic mass $A = 2$, ion charge $Z = 1$ and $T_i/T_e = 2$, the electron heat flux at the sheath entrance is

$$q_{\parallel e} = \alpha_e . e n_e T_e v_{th,e} \quad \text{where} \quad \alpha_e = 0.072. \tag{5.14}$$

In other words, the sheath boundary condition acts as a built-in electron heat flux limit with $\alpha_e \approx 0.07$ in the SOL strongly affected by the sheath (sheath entrance vicinity).

The ion energy flux at the sheath entrance is, by contrast, entirely convective, with the ion temperature gradient completely flat, $L_{T_i} \to \infty$. This is a consequence of the presheath electric field converting energy from the chaotic thermal movement to the organised convection at the sound velocity c_s. An interesting side effect is reduction of the ion temperature T_i toward the target. This adds up to the parallel T_i gradient caused by low ion thermal conductivity κ_i, resulting in very high $\nabla_\parallel T_i$ even in the absence of power and pressure losses. [12, Sec. 10.5] Fundamenski concludes that since ion conductive heat flux is zero anyway, we might as well use the classical thermal conductivity and not bother with ion heat flux limiting.

How far into the SOL does the sheath's heat flux limiting effect extend? This was already partially discussed in the introduction of this thesis, where the sheath-limited regime was named after the two divertor sheaths affecting the entire SOL. The sheath reach can be quantified by the distortion of the velocity distribution function along the magnetic field line. It has been argued that the sheath affects SOL about one mean free path from the sheath entrance [39] and kinetic simulations have showed distribution function distortions up to 5 electron mean free paths away from the target [44]. Luciani's model of non-local heat transport uses the mean free path as the characteristic size of the region contributing toward the heat flux in its center [226, 18], though this is an informed choice rather than a physical result. Considering that the upstream electron mean free path in the COMPASS H-mode #16908 is $\lambda_e = 2.1$ m while the connection length to the outer target is 6 m and to the inner target 12 m, the sheath influence is probably strong toward the outer target and less pronounced toward the inner target. Ion transport is strongly affected by the sheath all along the flux tube, as the mean free path is $\lambda_i = 28$ m and the velocity distribution function is non-Maxwellian everywhere (figure

5.4). In summary, the sheath boundary condition itself may be expected to prevent unphysically large classical heat fluxes in transport simulations of the COMPASS tokamak edge plasma, even without heat flux limiters and both for electrons and ions.

Interestingly, the heat flux limiting effect of the sheath has been known for a long time. A pioneering 1992 article on sheath physics writes the electron heat flux into the sheath edge as $q_{\parallel e} = 0.1 e n_e T_e v_{th,e}$. [19] The first version of the B2.5 code even adopted this expression as its divertor target boundary condition in favour of the currently used $q_{\parallel e} = \gamma_e e n_e T_e c_s$. [54]

In conclusion, in the typically isothermal, hot COMPASS SOL, energy conduction may be governed a transition between two plasma archetypes: at upstream the boundless plasma with weak sources/sinks, where parallel gradients build up to match the mean free path and the heat flux is self-limiting, and at downstream the plasma strongly affected by the sheath, where velocity distribution function distortions strongly suppress the electron heat flux ($q_{\parallel e} \approx 0.07 e n_e T_e v_{th,e}$) and eliminate the ion conductive heat flux, converting it into ion convective energy flux. In such a plasma, parallel T_e gradients are small, largely preventing the formation of a hot electron population at the target which would enhance the electron heat flux beyond classical values. [127] Kinetic effects are thus expressed only as heat flux *reduction* with regard to the classical value, and can be treated with heat flux limiters. In such a plasma, it has been proposed that large heat flux limiter values, $\alpha_e = \alpha_i = 1.5$, are optimal. [39, Sec. 2.6] They do not affect heat conduction strongly, as the self-limiting and sheath effects are at work already, and act more as safe-guards against extremely high heat fluxes and numerical instabilities. [43, Sec. 2.1.4] We conclude that, from the theoretical point of view, Fundamenski's recommendation of $\alpha_e = \alpha_i = 1.5$ may well be applicable to COMPASS SOL.

5.6 Heat flux limiting in action

Let us now investigate the inner workings of heat flux limiting with the harmonic average, in order to obtain a better intuition of how it affects a transport simulation.

It is instructive to rewrite the heat flux limiting equation (5.9) as not the manipulation of the heat flux density, but a reduction of thermal conductivity:

$$q_{\parallel a}^{(lim)} = \kappa_a^{(lim)} \nabla_\parallel T_a \qquad \text{where} \qquad \kappa_a^{(lim)} = \kappa_a \frac{1}{1 + \frac{q_{\parallel a}}{\alpha_a \cdot q_{FS,a}}} \tag{5.15}$$

In this manner, heat flux limiting can be understood as the reduction of parallel thermal conductivity. This is a simplified picture, as nearly all quantities in equation (5.15) depend on local plasma parameters and will change dynamically as the heat flux limiter α_a is adjusted. Halving the heat flux limiter does not mean that the limited heat flux density will halve as well. Nevertheless, the effect of heat flux limiting (lowering α_a) can be intuited as

lowering the parallel thermal conductivity of species a by some factor which will decrease with $\frac{q_{\parallel a}}{q_{FS,a}}$ and with α_a. We shall call it the

$$\text{heat flux limiting factor} = \frac{1}{1 + \frac{q_{\parallel a}}{\alpha_a . q_{FS,a}}}. \tag{5.16}$$

Interestingly, the $q_{\parallel a}$ term no longer corresponds to any physically meaningful heat flux. It is the heat flux particles a would carry, were their parallel temperature gradient the same as the real one, but their thermal conductivity were classical. As a consequence of the potentially high temperature gradients and high conductivity, the $q_{\parallel a}$ term can reach ridiculously high values. We will return to this later.

To demonstrate heat flux limiting in action, we investigate two simulations derived from the COMPASS H-mode discharge #16908. In the first simulation, both electron and ion heat flux limiting is off ($\alpha_e = \alpha_i = +\infty$) and the parallel heat transport is classical. The second simulation is the interpretative simulation presented in section 5.1 built to match the experiment closely, where $\alpha_e = \alpha_i = 0.3$. The former simulation was derived from the latter by changing the heat flux limiter values. Both simulations provide nearly identical results when it comes to experimentally observed parameters (upstream and target T_e and n_e profiles, target $q_\parallel$ profiles).

Figure 5.6 shows heat conduction parameters in the simulation with classical parallel heat transport. The parallel heat fluxes densities compare to their free-streaming counterparts differently for electrons and ions: $q_{\parallel e} \approx 0.07 q_{FS,e}$ while $q_{\parallel i} \approx q_{FS,i}$. This is because the parallel heat fluxes are comparable in magnitude, $q_{\parallel e} \approx 2 q_{\parallel i}$, but the electron free-streaming heat flux is much higher, $q_{FS,e} \approx 26 q_{FS,i}$. The ratio between the free-streaming heat fluxes follows simply from $\sqrt{m_i/m_e} \approx 60$ and $T_i/T_e \approx 2$. However, given that $\kappa_e \gg \kappa_i$ (figure 5.6, bottom left), it seems strange that the electron parallel heat flux is only double the ion parallel heat flux. This is where parallel temperature gradients comes in. As the bottom right part of figure 5.6 shows, the electron temperature only falls by about 30 % toward the inner target, while the ion temperature falls by 60 %. $\nabla_\parallel T$ compensates for the parallel thermal conductivities and causes the electron and ion heat fluxes to be comparable in magnitude. Drawing a conclusion on $\nabla_\parallel T_i$ is difficult as COMPASS lacks T_i measurements, but a small parallel gradient of T_e is in accord with previous transport investigations of the COMPASS SOL. In fact, within experimental uncertainties, this simulation reproduces the COMPASS H-mode #16908 remarkably well.

The marked difference between $\nabla_\parallel T_e$ and $\nabla_\parallel T_i$ has already been discussed in the theoretical part of this chapter. Large parallel gradients of T_e are usually associated with power and pressure losses, but the same is not necessarily true for T_i. As shown in section 5.1, power and pressure losses are low in the discussed plasma. The parallel gradient of T_i is instead caused by the presheath electric field, which distorts the ion velocity distribution function, making it narrower and displaced from 0 (see figure 5.4). [12, Fig. 2.5] In effect, it transfers ion energy from chaotic thermal movement (T_i) into the

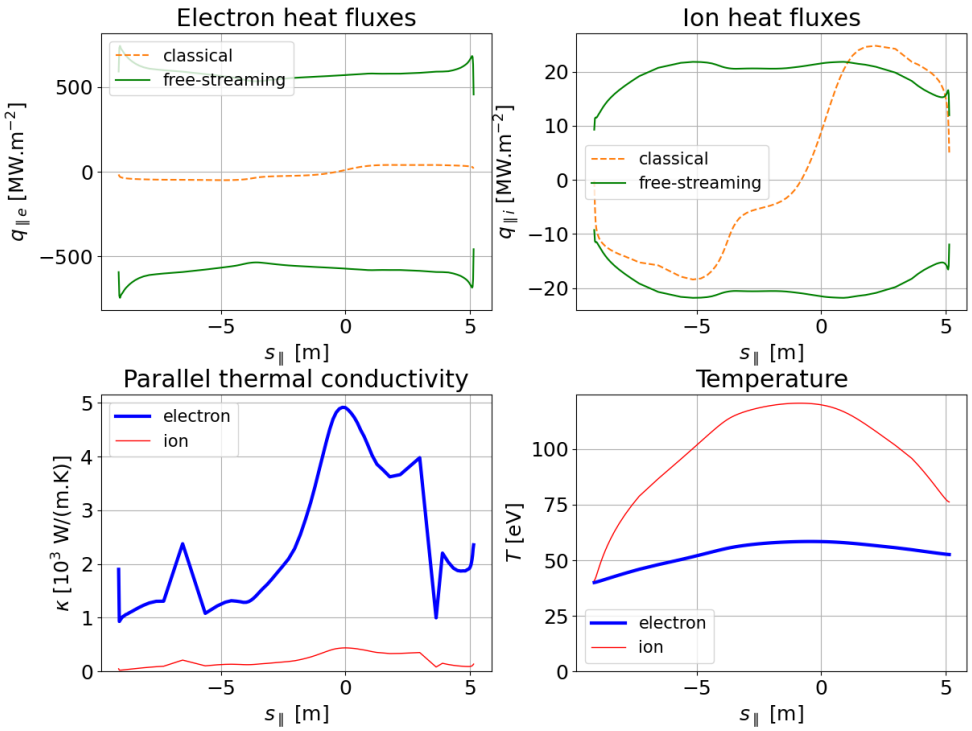

Figure 5.6: Parallel profiles of heat conduction parameters in a COMPASS H-mode #16908 simulation where heat flux limiting is off and parallel heat transport is fully classical, 3rd SOL flux tube. (Top) Comparison of electron and ion heat fluxes $q_{\parallel a}$ to the respective free-streaming energy fluxes $q_{FS,a}$. (Bottom) Parallel thermal conductivities (classical) and temperatures.

convective energy flux ($u_\parallel$). This effect may be compounded by the low κ_i and poor energy coupling between electrons and ions, which prevents ion energy from being transported through the electron channel. In the end, the larger T_i parallel gradient is what drives $q_{\parallel i}$ comparable to $q_{\parallel e}$.

Does this SOL plasma correspond to Fundamenski's theoretical vision of the hot, isothermal SOL, self-limiting at upstream (mean free path similar to the gradient size) and sheath-limited at downstream? The upstream electron mean free path is $\lambda_e = 1.6$ m, which is much smaller than the T_e parallel gradient size (tens of meters) and smaller than the connection length to the closer outer target (6 m). It would seem that sheath effects may dominate the electron transport rather than self-limiting. Indeed, $q_{\parallel e} \approx 0.067 q_{FS,e}$, where Fundamenski's theory of the sheath limiting the heat flux predicts $q_{\parallel e} = 0.072 q_{FS,e}$. The ion mean free path is $\lambda_i = 7$ m, which is comparable both to the T_i parallel gradient size (≈ 9 m) and to the connection length to the outer target (6 m). This appears to correspond rather to self-limiting effects. Indeed, the ion parallel heat flux saturates at $q_{\parallel i} \approx q_{FS,i}$. Fundamenski's theory predicts the self-limiting heat fluxes $q_{\parallel i} = 3\text{-}4 q_{FS,i}$, which is larger but still of a comparable magnitude. We tentatively conclude that Fundamenski's theory of the partly self-limiting, partly sheath-limited heat fluxes may apply in this classical parallel transport simulation of the COMPASS tokamak edge

plasma. This implies that heat flux limiting may not be needed in COMPASS SOL transport simulations, as the classical electron heat flux is limited by the sheath and the classical ion heat flux is self-limiting.

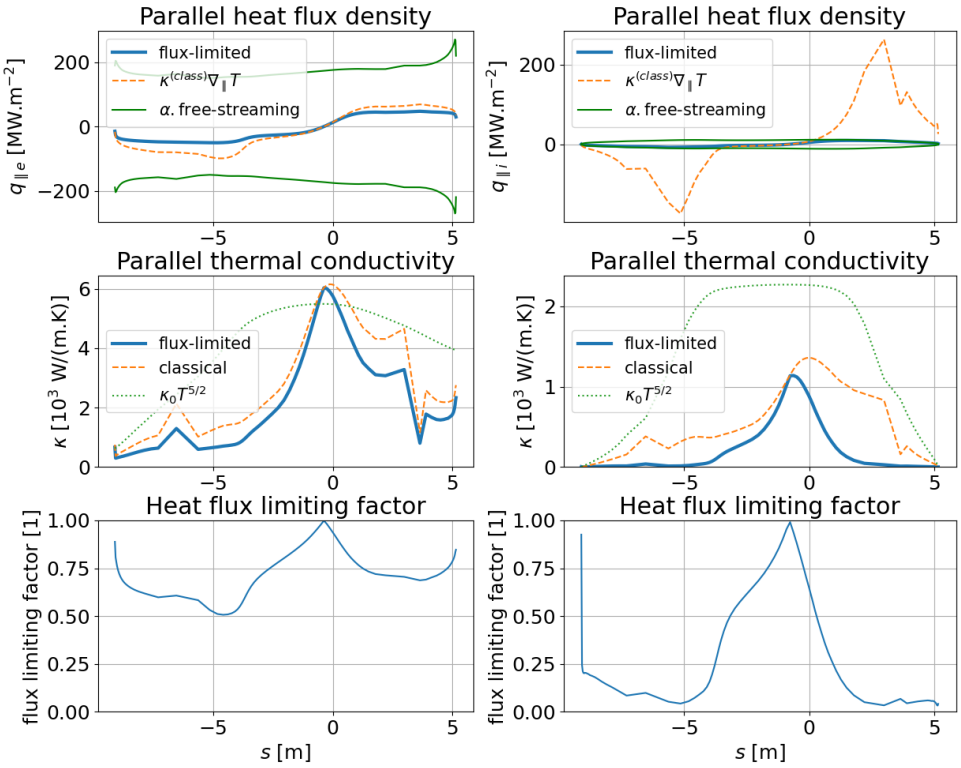

(a) : Electron heat flux limiting **(b) :** Ion heat flux limiting

Figure 5.7: Detail of the heat flux limiting action on electrons and ions parallel heat transport in the interpretative simulation of the COMPASS H-mode #16908, $\alpha_e = \alpha_i = 0.3$, 3rd SOL flux tube. (Top) Flux-limited, free-streaming and "artificial" $\kappa_a \nabla_\parallel T_a$ classical heat fluxes. (Middle) Flux-limited (5.15), classical (2.28) (2.29) and approximate (5.3) heat conductivities. (Bottom) The heat flux limiting factor (5.16).

In figure 5.7, electron and ion heat flux limiting are seen in action in the 3rd flux tube of the interpretative COMPASS tokamak simulation of the H-mode discharge #16908, where $\alpha_e = \alpha_i = 0.3$. In the top part of the figure, the limited heat flux $q_{\parallel a}^{(lim)}$ (5.9) is compared to the "artificial" classical heat flux ($q_{\parallel a}$ in the heat flux limiting factor (5.16)) and a fraction of the free-streaming heat flux $\alpha_a.q_{FS,a} = 0.3 q_{FS,a}$. In the case of electrons, the "artificial" classical heat flux only reaches about 50 % of $0.3 q_{FS,e}$. Accordingly, the limited parallel thermal conductivity $\kappa_e^{(lim)}$ (5.15) is only moderately reduced from its classical value, and the heat flux limiting factor does not fall below 0.5. Overall, the heat flux limiting effect on electrons is quite mild. The situation is diametrically different for ions. The "artificial" classical heat flux is 20x larger than $0.3 q_{FS,i}$, resulting in a drastic reduction of parallel thermal conductivity $\kappa_i^{(lim)}$ with regard to the classical value by the heat flux

limiting factor of about 0.05. The effect of $\alpha_i = 0.3$ on ion parallel transport is severe in comparison to $\alpha_e = 0.3$. Both of these results will be elaborated in the section 5.7, where a heat flux limiter scan $in\alpha_{e,i}$ =0.1-1.0 is performed. Finally, the reader is referred to figures 5.10c and 5.11c in the same section, where it is seen better that turning on heat flux limiting does, indeed, reduce the electron and ion heat fluxes.

The approximate parallel thermal conductivities used by Stangeby in equation (5.3), with $\kappa_{0e} = 2000$ and $\kappa_{0i} = 60$, are plotted in figure 5.7 next to the more sophisticated parallel conductivities evaluated by the Zhdanov closure inside the SOLPS-ITER code. For retaining only the T_a dependence in κ_a, the approximations capture the thermal conductivity magnitude well, though their spatial variation is simplified.

I would like to raise to the reader's attention that the "classical" heat fluxes shown in figures 5.6 and 5.7 are, qualitatively and quantitatively, not the same thing. The former are self-consistent classical heat fluxes — the real parallel heat fluxes used in the simulation. The latter are "artificial" classical heat fluxes, constructed using the real parallel temperature gradient but an imaginary parallel thermal conductivity. Just because the "artificial" classical heat flux in the flux-limited simulation reaches some value, does not mean that were that simulation redone without heat flux limiters, this is the value the parallel heat flux would attain. In fact, figures 5.6 and 5.7 show clearly that where the "artificial" classical $q_{\parallel e} \approx 100$ MW.m^{-2}, the self-consistent classical $q_{\parallel e} \approx 40$ MW.m^{-2}. The difference is even more marked in ions: the "artificial" classical $q_{\parallel i} \approx 200$ MW.m^{-2} where the self-consistent classical $q_{\parallel i} \approx 20$ MW.m^{-2}. In the literature, overblown "artificial" heat fluxes are occasionally used as a deterrent example of using classical conductivities. [127] The authors leave out the fact that using classical κ_a self-consistently will usually result in smaller parallel temperature gradients, which will stop the classical heat flux from acquiring such catastrophically high "artificial" values. It is all well and good if the parallel temperature gradient is fixed, for example to match another code or precise experimental measurements. But when $\nabla_\parallel T_a$ is free to evolve, such as in a typical edge transport code where the heating power rather than the temperature is fixed, using classical κ may not result in heat fluxes which are too high but rather parallel temperature profiles which are too flat.

In the literature, a closely related fine distinction often comes in the form of mistaking the heat flux limiter α_a for the ratio between the real parallel heat flux and the free-streaming heat flux $q_{\parallel a}/q_{FS,a}$. For example, some studies where parallel heat transport is modelled with a kinetic code report on $q_{\parallel a}/q_{FS,a}$ and imply this is a suitable heat flux limiter value. [219, 127] In the compilation of heat flux limiters in [39, Tab. 2], two instances of $q_{\parallel e}/q_{FS,e}$ referenced from [222] and [216], were listed alongside genuine α_e values. Even if an article avoids confusing the reported $q_{\parallel a}/q_{FS,a}$ with a heat flux limiter [197, 19, 209], $q_{\parallel a}/q_{FS,a}$ calculated from a kinetic simulation or a similar source is not very useful to a transport modeller. To decide on an optimal heat flux limiter value, it is most useful to see a scan of α_a employed in a

self-consistent, flux-limited transport simulation and compared to advanced heat flux calculations (non-local, Grad's 21-moment approach, kinetic etc.). Such an analysis has been done for electron parallel heat transport [220, 212, 226] and occasionally for ion parallel heat transport [207], but none of these studies is recent and all are 1D (only one flux tube is modelled). In this thesis, a large-scale electron and ion heat flux limiter scan with the 2D SOLPS-ITER is compared with experimental data and a 1D kinetic simulation at once. To our knowledge, this is an investigation of heat flux limiting of unprecedented depth and rigour.

5.7 Electron and ion heat flux limiter scan

Heat flux limiter scans are sets of edge transport simulations differing only in the value of the heat flux limiter $\alpha_{e,i}$. They have been performed as long as heat flux limiting. [212, 220, 51, 39, 46, 206] Their objective is to gauge the effect of heat flux limiting on parallel transport, its sensitivity, and the uncertainty stemming from a sub-optimal choice of $\alpha_{e,i}$. As the effect of heat flux limiters can depend on the particular plasma and it is difficult to predict in advance, it has been recommended to perform a heat flux limiter scan in every flux-limited transport simulation. [220]

Many articles introducing a novel parallel heat transport solver, indeed, benchmark their results against a two-point heat flux limiter scan equivalent to the one presented in the previous section: $\alpha = +\infty$, corresponding to the classical heat flux, and $\alpha \sim 0.1$. [49, 46, 207, 127] Detailed heat flux limiter scans, such as [206, 212, 220, 39], are, however, rare. To our knowledge, this work is the first which investigates the variation of electron and ion heat flux limiters simultaneously and with the inclusion of intrinsic carbon impurities. The enabling factor is the relative SOLPS-ITER speed and stability in modelling the COMPASS tokamak, allowing for performing dozens of simulations within a reasonable time frame. The ultimate goal of this heat flux limiter scan is to find optimal values of $\alpha_{e,i}$ for subsequent simulations of COMPASS and to build know-how for heat flux limiting in the COMPASS Upgrade tokamak.

Before we begin, it should be noted that heat flux limiter scans, like any parameter scans where only one input parameter is varied, are inherently unphysical in nature. Although they may be based on an interpretative simulation of a real experimental plasma, the plasmas produced by varying α_a may not correspond to any physically achievable experiment. At this step, we are not attempting to create a simulation which is as realistic as possible by setting optimal heat flux limiters in conjunction with other simulation inputs. We are seeking understanding of the heat flux limiter effect on a SOLPS-ITER simulation.

The setup of our heat flux limiter scan is visualised in figure 5.8. Ion and electron heat flux limiters $\alpha_{e,i}$ were varied systematically between 0.1 and 1.0, with four extra cases with very small heat flux limiters ($\alpha_e = 0.06$, $\alpha_i = 0.01$) and very large heat flux limiters ($\alpha_e = +\infty$, $\alpha_i = +\infty$). The latter

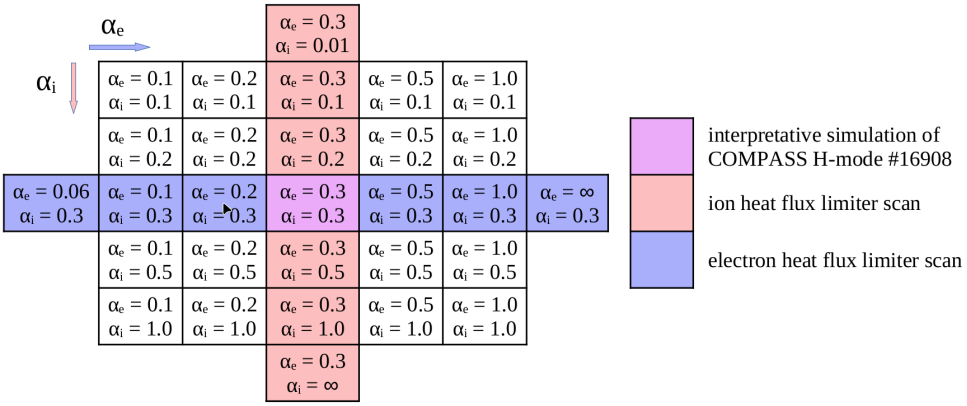

Figure 5.8: Setup of the heat flux parameter scan. Each cell corresponds to a simulation derived from the central interpretative simulation of COMPASS H-mode #16908 (section 5.1), with only the electron and ion heat flux limiter $\alpha_{e,i}$ values changed.

corresponds to no heat flux limiting, or classical parallel heat transport. The range of α_a was chosen with regard to the usual range of α values found in the literature and spaced approximately geometrically. [39]

The heat flux limiter scan was anchored in the interpretative simulation of COMPASS H-mode #16908 described in section 5. Upon Dr. Tskhakaya's recommendation, heat flux limiters in the initial simulation were set to $\alpha_e = \alpha_i = 0.3$, based on earlier kinetic simulations of this discharge with the BIT1 code. [127] As this lies approximately in the geometric middle of the usually employed heat flux limiter range, it was chosen as the point of departure for the rest of the simulations.

A challenge in performing the heat flux limiter scan was encountered when setting a very low electron heat flux limiter, $\alpha_e \leq 0.05$. As a majority of the parallel energy flux is carried by electron conduction in all simulations, it appears that throttling κ_e too much causes numerical instabilities in the code. Low values of α_e have been reported as detrimental previously. A simple analytic model has been used to show that no steady-state electron parallel transport solution exists for $\alpha_e < 0.1$. [220] This was corroborated in [12, Eq. 26.20] by deriving the criterion

$$\alpha_e < \frac{\gamma c_s(1\text{ eV})}{2v_{th,e}(1\text{ eV})}, \tag{5.17}$$

where the sound speed $c_s = \sqrt{2eT_e/m_i}$ and the electron thermal velocity $v_{th,e} = \sqrt{8eT_e/\pi m_e}$ are evaluated at $T_e = 1$ eV. Evaluated for the sheath heat transmission coefficient $\gamma = 7$, the critical α_e value is 0.05. If α_e decreases below this threshold, a non-monotonic T_e parallel profile is the only solution to the electron heat conduction problem. The unphysicality of such a result is reflected in the instability of transport simulations with very low α_e. This prevents too strict electron heat flux limiting and sheds suspicion on extremely low α_e recommendations. [219] On the other hand, the simulation with the

ion heat flux limiter $\alpha_i = 0.01$ converged without a problem, as the parallel heat flow was readily displaced onto electrons. This lower threshold for α_a is another indication that electron and ion heat flux limiters are not equals.

Having performed all 29 simulations of the heat flux limiter scan, we tackled the problem of quantifying the effect of heat flux limiters on the SOL. As a recent ion heat flux limiter scan showed, heat flux limiters do not affect only the heat flux densities but all SOL plasma parameters along the magnetic field line. [206] Furthermore, the effect of heat flux limiting may vary qualitatively in the radial direction, between the near and far SOL. To reduce this abundance of data to the first order and allow for physics-based insight, we performed an informed simplification of the SOLPS output. In the following paragraphs, radial variation will be shown to follow a single underlying principle in all flux tubes, allowing the reduction of data from 2D to 1D, and parallel variation will be demonstrated as simple and monotonic with α_a, allowing the reduction of data from 1D to 0D. In other words, the effect of heat flux limiting on each plasma parameter will finally be captured in one essential, characteristic number.

Plasma parameter	Characteristic scalar
Electron/ion temperature $T_{e,i}$	Parallel gradient toward inner target $T_{a,u}/T_{a,t}$
Electron density n_e	Inner target value $n_{e,t}$
Main ion parallel velocity $u_\parallel$	Peak value toward inner target
Parallel energy flux densities $q_\parallel$ (ion, electron, total, conductive, convective)	Peak value toward inner target
Pressure p (ion, electron, total)	Parallel gradient toward inner target p_u/p_t

Table 5.2: Plasma parameters whose variation in the heat flux limiter scan was investigated, and the characteristic quantity their 2D variation was reduced to.

The plasma parameters which were investigated are listed in table 5.2. Many other parameters could have been included, most notably neutral and impurity densities, but the analysis was found complicated enough even with a limited set of parameters. Exploring further effects of heat flux limiting is left to future works.

Let us begin by analysing the variation of heat flux limiting effects in the radial direction. Two illustrative examples are plotted in figure 5.9: the variation of T_i with α_i and the variation of T_e with α_e. In the upstream locations (the outer midplane and the plasma top), both T_e and T_i profiles *rise* as a whole when α is decreased (stronger heat flux limiting). The trend is the same for all flux tubes. Toward the targets, the temperatures fall but the rate varies; it is faster in the near SOL, toward the inner target, and for ions. The far SOL T_e and T_i remain approximately constant along the field line, so the upstream trend is copied at the target. In the near SOL, target T_e and T_i are *reduced* by stricter heat flux limiting (lower α), opposite to the upstream

trend. These disparate trends can be unified under the perspective that heat flux limiting *enhances existing parallel temperature gradients*. This explains why heat flux limiting effects are more pronounced near the separatrix (higher $\nabla_\parallel T_a$ than in the far SOL), toward the inner target (higher $\nabla_\parallel T_a$ than toward the outer target), and for T_i (higher $\nabla_\parallel T_i$ than $\nabla_\parallel T_e$). In this sense, heat flux limiting effects $T_i(\alpha_i)$ and $T_e(\alpha_e)$ do not vary radially, and a single SOL flux tube can represent the entire SOL.

The reason why heat flux limiting enhances existing parallel temperature gradients appears to be *compensation for reduced parallel thermal conductivity* κ_a. In the typical SOLPS-ITER simulation setup, the boundary condition of the electron and ion energy equations at the core interface is that a certain amount of power $P_{SOL,e,i}$ is injected into the electron and ion population. In steady state, all of this power must be depleted, be it transported to the targets, lost to the chamber wall, converted to radiation or passed on to neutrals. Upstream and target temperature values, meanwhile, are free to evolve so this energy balance is satisfied. Heat flux limiting is then analogous to thermally insulating a house in winter. If the heating inside the house is not reduced after installing the insulation, temperature inside the house will rise and temperature of the outer wall surface will fall. The built-up temperature gradient will compensate for the reduced thermal conductivity and allow all of the heat to be conducted away. In this sense, it is not strange that ion heat flux limiting should "heat" separatrix ions from 130 to 240 eV. The effect is, however, not physical in the context of core-edge interaction, and it must be accounted for when searching for optimal interpretative simulation input parameters including $P_{SOL,e,i}$ and $\alpha_{e,i}$.

The radial variation of heat flux limiting effects was analysed for all plasma parameters listed in table 5.2. Heat flux limiting was generally found to impact the near SOL more strongly, monotonically with α_a for all poloidal locations. By the nature of the radial variation, we can split the plasma parameters into three groups: conductive heat flux densities $q_{\parallel a,cond}$, temperatures T_a, and quantities regulated by $q_{\parallel a,cond}$ and T_a. Conductive heat fluxes are suppressed by heat flux limiting. Temperatures adjust their parallel gradients in response to heat flux limiting, existing $\nabla_\parallel T_a$, and species a parallel thermal conductivity. The radial variation of all other plasma parameters can be explained as a combination of trends in $q_{\parallel a,cond}$ and T_a. These will be elucidated later in this section, but we can give an example right away.

The main ion parallel velocity $u_\parallel$ can generally be driven by two mechanisms in the SOL: target presheath acceleration and parallel pressure gradient. The presheath electric field accelerates the parallel plasma flow so it is sonic at the sheath entrance, $u_\parallel = c_{s,t} = \sqrt{e(T_{e,t} + T_{i,t})/m_i}$. Therefore, the fall of target $T_{e,t}$ and $T_{i,t}$ will cause $u_\parallel$ to drop. On the other hand, the parallel pressure profile can be steepened if energy fluxes $q_\parallel$ are sufficiently reduced, causing an increased $\nabla_\parallel p$ and a rise in $u_\parallel$. (This effect is explained in full below.) Thus the variation of $u_\parallel$ radial profiles boils down to variation in $q_{\parallel a,cond}$ and T_a. Similar explanations can be given for other plasma parameters as well, allowing the reduction of their 2D variation to 1D by picking a representative

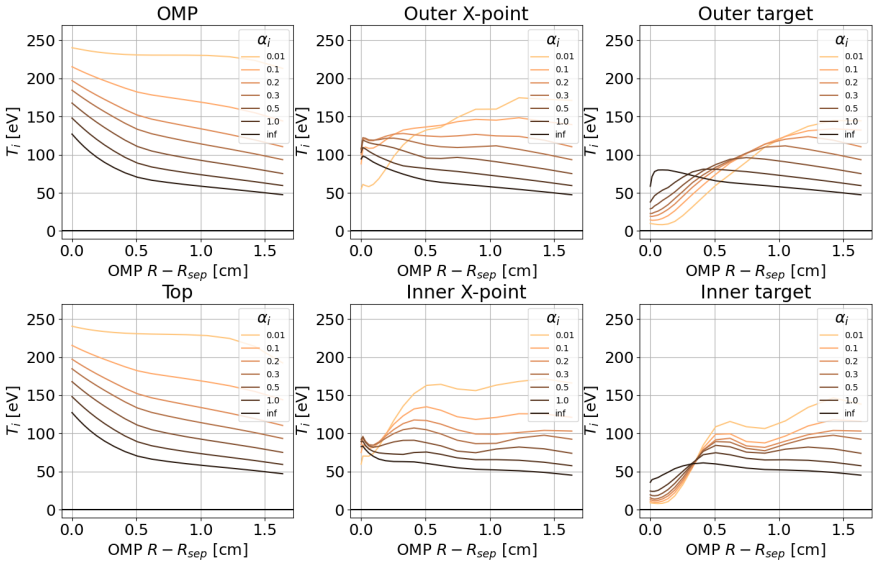

(a) : Ion heat flux limiting effect on the ion temperature T_i.

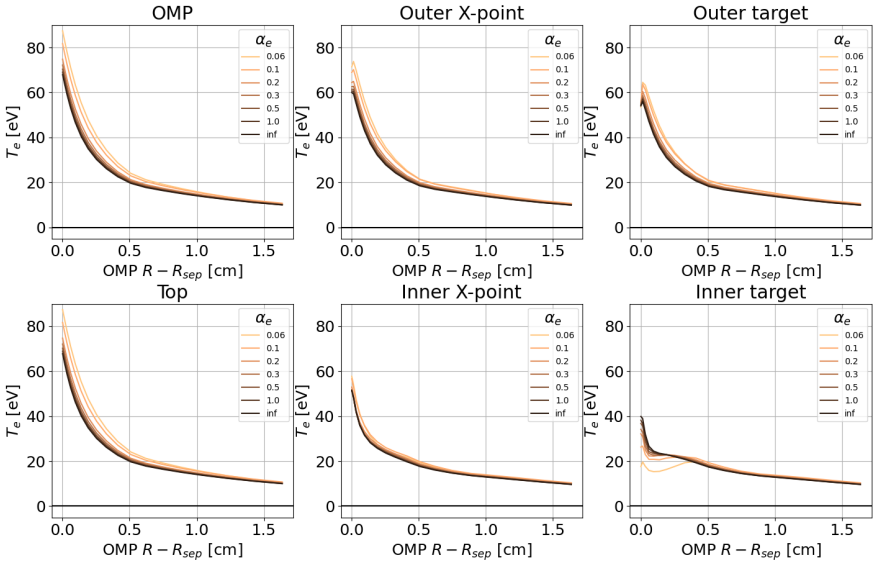

(b) : Electron heat flux limiting effect on the electron temperature T_e.

Figure 5.9: Heat flux limiting effect on radial profiles in the heat flux limiter scan. Profiles are plotted at six locations: the outer midplane (OMP), the outer X-point (or the outer divertor entrance, row of cells originating from the X-point and extending outward), the outer divertor target, the plasma top (location of the Thomson scattering diagnostic measurements), the inner X-point (or the inner divertor entrance, row of cells originating from the X-point and extending inward) and the inner divertor target.

flux tube.

We choose the 3rd SOL flux tube to represent the SOL response to heat flux limiting. This choice is informed by similar arguments as in section 6.4, where it is made for transport regime analysis. [11, 5, Sec. 5] The 3rd SOL flux tube is close to the separatrix, so its plasma parameters are high, but it does not suffer from radial transport into the private flux region as much as the 1st SOL flux tube. Additionally, the magnitude of heat flux limiting effects is highly pronounced here and typical of the near SOL. Overall, the 3rd SOL flux tube is a good representative sample of the SOL plasma reaction to heat flux limiting.

To analyse the 1D parallel profiles, we adapt the methodology of a recent ion heat flux limiter scan. [206] We plot various plasma parameters along the magnetic field line in the 7-point electron and ion heat flux limiter scan (blue and red respectively in figure 5.8), and draw conclusions by explaining their variation in terms of SOL physics.

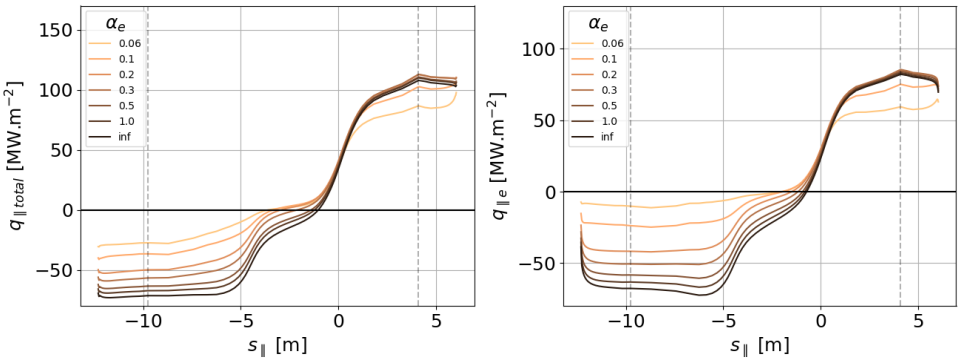

(a) : Total (electron+ion) energy flux density

(b) : Electron energy flux density

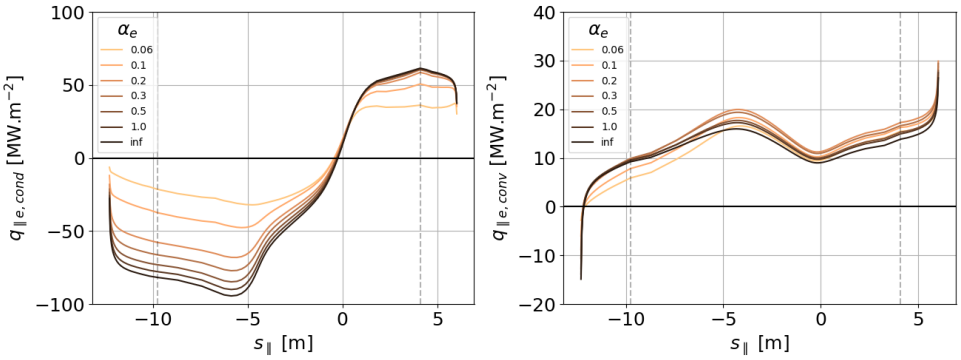

(c) : Electron (conductive) heat flux density

(d) : Electron convective energy flux density

Figure 5.10: Parallel energy flux density variation with the electron heat flux limiter α_e, in the 3rd SOL flux tube of the COMPASS H-mode #16908 simulation.

To begin with, let us inspect if heat flux limiting does what it's supposed to: decrease the parallel conductive heat flux densities $q_{\parallel a,cond}$. Their variation

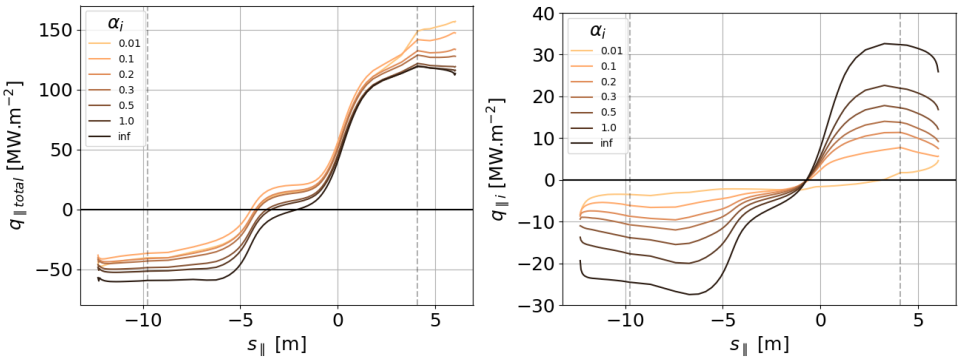

(a) : Total (electron+ion) energy flux density

(b) : Ion energy flux density

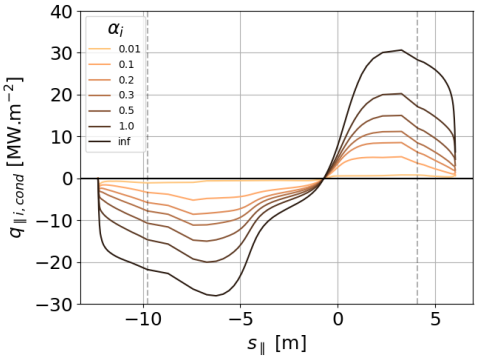

(c) : Ion (conductive) heat flux density

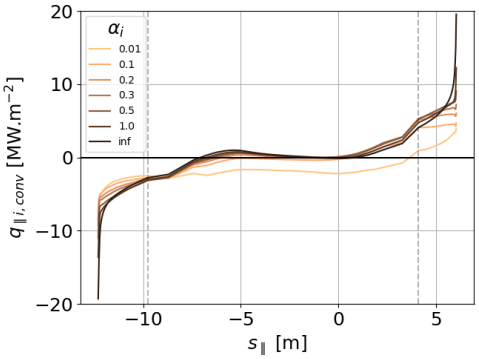

(d) : Ion convective energy flux density

Figure 5.11: Parallel energy flux density variation with the ion heat flux limiter α_i, in the 3rd SOL flux tube of the COMPASS H-mode #16908 simulation.

with regard to the respective heat flux limiter is plotted in figures 5.10c and 5.11c. Evidently the heat fluxes are reduced as α_a is lowered, but to a different degree. With $\alpha_e = 0.1$, the HFS electron heat flux density is reduced by 50 % with regard to the unlimited, classical heat flux of $\alpha_e = +\infty$. With $\alpha_i = 0.1$, in contrast, the ion heat flux density is reduced by 85 % with regard to the classical value. This difference follows from how the classical heat fluxes compare to the respective free-streaming heat fluxes, as explained in the previous section. Stressing the limits of heat flux limiting, ion conductive heat fluxes can be completely suppressed for $\alpha_i = 0.01$ and electron conductive heat fluxes substantially reduced for $\alpha_e = 0.06$ (before the solution becomes numerically unstable).

Next, let us investigate the impact of heat flux limiting on the total energy flux density make-up. Figures 5.10 and 5.11 show parallel profiles of the following quantities:

- Total parallel energy flux density $q_\parallel$, calculated by subtracting two variables from the `b2fplasmf` file, `fht` (total energy flux) and `fhj` (electrostatic energy flux, does not contribute toward divertor target heat loads) and converting them from poloidal energy fluxes to parallel energy flux densities. The total energy flux comprises the following parts:

  - Electron thermal energy flux density $q_{\parallel e}$ (`fhe`), constituted by the electron conductive heat flux, electron convective energy flux, and a minor contribution of the thermoelectric energy flux.
  - Ion thermal energy flux density $q_{\parallel i}$ (`fhi`), constituted by the ion conductive heat flux and the ion convective energy flux.
  - Electron and ion "additional" convective energy fluxes (`fnt`). Our SOLPS-ITER simulations solve an internal energy transport equation, where the convective energy flux density is $\frac{3}{2}\Gamma_{\parallel a}T_a$. To extract total energy fluxes to the targets, one must switch to the total energy transport equation, where the convective energy flux density is $\frac{5}{2}\Gamma_{\parallel a}T_a$. The internal B2.5 variable `fnt` accounts for this difference. Its calculation as $\Gamma_{\parallel a}T_a$ was mimicked from the SOLPS-ITER source code. [25, Energy fluxes deep dive]
  - Potential energy flux (`fhp`), energy released if all electrons and ions recombined. Negligible except right before the targets.
  - Kinetic energy flux (`fhm`), energy of the ion fluid flow summed over all ion species. Negligible except right before the targets.
- Thermal energy flux density $q_{\parallel a}$ (see above).
- Conductive heat flux density $q_{\parallel a,cond} = -\kappa_a \nabla_\parallel T_a$.
- Convective energy flux density $q_{\parallel a,conv} = \frac{3}{2}\Gamma_{\parallel a}T_a$.

These definitions of energy fluxes are used throughout this thesis.

Figures 5.10 and 5.11 allow us to draw two conclusions about the total energy flux make-up. Firstly, convective energy fluxes are not highly impacted by heat flux limiting of the same species, so the reduction in conductive heat flux translates directly into a reduction of the total energy flux $q_{\parallel a}$. The degree of $q_{\parallel a}$ reduction depends on the original balance between conduction and convection. Even though heat flux limiting is more pronounced in $q_{\parallel i,cond}$, the relatively large contribution of $q_{\parallel i,conv}$ makes the overall $q_{\parallel i}$ variation smaller. Secondly, ion heat flux limiting affects ion heat transport toward both targets, while the electron heat flux limiting effect is mostly confined to the inner target. As section 5.5 outlined, heat flux limiting effects are less pronounced in isothermal/sheath-affected plasmas, which is the case for T_e toward the outer target. The conditions for ion heat transport are, in contrast, more conduction-limited.

Next, we shall analyse how other plasma parameters than energy fluxes are affected by heat flux limiting. We shall address ion and electron heat flux limiting in turn.

Figure 5.12 shows the effects of ion heat flux limiting on other plasma parameters: ion temperature T_i, electron density n_e, main ion parallel velocity $u_\parallel$ and ion pressure p_i. Three observations can be made. One, heat flux limiting increases upstream T_i while reducing target T_i. In other words, it enhances the parallel T_i gradient, as previously observed in figure 5.9a. Two, ion heat flux limiting increases the target n_e, especially at the inner target. This is due to target T_i and T_e dropping while the total plasma pressure p remains approximately the same. Three, ion heat flux limiting reduces the parallel plasma flow, despite the fact that it causes a p_i gradient to build up.

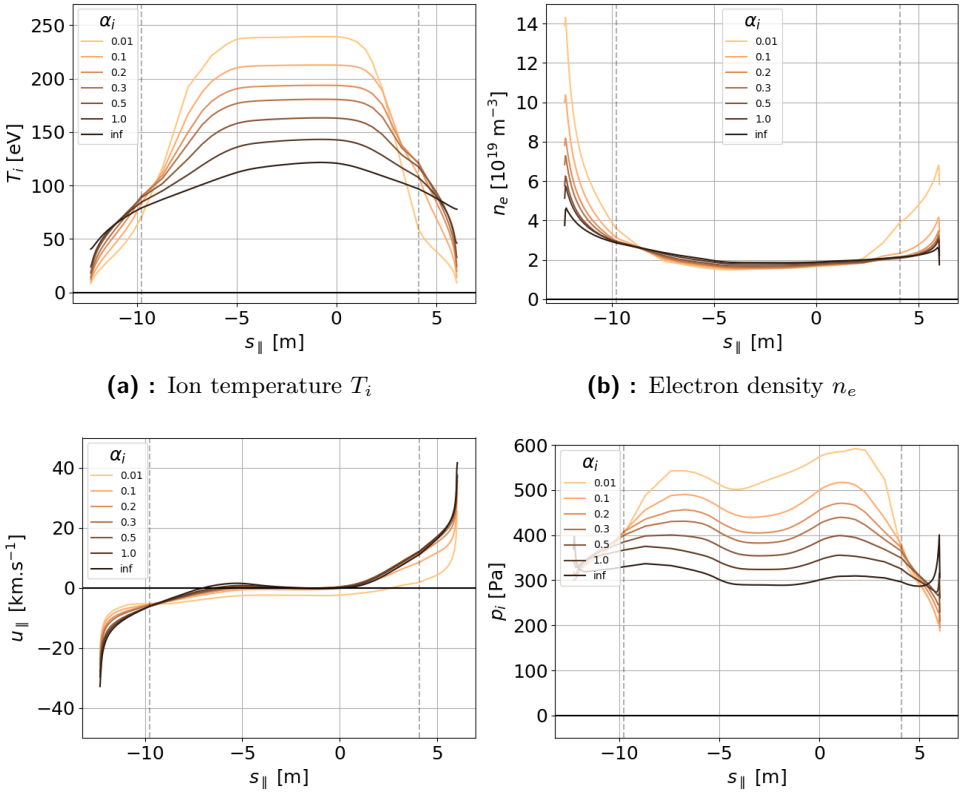

(a) : Ion temperature T_i

(b) : Electron density n_e

(c) : Main ion parallel velocity $u_\parallel$

(d) : Ion pressure p_i

Figure 5.12: Plasma parameters variation with the ion heat flux limiter α_i.

The sheath potential drop, made smaller by the decreased target T_i and T_e, may in this case drive $u_\parallel$ more potently than $\nabla_\parallel p_i$.

Figure 5.13 shows the effects of electron heat flux limiting on other plasma parameters: electron temperature T_e, electron density n_e, main ion parallel velocity $u_\parallel$ and electron heat flux limiting factor (5.16). Three observations can be made. One, electron heat flux limiting does not impact plasma parameters unless it is very strict, $\alpha_e \leq 0.1$, despite the substantial reduction in the heat flux limiting factor and $q_{\parallel e,cond}$. Even then, its effects are mostly confined to the HFS plasma. This can be attributed to the strong influence the outer target sheath exerts on the SOL electron heat transport. Two, electron heat flux limiting increases $\nabla_\parallel T_e$ toward the inner target, similarly to ion heat flux limiting. This is because the inner target sheath effect is weaker and extends a shorter distance into the SOL plasma. Three, strict electron heat flux limiting ($\alpha_e \leq 0.1$) has the opposite effect on the HFS n_e and $u_\parallel$ than ion heat flux limiting: it lowers n_e and increases $u_\parallel$. This has been called "power-starvation of the recycling process". [234] As the total energy flux toward the inner target is reduced, there is not sufficient power to ionise the recycled neutrals. Between $\alpha_e = 0.3$ and $\alpha_e = 0.06$, the EIRENE D^{1+} particle source in the inner divertor volume drops from 2.6×10^{21} s^{-1} to 1.3×10^{21} s^{-1}. The lack of ionisation causes a drop in density, which together

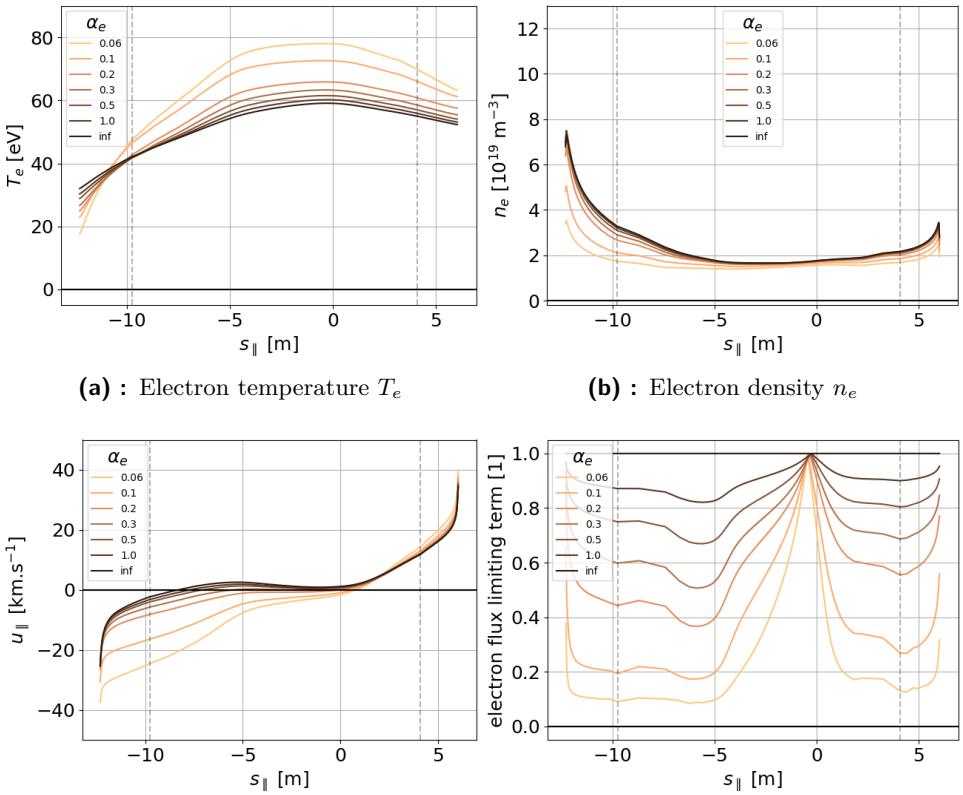

(a) : Electron temperature T_e

(b) : Electron density n_e

(c) : Main ion parallel velocity $u_\parallel$

(d) : Electron heat flux limiting factor (5.16)

Figure 5.13: Plasma parameters variation with the electron heat flux limiter α_e.

with the drop in inner target T_e causes a drop in electron and plasma pressure. The parallel gradient of p is so strong ($p_t/p_u = 0.66$,)that one would normally associate it with the impending onset of detachment. The physical process is different, however, and target temperatures remain relatively high ($T_{e,t} = 20$ eV). The drop of pressure is gradual over the entire HFS SOL, driving at last increased plasma flow $u_\parallel$.

To make an intermediate conclusion, electron and ion heat flux limiting share the feature of enhancing their respective $\nabla_\parallel T_a$, but setting very low α_a leads to different SOL response for electrons and ions. This will be expanded upon presently.

We have been investigating the heat flux limiting effect in the 7-point ion and electron α_a scans, focusing mostly on how α_a impacts heat transport in its own species. Heat flux limiting has, however, *cross-species effects* as well. I am not aware of this being reported in any previous work, because no previous work performed an independent ion and electron heat flux limiter scan at the same time. This may be, in part, because visualising the effect of a 2D α_e-α_i scan requires greatly simplifying the simulation results, from 2D down to 0D (a single scalar for each quantity in each simulation). In this thesis, we have leveraged the previous insights into SOL physics to distill

the parameter variation into characteristic scalars, listed in table 5.2. Fluxes and densities were checked for magnitude and temperatures and pressures for parallel gradients. Inner target quantities were generally preferred due to greater sensitivity. The impending pinnacle of this section is concerned 2D contour plots of plasma parameter variation in the 3rd SOL flux tube of the COMPASS H-mode #16908 simulation with α_e and α_i independently spanning the values $\{0.1, 0.2, 0.3, 0.5, 1.0\}$.

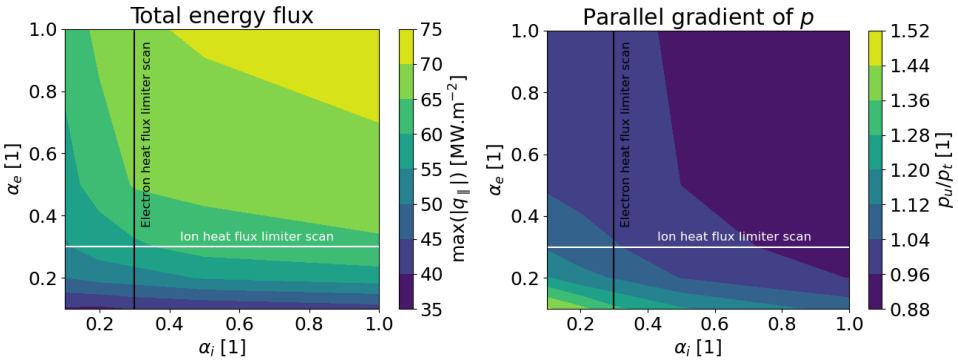

(a) : Total energy flux density $q_\parallel$

(b) : Plasma pressure p

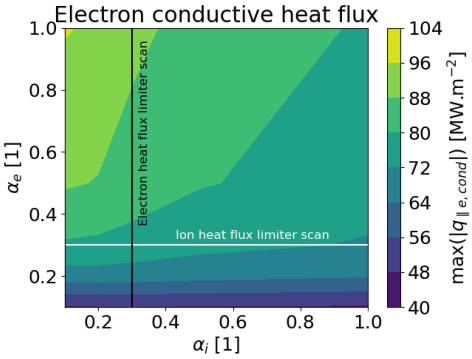

(c) : Electron conductive heat flux density $q_{\parallel e,cond}$

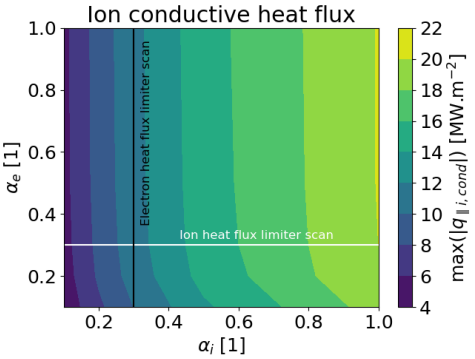

(d) : Electron conductive heat flux density $q_{\parallel i,cond}$

Figure 5.14: Plasma parameters variation with simultaneous electron and ion heat flux limiting.

Figure 5.14 shows how electron and ion heat flux limiting affect energy flux densities: total energy flux density $q_\parallel$, electron and ion conductive heat flux density $q_{\parallel e,i,cond}$; as well as the plasma pressure p. Three observations can be made. One, α_e reduces the total energy flux density $q_\parallel$ more strongly than α_i. This is because conduction mediates a larger part of electron energy transport than ion energy transport, so its suppression is more effective in reducing $q_{\parallel e}$ than $q_{\parallel i}$. Two, the ion conductive heat flux density $q_{\parallel i,cond}$ largely depends only on α_i and not on α_e, but electron conductive heat fluxes $q_{\parallel e,cond}$ are moderately reinforced by α_i. The former observation reflects the fact that electron heat flux limiting has little effect on plasma parameters unless it is very strict. Ion heat flux limiting, conversely, impacts the SOL at higher α_i values. The positive effect of α_i on $q_{e,cond}$ indicates increased heat transfer

from ions to electrons, due to higher $T_i - T_e$ at upstream. This is confirmed by energy balance analysis, where the ratio of electron and ion thermal fluxes impinging on the inner target changes from 1:1 at $\alpha_i = +\infty$ to 2:1 in favour of $q_{\parallel e}$ at $\alpha_i = 0.01$. This partially compensates for total energy flux reduction by α_i, which is why SOL power-starvation does not come into play during strict ion heat flux limiting. Three, both electron and ion heat flux limiting increase $\nabla_\parallel p$, although, as we shall see, the mechanism is different in each case.

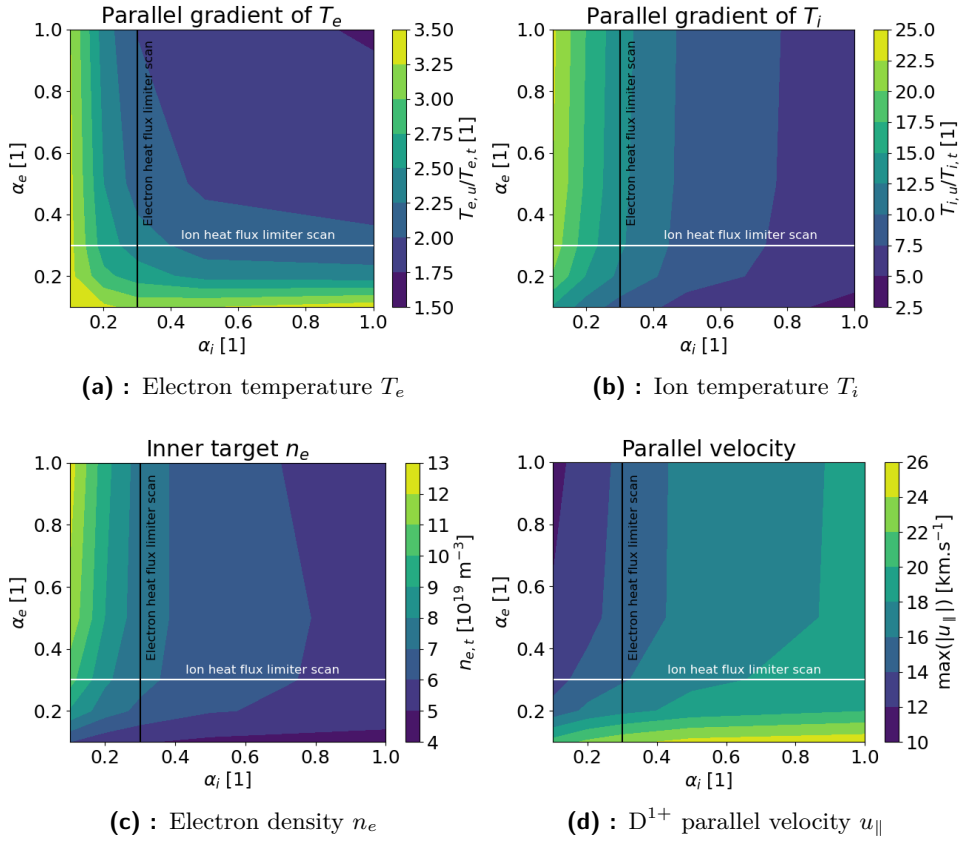

(a) : Electron temperature T_e

(b) : Ion temperature T_i

(c) : Electron density n_e

(d) : D^{1+} parallel velocity $u_\parallel$

Figure 5.15: Plasma parameters variation with simultaneous electron and ion heat flux limiting.

Figure 5.15 shows how electron and ion heat flux limiting affect basic plasma parameters: electron temperature T_e, ion temperature T_i, electron density n_e, and main ion parallel velocity $u_\parallel$. Two observations can be made. One, both electron and ion heat flux limiting elicit a steepening of the T_e parallel profile toward the inner target. This has already been explained for α_e in terms of $\nabla_\parallel T_e$ compensating for lowered thermal conductivity κ_e. Power-starvation of the HFS SOL might also reduce inner target $T_{e,t}$. For α_i, the answer lies in the already reported transfer of power from ions to electrons. The demand on electron parallel transport to carry more power acts similar to lowering electron thermal conductivity: it is met by the code by increasing $\nabla_\parallel T_e$. The second observation interprets figures 5.15b, 5.15c

and 5.15d in tandem, and has to do with the different SOL physics basis of extreme ion and electron heat flux limiting. Ion heat flux limiting does not starve the HFS SOL of power since $q_{\parallel i,cond}$ is readily displaced onto $q_{\parallel e,cond}$, and therefore preserves the inner target plasma pressure. Consequently, the drop in inner target $T_{i,t}$ (figure 5.15b) is compensated by an increase in $n_{e,t}$ (figure 5.15c). $T_{i,t}$ and $T_{e,t}$ dropping cause the target sound speed to decrease, slowing plasma flow $u_\parallel$ toward the inner target (figure 5.15d). Strict electron heat flux limiting, on the other hand, acts quite differently. Starving the HFS SOL of power, it preserves upstream plasma pressure but decreases inner target pressure p_t. Inner target $T_{e,t}$ and $n_{e,t}$ drop simultaneously. Meanwhile, target $T_{i,t}$ increases, because ion heat transport is unaffected (incoming power preserved) and recycling is reduced (lower fraction of cold recycling ions as compared to hot upstream ions). This helps offset the T_e effect on the target sound speed, allowing the pressure gradient to drive strong flows $u_\parallel$ along the entire HFS SOL.

To summarise the results of the ion and electron heat flux limiter scan:

- Ion heat flux limiting in the range $\alpha_i = 0.1\text{-}1.0$ has stronger effects than electron heat flux limiting in the same range. This is because classical $q_{\parallel i,cond}$ is comparable to the ion free-streaming flux density (self-limiting heat flux) while classical $q_{\parallel e,cond}$ is much smaller than the electron free-streaming flux density (heat flux limited by the sheath). Consequently, for a given value of α_a, the harmonic average method reduces ion heat fluxes more than electron heat fluxes.
- Ion heat flux limiting affects SOL parameters toward both targets, while electron heat flux limiting affects mostly the HFS SOL. This is because T_e is high and constant toward the outer target, corresponding to a hot plasma under the strong influence of a nearby sheath, so a reduction in thermal conductivity can be compensated by a small overall increase in T_e, which increases the thermal conductivity as $\kappa_e \sim T_e^{5/2}$. Conversely, T_e does drop somewhat toward the inner target, as does T_i toward both targets, corresponding more to conduction-limited SOL transport. In this regime, heat transport is more sensitive to the particular value of thermal conductivity and heat flux limiting has pronounced effects.
- In the near SOL, both ion and electron heat flux limiting cause the respective conductive heat flux densities to drop, reducing the total power transported toward the inner target. In response to lowered thermal conductivity, parallel temperature profiles, so that at least some input power can be transported toward the targets. These are the two primary effects of heat flux limiting, and all other plasma parameters are regulated through them.
- The physics associated with extreme heat flux limiting is different for electrons and ions. Constraining electron conduction leads to starving the HFS SOL of power, reducing recycling, making target n_e drop and introducing a parallel pressure gradient which drives plasma flow toward the target. Constraining ion conduction, on the other hand, leads to power transfer from ions to electrons, which keeps up inner target

recycling and allows n_e to rise in response to $T_{i,t}$ and $T_{e,t}$ falling. The drop in target sound speed then slows the plasma flow toward the target.

- Heat flux limiting exhibits interdependent cross-species effects. Both ion and electron heat flux limiting cause inner target $T_{e,t}$ to drop, increasing $\nabla_\parallel T_e$ and $\nabla_\parallel p$, though it is through different means. Furthermore, ion heat flux limiting affects plasma parameters (most notably T_i) throughout the investigated α_i range, changing the electron free-streaming energy flux density and altering the electron heat flux limiting factor even under constant α_e. Some effects of ion and electron heat flux limiting are synergic (increasing $\nabla_\parallel T_e$ toward inner target), others antagonistic (increasing/decreasing inner target $n_{e,t}$). Finally, simulation sensitivity to α_i depends on α_e. Extreme electron heat flux limiting overrides most effects otherwise expected of ion heat flux limiting.
- The influence of heat flux limiting on this SOLPS-ITER simulation of COMPASS tokamak H-mode #16908 is marked, but not catastrophic. Aside from the ion conductive heat flux density $q_{\parallel i,cond}$ and the inner target n_e, plasma parameters usually don't change more than within a factor of two. As shown in the next section, it is even hard to tell which values of α_a are correct based on experimental data. This lends us some perspective above the complicated findings of this section. As long as we keep track of general trends and lean on theoretical understanding, choosing the correct heat flux limiters for COMPASS simulations should not be a matter of making or breaking the SOLPS-ITER simulation.

5.8 Optimal heat flux limiter values

In this concluding section of the heat flux limiting chapter, we use theoretical insights of sections 5.2, 5.3 and 5.5, literary sources of section 5.4, the heat flux limiter scans of sections 5.6 and 5.7, and kinetic simulations with the BIT1 code to suggest the optimal heat flux limiter values for SOLPS-ITER simulations of the COMPASS tokamak. We shall also provide general heat flux limiting guidelines in edge transport simulations.

The BIT1 code is a 1D3V particle-in-cell kinetic code for modelling the tokamak SOL. [45] Its computational domain is a single SOL flux tube; its particle species include ions, electrons and neutrals. This section shows the results of a BIT1 simulation which builds on previous simulations published in [127]; the reader is directed there for more details on BIT1. Cross-comparison with these results was the reason for performing the SOLPS heat flux limiter scan in the COMPASS H-mode discharge #16908 at $t = 1130$ ms. However, it became clear that technical differences between the simulations prevented a meaningful comparison. Therefore, a new BIT1 simulation was carried out by D. Tskhakaya, with four key updates. One, flux tube geometry was set up to copy the 3rd SOL flux tube of the SOLPS simulation. Two, all charge states of carbon were modelled, where only C^{1+} was modelled previously. Three, upstream plasma parameters were chosen to match a simulation from the SOLPS heat flux limiter scan, see below. Four, parallel profiles of the

particle and energy source were set to follow the radial transport of the same SOLPS simulation, also see below. In consequence, the new BIT1 simulation presented herein represents a state-of-the-art kinetic model of the tokamak SOL.

	BIT1 simulation in [127]	BIT1 simulation herein
L	HFS 11 m, LFS 5 m	HFS 12.3 m, LFS 6 m
$T_{e,u}$	60 eV	61 eV
$n_{e,u}$	0.9×10^{19} m^{-3}	1.8×10^{19} m^{-3}
$T_{i,u}$	100 eV	155 eV

Table 5.3: Comparison of BIT1 input parameters in simulations in [127] and in this section: connection length L, upstream electron temperature $T_{e,u}$, upstream electron density $n_{e,u}$ and upstream ion temperature $T_{i,u}$.

The principal input parameters of a BIT1 simulation are the upstream electron density $n_{e,u}$, electron temperature $T_{e,u}$ and ion temperature $T_{i,u}$. The total magnitude of the energy and particle source is adjusted until these parameters are reached. Previous BIT1 simulations of COMPASS H-mode #16908 employed Thomson scattering diagnostic measurements of T_e and n_e from the time instant $t = 1130$ ms at $Z = 0.278$ m, see the left column of table 5.3. The ion temperature was estimated as $T_{i,u} = \frac{5}{3}T_{e,u}$. In the BIT1 simulation presented herein, upstream plasma parameters were informed by the average of several inter-ELM Thomson scattering measurements around $t = 1130$ ms and by the separatrix location found using SOLPS-ITE. In other words, we adopted the plasma parameters from the outer midplane of the 3rd SOL flux tube in the SOLPS heat flux limiter scan simulation where $\alpha_e = 0.3$ and $\alpha_i = 1.0$.[2] The central interpretative simulation ($\alpha_{e,i} = 0.3$) was not chosen because its $T_{i,u} = 190$ eV was too high to be realistic.

Previous BIT1 simulations have used a parallel profile of particle and power sources (corresponding to radial transport into the flux tube) in the shape of a bell curve peaking at the outer midplane. We have found, however, that radial transport in our SOLPS simulations does not follow this ballooning-like poloidal dependence. Figure 5.16 shows that the radial transport into the 3rd SOL flux tube of the SOLPS-ITER simulation used for BIT1 input has two peaks, one below the outer midplane and one at the inner midplane. This is a consequence of the poloidal invariability of diffusion coefficients and relative constancy of n_e, T_e and T_i along the field line. In such a situation, the anomalous diffusive transport, equation (6.7), is strongest where radial gradients are highest, that is, where magnetic surfaces are closest together. As figure 5.1b shows, this is at the midplanes. Such a result is not physical; rather, it is a technical consequence of a particular anomalous radial transport implementation. SOLPS-ITER offers the possibility to adjust the poloidal dependence of anomalous diffusion coefficients, suppressing the inner midplane

[2] As the entire heat flux limiter scan has since been transferred from SOLPS-ITER version 3.0.7 to version 3.0.9, there is currently no simulation in the heat flux limiter scan whose upstream parameters perfectly match the BIT1 upstream parameters.

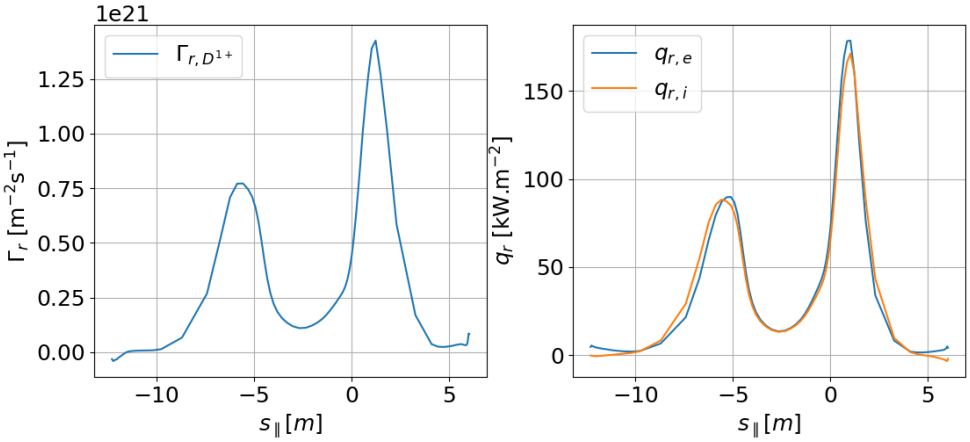

Figure 5.16: Parallel profile of the particle and power source by radial transport, originating from SOLPS-ITER simulation of the COMPASS H-mode #16908, employed in the BIT1 simulation.

radial transport, but it has been reported to have little effect on the results. [51] To improve the match in BIT1 and SOLPS-ITER parallel profiles, double-peaked particle and power sources modelled after figure 5.16 were adopted in the BIT1 simulation.

While comparing SOLPS-ITER and BIT1 results, the most natural strategy was to draw BIT1 results over the 1D parallel profiles of the two 7-point heat flux limiter scans (red and blue in figure 5.8) and to gauge which heat flux limiter comes the closest to the kinetic simulation. The problem with this approach is that different plasma parameters yield different optimal α_a, covering the entire range from "use very strict heat flux limiting" to "use no heat flux limiting". As reported previously, it is not feasible to find a spatially constant value of a heat flux limiter which will make a fluid simulation conform completely to a kinetic simulation. [212, 216, 207, 221, 40] As a result, we have turned to analysis which is qualitative rather than quantitative. Using previous knowledge of heat flux limiting impact on SOLPS simulations, we set out to make broad-stroke recommendations on α_a values which can be adapted to a particular SOL based on its sensitivity to α_e and α_i.

Our tenets of the SOLPS-ITER and BIT1 cross-comparison were the following. The aim is to make recommendations of heat flux limiter values which will bring an interpretative SOLPS-ITER simulation closer to experimental measurements, while using the kinetic simulation as guidance on the underlying parallel transport physics. Quantities which can be experimentally measured are given preference. Precise quantitative agreement is not sought; variance within ±30% is considered a match. Variance of more than ±50% or qualitative differences shall be investigated. We seek to describe trends rooted in edge plasma physics; we do not hunt for particular values of α_e or α_i. Our results reflect the modelled H-mode SOL, but generalisations should be made wherever possible.

Based on these tenets, we have made the following conclusions by comparing

the SOLPS-ITER density scan to the BIT1 simulation:

HFS SOL power starvation does not occur. BIT1 electron and total pressure do not fall toward the inner target, parallel velocity is consistent with $\alpha_e = 0.2$ and inner target electron density is consistent with $\alpha_e = +\infty$, see figures 5.17a-5.17d. Experimental measurements of target n_e, shown in figure 5.1, indicate higher $n_{e,t}$ at the inner target, disproving the suppression of HFS ionisation. We conclude that the HFS SOL is not starved of power, which rules out very small values of the electron heat flux limiter $\alpha_e \leq 0.1$ for the investigated SOL.

Parallel temperature gradients are higher in the kinetic simulation. A match in SOLPS and BIT1 $T_{a,u}/T_{a,t}$ is reached for strict heat flux limiting, $\alpha_{e,i} < 0.1$, figures 5.18a and 5.18b. Electron conductive heat flux density $q_{\parallel e,cond}$ is also consistent with $\alpha_i = 0.1$, figure 5.17e. Such a choice, however, also causes HFS SOL power starvation for electrons and unrealistically high $T_{i,u}$ for ions. Kinetic simulations have consistently reported higher $\nabla_\parallel T_a$ than fluid simulations [39, 198], but in our SOLPS simulations sufficiently high $\nabla_\parallel T_a$ cannot be achieved without unwanted side-effects. An option for future simulations is using different core boundary conditions for the electron and ion energy transport equations. Fixing the separatrix T_a instead of $P_{SOL,a}$ in conjunction with heat flux limiting may result in both realistic upstream temperatures and parallel temperature gradient similar to kinetic simulations. While using equally split P_{SOL}, the strong effect of α_i on $T_{i,sep}$ cannot be ignored in the investigated SOL.

Electron convective energy flux is strongly influenced by SOL parallel currents. There is only one quantity which shows qualitative disagreement between SOLPS-ITER and BIT1; the parallel electron convective energy flux density $q_{\parallel e,conv}$, shown in figures 5.18c and 5.18d. Its stagnation point (region where $q_{\parallel e,conv}$ reverses sign) in BIT1 is near the outer midplane, similar to ion convection, but in SOLPS it is just outside the inner target. This is a consequence of different boundary conditions for SOL currents. In BIT1, the divertor targets are floating, allowing no net current to flow into them and forcing the overall SOL parallel current to be near zero. In consequence, parallel transport is ambipolar and electrons and ions stream together from a common stagnation point. In SOLPS-ITER, the divertor targets are grounded, resulting in a rather strong parallel current $j_\parallel \approx 180$ kA.m^{-2} directed from the outer to the inner target. This direction is consistent with thermoelectric currents. [235] The parallel current $j_\parallel$ is carried mainly by electrons, which causes strong electron convection from the inner target to the outer target and, consequently, electron convective energy flux in the same direction. This was an oversight while setting the simulations up, but the BIT1-SOLPS difference in $q_{\parallel e,conv}$ is fortunately small compared to the total energy flux densities, so the different target biasing does not significantly impact the overall comparison.

Heat flux limiting affects heat load distribution between the inner and outer target. The total energy flux density toward the outer target is 50 % lower in the BIT1 simulation than in most SOLPS simulations, while

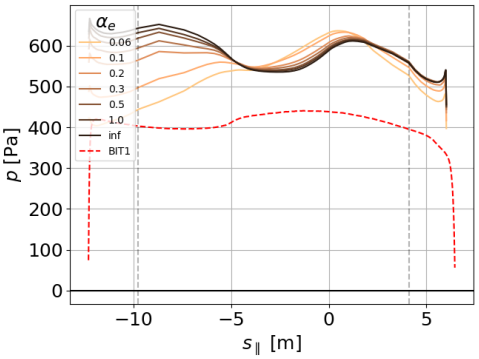

(a) : Total pressure p, electron heat flux limiter scan.

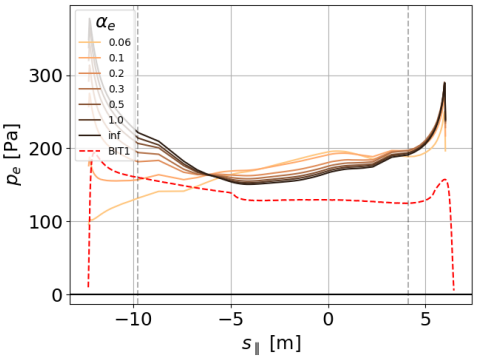

(b) : Electron pressure p_e, electron heat flux limiter scan.

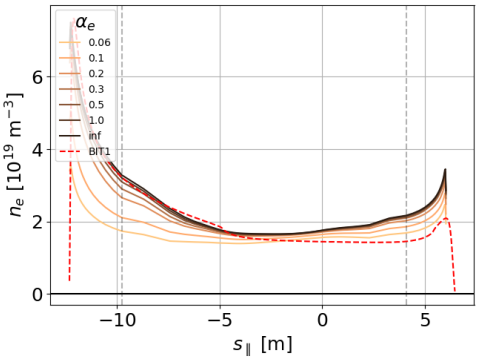

(c) : Electron density n_e, electron heat flux limiter scan.

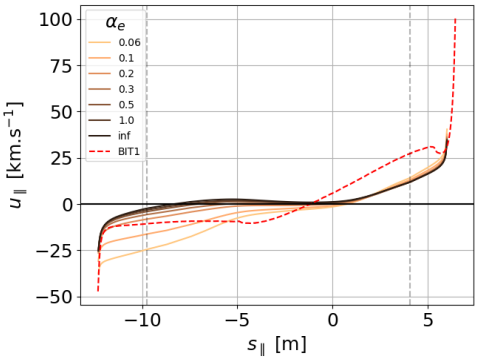

(d) : D^{1+} parallel velocity $u_\parallel$, electron heat flux limiter scan.

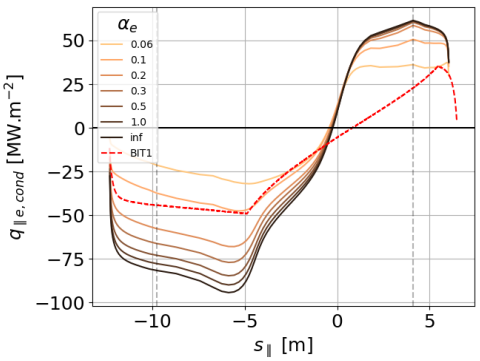

(e) : Electron conductive heat flux $q_{\parallel e,cond}$, electron heat flux limiter scan.

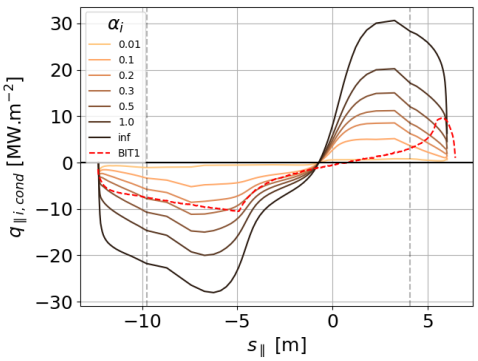

(f) : Ion conductive heat flux $q_{\parallel i,cond}$, ion heat flux limiter scan.

Figure 5.17: Selected results of the BIT1 kinetic simulation and SOLPS-ITER transport simulation in the 3rd SOL flux tube of the COMPASS H-mode #16908 SOLPS simulation.

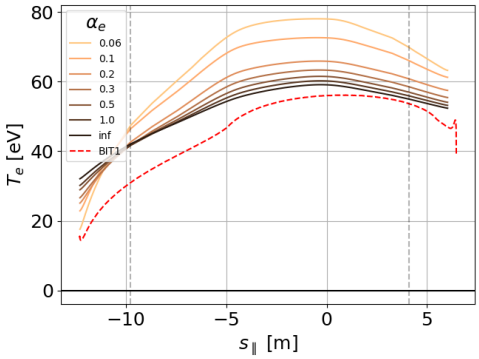

(a) : Electron temperature T_e, electron heat flux limiter scan.

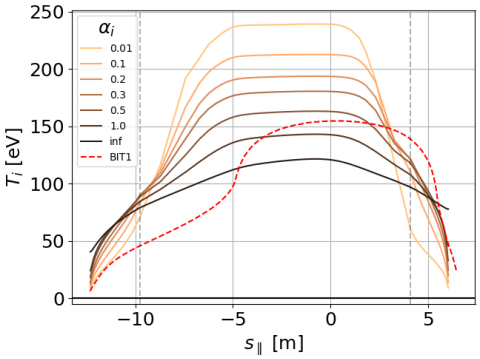

(b) : Ion temperature T_i, ion heat flux limiter scan.

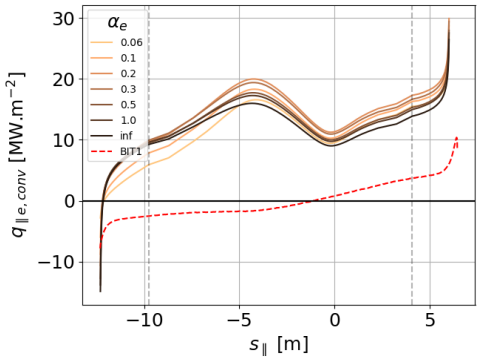

(c) : Electron convective energy flux density $q_{\parallel e,conv}$, electron heat flux limiter scan.

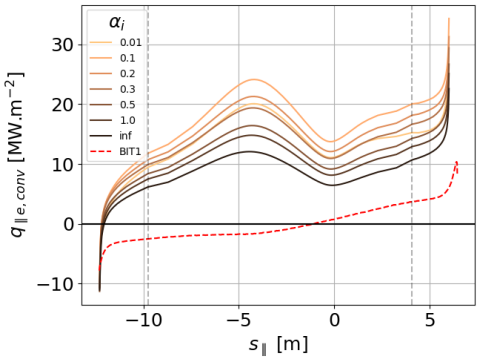

(d) : Electron convective energy flux density $q_{\parallel e,conv}$, ion heat flux limiter scan.

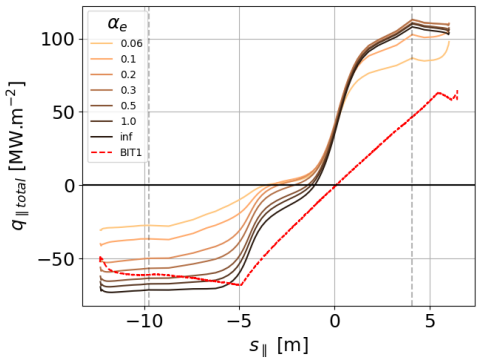

(e) : Total energy flux density $q_\parallel$, electron heat flux limiter scan.

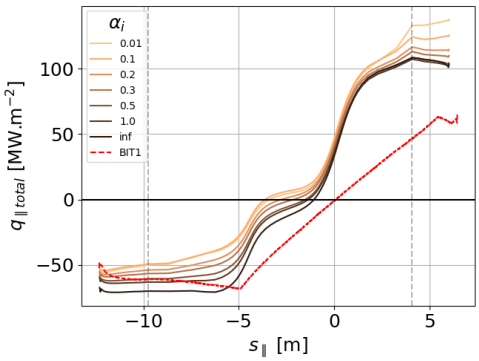

(f) : Total energy flux density $q_\parallel$, ion heat flux limiter scan.

Figure 5.18: Selected results of the BIT1 kinetic simulation and SOLPS-ITER transport simulation in the 3rd SOL flux tube of the COMPASS H-mode #16908 SOLPS simulation.

the inner target $q_{\parallel}$ is consistent with moderate α_e, as shown by figures 5.18e and 5.18f. The BIT1 target heat load distribution (in the near SOL) is 6:5 in favour of the outer target. Within the SOLPS heat flux limiter scan, the near SOL target heat load distribution varies from 6:5 to 4:1 in favour of the outer target, with both electron and ion heat flux limiting increasing the asymmetry. Heat flux limiting affects divertor asymmetry in the investigated SOL for two reasons. One, the inner target is more conduction-limited than the outer target, so heat flux limiting is more effective at reducing heat fluxes toward it. [39] Two, heat flux limiting increases upstream T_e, leading to better electron thermal conductivity in the mostly isothermal LFS SOL and enhancing outer target $q_{e,cond}$. Total target energy flux densities can be well measured in experiment by the infrared camera; the ratio of the peak energy flux density $q_{\parallel}$ is 3:2. This is consistent with mild heat flux limiting.

We do not make a special point about matching conductive energy fluxes, shown in figures 5.17e and 5.17f, even though this would seem like the ultimate criterion of α_a value. The goal of heat flux limiting is, after all, to prevent unrealistically high heat fluxes and correct the classical heat flux formulas (5.1) and (5.2) to resemble kinetic results. Our conception is, however, more holistic. Heat flux limiting has complicated effects. Decreasing SOL α_e can have no effect [236]; increase upstream T_e [39, 218], decrease downstream T_e [48] or both [211]; increase convection toward one divertor target (figure 5.13c); or change heat load distribution between the targets (figure 5.18e); all depending on the machine and its SOL transport regime. From this perspective, the point of heat flux limiting is no longer to "limit heat fluxes". It can help emulate kinetic effects in the SOL heat transport by affecting parallel temperature gradients, target heat load distribution or target densities — phenomena which can be experimentally measured and verified, unlike the magnitude of the conductive heat flux density. If we were to look only for SOLPS-BIT1 match in $q_{\parallel a,cond}$, shown in figures 5.17e and 5.17f, we would conclude that the optimal choice is $\alpha_e = 0.1$ and $\alpha_i = 0.2$ and ignore that the side-effects actually impair the experiment-model match. (In particular, inner target T_e falls even further below measured values and the outer-inner target heat load distribution diverges from the experiment.) In other words, if one aims to perform a good interpretative simulation rather than to achieve agreement between a kinetic and a fluid simulation, knock-on effects of heat flux limiting are more important than the magnitudes of heat flux densities themselves.

Let us conclude this section by making heat flux limiting recommendations for the COMPASS H-mode #16908 simulation investigated herein, and then for tokamak SOL transport modelling in general.

Heat flux limiter recommendations for the interpretative SOLPS-ITER simulations of the COMPASS H-mode #16908:

- Electron heat flux limiter α_e: The simulation is largely insensitive to $\alpha_e \geq 0.2$ and displays unwanted HFS SOL power starvation for $\alpha_e \leq 0.1$. Use an arbitrary value $\alpha_e \geq 0.2$, including no electron heat flux limiting. The SOL is so strongly sheath-limited that heat flux limiting by the

sheath boundary condition takes prevalence.

- Ion heat flux limiter α_i: The simulation is sensitive to α_i in its entire range. Make an informed estimate on upstream $T_{i,sep}$ and adjust the input power split $P_{SOL,e} : P_{SOL,i}$ in conjunction with α_i to achieve it. Increasing $P_{SOL,i}$ at the expense of $P_{SOL,e}$ increases $T_{i,sep}$; decreasing α_i also increases $T_{i,sep}$ while decreasing target $T_{i,t}$. Moderate ion heat flux limiting $\alpha_i \sim 0.3$ will probably deliver desired parallel T_i gradients while not causing unwanted side-effects such as steep target $n_{e,t}$ increase.

The heat flux limiter values $\alpha_e = \alpha_i = 0.3$ recommended by the previous study [127] are consistent with these recommendations, save for the fact that the high $T_{i,sep}$ should be controlled by a P_{SOL} split in favour of electrons. This raises the necessity to readjust the diffusion coefficient profiles, so it was left for future work.

Heat flux limiter recommendations for tokamak edge transport modelling in general:

1. Begin by gauging whether your simulation is sensitive to heat flux limiter values. The answer may depend on plasma density and be different for the inner and outer target. Calculate the upstream collisionality ν^* (5.6) toward both targets and assess parallel T_e gradients. If $\nu^* \sim 1$ and the SOL is sheath-limited ($T_{e,u} \approx T_{e,t}$), electron heat flux limiting may not have much effect. If $\nu^* \sim 50$ and the SOL is deeply conduction-limited or detached ($T_{e,u} \gg T_{e,t}$), heat flux limiting in general may not have much effect. In the moderately collisional transition between the two limits ($T_{e,u}/T_{e,t} \sim 3$), heat flux limiting may strongly impact the plasma solution and caution is recommended.
2. To confirm the above estimates, run a small heat flux limiter scan, possibly in a simplified version of your simulation (no impurities, simple boundary conditions, no drifts). As long as the SOL transport regime does not change, heat flux limiting effects should also remain the same (though this remains to be thoroughly tested). Vary electron and ion heat flux limiting in a 3-point scan from "strict" ($\alpha_a \leq 0.1$) through "moderate" ($\alpha_a \sim 0.5$) to "none" ($\alpha_a = +\infty$). Do not neglect ion heat flux limiting just because $q_{\parallel i} < q_{\parallel e}$; it strongly impacts other plasma parameters.
3. While evaluating the heat flux limiter scan, use as guidance that the primary effects of heat flux limiting are the reduction of conductive heat fluxes and enhancement of parallel temperature gradients. Knock-on effects may include transfer of power between electrons and ions, $\nabla_\parallel T$ enhancement in the other particle species or target heat load redistribution. Particularly in the case of fixed ion input power $P_{SOL,i}$, ion heat flux limiting can significantly influence upstream $T_{i,sep}$.
4. If your simulation is insensitive to varying heat flux limiters, use weak or no heat flux limiting, $\alpha_a = 1.5$-10 [39, 236]. Even if there are strong kinetic effects in the parallel heat transport, such as divertor heat flux enhancement by the presence of suprathermal electrons in the cold target plasma, heat flux limiting with the harmonic average will not be able to

emulate them. If your simulation is sensitive to varying heat flux limiters, their value can be set to control $\nabla_{\parallel} T_a$, inner/outer target heat load distribution and other plasma parameters. Decreasing α_a will increase $\nabla_{\parallel} T_a$; other effects depend on the SOL transport regime of the particular target.

5. General rules: SOL transport simulations are more sensitive to ion heat flux limiters than electron heat flux limiters, because ion free-streaming energy flux density $q_{FS,i}$ is comparable to the ion heat flux density $q_{\parallel i,cond}$. Beware of low heat flux limiter values, $\alpha_a \leq 0.1$, as they may cause numerical instabilities or unwanted side-effects in the plasma solution. Do not assume that $\alpha_e = \alpha_i$ is a reasonable choice "for lack of evidence"; electron and ion heat flux limiting are sensitive to α_a in different ranges of values and produce different effects on the plasma solution.
6. If accurate description of SOL parallel heat transport is imperative, do not use heat flux limiting. No value of α_a will reproduce the results of an advanced calculation. Consider using a state-of-the-art transport code with built-in kinetic corrections of parallel heat transport, such as KIPP [48] or SOLKiT [213].

Chapter 6

SOL transport regime

This chapter presents interpretative SOLPS-ITER simulations of a 5-point COMPASS density scan in L-mode, discharges #13812-#13825. With line-averaged densities[1] spanning from 2-10 $\times$ 10^{19} m^{-3}, the five discharges are a good representation of the COMPASS operational space in lower-single-null L-mode without impurity seeding.[2] The aim is to answer the first part of the research question of this thesis: How well can SOLPS-ITER model COMPASS tokamak edge plasmas?

This chapter is organised as follows. In section 6.1, I present interpretative simulations of the five density scan discharges and find that SOLPS-ITER can reproduce low and moderate densities, but significantly underestimates target electron temperatures $T_{e,t}$ at high densities. In section 6.2, I list six approaches I tried to increase the experiment-model match, and conclude that adjusting the ion-electron SOL input power split as well as including drifts should be helpful in future SOLPS-ITER simulations of COMPASS. In section 6.3, I describe the handling of realistic particle sources and sinks, implemented only in the density scan simulations, and gauge that their particle balance is satisfactory. In section 6.4, I assess the SOL transport regime in the SOLPS simulations as sheath-limited at low densities and conduction-limited at high densities, while the experimental plasma appears to transition into the conduction-limited regime at the highest density. Finally, in section 6.5, I show that deriving a quantitative value of the anomalous particle diffusion coefficient D_n is difficult, but that D_n can be related qualitatively with upstream plasma density depending on the transport regime.

6.1 COMPASS L-mode density scan #13812-#13825

Discharge description. COMPASS discharges #13812-#13825 constitute a five-point steady-state L-mode density scan in the lower single null divertor configuration. They were performed in deuterium without extrinsic impurities, neutral beam heating was off, and resonant magnetic perturbations were not applied. The horizontal reciprocating probe was measuring, cooling the edge plasma once inside the velocity shear layer. The line-averaged densities were

[1] These densities were measured by an interferometer. At high densities, they do not agree with measurements of the core Thomson scattering diagnostic. For example, in the highest-density discharge #13825, interferometer $\overline{n}_e = 10 \times 10^{19}$ m^{-3} while the Thomson scattering $\overline{n}_e = 7.5 \times 10^{19}$ m^{-3}. In this thesis, the interferometer $\overline{n}_e$ is used only to identify the density scan discharges. Physics analysis is carried out with the more relevant separatrix electron density $n_{e,sep}$. It should not be forgotten, however, that the line-averaged densities are likely overestimated.

[2] We acknowledge L-mode detachment experiments utilising density ramps, such as discharge #12284, which reached more extreme divertor conditions than the high-density experiments reported herein. Our interest lies in modelling plasma in steady-state, and during the investigated density scan campaign raising the line-averaged density to $\overline{n}_e = 11 \times 10^{19}$ m^{-3} resulted in a highly unstable discharge. We assume, therefore, that discharge #13825 represents the high end of densities comfortably achievable in the COMPASS tokamak. Chamber conditioning can also significantly impact the operational space, but it is outside the scope of this thesis.

Discharge	$\overline{n}_e$	P_{SOL}
#13812	2×10^{19} m^{-3}	180 kW
#13816	4×10^{19} m^{-3}	200 kW
#13820	6×10^{19} m^{-3}	180 kW
#13821	8×10^{19} m^{-3}	200 kW
#13825	10×10^{19} m^{-3}	220 kW

(a) : Discharge parameters: line-averaged electron density $\overline{n}_e$ and SOL input power P_{SOL}.

Discharge	Γ_{puff}	$\chi_{e,i}$	D_n
#13812	5.05×10^{18} s^{-1}	3 m^{2}s^{-1}	0.25 m^{2}s^{-1}
#13816	6.0×10^{18} s^{-1}	3 m^{2}s^{-1}	0.2 m^{2}s^{-1}
#13820	6.2×10^{18} s^{-1}	3 m^{2}s^{-1}	0.15 m^{2}s^{-1}
#13821	12.8×10^{18} s^{-1}	3 m^{2}s^{-1}	0.3 m^{2}s^{-1}
#13825	29×10^{18} s^{-1}	2 m^{2}s^{-1}	0.4^{2}s^{-1}

(b) : SOLPS-ITER input parameters: gas puff rate Γ_{puff}, electron and ion anomalous diffusion coefficients $\chi_{e,i}$, and the anomalous particle diffusion coefficient D_n.

Table 6.1: Parameters of the COMPASS L-mode density scan #13812-#13825.

in the range $\overline{n}_e = (2\text{-}10) \times 10^{19}$ m^{-3}, see table 6.1a. The plasma current was $I_p = 180$ kA and the toroidal magnetic field was $B_t = -1.15$ T at the magnetic axis (forward field). The edge safety factor was $q_{95} = 3.5$ and the ion grad-B drift was directed toward the divertor. The modelled time instance is $t = 1120$ ms, just before the horizontal reciprocating probe enters the velocity shear layer. At this time, the power crossing the separatrix according to experimental power balance varied between 180-220 kW, see table 6.1a.

Available diagnostics. The diagnostics coverage included the Thomson scattering diagnostic, the combined divertor probe array, the swept divertor array, and the horizontal reciprocating probe.

Simulation details. Figure 6.1a shows separatrix outlines of the modelled discharges calculated by the standard CDB equilibrium reconstruction at $t = 1120$ ms. The reconstruction of discharge #13816 was used to construct the SOLPS-ITER computational mesh, common for the entire density scan (figure 6.1b). The anomalous diffusion coefficients are listed in table 6.1b. Spatially constant particle and thermal diffusion coefficients were chosen in all cases for the sake of simplicity, although the precise n_e profile shape was not reproduced in the confined plasma of higher density discharges. The trend in D_n is investigated in section 6.5. The input power P_{SOL}, listed in table 6.1a, was spread evenly between electrons and ions and adjusted within ±20% of experimental values to match the divertor heat load footprints. The plasma density was controlled by deuterium puffing at the outer midplane at rates shown in table 6.1b, mirroring the LFS gas puff valve used in experiment. The entire first wall except for divertor targets was set up as a pumping surface with recycling coefficient $R = 0.99$. More on the particle balance is given in

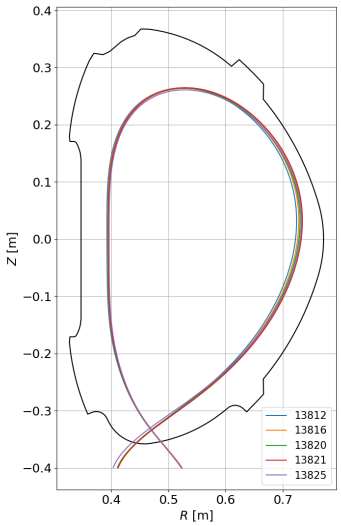

(a) : Separatrix outlines of the standard CDB reconstructions at $t = 1120$ ms.

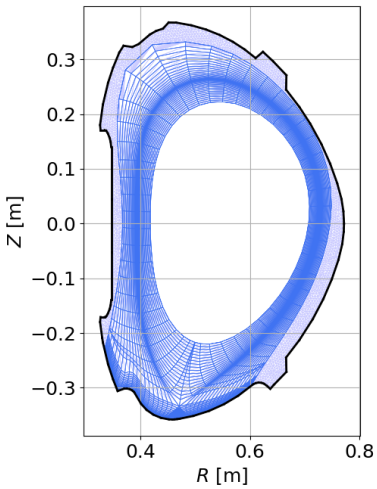

(b) : B2.5 (dark) and EIRENE (light) meshes based on discharge #13816 standard CDB reconstruction, common for all simulations of the density scan.

Figure 6.1: SOLPS-ITER mesh information of the COMPASS L-mode density scan #13812-#13825.

section 6.3. Heat flux limiters were set to $\alpha_e = \alpha_i = 0.3$. The main ion species was deuterium and additional carbon impurities were sputtered physically and chemically from the targets (chemical sputtering yield $\gamma_{chem} = 0.01$). The simulations were run at time step $\mathrm{d}t = 10^{-4}$ s until converged, except for the highest density where a smoothing run at $\mathrm{d}t = 10^{-5}$ s was performed. To avoid numerical instabilities, stemming from large acceleration forces on low-density impurity ion species and consequent high viscous heating and supra-luminal velocities, the minimum ion density was raised to 10^8 m^{-3}. Drifts were turned off. The SOLPS-ITER version was `3.0.9-27-g614fb016`.

Upstream. The upstream electron temperatures T_e and densities n_e are in reasonable agreement for all densities. SOL T_e fall-off length measured by HRCP is shorter than in SOLPS simulations, similarly to the outer target. If necessary, the match could be improved by reducing the anomalous thermal conductivities $\chi_{e,i}$ in the SOL. At low densities, it is difficult to align HRCP data both with T_e and n_e, as with a single profile shift, SOLPS overestimates T_e and underestimates n_e. The cause is not know. In discharge #13821, the HRCP T_e profile visibly bends inside the separatrix as the probe cools the plasma around it. This part of the data was taken with a grain of salt. SOLPS-ITER does not reproduce the plasma potential Φ profile in the confined plasma, presumably due to the lack of drifts and realistic confined plasma currents, but it does reproduce a velocity shear layer (VSL) in moderate and high densities. This was discussed in section 4.3.

Target. At low and moderate densities, the target measurements agree with SOLPS simulations within a factor of two, which is considered a success.

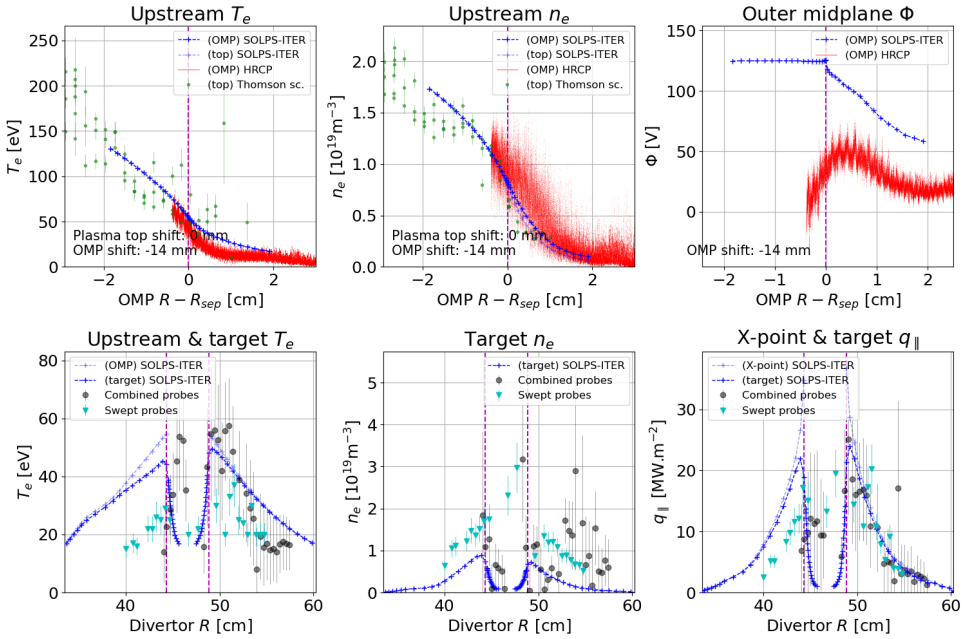

(a) : Discharge #13812, line-averaged density $\overline{n}_e = 2 \times 10^{19}$ m^{-3}.

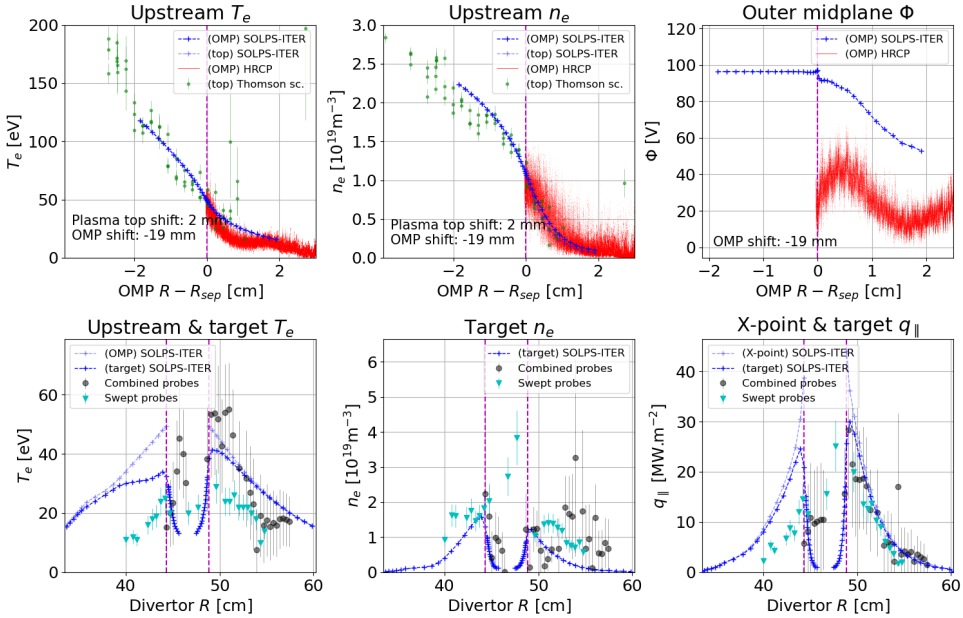

(b) : Discharge #13816, line-averaged density $\overline{n}_e = 4 \times 10^{19}$ m^{-3}.

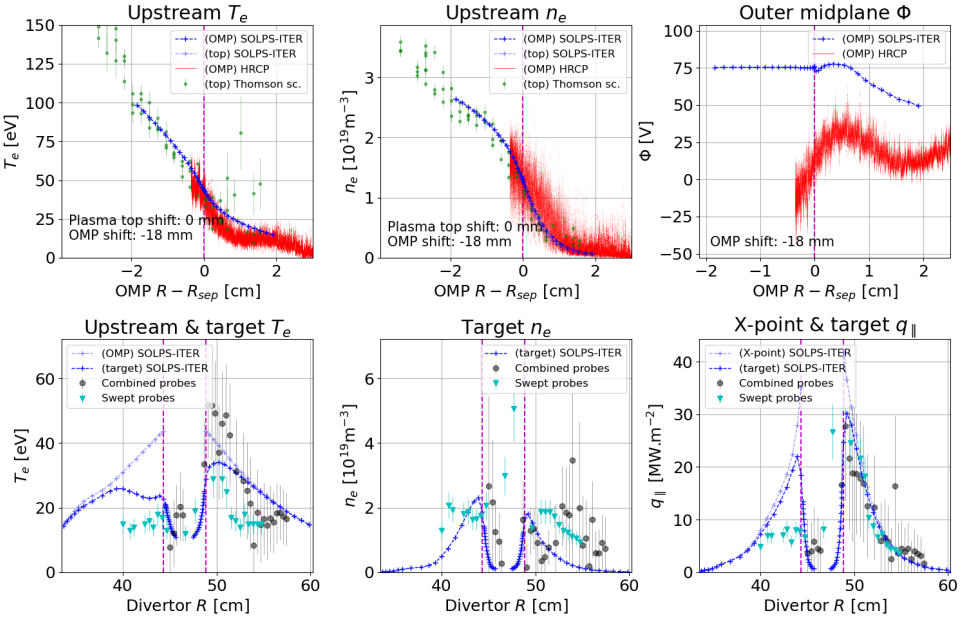

(c) : Discharge #13820, line-averaged density $\overline{n}_e = 6 \times 10^{19}$ m^{-3}.

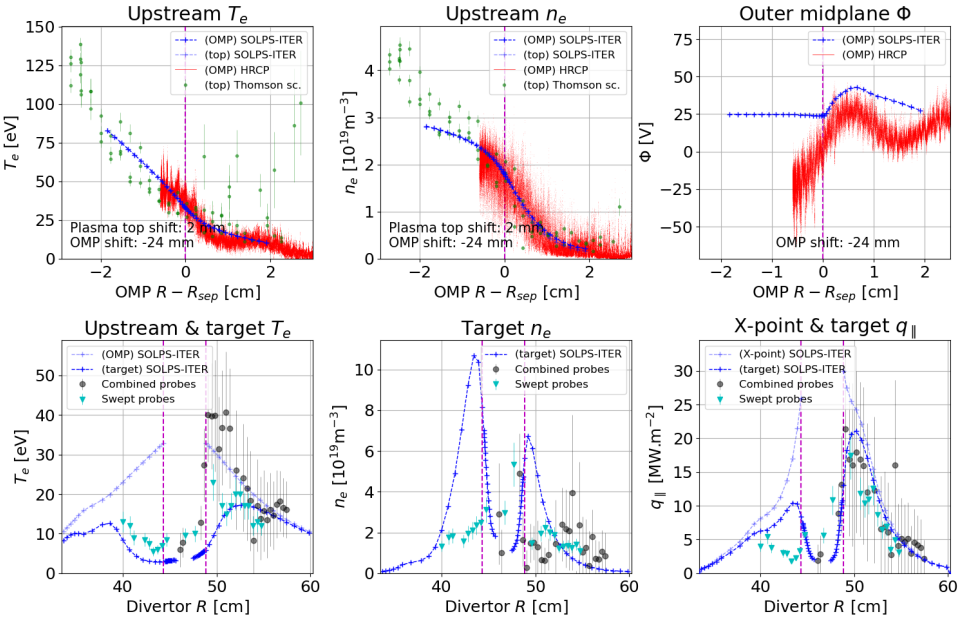

(d) : Discharge #13821, line-averaged density $\overline{n}_e = 8 \times 10^{19}$ m^{-3}.

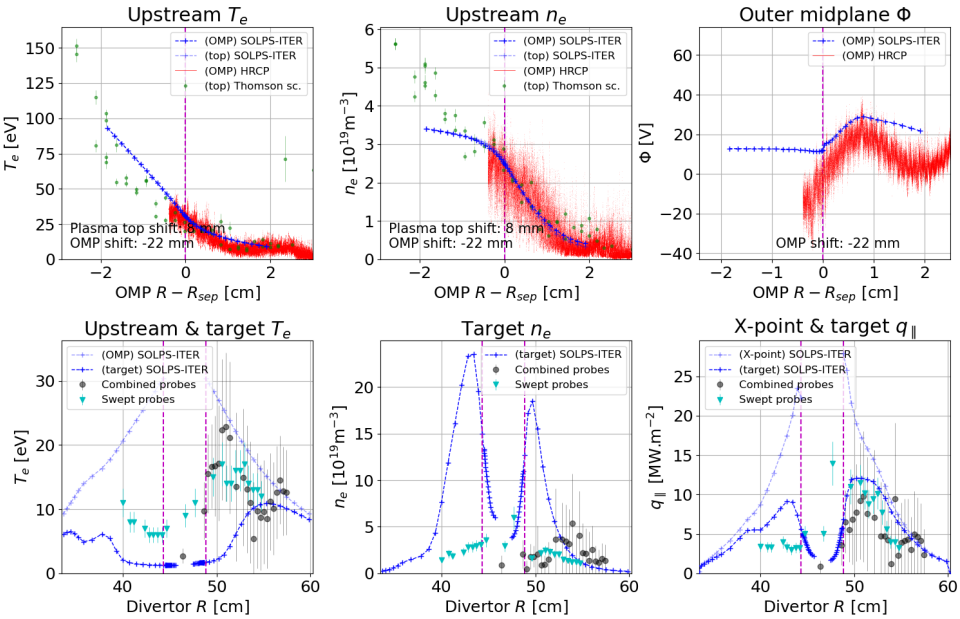

(e) : Discharge #13825, line-averaged density $\overline{n}_e = 10 \times 10^{19}$ m^{-3}.

Figure 6.2: Comparison of COMPASS L-mode density scan discharges #13812-#13825, $t = 1120$ ms, to their interpretative SOLPS-ITER simulations. The Thomson scattering data was mapped to the outer midplane (OMP) and shifted by $R_{shift,TS} = 0$-8 mm outward to correct for equilibrium reconstruction inaccuracy. The horizontal reciprocating probe data was shifted by $R_{shift,HRCP} = 14$-22 mm inward.

However, at the two highest densities, the SOLPS simulation transitions into the conduction limited regime with outer target $T_e < 10$ eV in the 3rd SOL flux tube, and the inner target begins to partially detach. See section 6.4 for details. This is nothing like what is observed in experiment, where peak outer target T_e remains above 20 eV. In the same breath as underestimating target T_e, SOLPS overestimates the target n_e by up to an order of magnitude. Interestingly, target energy flux density profiles are matched well at all densities, and their broadening is quantitatively captured in the simulation. Attempts to redress the discrepancy at high densities will be discussed in section 6.2. For now, suffice it to say that the most probable culprit is that the effect of drifts cannot be neglected in high-density COMPASS plasmas.

Transport regime. The SOLPS-ITER simulations of the density scan show a transition from the sheath-limited regime ($T_{e,u} \approx T_{e,t}$) at both targets to partial detachment ($p_t/p_u < 0.5$ in the 3rd SOL flux tube) at both targets. A full analysis of the SOL transport regime using two-point model formatting is carried out in section 6.4.

Comments. Interpretative simulations of the COMPASS L-mode density scan #13812-#13825 have revealed problems with simulating high-density COMPASS discharges. As plasma density rises, the simulated SOL gradually becomes conduction-limited and then partially detaches, while the experimen-

tal SOL remains firmly attached. Outer target measurements may indicate a transition toward conduction-limited regime at the highest density, as T_e and $q_{\parallel}$ profiles widen and their peak moves away from the strike point to the SOL. Assuming that the process of experiment-model matching determined the upstream separatrix location with good accuracy, at the highest density, experimental $T_{e,sep} = 30$ eV while outer strike point $T_e = 15$ eV. Under the same assumption, however, outer strike point T_e exceeds the separatrix $T_{e,sep}$ at lower densities. It is questionable if the upstream separatrix position is actually this accurate. It seems unlikely that electron temperature would rise from upstream (energy source region) to target (energy sink region), even with the effect of drifts.

6.2 Fixing the high density cases of the COMPASS density scan

The research question of this thesis is how well SOLPS-ITER can model edge plasmas in the COMPASS tokamak. The idea behind modelling a real density scan was to benchmark SOLPS-ITER against experiment at the full extent of COMPASS L-mode operational space, excepting experiments such as impurity seeding. The fact, then, that SOLPS simulations detach at high upstream densities, while experimental plasmas remain attached and only marginally conduction-limited at the outer target, is a pressing issue. In this section, we shall list the methods which were attempted to improve the experiment-model match. They are: adjusting heat flux limiters, implementing diffusion coefficient profiles, changing the ratio of electron and ion input power P_{SOL} based on results of the METIS core transport code, implementing realistic particle sources and sinks, increasing particle diffusion coefficient D_n in the divertor volume, and increasing it throughout the SOL.

Adjusting heat flux limiters. Chapter 5 concluded that heat flux limiters α_a can control the parallel gradient of temperature T_a. The original simulations had $\alpha_e = 0.3$, and increasing the electron heat flux limiter should have decreased the T_e drop between upstream and target. Simulations with $\alpha_e = +\infty$ (classical electron heat conduction) were performed, with the effects that target T_e did rise, but only by a few percent. Heat flux limiter $\alpha_e = 0.3$ is in the zone where the H-mode simulation #16908 was not particularly sensitive to the specific value of α_e. It appears that electron heat flux limiting is not the cause of the large T_e gradients found in the high-density simulations of the COMPASS density scan.

Implementing a diffusion coefficients profile. In section 6.1, diffusion coefficients in the two high-density simulations were chosen spatially constant, so as to reproduce upstream n_e and T_e profiles in the SOL but sacrifice the confined plasma profile if needed. Although the separatrix and SOL values could be matched well with this approach (within experimental uncertainties), perhaps precisely tailoring the D_n and $\chi_{e,i}$ profiles would have alleviated the unwanted detachment. A considerable amount of time was spent iterating

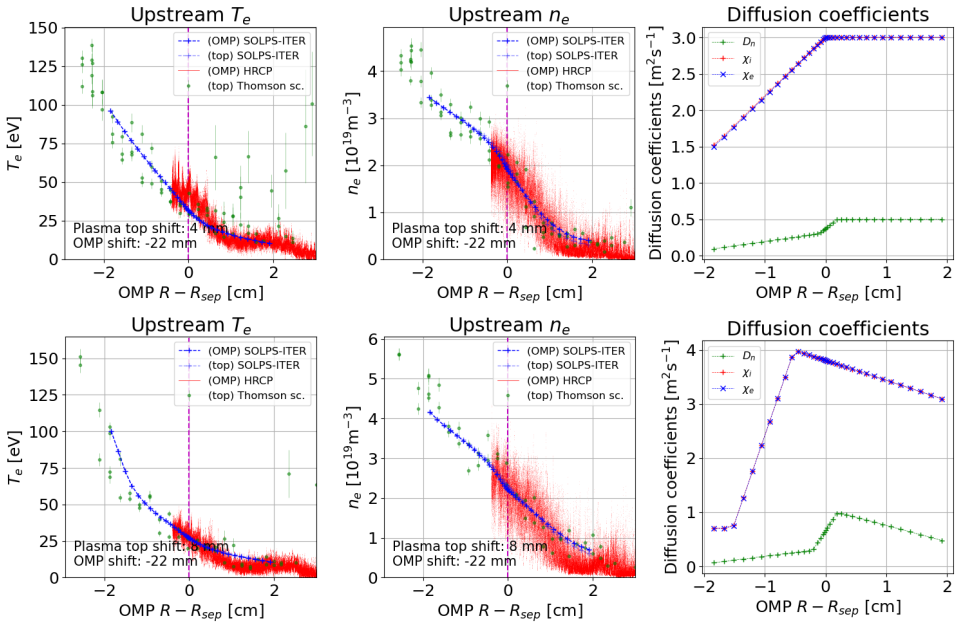

Figure 6.3: Upstream profiles in SOLPS simulations and experimental measurements in discharges #13821 (top) and #13825 (bottom): electron temperature T_e, electron density n_e, and particle diffusion coefficient D_n and thermal diffusion coefficients χ_i and χ_e.

through D_n and $\chi_{e,i}$ profiles for the two high-density discharges, and a more precise agreement was finally reached. Figure 6.3 shows the resulting upstream profiles and profiles of diffusion coefficient. (It should be noted that these simulations were performed with a fixed main ion density at the core boundary $n_{i,core}$, not with puffing and pumping. However, as we shall shortly see, this very likely does not make a difference.) Despite the better upstream match, the target quantities did not significantly change. In the end, manual profile tailoring was abandoned as an exercise in overfitting.

Changing the ratio of electron and ion input power. The input power P_{SOL}, calculated by experimental power balance, is usually split evenly between ions and electrons in interpretative modelling. [237, 238] The commonly cited reason is that no data is available about the actual power split. To get an approximation of $P_{SOL,e} : P_{SOL,i}$, the 1D core transport code METIS [143] was run by Fabien Jaulmes for all five discharges in the COMPASS density scan #13812-#13825. The profiles of T_e and n_e were fixed in this run, using a smoothed profile of Thomson scattering diagnostic measurements where the separatrix position was chosen the same as in SOLPS-ITER modelling. Among other outputs, the code produced the electron and ion power crossing the separatrix; $P_{SOL,e} = 245$ kW and $P_{SOL,i} = 12$ kW for the moderate-density discharge #13820. Electrons dominated P_{SOL} because ohmic heating is presumed to heat only electrons, while ions are heated by equipartition with electrons. This notably means that T_i can only rise as high as T_e. The input powers $P_{SOL,e} = 170$ kW and $P_{SOL,i} = 12$ kW, lowered to better match the experimental target energy fluxes, were tested in a deuterium-

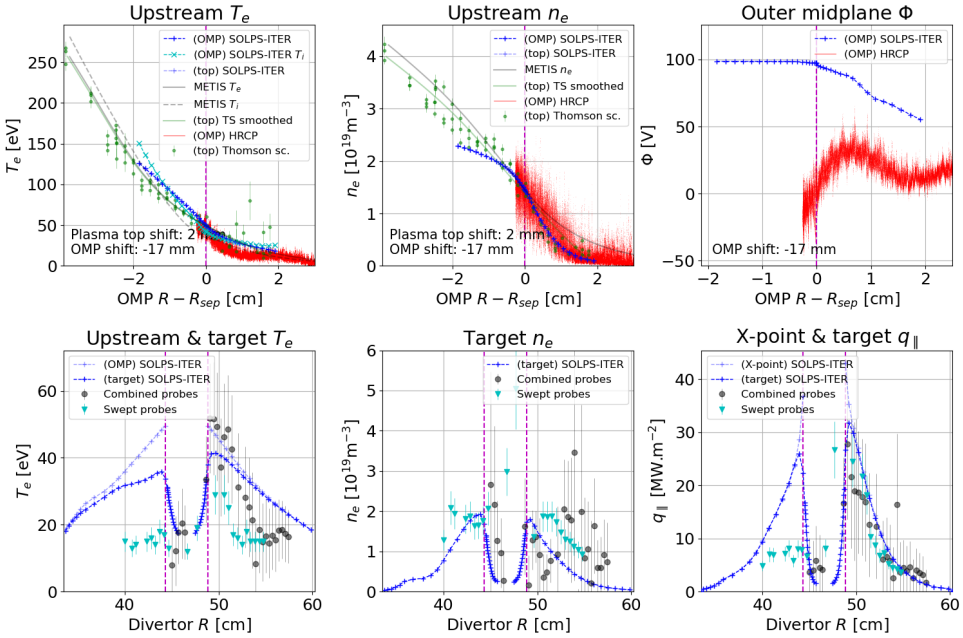

Figure 6.4: A variant of the the interpretative SOLPS-ITER simulation of the moderate-density discharge #13820, using $P_{SOL,e} = 170$ kW and $P_{SOL,i} = 12$ kW as given by the METIS code.

only simulation of discharge #13820. The results are shown in figure 6.4. The additional T_i and $P_{SOL,i}$ data allowed the independent determination of anomalous thermal diffusion coefficients: $\chi_e = 4$ m^{2}s^{-1} and $\chi_i = 0.05$ m^{2}s^{-1}. The METIS and SOLPS-ITER data converge on $T_i \approx T_e$, where previously SOLPS yielded $T_{i,sep} = 110$ eV. The peak outer target T_e also rose from from 32 eV to 41 eV, which is in the desired direction. Input power split 14:1 in favour of electrons seems a little extreme, given that acceptable results are normally achieved with 1:1. Experimental measurements of T_i would be invaluable for verification, but they were sadly scarce on the COMPASS tokamak. Outer midplane measurements with the retarding field analyser (RFA) in the L-mode discharge #11204 have shown $T_i \approx 40$ eV 3 cm radially outside the separatrix. [239] The ion branch of the ball-pen probe $I - V$ characteristic has been fitted to yield a T_i profile in the L-mode discharge #7029; here $T_i \approx 35$ eV was found throughout the SOL with $T_e \approx T_i$ at the separatrix. [240] The parameters of these discharges are not drastically different from #13820; they are both ohmically heated and with moderate plasma densities. If $T_e \approx T_i$ at the separatrix and $T_e < T_i$ in the SOL can be assumed, then P_{SOL} split in favour of electrons may be more realistic for COMPASS discharges with ohmic heating. This will be investigated in the future, together with more sophisticated interpretative core transport modelling, e.g. with the ASTRA [241, 242] code.

Implementing realistic particle sources and sinks. The degree of detachment may be influenced by the details in particle transport. [5, 14] To capture possible local effects of neutral gas puffing and pumping, we

switched the COMPASS density scan simulations from simple boundary conditions for the deuterium ion continuity equation (fixed density $n_{i,core}$ at the innermost flux surface, fully recycling $R = 1$ walls) to a more realistic setup reflecting experimental puffing and pumping. Details are given in section 6.3. Here it is sufficient to say that the switch had little impact on the simulations. The upstream and target profiles did not change, and there was no adjustment needed for the anomalous diffusion coefficients nor for the upstream separatrix position. The simple boundary equations may be quite adequate for interpretative simulations of the COMPASS tokamak. However, controlling the simulation plasma density with gas puff rate and not with $n_{i,core}$ can still be preferable. Not only does it allow for density control with a feedback scheme on the gas puff rate, similar to experimental conditions; it also opens the door toward quantitative investigations of the particle balance, such as determining the recycling coefficient of the first wall. [185] Thoroughly investigating this route is, furthermore, valuable experience for predictive modelling of the COMPASS Upgrade tokamak, where design of the vacuum and gas puffing systems benefit from SOLPS-ITER simulations which are quantitatively as accurate as possible. In consequence, realistic particle sources and sinks were implemented in the "flagship" simulations of the COMPASS density scan, even though they slow down convergence by an order of magnitude and do not improve the experiment-simulation match.

Increasing the particle diffusion coefficient D_n in the divertor volume. Radial particle transport can be enhanced in the divertor volume due to strong flux expansion around the X-point (flux tube widens, allowing for more interactions over the mean free path) and higher densities (increased local collisionality). [238, 243] Enhancing D_n in the divertor volume has been found necessary in detachment modelling of ASDEX Upgrade. [244] We have, therefore, performed a scan in the divertor D_n enhancement factor from $\times 2$ to $\times 16$ in interpretative simulations of COMPASS discharges #13820, #13821 and #13825 (moderate to high densities), implemented in SOLPS-ITER using the switches `b2tqna_pfr_rescale` and `b2tqna_divsol_rescale` while the OMP separatrix density $n_{e,sep}$ was kept constant using a feedback scheme controlling the gas puff rate. The result was the broadening of target n_e profiles, while other quantities, both upstream and target, remained approximately constant. The broadening was accompanied by a decrease in peak $n_{e,t}$ values, as the particles arriving at the divertor from upstream were distributed over a larger area. The effect was stronger at higher densities and with higher D_n enhancement factor; the peak $n_{e,t}$ was reduced by up to a factor of two at the outer target. However, neither the degree of detachment nor the parallel T_e drop changed. While increasing radial diffusion in the divertor volume did not alleviate the unwanted detachment, it is an interesting way to control the target n_e profile without impacting other plasma parameters.

Increasing particle diffusion coefficient D_n in the entire SOL. At high plasma densities, parallel resistivity of the SOL plasma increases, slowing the parallel depletion of turbulent structures and tilting the balance of parallel to radial transport in favour of radial transport. [245, Sec. 5] The

result can be significant broadening of the SOL n_e profile, so-called shoulder formation. [55, 133] In the COMPASS density scan, D_n necessary to match experimental SOL profiles was indeed found to rise from moderate to high density discharges (see table 6.1b). We have, therefore, performed simulations of COMPASS discharges #13820, #13821 and #13825 (moderate to high densities) where the D_n radial profile followed a step-wise function, doubling in the SOL, and the OMP separatrix density $n_{e,sep}$ was fixed using a feedback scheme on the gas puff rate. The result was that n_e profile broadened in the upstream SOL and the conduction-limited regime/detachment deepened. Unlike in the previous case of increasing D_n only in the divertor volume, where the upstream source of particles remained fixed and the available deuterium ions were distributed over a larger area, increasing D_n in the upstream SOL increased the radial particle flux over the separatrix and raised n_e across the entire SOL, leading to deeper detachment. We do note, however, that despite this unwanted effect, the match of experimental to modelled profiles was improved by raising SOL D_n. Manually tailoring the D_n and $\chi_{e,i}$ profiles (figure 6.3) also confirmed heightened anomalous diffusion in the SOL. It appears that when very close experiment-simulation agreement is sought in high-density COMPASS discharges, raising SOL D_n is desirable.

In conclusion, most of the paths toward decreasing the unwanted detachment in the high-density interpretative simulations had little impact. Only changing the input power P_{SOL} split in favour of electrons had the desired effect of increasing target T_e. The additional data from the METIS core transport code also allowed decoupling electron and ion anomalous thermal diffusion coefficients χ_e and χ_i. What little experimental data we have suggests that $T_{i,sep}$ may be close to $T_{e,sep}$ in ohmically heated COMPASS plasmas of moderate densities. Such a result cannot be achieved by an equal P_{SOL} split, which in my experience always leads to $T_{i,sep}$ 2-3x higher than $T_{e,sep}$. This indicates that adjusting $P_{SOL,e} : P_{SOL,i}$ may be a viable option for COMPASS L-mode ohmic plasmas.

Despite this interesting finding, all of the simulations in this thesis were performed for $P_{SOL,e} : P_{SOL,i} = 1 : 1$. The reason is that METIS results were tested rather late in the writing of this thesis, so there has only been time to make a prototype simulation. Decoupling radial electron and ion transport also introduces two additional free parameters, the actual input power split and ion thermal diffusivity χ_i. Exploring uneven P_{SOL} splits, as well as core-edge transport code coupling in general, is a promising topic for future research.

Excepting uneven input power split, what can be done to improve the experiment-model match in the high-density cases of the COMPASS density scan? The obvious avenue, which I have avoided approaching, is switching on drifts in the simulations. In SOLPS-ITER, this essentially amounts to adding several terms to the Braginskii equations, corresponding to diamagnetic, grad-B and $\mathbf{E} \times \mathbf{B}$ drifts and currents driven by parallel viscosity. [174] An unfortunate side-effect is that this renders the plasma solution calculation extremely unstable. Switching on drifts requires a drastic time step reduction

(for COMPASS, from 10^{-4} s to 10^{-7} s), careful tailoring of the diffusion coefficient profiles, and minute adjustments of simulation parameters such as plasma resistivity and viscosity. [182, 125] Consequently, drift implementation in a new tokamak is a PhD topic in its own, and I have not attempted it.

Still, it is known that field reversal in the COMPASS tokamak has significant impact on the divertor conditions. [191, 192, 2, 246] Preliminary SOLPS-ITER calculations, performed by Jan Hecko as part of his PhD, show significant alterations in the target T_e and n_e profile shape. [193] The drift-related SOL currents give rise to a complicated structure of electric field $\mathbf{E}$, which causes particle flux redistribution via the $\mathbf{E} \times \mathbf{B}$ drift. [189] The resulting concentration of particles in some locations along the divertor targets causes local n_e increase and T_e decrease, and vice versa elsewhere. [238] The $\mathbf{E} \times \mathbf{B}$ drift direction changes upon field reversal, which is why the shape of n_e and T_e profiles changes. This target n_e-T_e trade-off may be the missing ingredient from the SOLPS-ITER simulations presented in this thesis. Future simulations will show whether this hypothesis is correct.

6.3 Particle balance

Simulations of the COMPASS density scan #13812-#13825 have a distinguishing feature from the simulations presented in chapters 4 and 5: realistic particle sources and sinks, implemented through neutral deuterium gas puffing and pumping, and a rigorous check of particle balance. As the satisfaction of particle balance is an important convergence criterion for SOLPS-ITER simulations [1], this is an important step toward sophisticated transport simulations of the COMPASS and COMPASS Upgrade edge plasmas.

The modelled puffing and pumping was set up to reflect experimental conditions. The puffing location was at the outer midplane, mirroring the location of the COMPASS LFS piezovalve for deuterium puffing. In experiment, the puffing is toroidally localised in a single outer midplane port, where in simulations it is necessarily distributed uniformly along the toroidal angle. In experiment, high vacuum was provided by turbomolecular pumps, which did not have sufficient pumping speed to impact the plasma during its ~ 100 ms of existence. Inbetween discharges, gas pressure inside the chamber falls with the time constant of approximately 1 s. Despite this, sustaining moderate and high line-averaged densities in experiment required deuterium puff, controlled by a real-time feedback mechanism. Evidently, a more powerful "vacuum pump" was at play, which the gas puff had to compensate for. This was the first wall. After each COMPASS discharge, a glow discharge in helium was performed to clean the first wall of impurities. This also removed D_2 adsorbed before, during and after the discharge. Consequently, the chamber did not reach saturation with neutral gas and acted as a vacuum pump with a large surface and near to the plasma.

To note some additional features of COMPASS wall conditioning, the glow discharge also introduced a significant source of helium impurity, whose concentration could reach 15 %. Helium was not included in our SOLPS-ITER

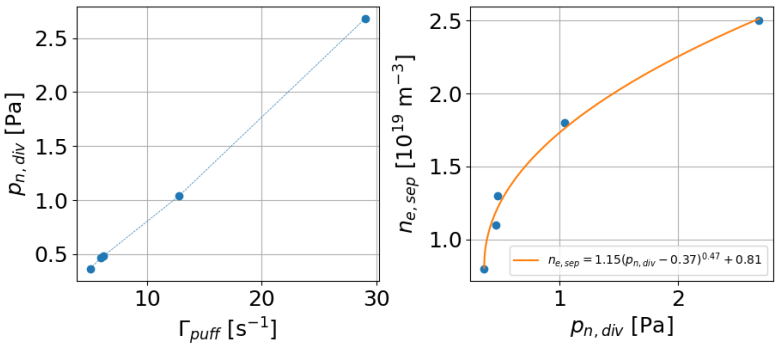

Figure 6.5: Deuterium fuelling in the COMPASS density scan: (left) linear scaling of divertor neutral pressure $p_{n,div}$ with the gas puff rate Γ_{puff}, (right) square root scaling of outer midplane separatrix electron density $n_{e,sep}$ with the divertor neutral pressure $p_{n,div}$. The divertor neutral pressure $p_{n,div}$ was volume-averaged over the entire PFR.

simulations for the sake of simplicity and run time. The same applies to boron, an intrinsic impurity supplied by regular chamber boronisation. The density scan #13812-#13825 was carried out 21 days after the previous boronisation. This is enough time to settle back into normal first wall operation after the transient enhancement of main chamber pumping immediately after boronisation.

A quantitative calibration of the gas puff rate and the first wall recycling coefficient R was not performed. The recycling coefficient was set to $R = 0.99$ (of 100 particles reaching the solid surface, 99 are recycled and 1 is absorbed) everywhere except for the divertor targets. This value is in the range commonly used for tokamak interpretative modelling. [185, 247] The modelled gas puff rate (table 6.1b) was then chosen in order to match experimental plasma density. The reason is, on one hand, that absolute calibrations of the COMPASS LFS gas puff piezovalve are not readily available. On the other hand, the desired divertor neutral pressures and upstream densities can be reached at multiple values of deuterium throughput. Given a constant pump recycling coefficient R, the divertor neutral pressure $p_{n,div}$ should scale linearly with the gas puff rate Γ_{puff} and the outer midplane separatrix density should scale approximately as $n_{e,sep} = p_{n,div}^{0.5}$. [5, 247, 248] This behaviour is reproduced in our simulations of the COMPASS density scan, as shown in figure 6.5. Changing the first wall recycling coefficient R would simply change Γ_{puff} needed to reach a certain $p_{n,div}$, but it should not qualitatively impact the plasma parameters, nor the relationship of $p_{n,div}$ and $n_{e,sep}$.

In the initial stage of the COMPASS density scan simulations, appropriate gas puff rates Γ_{puff} were found using feedback on the outer midplane separatrix density $n_{e,sep}$. The solutions with feedback, however, were unstable and prone to sustained oscillations in the plasma density. The time scale of these oscillations depended on the particle transport times inside the simulation region and on the feedback time scale settings. Their magnitude was more pronounced at lower plasma densities, to the point one could hardly speak

of a converged solution. For example, in the low-density discharge #13812, Γ_{puff} oscillated between 4.3 - 7×10^{18} s^{-1} while $n_{e,sep}$ varied between 7.8 - 8.2×10^{18} m^{-3}. The $\Gamma_{puff} - n_{e,sep}$ phase shift indicated a causal relationship; the most gas was puffed at the times when $n_{e,sep}$ was falling the fastest, and vice versa. To suppress these oscillations and arrive at converged plasma solutions, Γ_{puff} was fixed at a constant value within the oscillation range needed to maintain the desired $n_{e,sep}$. These are the gas puff rates listed in table 6.1b.

Interestingly, similar oscillations have been reported previously. A recent work attributes them to resonant particle exchange between neighbouring flux tubes above the target, caused by rhythmic transitions between two stable solutions in the phase space. [249] In our case, the oscillations were caused by an external particle source rather than an internal particle exchange, but we *have* observed bifurcations in stable plasma solutions. During our first tests of density control with gas puff, which were performed in the moderate-density discharge #13820, a range of static Γ_{puff} resulted in one of two plasma solutions: a low-density one where $n_{e,sep} = 2.5 \times 10^{18}$ m^{-3}, or a high-density one where $n_{e,sep} = 4 \times 10^{19}$ m^{-3}. The critical Γ_{puff} seemed to be around 4.4×10^{19} m^{-3}; lower gas puff rate would result in the low-density solution, higher gas puff rate in the high-density solutions.[3] These two states correspond to phase space attractors, and transiting between their spheres of influence may have caused the sustained feedback oscillations. Ultimately, it was found that less volatile feedback solutions can be reached by starting from a high-density state and lowering $n_{e,sep}$ step-wise. Even these solutions, however, were susceptible to renewed oscillations when their input parameters were changed, for example when the particle diffusion coefficient was lowered. This suggests a complicated phase space of plasma solutions. This is uncommon for SOLPS-ITER simulations of the COMPASS tokamak, which are typically fast, robust and will converge to a common solution from a number of starting states. Implementing realistic particle sources and sinks may not impact the global characteristic of a COMPASS plasma solution, but it definitely impacts its finer aspects, perhaps minute details in density distribution in the target area.

In a simulation with a realistic setup of particle sources and sinks, it is possible to gauge the level of convergence with regard to *particle balance*. Generally, particle balance is satisfied when the number of particles entering/leaving the simulation region per second $\Gamma_{\text{enter/leave}}$ is equal to the temporal change of particle content in the simulation region $\mathrm{d}N/\mathrm{d}t$. This is essentially the continuity equation without any sources on the right-hand side. In a transport simulation, particle balance is typically not completely satisfied and some particles go missing or are created from nothing, for example due to grid discretisation errors. For a simulation to be considered converged, the level of this error must remain small compared to particle fluxes which fuel the edge

[3] The magnitude of this gas puff rate is not comparable to those listed in table 6.1b, as by this point correct sources and sinks of particles were not implemented yet. The large gas puff compensated for missing flux of ions from the core.

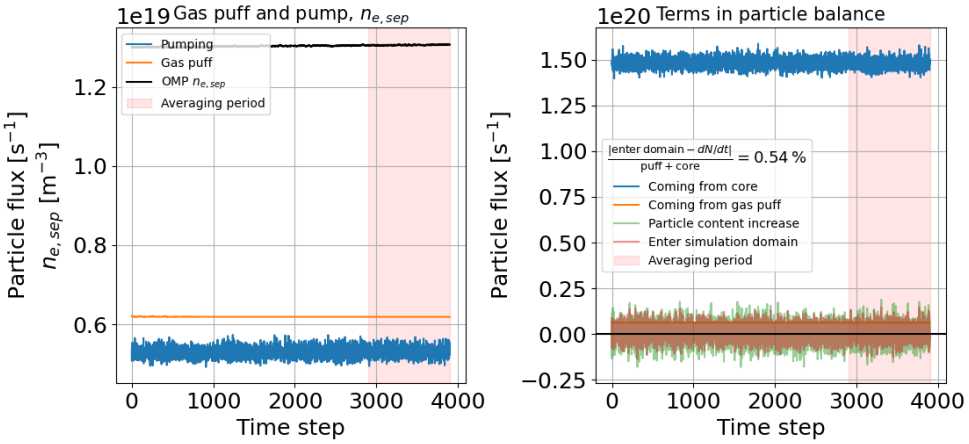

Figure 6.6: Particle balance assessment for an interpretative SOLPS-ITER simulation of the COMPASS discharge #13820.

plasma: the ion influx from the core region Γ_{core} and the gas puff rate Γ_{puff}. We posit that particle balance is satisfied if main ion (deuterium) fluxes Γ [s^{-1}] satisfy

$$\frac{\left|\Gamma_{\text{enter/leave}} - \frac{\mathrm{d}N}{\mathrm{d}t}\right|}{\Gamma_{\text{core}} + \Gamma_{\text{puff}}} < 1\%. \tag{6.1}$$

This criterion was met for all simulations in the COMPASS density scan, except for the highest density where the particle balance was only satisfied at 1.5 % for the time step $\mathrm{d}t = 10^{-4}$ s. A smoothing run at $\mathrm{d}t = 10^{-5}$ s lowered this number to 0.8 %.

Figure 6.6 shows the particle fluxes appearing in the particle balance assessment of the moderate-density discharge #13820, as taken from the tracing file `blnn_SPb.trc`. On the left, the gas puff rate Γ_{puff} (`ntr_puff_D`) is compared to the pumping rate Γ_{pump} (`ntr_wall_pmp_D`), and the time evolution of the outer midplane separatrix density $n_{e,sep}$ is shown. On the right, the figure compares the particle fluxes listed above: $\Gamma_{\text{enter/leave}}$ (`flux_tot_D`), $\mathrm{d}N/\mathrm{d}t$ (`ion_dn/dt_D`), Γ_{core} (`ion_core_D`), and again Γ_{puff}. It was found that $\Gamma_{\text{enter/leave}} \approx \Gamma_{\text{puff}} - \Gamma_{\text{pump}}$. This makes sense, given that these are the two principal ways that particles can enter or leave the simulation domain.[4] In all simulations of the density scan, the gas puff rate was higher than the pumping rate. The error in our particle balance is, therefore, an overall loss of deuterium particles. Where and why these deuterons go missing was not investigated; the important thing is that their number is not significant compared to deuterium fluxes fuelling the edge plasma.

[4] Using the B2.5 switch `eirene_ionising_core=1`, no particles are exchanged with the core region. All neutrals which enter the core are returned as ions. This is similar to main wall and divertor target recycling, where the number of particles is preserved to a good accuracy, even though recycling particle fluxes are 2 orders of magnitude higher than fuelling particle fluxes.

6.4 SOL transport regime

SOL transport regimes are useful broad terms characterising overall SOL conditions. [12, Ch. 4] Their basic characteristic were outlined in section 1.1. The *sheath-limited regime*, also called the simple SOL, is a regime with high overall electron temperature, small parallel temperature gradients ($T_{e,u}/T_{e,t} < 1.5$) and small power and pressure losses from the plasma to neutrals and radiation. The *conduction-limited regime*, also called the high-recycling regime, is a regime with substantial T_e parallel gradients ($T_{e,u}/T_{e,t} > 3$) but small pressure losses ($p_t/p_u \approx 1$). *Divertor detachment* can be defined in multiple ways, but generally it is a regime where target T_e falls so low that the divertor plasma becomes dominated by neutrals, which absorb a majority of plasma energy and momentum ($p_t/p_u \ll 1$). This neutral "pillow" above the divertor target shields it from large energy fluxes and erosion. This is the regime desirable for tokamak fusion reactor operation.

The labels of SOL transport regimes invoke many interconnected properties of the edge plasma. For example, hearing that a SOL is sheath-limited, a transport modeller can immediately make several educated guesses. The peak target T_e is probably a good proxy for the upstream $T_{e,sep}$, which can be used to estimate the upstream separatrix position (chapter 4). Electron parallel heat transport is probably regulated by the sheath, so electron heat flux limiting won't affect the edge plasma very much (chapter 5). Power radiated in the SOL is probably low, particle fluxes on the target aren't very high, but individual ions have high energy due to the large sheath potential drop and may cause significant sputtering over time. The list goes on; all on the basis that the SOL is "sheath-limited". In this section, we shall qualify SOL transport regimes in the COMPASS density scan #13812-#13825 and discuss how simulation results differ from experimental. The aim is to gauge the typical SOL transport regime of the COMPASS tokamak.

While performing the SOL transport regime analysis, we have adopted two-point model formatting (2PMF), an extension of the two-point model specifically adapted to help interpret edge transport simulations. [250, 251, 252, 11] 2PMF relates upstream (u) and target (t) plasma parameters in a single magnetic flux tube with three analytic expressions:

$$T_{e,t} = \left[\frac{8m_i}{e\gamma^2}\cdot\frac{q_{\parallel u}^2}{p_u^2}\right]\left[\frac{(1-f_{pow})^2}{(1-f_{mom})^2}\right]\left[\frac{1+\frac{\tau_t}{z_t}}{2}\cdot\frac{(1+M_t^2)^2}{4M_t^2}\cdot\frac{R_u^2}{R_t^2}\right] \tag{6.2}$$

$$n_{e,t} = \left[\frac{\gamma^2}{32m_i}\cdot\frac{p_u^3}{q_{\parallel u}^2}\right]\left[\frac{(1-f_{mom})^3}{(1-f_{pow})^2}\right]\left[\frac{4}{\left(1+\frac{\tau_t}{z_t}\right)^2}\cdot\frac{8M_t^2}{(1+M_t^2)^3}\cdot\frac{R_t^2}{R_u^2}\right] \tag{6.3}$$

$$\Gamma_{\parallel e,t} = \left[\frac{\gamma}{8m_i}\cdot\frac{p_u^2}{q_{\parallel u}}\right]\left[\frac{(1-f_{mom})^2}{1-f_{pow}}\right]\left[\frac{2}{1+\frac{\tau_t}{z_t}}\cdot\frac{4M_t^2}{(1+M_t^2)^2}\cdot\frac{R_t}{R_u}\right] \tag{6.4}$$

Its variables are:

The subscript a refers to electrons, ions or individual ion species according to context.

Target electron temperature $T_{e,t}$ [eV]
Target electron density $n_{e,t}$ [m^{-3}]
Target parallel electron flux density $\Gamma_{\parallel e,t}$ [$\mathrm{s}^{-1}\mathrm{m}^{-2}$]
Effective ion mass $m_i = \frac{\sum_a n_a m_a}{\sum_a n_a}$ [kg]
Electron charge $e = 1.602 \times 10^{-19}$ C
Sheath heat transmission coefficient $\gamma = \frac{q_{\parallel t}}{n_{e,t} T_{e,t} c_{s,t}}$ [1]
Upstream and target parallel energy flux density

$$q_\parallel = q_{\parallel e+i,cond} + q_{\parallel e+i,conv} + q_{\parallel i,kin} \text{ [W.m}^{-2}\text{]}$$

– conductive, $q_{\parallel a,cond} = -\kappa_a \nabla_\parallel T_a$ (SOLPS-ITER output as a whole)
– convective, $q_{\parallel a,conv} = \frac{3}{2} e n_a T_a u_{\parallel a}$ (SOLPS-ITER output as a whole)
– kinetic, $q_{\parallel i,kin} = \sum_a \frac{1}{2} m_a n_a u_{\parallel a}^3$ (SOLPS-ITER output as a whole)

Target sound speed $c_{s,t} = \sqrt{\frac{\left(1+\frac{\tau_t}{z_t}\right) e T_{e,t}}{m_i}}$ [$\mathrm{m.s}^{-1}$]
Target ion-electron temperature ratio $\tau_t = \frac{T_{i,t}}{T_{e,t}}$[1]
Target effective plasma charge $z_t = \frac{n_{e,t}}{\sum_a n_{a,t}}$ [1]
Upstream and target plasma pressure $p = p_{e+i,stat} + p_{e+i,dyn}$ [Pa]
– static, $p_{e+i,stat} = \sum_a e n_a T_a$
– dynamic, $p_{e+i,dyn} = \sum_a m_a n_a u_{\parallel a}^2$
Power loss factor $1 - f_{pow} = \frac{q_{\parallel t} R_t}{q_{\parallel u} R_u}$ [1]
Momentum loss factor $1 - f_{mom} = \frac{p_t}{p_u}$ [1]
Mach number $M = \frac{u_\parallel}{c_s}$ [1]
Radial position R [m]

Though 2PMF can be used to calculate power and momentum loss factors f_{pow} and f_{mom}, its main application is verification that a modeller understands the output of their edge transport simulation. Adopting it was surprisingly difficult, so the verification process shall be presented as a small tangent from the topic of SOL transport regime.

Full 2PMF analysis is carried out by calculating the right-hand side of equations (6.2)-(6.4) using direct transport simulation output, and comparing the result to the simulated value of the left-hand-side quantity. If the match is close, the modeller can rest assured that their understanding of the code output is good. The remarkable fact that the output of a complicated 2D simulation can be captured by analytic expressions stems from the original derivation of equations (6.2)-(6.4) by V. Kotov and D. Reiter. [16] They are essentially the equations of the 2009 version of the B2 edge transport code, reduced to the frame of the two-point model (analytical relations between plasma parameters at upstream and target locations). The equations were adjusted to make them more comparable to the basic two-point model [12, Sec. 5.2]; for example, some variables were renamed and equation terms were

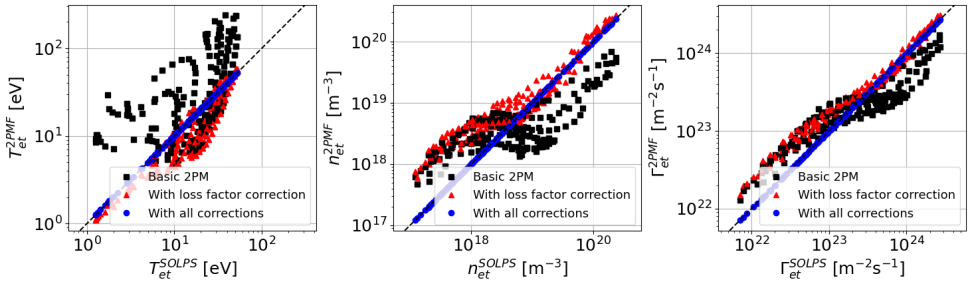

Figure 6.7: Verification of 2PMF, equations (6.2)-(6.4). "Basic 2PM" data points were calculated using the first square bracket group in the equations. "With loss factor corrections" data points used the first and second square bracket group. "With all corrections" are the full equations.

aggregated into groups denoted by square brackets. [252]

The three square bracket groups in equations (6.2)-(6.4) constitute basic two-point model predictions, loss factor corrections, and other corrections. Basic two-point model predictions assume that power and pressure losses are zero, $T_e = T_i$, target Mach number $M_t = 1$, target effective charge $z_t = 1$ and $R_t = R_u$. They are not identical to the basic two-point model of [12, Eq. (5.4)-(5.6)], as they do not presume that parallel energy transport is purely conductive. Performing a calculation based on these two "basic two-point models" (for instance, calculating T_u from $q_\parallel$ and n_u) does not yield the same results. Loss factor corrections, starring the power and momentum loss factors f_{pow} and f_{mom}, take into account that energy and momentum are not preserved along the field line due to volumetric and radial transport losses. "Other" corrections account for realistic values of T_e/T_i, target Mach number, multiple ion species and flux expansion.

When evaluating 2PMF equations for a converged SOLPS-ITER equation, target energy and particle fluxes are evaluated as fluxes into B2.5 "ghost cells", thin virtual cells which serve for boundary equation calculation. Target temperatures, densities and velocities are evaluated inside the ghost cells, not the last real plasma cells. Flux tube radial coordinate R is evaluated at the cell centres.

Figure 6.7 verifies the correct application of 2PMF using the COMPASS density scan #13812-#13825 SOLPS-ITER simulation data, all flux tubes (one point = one SOL flux tube), both the outer and the inner target. It is a reproduction of [252, Fig. 3]. The results of full equations (6.2)-(6.4) (blue dots) match the simulated target electron temperature $T_{e,t}$, electron density $n_{e,t}$ and parallel electron particle flux density $\Gamma_{\parallel e,t}$ to a good accuracy, though not identically. Reproducing this figure yielded valuable insight into SOLPS-ITER quantities, particularly the distinction between ghost cells and last real plasma cells and the components of parallel energy fluxes.

To qualify the COMPASS SOL transport regime, we use a definition of the momentum loss factor f_{mom} identical to 2PMF. In particular, the target pressure p_t is taken from the target ghost cell, not the last plasma cell. However, our definition of the power loss factor f_{pow} shall be different from 2PMF.

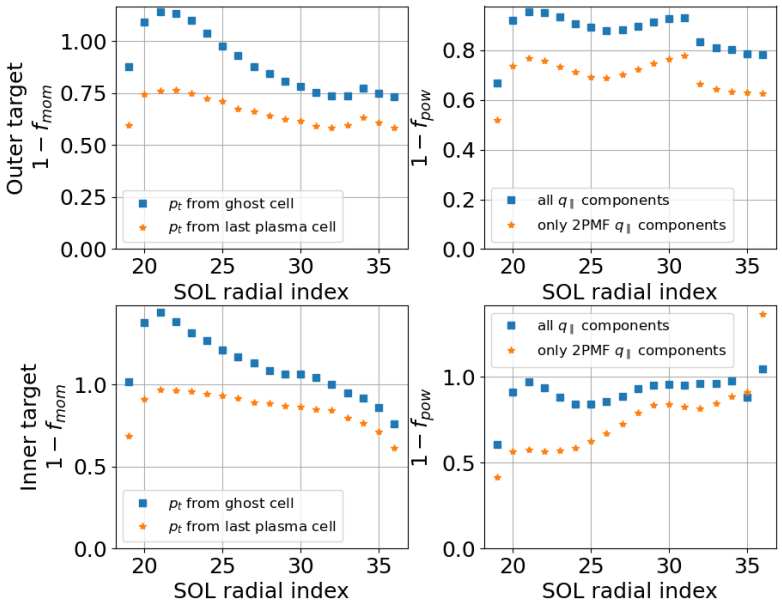

Figure 6.8: Comparison of different calculations of power and momentum loss factors f_{pow} and f_{mom}. Data were taken from the interpretative SOLPS-ITER simulation of the COMPASS H-mode #16908.

This is because the "total" energy flux density $q_\parallel$ used in 2PMF does not include all components relevant to SOL power dissipation. As described in section 5.7, the total energy flux has the following components: electron conductive+convective+thermoelectric energy flux, ion conductive+convective energy flux, "additional" electron+ion convective energy flux, potential energy flux, and kinetic energy flux. 2PMF takes into account only the conductive, "internal" convective and kinetic energy fluxes, and neglects the rest. The potential and "additional" convective energy fluxes typically make up a substantial portion of the total energy flux near the target, so 2PMF will typically indicate higher power losses than if all components of the total energy flux were considered. An example of the difference is shown in figure 6.8, for the SOLPS-ITER simulation of COMPASS H-mode #16908. The different definitions of f_{mom} and f_{pow} yield values which differ by tens of percent. Using the threshold $p_t/p_u < 0.5$ for divertor detachment, for example, this technical distinction can make the difference between attached and detached plasma.

In the following, we calculate the power loss factor as

$$1 - f_{pow} = \frac{q_{\parallel t} R_t}{q_{\parallel u} R_u}, \tag{6.5}$$

where $q_\parallel$ is the total parallel energy flux density as defined in section 5.7. In our simulations, this yields results nearly identical to the most natural definition of f_{pow}, which compares the total energy flux $Q_\parallel$ [W] flowing along the flux tube at its target and upstream end.

SOL transport regime in the COMPASS density scan is analysed in figure

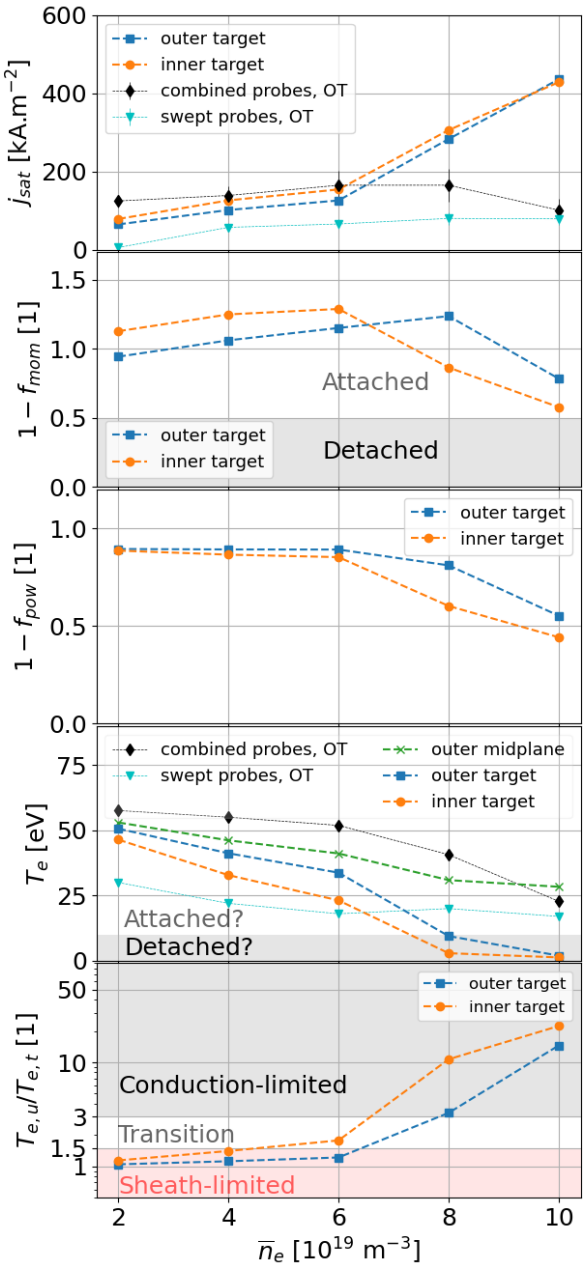

Figure 6.9: Transport regime analysis in the COMPASS density scan #13812-#13825. Unless indicated otherwise, SOLPS-ITER results are shown. From the top: (1) Ion saturated current density j_{sat}, supplemented by peak outer target (OT) j_{sat} measured by the combined and swept divertor probe array. (2) Momentum loss factor $1 - f_{mom}$. (3) Power loss factor $1 - f_{pow}$. (4) Electron temperatures T_e at the outer midplane, inner target and outer target, and peak outer target T_e measured by the combined and swept divertor probe array. (5) Parallel temperature gradient $T_{e,u}/T_{e,t}$ from the outer midplane.

6.9. SOLPS-ITER data are taken from the 3rd SOL flux tube, which features plasma parameters nearly as high as the 1st SOL flux tube, but does not suffer from radial losses into the PFR. Experimental data are taken as peaks of the respective profiles. From the top, its subfigures show:

1. **Rollover.** A detachment hallmark which is easy to measure in experiment is the decrease of target ion saturated current density j_{sat} with plasma density. [12, Sec. 16.3] Our SOLPS-ITER simulations do not exhibit such a rollover, and reach only the high-recycling regime. It is not likely that the decrease of j_{sat} measured by the combined probe array expresses experimental rollover.
2. **Momentum losses.** Another definition of detachment are "substantial pressure losses". We place the threshold at $p_t/p_u = 0.5$. At low densities, $p_t > p_u$ implies strong local ionisation, possibly local flow reversal. Momentum losses grow with higher densities, but do not reach 0.5, so both targets remain attached in the simulations.
3. **Power losses.** There is no detachment criterion based solely on f_{pow}, though the global energy balance can be used to assess how much of the input power P_{SOL} reaches the targets and how much is radiated or passed on to neutrals. In our simulations of the COMPASS density scan, power losses remain small until the highest density, where 65 kW of the total input power $P_{SOL} = 220$ kW is radiated and 20 kW is passed to neutrals in the divertor volume.
4. **Target electron temperature.** It has been suggested that detachment sets in at sufficiently low target temperatures, namely $T_{e,t} < 10$ eV. [11] In the COMPASS density scan, experimental outer target T_e stays well above this threshold, while simulated $T_{e,t}$ falls under 10 eV but the plasma does not detach. We conclude that $T_{e,t} < 10$ eV is not a sufficient detachment criterion in these simulations.
5. **Parallel T_e gradient.** The T_e parallel gradient size L_{T_e} determines the SOL electron collisionality and indicates how far the sheath influence extends. If $T_{e,u}/T_{e,t} \lesssim 1.5$, the sheath can be expected to dominate the parallel transport. If $T_{e,u}/T_{e,t} \gtrsim 3$, the gradient size is smaller than the system size and collisional effects such as heat conduction become more important than the sheath. In the COMPASS density scan, the SOL is isothermal at low densities but begins to develop substantial $\nabla_\parallel T_e$ only high densities. The likely $\nabla_\parallel T_e$ in experiment is assessed below.

In summary, the SOL transport regime in our SOLPS-ITER simulations of the COMPASS density scan is:

Figure 6.10 shows radial profiles of loss factors for the low-density discharge #13812, moderate-density discharge #13820 and high-density discharge #13825, all toward the inner target. At low plasma density, the upstream and target are in pressure balance and little power is lost from the flux tubes (sheath-limited regime). At moderate plasma density, p_t somewhat exceeds p_u because of the stronger recycling and ionisation, while power losses continue to be small (transition to conduction-limited regime). At high plasma density, there is a marked pressure drop from upstream to inner target

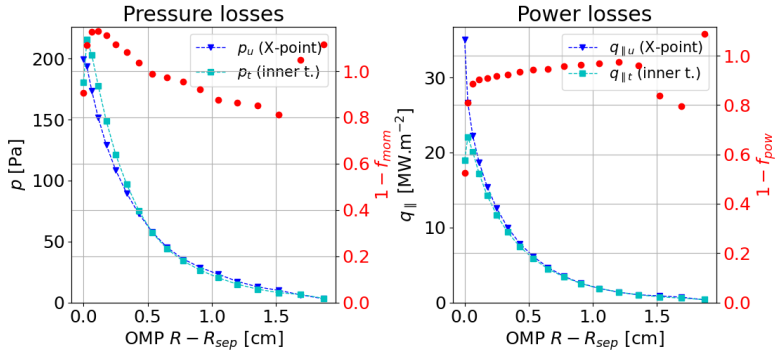

(a) : Discharge #13812, $\overline{n}_e = 2 \times 10^{19}$ m^{-3}, sheath-limited regime.

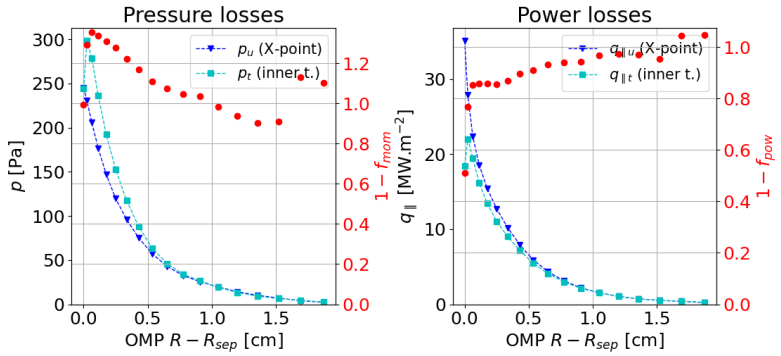

(b) : Discharge #13820, $\overline{n}_e = 6{\times}10^{19}$ m^{-3}, transition from sheath-limited to conduction-limited regime.

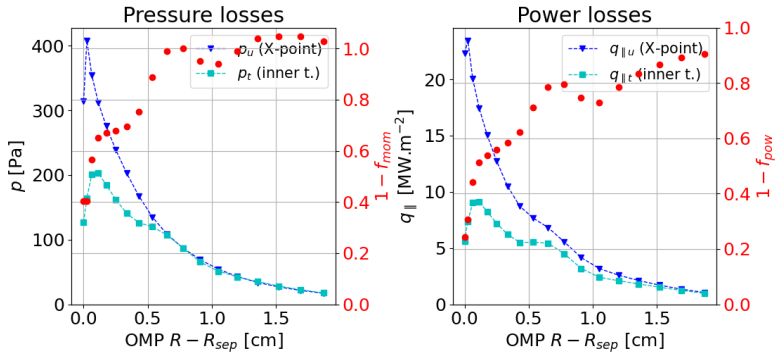

(c) : Discharge #13825, $\overline{n}_e = 10 \times 10^{19}$ m^{-3}, conduction-limited regime.

Figure 6.10: Radial profiles of pressure and power losses for selected discharges of the COMPASS density scan. (Left) Upstream and target total pressure p profiles, momentum loss factor $1 - f_{mom} = \frac{p_t}{p_u}$. (Right) Upstream and target parallel energy flux density profiles, power loss factor $1 - f_{pow} = q_{\parallel t} R_t / q_{\parallel u} R_u$.

Discharge	$\overline{n}_e$	Outer target	Inner target
#13812	2×10^{19} m^{-3}	sheath-limited	sheath-limited
#13816	4×10^{19} m^{-3}	sheath-limited	sheath-limited
#13820	6×10^{19} m^{-3}	sheath-limited	transition
#13821	8×10^{19} m^{-3}	transition	conduction-limited
#13825	10×10^{19} m^{-3}	conduction-limited	conduction-limited

Table 6.2: SOL transport regimes toward of the COMPASS tokamak density scan #13812-#13825 SOLPS-ITER simulations.

as divertor detachment approaches (conduction-limited regime). In the near SOL, about 50 % of the upstream energy flux is lost. The far SOL remains attached with little momentum or power losses.

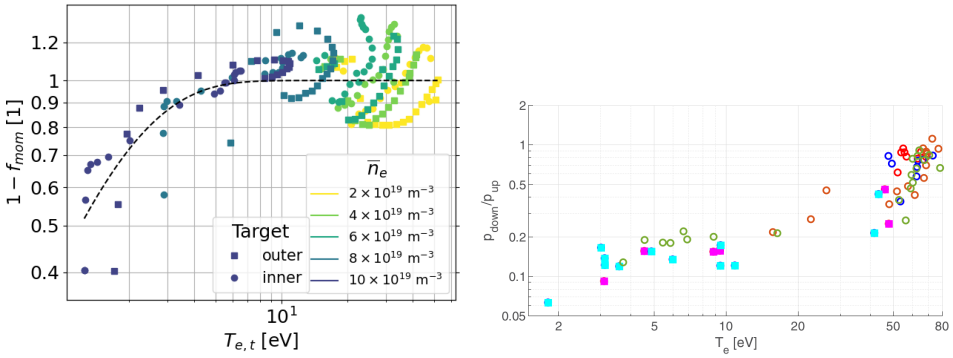

(a) : Simulation data across the SOL of the outer and inner target of the COMPASS density scan, fitted with (6.6).

(b) : Experimental data from COMPASS nitrogen seeding experiments. Reprinted from [85].

Figure 6.11: Dependence of the pressure loss factor $1 - f_{mom} = p_t/p_u$ on the target electron temperature $T_{e,t}$ in COMPASS tokamak simulations (only carbon impurities) and experiment (nitrogen seeding).

A tight correlation between the target electron temperature $T_{e,t}$ and the momentum loss factor $1 - f_{mom}$ has been reported. [11, Fig. 7] Figure 6.11a reproduces this figure with similar results, which can be fitted by the function

$$1 - f_{mom} = \left[1 - \exp\left(\frac{T_{e,t}}{1.3 \pm 0.4}\right)\right]^{1.4 \pm 0.7}. \tag{6.6}$$

Experimental data from a COMPASS nitrogen seeding campaign (figure 6.11b), on the other hand, follow a trend which does not saturate at $1 - f_{mom} = 1$ for a range of $T_{e,t}$. [85] Even for relatively high temperatures $T_{e,t} = 20$ eV, as much as 70 % of upstream pressure was found dissipated. This is likely an artifact of inaccurate upstream separatrix position, rather than a sign of profound differences in momentum dissipation. In this experiment, the upstream pressure p_u (equated to the electron pressure, as T_i was not known) was taken at the separatrix location calculated with the standard CDB reconstruction (see section 4.2). This may have yielded separatrix position

too inward, overestimating the upstream pressure p_u and inflating momentum losses to unrealistic values. The error of the default equilibrium reconstruction variant has a significant systematic component [142], so it is likely that correcting the separatrix position and p_u would increase experimental $1-f_{mom}$ to values comparable to figure 6.11a while preserving the trend of momentum losses growing at small $T_{e,t}$.

We have shown that the SOL transport regime in SOLPS-ITER simulations of the COMPASS density scan changes from sheath-limited to conduction-limited bordering on detachment onset at the inner target, but what about the experimental SOL? The high-density SOLPS cases significantly underestimated outer target T_e measurements, so their results are not representative of the experimental SOL condition. We can safely conclude that at low to moderate densities, the COMPASS SOL is sheath-limited, with the inner target gradually transitioning into the conduction-limited regime. At high densities, however, a more careful analysis is required. Information on power radiated in the SOL is scarce and calculating the total pressure would require upstream and target T_i measurements; therefore, our primary criterion for SOL transport regime classification will be the separatrix parallel T_e gradient. This immediately begs two questions: Where is the upstream separatrix, and how far from the strike point is the target T_e peak?

In this thesis, our best guide to the upstream separatrix position is usually the interpretative SOLPS-ITER simulation itself. However, since the presented simulation failed to reproduce target plasma parameters, its upstream separatrix location is also thrown into doubt. The experimental velocity shear layer (VSL) forms roughly 7 mm outside the SOLPS separatrix, which is consistent with lower-density simulations, while my systematic analysis of probe data showed no dependence of the separatrix-VSL distance on the line-averaged density. [253] Furthermore, it seems unlikely that this uncertainty could compete with the error 22 mm in the standard CDB reconstruction. In conclusion, we take $T_{e,sep} = (30 \pm 10)$ eV as the best estimate of the upstream separatrix temperature.

The main question in assessing the outer target strike point temperature $T_{e,t}$ is whether to take it as the profile peak value $T_{e,peak} = (23 \pm 10)$ eV or as the strike point value $T_{e,SP} = (15 \pm 7)$ eV. The outer strike point position is significantly more accurate in standard CDB reconstructions than the upstream separatrix position, and it does not change much between the five discharges. In discharges with lower densities, outer target T_e and $q_\parallel$ peak at or just outside the strike point. In discharge #13825, in contrast, T_e at the strike point is suppressed and the $q_\parallel$ profile is washed out, similarly to the conduction-limited simulation. This is evidence that the T_e peak forms further in the SOL, where the sheath-limited regime is restored, and that the flux tube counterpart to the separatrix should be the EFIT strike point, where $T_{e,t} = (15 \pm 7)$ eV.

The ratio $T_{e,u}/T_{e,t} = 2$ corresponds to the transition between the sheath-limited and conduction-limited regime at the outer target. The inner target can then be safely presumed to be conduction-limited, even without reliable

$T_{e,t}$ measurements. Therefore, in the high-density discharge #13825, experimental SOL on the whole may be considered as transitioning toward the conduction-limited regime.

In conclusion, in L-mode deuterium discharges without impurity seeding, the COMPASS tokamak operates in the sheath-limited regime at low densities ($\overline{n}_e = 2 - 5 \times 10^{19}$ m^{-3}). At moderate densities ($\overline{n}_e = 5 - 8 \times 10^{19}$ m^{-3}), the outer target is sheath-limited while the inner target transitions into the conduction-limited regime. At the highest achievable densities, the outer target begins to transition to the conduction-limited regime while the inner target is conduction-limited. It seems implausible that divertor detachment ($p_t/p_u < 0.5$) can be reached without extrinsic impurity seeding, as our SOLPS-ITER simulations only border on inner target partial detachment at the highest plasma density while significantly overestimating the SOL progress toward detachment. As to COMPASS H-mode, we have only performed one simulation, which was in the sheath-limited regime. Since H-mode operating space can be significantly larger than L-mode, this is not enough to draw general conclusions. [254] As a result, unless one is dealing with a discharge of remarkably high density ($\overline{n}_e = 1 \times 10^{20}$ m^{-3} or with extrinsic impurities, it is safe to assume that, toward the better diagnosed outer target, the COMPASS SOL is isothermal and T_e profiles are poloidally symmetric.

The COMPASS SOL does not transition from the sheath-limited to the conduction-limited regime in the sense that upstream parameters remain the same while the target T_e decreases. As figure 6.9 shows, both upstream and target T_e decrease with increasing $\overline{n}_e$. In the COMPASS density scan, experimental upstream $T_{e,sep}$ gradually decreased from 50 eV to 30 eV, while the outer target $T_{e,t}$ fell from 55 eV to 15 eV. The same concurrent T_e reduction was observed during nitrogen seeding experiments, where it was difficult to introduce a parallel pressure gradient because upstream and target cooled simultaneously. [85] Substantial pressure gradients were only achieved with additional NBI heating, which delivered so much power into the plasma that it would have entered H-mode were it not for the nitrogen seeding. It can be conjectured that, due to the short COMPASS SOL field lines, open divertor and low X-point height above the divertor, upstream and target plasma are not "insulated" from one another. This is the basic characteristic of the sheath-limited regime, which truly seems to be native to the COMPASS tokamak SOL.

6.5 Anomalous diffusion coefficients

The tokamak edge perpendicular transport is largely turbulent. [245] Modelling self-consistent global turbulence, for instance by the GBS code [183, 184], is, however, computationally very demanding. While efforts have been underway toward developing a turbulence-informed transport model in SOLPS-ITER [23, 24, 255], the most common description of perpendicular transport in edge transport models remains the anomalous diffusion, or the *diffusive ansatz*.

Under the diffusive ansatz, particle and energy fluxes are purely diffusive and described by Fick's law:

$$\Gamma_r = -D_n \frac{\mathrm{d}n}{\mathrm{d}r} \qquad (6.7) \qquad\qquad q_r = -\chi \frac{\mathrm{d}T}{\mathrm{d}r} \qquad (6.8)$$

Diffusive particle transport (6.7) is sometimes supplemented by a convective flux nu_r, allowing for inward transport of e.g. impurities. The variables D_n and χ are the *anomalous particle and thermal diffusion coefficients*, and describe the effective magnitude of perpendicular transport. Broadly speaking, if diffusion coefficients are low, perpendicular fluxes are low, profiles are steep and confinement is good. If they are high, perpendicular fluxes are high, profiles are flat and confinement is poor. This straightforward interpretation may have contributed to the popularity and ubiquity of anomalous diffusion in edge transport research.

Anomalous diffusion is qualitatively similar to heat flux limiting, described in chapter 5. Both apply a local formula to an inherently non-local process (turbulence in the former case, kinetic heat transport in the latter) but retain the option to tweak the transport magnitude with free parameters (anomalous diffusion coefficients/heat flux limiters). A local description means that the flux at one point in space and time only depends on the plasma parameters at that spatial and temporal point. Real edge plasma perpendicular transport, however, typically stems from events which happened prior and elsewhere, such as the formation of turbulent structures in the region susceptible to the interchange instability. The simplified description is easy to implement, computationally inexpensive and, if given enough leeway, able to reproduce plasma experiments accurately. Its disadvantage lies in its low predictive power. It is easy enough to tailor D_n and $\chi_{i,e}$ profiles to fit an existing experiment, like in section 5.1.[5] However, predicting anomalous diffusion coefficients of future experiments, such as COMPASS Upgrade H-mode plasmas, based on first principles is extremely difficult. Anomalous diffusion has no first principles to begin with. That is why it is called anomalous. The transport is not even diffusive.

Unlike heat flux limiters, anomalous diffusion coefficients have been in the spotlight of tokamak research for decades. [12, 42, 256, 257] This is because 2D transport codes such as SOLPS-ITER, which entirely rely on anomalous diffusivities to model perpendicular transport, are the primary tool for predicting edge plasma parameters in fusion reactors. Heat flux limiters are merely a correction to an already (somewhat) reliable formula for parallel heat transport. Urgent questions depend on the exact values of D_n and $\chi_{e,i}$ in fusion reactors. What is the SOL heat flux fall-off length λ_q, which determines the degree of heat load localisation on the strike points? [258] How much plasma will travel radially toward the first wall, sputtering tungsten impurities and enhancing radiative energy losses from the core? [259] In response to these and other questions, a number of models for explaining and predicting anomalous diffusivities have been put forth. [50, 260, 261, 190,

[5] Easy, but not fast.

262, 263] In this section, we compare several methods to calculate the particle diffusion coefficient D_n and investigate how D_n scales with plasma density in interpretative SOLPS-ITER simulations of the COMPASS density scan #13812-#13825.

The particle perpendicular diffusion coefficient D_n will be evaluated for the moderate-density COMPASS discharge #13820 using the following methods:

- Zeroth-order approximation of Fick's law, $D_n = \lambda_n^2 v_\parallel / L_\parallel$ [12, Eq. (1.10)], where λ_n is the density fall-off length, $v_\parallel = 0.2 c_s = 0.2\sqrt{2eT_e/m_i}$ is the upstream parallel plasma flow velocity, a fraction of the ion sound speed, and $L_\parallel$ is the connection length to the outer target (calculated from the standard CDB equilibrium reconstruction)
- Bohm diffusion coefficient $D_n = 0.06 T_e/B$ [12, Eq. (4.8)]
- Gyro-Bohm diffusion coefficient $D_n = (\rho_s/\lambda_n) T_e/B$ where $\rho_s = \sqrt{m_i T_e/e}/B$ is the ion gyroradius
- D_n obtained from interpretative core transport simulations using the METIS code [143], performed by Fabien Jaulmes (refer to section 6.2)
- Time-averaged ballistic spreading of turbulent structures, $D_n = u_b^2 \tau$, where u_b is the typical radial velocity and τ is the correlation of the radial velocity [50] (see below)

In all of the above, temperature is given in eV. The density fall-off length λ_n was approximated by a step function based on experimental outer midplane n_e data, see figure 6.14b. The last and most complicated method of D_n calculation will now be described.

It has been proposed that edge transport codes using the diffusive ansatz have yielded satisfactory results because intermittent turbulent transport, in fact, averages to a diffusion-like transport at large time scales. [50] By modelling ballistically propagating turbulent structures, exponentially decaying SOL density profiles were recovered and the resulting particle flux was shown to be diffusion-like. Its "diffusion" coefficient relates directly to the turbulent structures properties: the typical radial velocity u_b and the correlation time τ of the radial velocity.

$$D_n = u_b^2 \tau \tag{6.9}$$

To gauge whether this approach can reproduce anomalous diffusion in COMPASS simulations, let us calculate this diffusion coefficient in the COMPASS L-mode discharge #13820. The radial velocity v_r was measured at high temporal resolution (sampling frequency 5 MHz) with the outer midplane horizontal reciprocating probe (HRCP, section 3.1.2) as $\mathbf{E} \times \mathbf{B}$ drift velocity

$$v_r = \frac{E_p}{B}. \tag{6.10}$$

Figure 6.12 demonstrates the turbulent nature of the SOL radial transport. On the left, it shows the profile of the ion saturated current I_{sat} during the probe movement inward. Approximately 3 mm outside the velocity shear layer (VSL), a 3ms window was chosen for sampling the I_{sat} and v_r fluctuations. On the right of figure 6.12, the I_{sat} histogram is plotted. A positively skewed

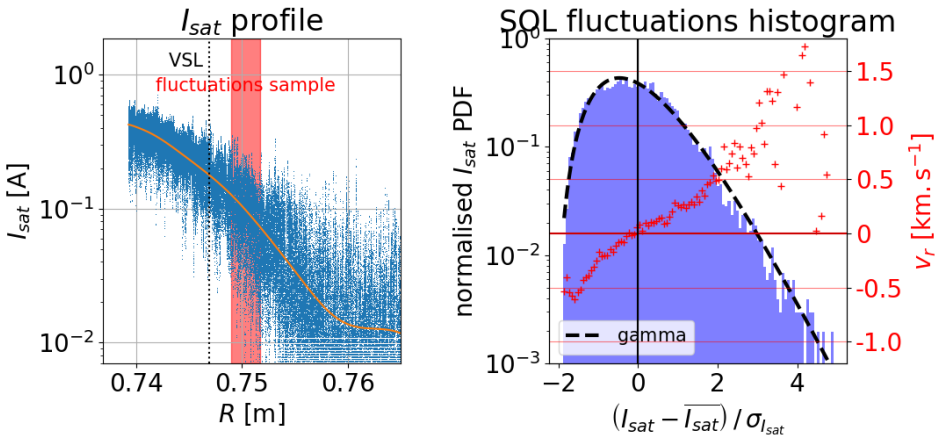

Figure 6.12: Ion saturated current I_{sat} profile in the COMPASS discharge #13820 and the histogram of its fluctuations 3 mm outside the velocity shear layer (VSL, $E_r = 0$). The radial velocity (red crosses) was calculated for each bin of the I_{sat} signal, so it corresponds to the velocity of turbulent structures of various sizes.

distribution emerges, reminiscent of the gamma function. [264] For each I_{sat} histogram bin (plasma fluctuation of a certain magnitude), the average v_r was calculated and plotted into the same graph in red. One observes that positive fluctuations ("blobs") propagate outward while the negative fluctuations ("holes") propagate inward, and that larger fluctuations move faster. This is consistent with the process of interchange turbulence. [245]

To calculate the blob velocity u_b and the correlation time τ from v_r measurements, we adopt the following approach. The blob velocity u_b is calculated inside consecutive 1ms windows as the standard deviation of the radial velocity. This is in accord with [50], where $u_b^2 = C_0$ is the peak value of the v_r autocorrelation function, that is, the v_r variance. The correlation time τ is calculated inside the same consecutive 1ms windows by fitting the peak of the v_r autocorrelation function with the exponential $\mathrm{e}^{-|t|/\tau}$. The resulting profiles of blob velocity u_b and correlation time τ are plotted in figure 6.13. The correlation time spans an order of magnitude from 3 μs to 25 μs, indicating a large number of rapidly exchanging turbulent structures inside the VSL and a smaller number of longer-lasting events in the far SOL. The blob velocity peaks at 0.7 km.s^{-1} inside the VSL and then quickly decays to 0.45 km.s^{-1}, where it stabilises in the far SOL. These results support the idea of turbulent structures being mixed and torn in the VSL and then spreading through the SOL while slowing down due to parallel losses dissipating their internal electric field.

All of the perpendicular diffusion coefficients D_n, listed on page 144 are plotted in figure 6.14a. The various methods yield an appreciable quantitative disagreement (note the logarithmic y axis scale), but also their dependence on r is different. The Bohm and gyro-Bohm diffusion coefficients fall from the separatrix to the far SOL. D_n approximated from Fick's law exhibits an order-of-magnitude drop in the region of n_e profile steepening. SOLPS-ITER

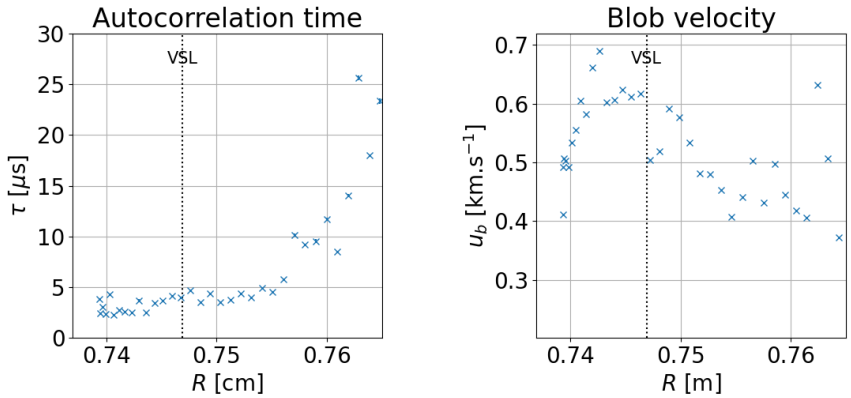

Figure 6.13: Outer midplane turbulence properties in the COMPASS discharge #13820: correlation time τ and blob velocity u_b. The velocity shear layer (VSL) position is plotted in black.

D_n is flat. Finally, D_n calculated from turbulence properties and by METIS rise from the separatrix to the far SOL. Profile tailoring experiments in higher-density discharges, as well as close inspection of the outer midplane experiment-model n_e match in discharge #13820, suggest that D_n rising in the SOL may be applicable to SOLPS-ITER simulations as well. A similar trend was found in the low-density case studied in [50]; however, COMPASS values of $D_n = u_b^2\tau$ are larger than in ASDEX Upgrade.

While upstream profiles of n_e may be better matched with a profile of D_n which grows in the SOL, the same is not the case for target profiles. As section 6.2 explored, flattening upstream SOL n_e profile leads to higher target densities, and therefore the unwanted deepening of the conduction-limited regime or even detachment. A similar result was achieved when a smoothed $D_n = u_b^2\tau$ profile was implemented into the simulation of discharge #13820: SOL density rose and target T_e fell precipitously. If a rising D_n profile in SOLPS-ITER simulations leads to a significantly poorer match with target experimental observations, it is dubious whether it is preferable to a flat profile, even if it yields a slightly better upstream match.

The focus on upstream profiles as opposed to target plasma parameters was already pointed out in section 4.4, while commenting on an automated algorithm seeking the optimal separatrix location in SOLPS-ITER simulations of ASDEX Upgrade. [55] In this work, D_n value was specified cell for cell in order to achieve perfect agreement with upstream n_e measurements. (Let us tangentially note that, for the ASDEX case labeled "low density, low transport", this D_n rose in the far SOL.) In contrast, the algorithm did not seek a match with target plasma parameters at all.

Such preference for upstream over target becomes understandable once we take into account the usual success rate of interpretative edge transport modelling reproducing target measurements. Especially in detachment modelling, qualifying a result as "good" is often significantly more lenient than the factor-of-two criterion used in this thesis. Alcator C-Mod interpretative modelling has been published where simulated target T_e is completely sup-

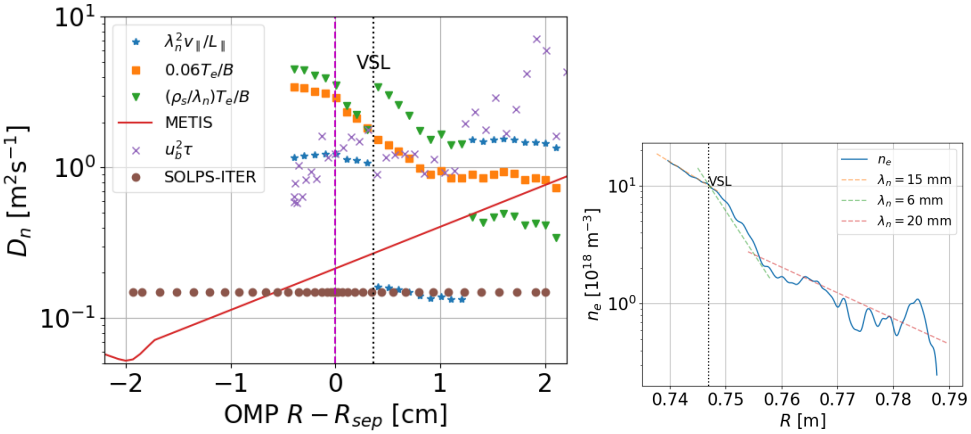

(a) : Particle diffusion coefficient D_n, listed on page 144. The separatrix position was corrected by the same amount as in figure 6.2c.

(b) : Outer midplane electron density n_e profile. Dashed lines denote n_e fall-off lengths.

Figure 6.14: Calculation of the perpendicular diffusion coefficient D_n in the COMPASS tokamak L-mode #13820.

pressed (below 0.5 eV) while experimental measurements show $T_{e,t}$ = 5-10 eV. [237] ASDEX Upgrade H-mode detachment "could be reproduced with SOLPS modelling", when experimental outer target T_e was 10× higher than in modelling, and vice versa for outer target n_e. [244] Such results are not the rule; there are plenty examples of SOLPS-ITER modelling where target plasma parameters were reproduced. [238, 265] They do show, however, that edge transport simulations can be volatile and unforgiving in their estimation of target parameters. Upstream profiles are easier to match in details, since the free choice of anomalous diffusion coefficients offers a great degree of control.

In spite of quantitative SOL D_n predictions proving difficult, we can still observe qualitative trends. In the remainder of this section, we investigate two possible D_n scalings with plasma density: using the density scan experimental data $D_n = u_b^2 \tau$, and using the D_n value employed in interpretative SOLPS-ITER simulations. A number of tokamak experiments have observed that plasma density influences D_n, or the SOL density fall-off length λ_n. Of particular interest is the flattening of n_e SOL profile at high densities, so-called shoulder formation. [266, 267, 268, 269] The associated increase of far SOL density leads to higher main chamber erosion and impurity production, which can cause lowered core plasma performance. Additionally, experimental or interpretative D_n scalings are intriguing for predictive modelling, as they help guide the choice of D_n in simulations of future machines. It is, of course, questionable if COMPASS scalings can be relevant to COMPASS Upgrade. The plasma densities achieved in COMPASS Upgrade will be an order of magnitude higher than in COMPASS, and current SOLPS-ITER simulations show it to be deeply conduction-limited. [270] Still, the aim of this thesis is to glean whatever knowledge we can from interpretative COMPASS simulations to apply to COMPASS Upgrade. Even if quantitative D_n values from Alcator

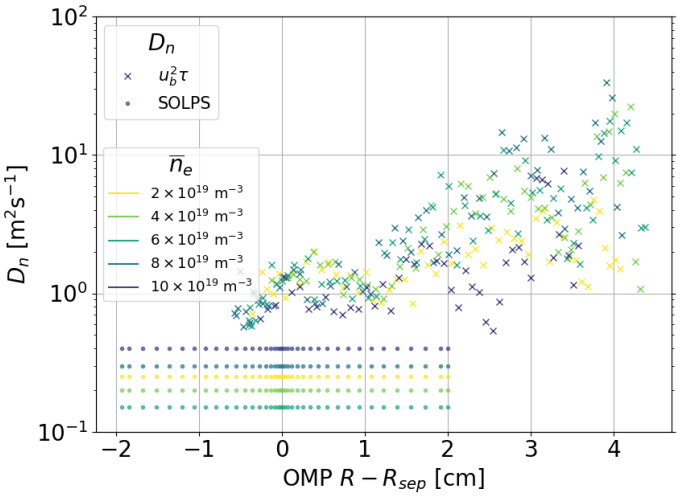

Figure 6.15: Particle diffusion coefficients D_n in the COMPASS L-mode density scan #13812-#13825. D_n calculated with equation 6.9 are plotted with crosses, values used in SOLPS-ITER interpretative simulations are plotted with dots. The experimental profiles were shifted radially by the same amount as in figures 6.2a-6.2e.

C-Mod or JET are more relevant to COMPASS Ugprade, there is only one tokamak edge plasma physics, and the COMPASS tokamak can contribute toward its understanding across SOL transport regimes.

Figure 6.15 shows the experimental profiles of $D_n = u_b^2\tau$ calculated for all five density scan discharges, and compares them to their SOLPS-ITER counterparts. No discernible dependence on plasma density is present. This is an interesting negative result; it would seem to suggest that some properties of L-mode turbulent transport in the COMPASS edge plasma do not change across a large span of densities. The neat radial alignment of the experimental D_n profiles, which was achieved by the same separatrix position corrections as in the interpretative simulations themselves, indicates the robustness of these corrections. However, the result remains: our data of experimental $D_n = u_b^2\tau$ do not provide basis for D_n scaling with density.

Figure 6.16 shows the dependence of the particle diffusion coefficient D_n, used in interpretative SOLPS-ITER modelling (table 6.1b), on the electron density in the 3rd SOL flux tube $n_{e,u}$ and the upstream SOL collisionality ν^* 5.6 at the same place. The two dependencies are similar as $\nu^* \sim n_{e,u}$; however, D_n scaling with local collisionality is more direct than with the local plasma density. [243] Two opposing trends are observed. At low densities, D_n falls and the SOL n_e profile steepens with increasing plasma density. At high densities, D_n rises and the SOL n_e profile flattens with increasing plasma density. Fitting the latter with a power law, one finds approximately $D_n \sim n_{e,u}^{0.4}$. This is an interesting result, as radial transport is usually presumed to grow monotonically with plasma density/collisionality. [12, Sec. 4.9]

The largely turbulent SOL radial transport can be understood in terms of

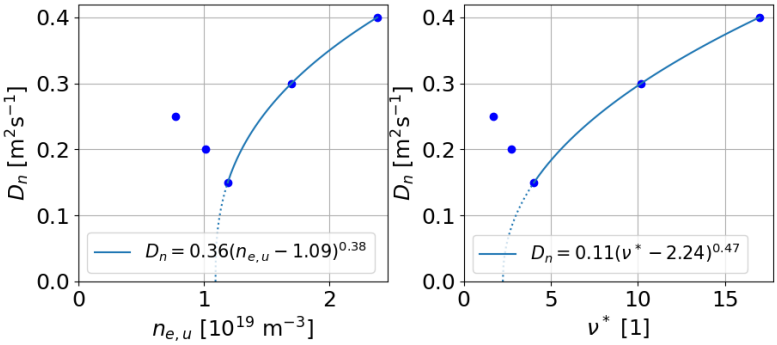

Figure 6.16: Particle diffusion coefficients D_n in the COMPASS L-mode density scan #13812-#13825 (table 6.1b), as depending on the upstream density $n_{e,u}$ and collisionality ν^*. The fits were made with the least squares method.

competition between parallel transport and perpendicular transport. [245] Parallel transport is driven by large conductivities along the magnetic field lines: electron thermal conductivity κ_e depletes electron energy from the propagating blobs, while electric conductivity $\sigma_{\parallel}$ dissipates the blob internal electric field, which drives the structure across magnetic field lines via the $\mathbf{E} \times \mathbf{B}$ drift. Perpendicular transport is, therefore, stymied by large parallel transport and can unfold fully when parallel transport is weak. Both parallel thermal and electric conductivity are collisionality-dependent. Large SOL collisionalities usually result in low T_e, lowering the classical thermal conductivity, and large SOL densities increase the SOL parallel resistivity. [195] As a result, increasing plasma density weakens parallel transport and enhances radial transport. Why, then, do anomalous diffusion coefficients D_n initially fall with plasma density?

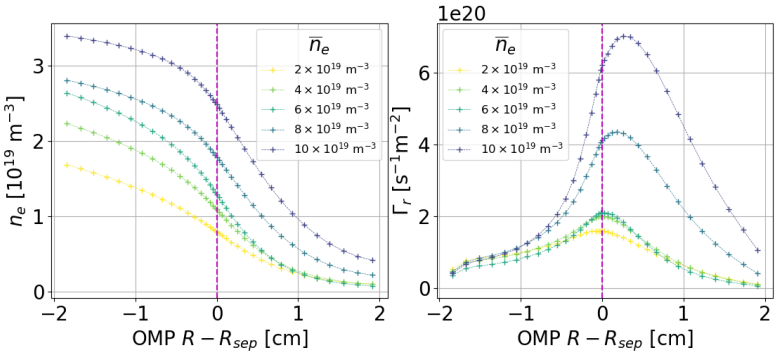

Figure 6.17: Radial profiles of electron density n_e and radial D^{1+} particle flux density Γ_r in SOLPS-ITER simulations of the COMPASS L-mode density scan #13812-#13825 (table 6.1b).

Figure 6.17 compares radial profiles of electron density n_e and radial D^{1+} particle flux density Γ_r across the SOLPS-ITER simulations of the COMPASS density scan. We observe that radial transport does not actually fall with plasma density. At low densities, D_n decrease is compensated by n_e profile steepening. The anomalous diffusion equation 6.7 then yields

approximately constant radial particle flux density Γ_r. Radial transport only starts significantly growing at higher densities, when D_n increases and the n_e profile somewhat flattens. This outpouring of particles into the SOL may be part of the reason for heightened target densities in the SOLPS simulations compared to experimental data. Indeed, boosting this upstream transport by doubling SOL D_n resulted in target $n_{e,t}$ increase and even deeper conduction-limited regime in section 6.2.

Discharge	λ_n
#13812	8.4 mm
#13816	7.3 mm
#13820	6.2 mm
#13821	9.5 mm
#13825	11.7 mm

Table 6.3: Electron density SOL fall-off length λ_n at the outer midplane in SOLPS-ITER simulations of the COMPASS density scan.

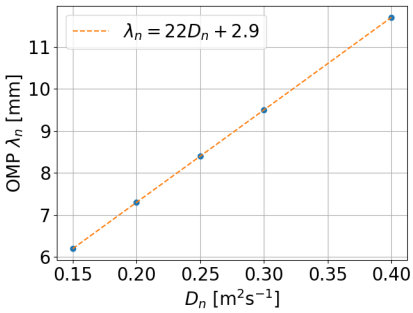

Figure 6.18: Relationship of the electron density SOL fall-off length λ_n to the particle diffusion coefficient D_n in SOLPS-ITER simulations of the COMPASS density scan.

Figure 6.18 shows that the diffusion coefficient D_n correlates with the electron density fall-off length λ_n in our SOLPS-ITER simulations, rather than with radial particle flux density Γ_r. The dependence is linear to a surprising degree of accuracy. This is likely a numerical artifact of the simulation rather than a tight physical correlation, but it does suggest that λ_n scalings can be used to estimate D_n in predictive simulations. [271, 272, 273] Interestingly, theoretical considerations of radial transport yield a square rather than linear dependence,

$$\lambda_n \approx \left(\frac{2 D_n L}{v_\parallel} \right)^{0.5} \tag{6.11}$$

for both sheath-limited and conduction-limited regime. [12, Ch. 21] The reason for this discrepancy is not clear at the moment.

In conclusion, justifying values of anomalous particle diffusion coefficients D_n used in interpretative transport simulations is difficult. Calculating D_n from first principles, from experimental measurement of turbulence properties or with core transport codes, we have obtained values varying within two orders of magnitude. This is not sufficient accuracy for predictive modelling. We have, however, found evidence of qualitative scaling in D_n. In our interpretative SOLPS-ITER simulations, there is a tight linear relationship between D_n and the electron density SOL fall-off length λ_n. D_n furthermore varies with the line-averaged plasma density $\overline{n}_e$, but the trend depends on the SOL transport regime. In the sheath-limited regime (low densities), outer midplane SOL n_e profile steepens and D_n falls. In the conduction-limited regime (high densities), outer midplane n_e profile flattens and D_n rises. In the future, it would be interesting to explain this variation by an in-depth

analysis of experimental turbulence properties. For now, let us note that in the conduction-limited, high-recycling regime, $D_n \propto n_{e,u}^{0.4}$. This is the regime which is likely relevant to COMPASS Upgrade SOL transport simulations.

Chapter 7

Conclusion

This thesis has presented interpretative SOLPS-ITER simulations of the COMPASS tokamak edge plasma transport. Its introducing chapter 1 showed what a key role edge plasma transport plays in the problem of fusion reactor heat exhaust. Chapter 2 described the derivation and meaning of plasma transport equations, or Braginskii equations, and outlined several weaknesses of transport codes built upon them. Chapter 3 introduced the COMPASS and COMPASS Upgrade tokamaks. The following three chapters were dedicated to three sources of uncertainty in interpretative SOLPS-ITER simulations. Chapter 4 dealt with inaccuracies in reconstructions of tokamak magnetic equilibria and their corrections in interpretative modelling. Chapter 5 investigated parallel heat transport in the SOL and its corrections for kinetic effects using heat flux limiters. Finally, chapter 6 qualified the COMPASS SOL transport regime and explored its effect on the radial particle transport via the anomalous particle diffusion coefficient. Let us now restate the findings of the three "result" chapters and put them into the context of current tokamak research.

Chapter 4: Magnetic equilibrium reconstruction inaccuracy. Accurate reconstructions of the tokamak magnetic equilibrium are an indispensable tool of tokamak experiments. They are also the foundation for computation grid construction in interpretative edge transport simulations. If the reconstruction is inaccurate, the grid is built in the wrong place relative to diagnostic measurements and performing an interpretative transport simulation which matches these measurements requires correcting for the reconstruction errors. I have presented three approaches to this correction: intuitive, systematic, and aiming to correct the reconstruction itself. In a simulation using the standard (default) COMPASS equilibrium reconstruction of the COMPASS L-mode discharge #17588, the intuitive and systematic approach yielded the same results within a few millimetres accuracy. SOLPS data had to be shifted radially outward by about 1.5 cm at the plasma top before they matched experimental measurements. This agreement lends credibility to using intuitive reconstruction corrections, as it suggests the existence of a robust optimal separatrix position. Next, to test whether SOLPS-ITER can be used to validate equilibrium reconstructions, I have performed a simulation of discharge #17588 using a reconstruction with optimised magnetic input data. The result was favourable; the new simulation did not require any grid corrections. Finally, I have used the optimal separatrix position found in the first step to constrain a new reconstruction variant. The SOLPS simulation using this new reconstruction, again, required no corrections to match experimental data at the plasma top. This is an encouraging first result that SOLPS simulations can be used to validate and improve tokamak magnetic equilibrium reconstructions.

The findings of chapter 4 are innovative in their focus on using the SOLPS-ITER code to find the optimal separatrix position and create better equilibrium reconstructions. Corrections of equilibrium reconstructions have been considered a "necessary evil" of interpretative edge transport simulations, and their value as a free parameter was not thought to carry significance

beyond the simulation itself. On the contrary, I have found that not only are such corrections rather robust, but the newfound separatrix position also correlates strongly with the position of the velocity shear layer and it can be used to produce a more accurate equilibrium reconstruction. In COMPASS edge plasma research, the velocity shear layer has been used as a proxy for the separatrix position. I have presented evidence that the velocity shear layer actually forms 0.5-1 cm outside the outer midplane separatrix in the COMPASS tokamak. Concerning the application of this research to the COMPASS Upgrade tokamak, I provide the framework for testing the accuracy of its eventual equilibrium reconstructions and for improving it in cases where special accuracy is needed. Furthermore, I suggest that its future EFIT++ reconstructions should be set up from the beginning to account for realistic plasma pressure profiles and their magnetic measurement inputs should be carefully calibrated and subsequently recalibrated. The equilibrium reconstruction of any tokamak can be validated with an edge transport code, contributing toward the quality of an indispensable, basic tool of tokamak fusion reactor research.

The framework of validating equilibrium reconstruction with SOLPS-ITER has been successfully applied in a recent Master's thesis under my supervision to the COMPASS L-mode discharge #17692. [136] The results were in line with my findings. Another recent Master's thesis has prototyped an automatic algorithm searching for optimal SOLPS-ITER inputs using Bayesian processes. [186] This avenue of research promises automated running of L-mode SOLPS-ITER simulations, closely examining the phase space of simulation inputs including equilibrium reconstruction corrections and helping to constrain this source of uncertainty in edge transport simulations.

Chapter 5: Heat flux limiting. Transport equations at the heart of edge transport codes are built upon the assumption that the edge plasma is highly collisional. In the SOL parallel transport, however, electron and ion mean free paths are often longer than the system size or the gradient size. This causes velocity distribution functions to depart from Maxwellian, so the classical (Spitzer-Härm) formula for parallel heat flux density is no longer applicable. Currently, edge transport codes most widely correct for kinetic effects in parallel heat transport by heat flux limiting with the harmonic average, reducing the heat flux magnitude so it cannot exceed a fraction of the free-streaming heat flux. This fraction is a free parameter called the electron or ion heat flux limiter, and its optimal value and effectiveness in emulating kinetic effects have long been disputed. I have investigated the role of heat flux limiters in a SOLPS-ITER simulation of the COMPASS H-mode #16908 using a 2D heat flux limiter scan in comparison to a 1D3V kinetic simulation with the BIT1 code. I have found that knock-on effects of heat flux limiting are more important to an interpretative simulation than the parallel heat flux magnitude itself. Using the common boundary condition of set SOL input power, employing the classical formula for parallel heat transport does not lead to high heat fluxes, but rather to flat parallel profiles of temperature. Strict electron and ion heat flux limiting was able to emulate

the steep parallel temperature profiles seen in kinetic results, but it was at the cost of unrealistically high outer midplane ion temperature and inner target energy fluxes so low, they could not fully maintain plasma recycling. In other words, overfocusing on the exact match between fluid and kinetic parallel transport can negatively impact the interpretative simulation as a whole. I posit that heat flux limiter values should be chosen primarily with regard to their effect of measurable plasma parameters, and I provide physics-based explanation of their knock-on effects for orientation. Finally, it should be kept in mind that heat flux limiters may not have any impact on the parallel heat transport, depending on the SOL transport regime. This constitutes a thorough analysis of the edge transport code free parameters which are the electron and ion heat flux limiters.

The innovation of chapter 5 lies in the extensive 2D heat flux limiter scan and its comprehensive examination focused on matching experimental data. Instead of seeking agreement between fluid and kinetic codes (and inevitably concluding that heat flux limiting is too crude to reproduce kinetic results), I have taken heat flux limiters as a given, as free parameters with far-reaching, complex effects, and sought how they can improve the experiment-model match. Additionally, to our knowledge, ion and electron heat flux limiting have never been treated with the same importance and concurrently. Although ions do conduct less heat along magnetic field lines than electrons, they are more sensitive to heat flux limiter values and cause stronger knock-on effects in other plasma parameters. This is the first time a 2D scan in electron and ion heat flux limiters has been performed, presumably because of the large computational demands of so many edge transport simulations. This is where the COMPASS tokamak shines as a test bed for interpretative simulations. Although it does not reach the plasma parameters of a fusion reactor and its SOL has potentially different sensitivity to heat flux limiters, as long as its results are set within the frame of SOL transport regimes, its parallel transport physics can be extrapolated to other tokamaks. Consequently, this research universally increases our understanding of heat flux limiting and its ability to emulate kinetic effects in the SOL parallel heat transport, improving the quality of both interpretative and predictive tokamak edge transport simulations, no matter the machine.

Chapter 6: SOL transport regime. SOL transport regimes, sheath-limited, conduction-limited and detachment, are useful labels characterising overall edge plasma conditions, such as the dominant mean of parallel transport, target plasma temperatures or turbulence properties. Quantifying the SOL transport regime helps us perform generalisations in edge plasma physics and make sweeping, qualitative statements about its scalings. To characterise the typical SOL transport regime of the COMPASS tokamak, I have performed five interpretative simulations of a COMPASS L-mode steady-state density scan #13812-#13825, representative of the COMPASS L-mode operational space without impurity seeding. I have found that most experimental COMPASS plasmas are sheath-limited, only beginning to transition toward conduction-limited at the highest densities. I have also gauged how adequate

SOLPS-ITER is at reproducing COMPASS edge plasmas. Achieving a reasonable experiment-simulation match was simple in low- to moderate-density COMPASS plasmas; however, in high-density plasmas, SOLPS-ITER significantly underestimated target electron temperatures. I have concluded that implementing drifts and an uneven electron-ion input power split is key to more faithful SOLPS-ITER simulations of the COMPASS tokamak.

Next, I have studied the values and scalings of the anomalous particle diffusion coefficient, an important free parameter in edge transport simulations quantifying the strength of radial transport. I have shown that the diffusion coefficient does not scale uniformly with plasma density, but rather depends on the SOL transport regime. My attempt to explain its value quantitatively was unsuccessful, as estimates from several theoretical, experimental and modelling sources varied within two orders of magnitude. This means, unfortunately, that my research cannot provide a quantitative prediction of anomalous particle diffusion coefficient values for COMPASS Upgrade. Two things can be said. One, in the typically conduction-limited COMPASS Upgrade SOL, diffusion coefficients will likely increase with plasma density, possibly as the square root of the separatrix electron density. Two, theoretical predictions of COMPASS Upgrade SOL diffusivities will likely be too inaccurate to employ directly in its predictive SOLPS-ITER simulations. As a result, a major source of information on the edge plasma transport will be interpretative simulations of similar plasmas in other tokamaks, such as Alcator C-mod, and windows of operation using scans in diffusion coefficients will have more predictive value than one-point simulations.

The innovation of chapter 6 lies in the comprehensive pursuit of high-quality interpretative simulations of the COMPASS tokamak L-mode. Its previously published SOLPS-ITER simulations have been code experiments in the geometry of COMPASS, rather than simulations reproducing experimental measurements. I have mapped the parameter space of COMPASS steady-state discharges in L-mode and made a case study of its H-mode. I have gauged the aptitude of transport equations to capture its edge transport phenomena and carefully considered several free parameters of the SOLPS-ITER code as applied to COMPASS transport modelling. Gauging the SOL transport regime of experimental and simulated SOLs is not, in itself, new. It does, however, strongly support other investigations of the edge transport and allow their generalisation and connection. The dominance of the sheath-limited regime on COMPASS has far-reaching implications. It means that the upstream electron temperature will typically be very close to the peak outer target temperature, allowing for quick gauging of the separatrix position. It also implies that electron velocity distribution functions will not differ much along the SOL field lines (excepting its distortion in the sheath), so kinetic effects are likely not strong in SOL electron parallel transport. As a result, the methods and findings of chapter 6 are not necessarily innovative; above all, they are useful.

Let us now answer the research question of this thesis.

"How well can SOLPS-ITER model COMPASS tokamak edge plasma

transport, and what can we learn from these simulations?"

At low L-mode densities and in sheath-limited H-mode, a simple version of SOLPS-ITER is fully adequate at modelling the COMPASS plasma edge. At high densities, reproducing experimental data likely demands implementing drifts. Uneven electron-ion power split together with ion heat flux limiters should be used to achieve realistic outer midplane ion temperatures. The COMPASS L-mode SOL is typically sheath-limited and only begins to transit toward conduction-limited at the highest densities. Its inner target is more conduction-limited than its outer target. Kinetic effects are strong in parallel ion heat transport but typically insignificant in parallel electron transport. SOLPS-ITER simulations can be used to validate and improve magnetic equilibrium reconstructions.

This thesis contributes toward the world-wide research of tokamak nuclear fusion by furthering our understanding of edge transport codes and their free parameters, facilitating the physics-based interpretation of simulations of existing tokamak experiments and the improving credibility of predictive simulations of future fusion reactors. The COMPASS tokamak may not be a fusion reactor, but there is but one physics. Using the framework of SOL transport regimes for orientation, we believe this work is applicable and useful to a number of tokamak experiments around the globe.

Bibliography

[1] S. Wiesen et al. "The new SOLPS-ITER code package". In: *Journal of Nuclear Materials* 463 (2015). PLASMA-SURFACE INTERACTIONS 21, pp. 480–484. ISSN: 0022-3115. DOI: https://doi.org/10.1016/j.jnucmat.2014.10.012. URL: http://www.sciencedirect.com/science/article/pii/S0022311514006965.

[2] M. Hron et al. "Overview of the COMPASS results *". In: *Nuclear Fusion* 62.4 (2022). ISSN: 0029-5515. DOI: 10.1088/1741-4326/ac301f. URL: https://iopscience.iop.org/article/10.1088/1741-4326/ac301f.

[3] P. Vondracek et al. "Preliminary design of the COMPASS upgrade tokamak". In: *Fusion Engineering and Design* 169 (2021), p. 112490. ISSN: 0920-3796. DOI: https://doi.org/10.1016/j.fusengdes.2021.112490. URL: https://www.sciencedirect.com/science/article/pii/S0920379621002660.

[4] R. A. Pitts et al. "Physics basis for the first ITER tungsten divertor". In: *Nuclear Materials and Energy* 20 (2019), p. 100696. ISSN: 2352-1791. URL: http://www.sciencedirect.com/science/article/pii/S2352179119300237.

[5] J. D. Lore et al. "High gas throughput SOLPS-ITER simulations extending the ITER database to strong detachment". In: *Nuclear Fusion* 62.10 (Sept. 2022), p. 106017. DOI: 10.1088/1741-4326/ac8a5f. URL: https://dx.doi.org/10.1088/1741-4326/ac8a5f.

[6] J. Horacek et al. "Modeling of COMPASS tokamak divertor liquid metal experiments". In: *Nuclear Materials and Energy* 25 (2020), p. 100860. ISSN: 2352-1791. DOI: https://doi.org/10.1016/j.nme.2020.100860. URL: http://www.sciencedirect.com/science/article/pii/S2352179120301277.

[7] H. Zohm et al. "On the physics guidelines for a tokamak DEMO". In: *Nuclear Fusion* 53.7 (June 2013), p. 073019. DOI: 10.1088/0029-5515/53/7/073019. URL: https://iopscience.iop.org/article/10.1088/0029-5515/53/7/073019.

[8] J. P. Gunn et al. "Surface heat loads on the ITER divertor vertical targets". In: *Nuclear Fusion* 57.4 (Mar. 2017), p. 046025. DOI: 10.1088/1741-4326/aa5e2a. URL: https://doi.org/10.1088/1741-4326/aa5e2a.

[9] G. De Temmerman, T. Hirai, and R. A. Pitts. "The influence of plasma-surface interaction on the performance of tungsten at the ITER divertor vertical targets". In: *Plasma Physics and Controlled Fusion* 60.4 (Mar. 2018), p. 044018. DOI: 10.1088/1361-6587/aaaf62. URL: https://iopscience.iop.org/article/10.1088/1361-6587/aaaf62.

[10] M. Li and J.-H. You. "Interpretation of the deep cracking phenomenon of tungsten monoblock targets observed in high-heat-flux fatigue tests at 20MW/m2". In: *Fusion Engineering and Design* 101 (2015), pp. 1–8. ISSN: 0920-3796. DOI: https://doi.org/10.1016/j.fusengdes.2015.09.008. URL: http://www.sciencedirect.com/science/article/pii/S0920379615302775.

[11] P. C. Stangeby. "Basic physical processes and reduced models for plasma detachment". In: *Plasma Physics and Controlled Fusion* 60.4 (Mar. 2018), p. 044022. DOI: 10.1088/1361-6587/aaacf6. URL: https://iopscience.iop.org/article/10.1088/1361-6587/aaacf6/meta.

[12] P. C. Stangeby. *The plasma boundary of magnetic fusion devices*. Philadelphia: Institute of Physics Pub., 2000. ISBN: 07-503-0559-2.

[13] E. Kaveeva et al. "SOLPS-ITER modelling of ITER edge plasma with drifts and currents". In: *Nuclear Fusion* 60.4 (Mar. 2020), p. 046019. DOI: 10.1088/1741-4326/ab73c1. URL: https://dx.doi.org/10.1088/1741-4326/ab73c1.

[14] E. Kaveeva et al. "SOLPS-ITER modeling of deuterium throughput impact on the ITER SOL plasma". In: *Nuclear Materials and Energy* 35 (2023), p. 101424. ISSN: 2352-1791. DOI: https://doi.org/10.1016/j.nme.2023.101424. URL: https://www.sciencedirect.com/science/article/pii/S2352179123000637.

[15] A. Loarte et al. "Progress on the application of ELM control schemes to ITER scenarios from the non-active phase to DT operation". In: *Nuclear Fusion* 54.3 (Feb. 2014), p. 033007. DOI: 10.1088/0029-5515/54/3/033007. URL: https://dx.doi.org/10.1088/0029-5515/54/3/033007.

[16] V. Kotov and D. Reiter. "Two-point analysis of the numerical modelling of detached divertor plasmas". In: *Plasma Physics and Controlled Fusion* 51.11 (Oct. 2009), p. 115002. DOI: 10.1088/0741-3335/51/11/115002. URL: https://iopscience.iop.org/article/10.1088/0741-3335/51/11/115002/meta.

[17] M. Siccinio et al. "A 0D stationary model for the evaluation of the degree of detachment on the divertor plates". In: *Plasma Physics and Controlled Fusion* 58.12 (Nov. 2016), p. 125011. DOI: 10.1088/0741-3335/58/12/125011. URL: https://iopscience.iop.org/article/10.1088/0741-3335/58/12/125011.

[18] G. Ciraolo et al. "Fluid and kinetic modelling for non-local heat transport in magnetic fusion devices". In: *Contributions to Plasma Physics* 58.6-8 (2018), pp. 457–464. DOI: https://doi.org/10.1002/ctpp.201700222. eprint: https://onlinelibrary.wiley.com/doi/pdf/10.1002/ctpp.201700222. URL: https://onlinelibrary.wiley.com/doi/abs/10.1002/ctpp.201700222.

[19] R. Chodura. "Kinetic Effects in the Scrape Off Layer". In: *Contributions to Plasma Physics* 32.3-4 (1992), pp. 219–230. DOI: https://doi.org/10.1002/ctpp.2150320308. eprint: https://onlinelibrary.wiley.com/doi/pdf/10.1002/ctpp.2150320308. URL: https://onlinelibrary.wiley.com/doi/abs/10.1002/ctpp.2150320308.

[20] M. Giacomin et al. "First-Principles Density Limit Scaling in Tokamaks Based on Edge Turbulent Transport and Implications for ITER". In: *Phys. Rev. Lett.* 128 (18 May 2022), p. 185003. DOI: 10.1103/PhysRevLett.128.185003. URL: https://link.aps.org/doi/10.1103/PhysRevLett.128.185003.

[21] T. Eich et al. "Turbulence driven widening of the near-SOL power width in ASDEX Upgrade H-Mode discharges". In: *Nuclear Fusion* 60.5 (Apr. 2020), p. 056016. DOI: 10.1088/1741-4326/ab7a66. URL: https://dx.doi.org/10.1088/1741-4326/ab7a66.

[22] R. Panek et al. "Conceptual design of the COMPASS upgrade tokamak". In: *Fusion Engineering and Design* 123 (2017). Proceedings of the 29th Symposium on Fusion Technology (SOFT-29) Prague, Czech Republic, September 5-9, 2016, pp. 11–16. ISSN: 0920-3796. DOI: https://doi.org/10.1016/j.fusengdes.2017.03.002. URL: http://www.sciencedirect.com/science/article/pii/S0920379617302053.

[23] S. Carli et al. "Interchange-turbulence-based radial transport model for SOLPS-ITER: A COMPASS case study". In: *Contributions to Plasma Physics* 60.5-6 (2020), e201900155. DOI: https://doi.org/10.1002/ctpp.201900155. eprint: https://onlinelibrary.wiley.com/doi/pdf/10.1002/ctpp.201900155. URL: https://onlinelibrary.wiley.com/doi/abs/10.1002/ctpp.201900155.

[24] S. Carli et al. "Bayesian maximum a posteriori-estimation of K turbulence model parameters using algorithmic differentiation in SOLPS-ITER". In: *Contributions to Plasma Physics* 62.5-6 (2022), e202100184. DOI: https://doi.org/10.1002/ctpp.202100184. eprint: https://onlinelibrary.wiley.com/doi/pdf/10.1002/ctpp.202100184.

URL: https://onlinelibrary.wiley.com/doi/abs/10.1002/ctpp.202100184.

[25] K. Hromasova et al. *SOLPS-doc: SOLPS-ITER documentation for beginners*. Ed. by Katerina Hromasova. May 31, 2023. URL: https://solps.pages.tok.ipp.cas.cz/solps-doc/.

[26] S. I. Braginskii. "Transport Processes in Plasma". In: *Reviews of Plasma Physics* 1 (1965), p. 205.

[27] R. Balescu. *Transport processes in plasmas I*. North Holland, New York, 1998.

[28] V. Zhdanov. *Transport Processes in Multicomponent Plasma*. Taylor, Francis, New York, and London, 2002.

[29] E. Havlickova et al. "Benchmarking of a 1D scrape-off layer code SOLF1D with SOLPS and its use in modelling long-legged divertors". In: *Plasma Physics and Controlled Fusion* 55.6 (May 2013), p. 065004. DOI: 10.1088/0741-3335/55/6/065004. URL: https://iopscience.iop.org/article/10.1088/0741-3335/55/6/065004.

[30] H. Bufferand et al. "Implementation of drift velocities and currents in SOLEDGE2D-EIRENE". In: *Nuclear Materials and Energy* 12 (2017). Proceedings of the 22nd International Conference on Plasma Surface Interactions 2016, 22nd PSI, pp. 852–857. ISSN: 2352-1791. DOI: https://doi.org/10.1016/j.nme.2016.11.031. URL: http://www.sciencedirect.com/science/article/pii/S2352179116301946.

[31] Y. Feng et al. "3D Edge Modeling and Island Divertor Physics". In: *Contributions to Plasma Physics* 44.1-3 (2004), pp. 57–69. DOI: 10.1002/ctpp.200410009. eprint: https://onlinelibrary.wiley.com/doi/pdf/10.1002/ctpp.200410009. URL: https://onlinelibrary.wiley.com/doi/abs/10.1002/ctpp.200410009.

[32] M. Baelmans D. Reiter and P. Borner. "The EIRENE and B2-EIRENE Codes". In: *Fusion Science and Technology* 47.2 (2005), pp. 172–186. DOI: 10.13182/FST47-172. eprint: https://doi.org/10.13182/FST47-172. URL: https://doi.org/10.13182/FST47-172.

[33] D. P. Coster et al. *SOLPS-ITER manual*. SOLPS-ITER version 3.0.9-27-g614fb016.

[34] P. Kulhanek. *Uvod do teorie plazmatu*. 2017. ISBN: 978-80904582-2-2. URL: https://www.aldebaran.cz/studium/fpla.pdf.

[35] R. D. Hazeltine and P. J. Catto. "Tokamak Edge Transport Theory". In: *Contributions to Plasma Physics* 36.2-3 (1996), pp. 177–181. DOI: https://doi.org/10.1002/ctpp.2150360215. eprint: https://onlinelibrary.wiley.com/doi/pdf/10.1002/ctpp.2150360215. URL: https://onlinelibrary.wiley.com/doi/abs/10.1002/ctpp.2150360215.

[36] R. D. Hazeltine. "Transport theory in the collisionless limit". In: *Physics of Plasmas* 5.9 (Sept. 1998), pp. 3282–3286. ISSN: 1070-664X. DOI: 10.1063/1.872996. eprint: https://pubs.aip.org/aip/pop/article-pdf/5/9/3282/12309197/3282_1_online.pdf. URL: https://doi.org/10.1063/1.872996.

[37] T. D. Rognlien and D. D. Ryutov. "Analysis of Classical Transport Equations for the Tokamak Edge Plasma". In: *Contributions to Plasma Physics* 38.1-2 (1998), pp. 152–157. DOI: https://doi.org/10.1002/ctpp.2150380123. eprint: https://onlinelibrary.wiley.com/doi/pdf/10.1002/ctpp.2150380123. URL: https://onlinelibrary.wiley.com/doi/abs/10.1002/ctpp.2150380123.

[38] E. Zawaideh, N. S. Kim, and F. Najmabadi. "Generalized parallel heat transport equations in collisional to weakly collisional plasmas". In: *The Physics of Fluids* 31.11 (Nov. 1988), pp. 3280–3285. ISSN: 0031-9171. DOI: 10.1063/1.866940. eprint: https://pubs.aip.org/aip/pfl/article-pdf/31/11/3280/12354109/3280_1_online.pdf. URL: https://doi.org/10.1063/1.866940.

[39] W. Fundamenski. "Parallel heat flux limits in the tokamak scrape-off layer". In: *Plasma Physics and Controlled Fusion* 47.11 (Oct. 2005), R163–R208. DOI: 10.1088/0741-3335/47/11/r01. URL: https://doi.org/10.1088/0741-3335/47/11/r01.

[40] A. V. Chankin, G. Corrigan, and A. E. Jarvinen. "Assessment of the strength of kinetic effects of parallel electron transport in the SOL and divertor of JET high radiative H-mode plasmas using EDGE2D-EIRENE and KIPP codes". In: *Plasma Physics and Controlled Fusion* 60.11 (2018). ISSN: 0741-3335. DOI: 10.1088/1361-6587/aae0a0. URL: https://iopscience.iop.org/article/10.1088/1361-6587/aae0a0.

[41] F. I. Parra. *Braginskii fluid equations*. Rudolf Peierls Centre for Theoretical Physics, University of Oxford. 2019. URL: http://www-thphys.physics.ox.ac.uk/people/FelixParra/CollisionalPlasmaPhysics/notes/lecIV%5C_braginskii.pdf.

[42] J. Wesson and D. Campbell. *Tokamaks*. 4th ed. New York: Oxford University Press, 2011. ISBN: 0199592233.

[43] R. Schneider et al. "Plasma Edge Physics with B2-Eirene". In: *Contributions to Plasma Physics* 46.1-2 (2006), pp. 3–191. DOI: 10.1002/ctpp.200610001. eprint: https://onlinelibrary.wiley.com/doi/pdf/10.1002/ctpp.200610001. URL: https://onlinelibrary.wiley.com/doi/abs/10.1002/ctpp.200610001.

[44] M. Zhao, A. V. Chankin, and D. P. Coster. "Kinetic simulations of electron heat flux in the scrape-off layer". In: *Nuclear Materials and Energy* 12 (2017). Proceedings of the 22nd International Conference on Plasma Surface Interactions 2016, 22nd PSI, pp. 819–824. ISSN: 2352-1791. DOI: https://doi.org/10.1016/j.nme.2017.01.025.

URL: https://www.sciencedirect.com/science/article/pii/S2352179116300576.

[45] D. Tskhakaya et al. "On Kinetic Effects during Parallel Transport in the SOL". In: *Contributions to Plasma Physics* 48.1-3 (2008), pp. 89–93. DOI: https://doi.org/10.1002/ctpp.200810015. eprint: https://onlinelibrary.wiley.com/doi/pdf/10.1002/ctpp.200810015. URL: https://onlinelibrary.wiley.com/doi/abs/10.1002/ctpp.200810015.

[46] M. R. K. Wigram et al. "Incorporating nonlocal parallel thermal transport in 1D ITER SOL modelling". In: *Nuclear Fusion* 60.7 (2020). ISSN: 0029-5515. DOI: 10.1088/1741-4326/ab868b. URL: https://iopscience.iop.org/article/10.1088/1741-4326/ab868b.

[47] Z. Abou-Assaleh et al. "Fokker-Planck Modelling of Edge Plasma Near the Neutralizer Plate in a Tokamak". In: *Contributions to Plasma Physics* 32.3-4 (1992), pp. 268–272. DOI: https://doi.org/10.1002/ctpp.2150320315. eprint: https://onlinelibrary.wiley.com/doi/pdf/10.1002/ctpp.2150320315. URL: https://onlinelibrary.wiley.com/doi/abs/10.1002/ctpp.2150320315.

[48] M. Zhao, A. Chankin, and D. Coster. "An iterative algorithm of coupling the Kinetic Code for Plasma Periphery (KIPP) with SOLPS". In: *Computer Physics Communications* 235 (2019), pp. 133–152. ISSN: 0010-4655. DOI: https://doi.org/10.1016/j.cpc.2018.09.012. URL: https://www.sciencedirect.com/science/article/pii/S0010465518303266.

[49] R. H. Cohen and T. D. Rognlien. "Finite Mean-Free-Path Effects in Tokamak Scrape-Off Layers". In: *Contributions to Plasma Physics* 34.2-3 (1994), pp. 198–203.

[50] P. Manz et al. "The diffusion limit of ballistic transport in the scrape-off layer". In: *Physics of Plasmas* 27.2 (2020), p. 022506. DOI: 10.1063/1.5133839. eprint: https://doi.org/10.1063/1.5133839. URL: https://doi.org/10.1063/1.5133839.

[51] D. P. Coster et al. "Simulation of the Edge Plasma in Tokamaks". In: *Physica Scripta* (2004). ISSN: 0031-8949. DOI: 10.1238/Physica.Topical.108a00007. URL: https://iopscience.iop.org/article/10.1238/Physica.Topical.108a00007.

[52] D. Coster. *Personal communication*. Oct. 2019.

[53] L. Balbinot et al. "Multi-code estimation of DTT edge transport parameters". In: *Nuclear Materials and Energy* 34 (2023), p. 101350. ISSN: 2352-1791. DOI: https://doi.org/10.1016/j.nme.2022.101350. URL: https://www.sciencedirect.com/science/article/pii/S2352179122002319.

[54] B. J. Braams. "Computational studies in tokamak equilibrium and transport". PhD thesis. Rijksuniversiteit Utrecht (Netherlands), 1982.

[55] A. Zito et al. "Numerical modelling of an enhanced perpendicular transport regime in the scrape-off layer of ASDEX Upgrade". In: *Plasma Physics and Controlled Fusion* 63.7 (2021). ISSN: 0741-3335. DOI: 10.1088/1361-6587/abfcb6. URL: https://iopscience.iop.org/article/10.1088/1361-6587/abfcb6.

[56] Czech Academy of Sciences Institute of Plasma Physics. *COMPASS Tokamak*. Sept. 1, 2023. URL: https://www.ipp.cas.cz/vedecka_struktura_ufp/tokamak/COMPASS/.

[57] R. Panek et al. "Reinstallation of the COMPASS-D tokamak in IPP ASCR". In: *Czechoslovak Journal of Physics* 56.S2 (2006), B125–B137. ISSN: 0011-4626. DOI: 10.1007/s10582-006-0188-1. URL: http://link.springer.com/10.1007/s10582-006-0188-1.

[58] R. Panek et al. "Status of the COMPASS tokamak and characterization of the first H-mode". In: *Plasma Physics and Controlled Fusion* vol. 58.issue 1 (Jan. 1, 2016), p. 014015. ISSN: 07413335. DOI: 10.1088/0741-3335/58/1/014015. URL: http://stacks.iop.org/0741-3335/58/i=1/a=014015?key=crossref.cbd9509a544f4d9eb76fe62b71a66a58.

[59] V. Weinzettl et al. "Overview of the COMPASS diagnostics". In: *Fusion Engineering and Design* 86.6-8 (2011), pp. 1227–1231. ISSN: 09203796. DOI: 10.1016/j.fusengdes.2010.12.024. URL: http://linkinghub.elsevier.com/retrieve/pii/S0920379610005594.

[60] V. Weinzettl et al. "Progress in diagnostics of the COMPASS tokamak". In: *Journal of Instrumentation* 12.12 (2017), p. C12015. URL: http://stacks.iop.org/1748-0221/12/i=12/a=C12015.

[61] P. Bilkova et al. "Design of new Thomson scattering diagnostic system on COMPASS tokamak". In: *Nuclear Instruments and Methods in Physics Research Section A: Accelerators, Spectrometers, Detectors and Associated Equipment* 623.2 (2010). 1rs International Conference on Frontiers in Diagnostics Technologies, pp. 656–659. ISSN: 0168-9002. DOI: https://doi.org/10.1016/j.nima.2010.03.121. URL: https://www.sciencedirect.com/science/article/pii/S0168900210007047.

[62] P. Bilkova et al. "High resolution Thomson scattering on the COMPASS tokamak - extending edge plasma view and increasing repetition rate". In: *Journal of Instrumentation* 13.01 (2018), p. C01024. URL: http://stacks.iop.org/1748-0221/13/i=01/a=C01024.

[63] G. Anda et al. "Lithium beam diagnostic system on the COMPASS tokamak". In: *Fusion Engineering and Design* 108 (2016), pp. 1–6. ISSN: 0920-3796. DOI: https://doi.org/10.1016/j.fusengdes.2016.04.022. URL: https://www.sciencedirect.com/science/article/pii/S0920379616303131.

[64] M. Berta et al. "Li-BES detection system for plasma turbulence measurements on the COMPASS tokamak". In: *Fusion Engineering and Design* 96-97 (2015). Proceedings of the 28th Symposium On Fusion Technology (SOFT-28), pp. 795–798. ISSN: 0920-3796. DOI: https://doi.org/10.1016/j.fusengdes.2015.06.030. URL: https://www.sciencedirect.com/science/article/pii/S0920379615300442.

[65] J. Adamek et al. "Profile measurements of the electron temperature on the ASDEX Upgrade, COMPASS, and ISTTOK tokamak using Thomson scattering, triple, and ball-pen probes". In: *Review of Scientific Instruments* 87.4 (2016), p. 043510. ISSN: 0034-6748. DOI: 10.1063/1.4945797. URL: http://aip.scitation.org/doi/10.1063/1.4945797.

[66] C. G. Silva et al. "Divertor Langmuir Probe Measurements on COMPASS-D". In: *Contributions to Plasma Physics* 38.S1 (1998), pp. 47–52. DOI: https://doi.org/10.1002/ctpp.19980380112. eprint: https://onlinelibrary.wiley.com/doi/pdf/10.1002/ctpp.19980380112. URL: https://onlinelibrary.wiley.com/doi/abs/10.1002/ctpp.19980380112.

[67] P. Vondracek et al. "Fast infrared thermography on the COMPASS tokamak". In: *Fusion Engineering and Design* 123 (2017). Proceedings of the 29th Symposium on Fusion Technology (SOFT-29) Prague, Czech Republic, September 5-9, 2016, pp. 764–767. ISSN: 0920-3796. DOI: https://doi.org/10.1016/j.fusengdes.2017.05.004. URL: https://www.sciencedirect.com/science/article/pii/S0920379617305392.

[68] IPP Prague. *Tokamak COMPASS Parameters*. URL: http://www.ipp.cas.cz/vedecka%5C_struktura%5C_ufp/tokamak/tokamak%5C_compass/.

[69] M. Spolaore et al. "Electromagnetic ELM and inter-ELM filaments detected in the COMPASS Scrape-Off Layer". In: *Nuclear Materials and Energy* 12 (2017). Proceedings of the 22nd International Conference on Plasma Surface Interactions 2016, 22nd PSI, pp. 844–851. ISSN: 2352-1791. DOI: https://doi.org/10.1016/j.nme.2016.12.014. URL: https://www.sciencedirect.com/science/article/pii/S2352179116301934.

[70] J. Adamek et al. "Electron temperature and heat load measurements in the COMPASS divertor using the new system of probes". In: *Nuclear Fusion* 57.11 (2017), p. 116017. URL: http://stacks.iop.org/0029-5515/57/i=11/a=116017.

[71] D. Carralero et al. "Implications of high density operation on SOL transport: A multimachine investigation". In: *Journal of Nuclear Materials* 463 (2015). PLASMA-SURFACE INTERACTIONS 21, pp. 123–127. ISSN: 0022-3115. DOI: https://doi.org/10.1016/j.

jnucmat.2014.10.019. URL: https://www.sciencedirect.com/science/article/pii/S002231151400703X.

[72] E. Stefanikova et al. "Fitting of the Thomson scattering density and temperature profiles on the COMPASS tokamak". In: *Review of Scientific Instruments* 87.11 (2016), 11E536. DOI: 10.1063/1.4961554. eprint: https://aip.scitation.org/doi/pdf/10.1063/1.4961554. URL: https://aip.scitation.org/doi/abs/10.1063/1.4961554.

[73] M. Komm et al. "First detachment studies on COMPASS tokamak using nitrogen seeding". In: *44th EPS Conference on Plasma Physics*. 2017.

[74] E. Stefanikova et al. "Effect of the relative shift between the electron density and temperature pedestal position on the pedestal stability in JET-ILW and comparison with JET-C". In: *Nuclear Fusion* 58.5 (Mar. 2018), p. 056010. DOI: 10.1088/1741-4326/aab216. URL: https://doi.org/10.1088/1741-4326/aab216.

[75] O. Grover et al. "Limit cycle oscillations measurements with Langmuir and ball-pen probes on COMPASS". In: *Nuclear Fusion* 58.11 (Oct. 2018), p. 112010. DOI: 10.1088/1741-4326/aabb19. URL: https://doi.org/10.1088/1741-4326/aabb19.

[76] J. Adamek et al. "Fast measurements of the electron temperature and parallel heat flux in ELMy H-mode on the COMPASS tokamak". In: *Nuclear Fusion* 57.2 (Sept. 2016), p. 022010. DOI: 10.1088/0029-5515/57/2/022010. URL: https://doi.org/10.1088/0029-5515/57/2/022010.

[77] T. Markovic et al. "Measurements and modelling of plasma response field to RMP on the COMPASS tokamak". In: *Nuclear Fusion* 56.9 (July 2016), p. 092010. DOI: 10.1088/0029-5515/56/9/092010. URL: https://doi.org/10.1088/0029-5515/56/9/092010.

[78] J. Horacek et al. "ELM temperature in JET and COMPASS tokamak divertors". In: *Nuclear Fusion* 63.5 (Mar. 2023), p. 056007. DOI: 10.1088/1741-4326/acbf68. URL: https://dx.doi.org/10.1088/1741-4326/acbf68.

[79] F. Camilo de Souza et al. "Geodesic mode instability driven by electron and ion fluxes during neutral beam injection in tokamaks". In: *Physics Letters A* 381.36 (2017), pp. 3066–3070. ISSN: 0375-9601. DOI: https://doi.org/10.1016/j.physleta.2017.07.033. URL: https://www.sciencedirect.com/science/article/pii/S0375960117306989.

[80] J. Seidl et al. "Electromagnetic characteristics of geodesic acoustic mode in the COMPASS tokamak". In: *Nuclear Fusion* 57.12 (Dec. 1, 2017), p. 126048. ISSN: 0029-5515. DOI: 10.1088/1741-4326/aa897e. URL: http://stacks.iop.org/0029-5515/57/i=12/a=126048?key=crossref.8e41de493084efddc3884bd2b69878d2.

[81] R. Dejarnac et al. “Understanding narrow SOL power flux component in COMPASS limiter plasmas by use of Langmuir probes”. In: *Journal of Nuclear Materials* 463 (2015). PLASMA-SURFACE INTERACTIONS 21, pp. 381–384. ISSN: 0022-3115. DOI: https://doi.org/10.1016/j.jnucmat.2014.12.100. URL: https://www.sciencedirect.com/science/article/pii/S0022311514010538.

[82] M. Kocan et al. “Modelling ELM heat flux deposition on the ITER main chamber wall”. In: *Journal of Nuclear Materials* vol. 463.1 (2015), pp. 709–713. ISSN: 00223115. DOI: 10.1016/j.jnucmat.2014.11.130. URL: http://linkinghub.elsevier.com/retrieve/pii/S0022311514009374.

[83] J. Horacek et al. “Narrow heat flux channels in the COMPASS limiter scrape-off layer”. In: *Journal of Nuclear Materials* 463 (2015). PLASMA-SURFACE INTERACTIONS 21, pp. 385–388. ISSN: 0022-3115. DOI: https://doi.org/10.1016/j.jnucmat.2014.11.132. URL: https://www.sciencedirect.com/science/article/pii/S0022311514009398.

[84] J. Horacek et al. “Multi-machine scaling of the main SOL parallel heat flux width in tokamak limiter plasmas”. In: *Plasma Physics and Controlled Fusion* vol. 58.issue 7 (July 1, 2016), p. 074005. ISSN: 07413335. DOI: 10.1088/0741-3335/58/7/074005. URL: http://stacks.iop.org/0741-3335/58/i=7/a=074005?key=crossref.82c59846a9ca0582d8eea37c24368b57.

[85] M. Komm et al. “Divertor impurity seeding experiments at the COMPASS tokamak”. In: *Nuclear Fusion* 59.10 (Sept. 2019), p. 106035. DOI: 10.1088/1741-4326/ab34d2. URL: https://doi.org/10.1088/1741-4326/ab34d2.

[86] M. Komm et al. “Power exhaust by core radiation at COMPASS tokamak”. In: *Nuclear Fusion* (2020). URL: http://iopscience.iop.org/article/10.1088/1741-4326/abd3ea.

[87] C. Silva et al. “Comparison of fluctuations properties measured by Langmuir and ball-pen probes in the ISTTOK boundary plasma”. In: *Plasma Physics and Controlled Fusion* 57.2 (Dec. 2014), p. 025003. DOI: 10.1088/0741-3335/57/2/025003. URL: https://doi.org/10.1088/0741-3335/57/2/025003.

[88] N. R. Walkden et al. “Profile measurements in the plasma edge of mega amp spherical tokamak using a ball pen probe”. In: *Review of Scientific Instruments* 86.2 (2015), p. 023510. DOI: 10.1063/1.4908572. eprint: https://doi.org/10.1063/1.4908572. URL: https://doi.org/10.1063/1.4908572.

[89] J. Cavalier et al. “Tomographic reconstruction of tokamak edge turbulence from single visible camera data and automatic turbulence structure tracking”. In: *Nuclear Fusion* 59.5 (Apr. 2019), p. 056025.

DOI: 10.1088/1741-4326/ab0d4c. URL: https://doi.org/10.1088/1741-4326/ab0d4c.

[90] O. Grover et al. "First simultaneous measurements of Reynolds stress with ball-pen and Langmuir probes". In: *Review of Scientific Instruments* 88.6 (2017). ISSN: 0034-6748. DOI: 10.1063/1.4984240. URL: http://aip.scitation.org/doi/10.1063/1.4984240.

[91] R. Dejarnac et al. "Overview of power exhaust experiments in the COMPASS divertor with liquid metals". In: *Nuclear Materials and Energy* 25 (2020), p. 100801. ISSN: 2352-1791. DOI: https://doi.org/10.1016/j.nme.2020.100801. URL: http://www.sciencedirect.com/science/article/pii/S2352179120300776.

[92] J. Horacek et al. "Predictive modelling of liquid metal divertor: from COMPASS tokamak towards Upgrade". In: *Physica Scripta* 96.12 (Aug. 2021), p. 124013. DOI: 10.1088/1402-4896/ac1dc9. URL: https://dx.doi.org/10.1088/1402-4896/ac1dc9.

[93] A. V. Melnikov et al. "Quasicoherent modes on the COMPASS tokamak". In: *Plasma Physics and Controlled Fusion* 57.6 (Apr. 2015), p. 065006. DOI: 10.1088/0741-3335/57/6/065006. URL: https://doi.org/10.1088/0741-3335/57/6/065006.

[94] I. Borodkina et al. "An Analytical Expression for the Electric Field and Particle Tracing in Modelling of Be Erosion Experiments at the JET ITER-like Wall". In: *Contributions to Plasma Physics* 56.6-8 (2016), pp. 640–645. DOI: https://doi.org/10.1002/ctpp.201610032. eprint: https://onlinelibrary.wiley.com/doi/pdf/10.1002/ctpp.201610032. URL: https://onlinelibrary.wiley.com/doi/abs/10.1002/ctpp.201610032.

[95] J. Cavalier et al. "Strongly emissive plasma-facing material under space-charge limited regime: Application to emissive probes". In: *Physics of Plasmas* 24.1 (2017), p. 013506. DOI: 10.1063/1.4973557. eprint: https://doi.org/10.1063/1.4973557. URL: https://doi.org/10.1063/1.4973557.

[96] R. Dejarnac et al. "Heat loads on poloidal and toroidal edges of castellated plasma-facing components in COMPASS". In: *Nuclear Fusion* 58.6 (Apr. 2018), p. 066003. DOI: 10.1088/1741-4326/aab973. URL: https://doi.org/10.1088/1741-4326/aab973.

[97] O. Ficker et al. "Runaway electron beam stability and decay in COMPASS". In: *Nuclear Fusion* 59.9 (Aug. 2019), p. 096036. DOI: 10.1088/1741-4326/ab210f. URL: https://doi.org/10.1088/1741-4326/ab210f.

[98] O. Ficker et al. "Losses of runaway electrons in MHD-active plasmas of the COMPASS tokamak". In: *Nuclear Fusion* 57.7 (May 2017), p. 076002. DOI: 10.1088/1741-4326/aa6aba. URL: https://doi.org/10.1088/1741-4326/aa6aba.

[99] S. N. Gerasimov et al. "JET and COMPASS asymmetrical disruptions". In: *Nuclear Fusion* 55.11 (Sept. 2015), p. 113006. DOI: 10.1088/0029-5515/55/11/113006. URL: https://doi.org/10.1088/0029-5515/55/11/113006.

[100] J. Mlynar et al. "Runaway electron experiments at COMPASS in support of the EUROfusion ITER physics research". In: *Plasma Physics and Controlled Fusion* 61.1 (Nov. 2018), p. 014010. DOI: 10.1088/1361-6587/aae04a. URL: https://doi.org/10.1088/1361-6587/aae04a.

[101] M. Vlainic et al. "Post-disruptive runaway electron beams in the COMPASS tokamak". In: *Journal of Plasma Physics* 81.5 (2015), p. 475810506. DOI: 10.1017/S0022377815000914.

[102] V. V. Plyusnin et al. "Comparison of runaway electron generation parameters in small, medium-sized and large tokamaks - A survey of experiments in COMPASS, TCV, ASDEX-Upgrade and JET". In: *Nuclear Fusion* 58.1 (Nov. 2017), p. 016014. DOI: 10.1088/1741-4326/aa8f05. URL: https://doi.org/10.1088/1741-4326/aa8f05.

[103] M. Aftanas et al. "Thomson scattering on COMPASS — commissioning and first data". In: *Journal of Instrumentation* 7.01 (Jan. 2012), p. C01074. DOI: 10.1088/1748-0221/7/01/C01074. URL: https://dx.doi.org/10.1088/1748-0221/7/01/C01074.

[104] P. Bohm et al. "Edge Thomson scattering diagnostic on COMPASS tokamak". In: *Review of Scientific Instruments* 85.11 (2014), p. 431. ISSN: 00346748. DOI: 10.1063/1.4893995. URL: http://scitation.aip.org/content/aip/journal/rsi/85/11/10.1063/1.4893995.

[105] M. Aftanas. "Thomson Scattering Diagnostic on COMPASS Tokamak". PhD thesis. Charles University in Prague, Faculty of Mathematics and Physics, 2015.

[106] M. Aftanas et al. "High-resolution Thomson scattering system on the COMPASS tokamak: Evaluation of plasma parameters and error analysisa)". In: *Review of Scientific Instruments* 83.10 (Aug. 2012), 10E350. ISSN: 0034-6748. DOI: 10.1063/1.4743956. eprint: https://pubs.aip.org/aip/rsi/article-pdf/doi/10.1063/1.4743956/13705285/10e350_1_online.pdf. URL: https://doi.org/10.1063/1.4743956.

[107] M. Sos. *Personal communication*. Sept. 2023.

[108] M. Dimitrova et al. "Plasma potential and electron temperature evaluated by ball-pen and Langmuir probes in the COMPASS tokamak". In: *Plasma Physics and Controlled Fusion* 59.12 (Dec. 1, 2017), p. 125001. ISSN: 0741-3335. DOI: 10.1088/1361-6587/aa8689. URL: http://stacks.iop.org/0741-3335/59/i=12/a=125001?key=crossref.716f6ad2dc28954893adc5aba3c075e7.

[109] J. Adamek et al. “A novel approach to direct measurement of the plasma potential”. In: *Czechoslovak Journal of Physics* 54.3 (2004), pp. 95–99. ISSN: 00114626. DOI: 10.1007/BF03166386. URL: http://link.springer.com/10.1007/BF03166386.

[110] J. Adamek et al. “Direct Measurements of the Electron Temperature by a Ball-pen/Langmuir probe”. In: *32nd EPS Conference on Plasma Physics, Tarragona*. 2005.

[111] J. Adamek et al. “Ball-Pen Probe Measurements in L-Mode and H-Mode on ASDEX Upgrade”. In: *Contributions to Plasma Physics* 50.9 (2010), pp. 854–859. ISSN: 08631042. DOI: 10.1002/ctpp.201010145. URL: http://doi.wiley.com/10.1002/ctpp.201010145.

[112] S. Murphy-Sugrue et al. “Improved understanding of the ball-pen probe through particle-in-cell simulations”. In: *Plasma Physics and Controlled Fusion* 59.5 (Mar. 2017), p. 055007. DOI: 10.1088/1361-6587/aa60d0. URL: https://dx.doi.org/10.1088/1361-6587/aa60d0.

[113] K. Uehara et al. “Direct Measurement of Ion Behavior using Modified Ion Sensitive Probe in Tokamak Boundary Plasma”. In: *Journal of the Physical Society of Japan* 66.4 (1997), pp. 921–924. DOI: 10.1143/jpsj.66.921.

[114] K. Uehara et al. “Evaluation of Ion Temperature Using Ion Sensitive Probe in the Boundary Plasma of the JFT-2M Tokamak”. In: *Journal of the Physical Society of Japan* 72.11 (2003), pp. 2804–2810. DOI: 10.1143/JPSJ.72.2804. eprint: https://doi.org/10.1143/JPSJ.72.2804. URL: https://doi.org/10.1143/JPSJ.72.2804.

[115] M. Komm et al. “Transport of electrons in the tunnel of an ion sensitive probe”. In: *Plasma Physics and Controlled Fusion* 53.1 (Nov. 2010), p. 015005. DOI: 10.1088/0741-3335/53/1/015005. URL: https://dx.doi.org/10.1088/0741-3335/53/1/015005.

[116] I. Katsumata and M. Okazaki. “Ion Sensitive Probe-A New Diagnostic Method for Plasma in Magnetic Fields”. In: *Japanese Journal of Applied Physics, Part 1: Regular Papers and Short Notes and Review Papers* 6.1 (1967), pp. 123–124. DOI: 10.1143/JJAP.6.123. URL: https://www.scopus.com/inward/record.uri?eid=2-s2.0-84996382127&doi=10.1143%2fJJAP.6.123&partnerID=40&md5=938de3de91fd8618eaeae5a78d90d079.

[117] J. Adamek et al. “Simultaneous Measurements of Ion Temperature by Segmented Tunnel and Katsumata Probe”. In: *Contributions to Plasma Physics* 48.5-7 (2008), pp. 395–399. DOI: https://doi.org/10.1002/ctpp.200810063. eprint: https://onlinelibrary.wiley.com/doi/pdf/10.1002/ctpp.200810063. URL: https://onlinelibrary.wiley.com/doi/abs/10.1002/ctpp.200810063.

[118] K. Jirakova. "Study of edge plasma of tokamak COMPASS and its poloidal variations". MA thesis. Faculty of Nuclear Sciences and Physical Engineering, Czech Technical University, Czech Republic, Sept. 30, 2018.

[119] J. Horacek et al. "Interpretation of fast measurements of plasma potential, temperature and density in SOL of ASDEX Upgrade". In: *Nuclear Fusion* 50.10 (2010). ISSN: 00295515. DOI: 10.1088/0029-5515/50/10/105001. URL: http://stacks.iop.org/0029-5515/50/i=10/a=105001?key=crossref.176b9ce6cd2ce3fcc74a48317cd3a88c.

[120] P. Macha. *Personal communication*. Dec. 2023.

[121] A. Podolnik et al. "3D particle-in-cell modeling of Langmuir probe effective collecting area in magnetized plasma". In: *Plasma Physics and Controlled Fusion* 60.8 (June 2018), p. 085008. DOI: 10.1088/1361-6587/aac701. URL: https://dx.doi.org/10.1088/1361-6587/aac701.

[122] M. Komm et al. "On the applicability of three and four parameter fits for analysis of swept embedded Langmuir probes in magnetised plasma". In: *Nuclear Fusion* 62.9 (Aug. 2022), p. 096021. DOI: 10.1088/1741-4326/ac8011. URL: https://dx.doi.org/10.1088/1741-4326/ac8011.

[123] P. Vondracek. "Plasma Heat Flux to Solid Structures in Tokamaks". PhD thesis. Faculty of Mathematics and Physics, Charles University in Prague, Apr. 29, 2019.

[124] J. Hecko et al. "Experimental evidence of very short power decay lengths in H-mode discharges in the COMPASS tokamak". In: *Plasma Physics and Controlled Fusion* 66.1 (Dec. 2023), p. 015013. DOI: 10.1088/1361-6587/ad08f0. URL: https://dx.doi.org/10.1088/1361-6587/ad08f0.

[125] J. Hecko et al. "Investigating drift effects in the COMPASS tokamak". In: *Fusenet PhD Event, Lausanne, Switzerland*. Aug. 24, 2023.

[126] D. Brunner et al. "The dependence of divertor power sharing on magnetic flux balance in near double-null configurations on Alcator C-Mod". In: *Nuclear Fusion* 58.7 (May 2018), p. 076010. DOI: 10.1088/1741-4326/aac006. URL: https://dx.doi.org/10.1088/1741-4326/aac006.

[127] D. Tskhakaya et al. "Kinetic model of the COMPASS tokamak SOL". In: *Nuclear Materials and Energy* 26 (2021), p. 100893. ISSN: 2352-1791. DOI: https://doi.org/10.1016/j.nme.2020.100893. URL: http://www.sciencedirect.com/science/article/pii/S2352179120301551.

[128] E. Hasan et al. "Advantages of the first-derivative probe technique over the three- and four-parameter probe techniques in fusion plasmas diagnostics". In: *Journal of Instrumentation* 13.04 (Apr. 2018), P04005. DOI: 10.1088/1748-0221/13/04/P04005. URL: https://dx.doi.org/10.1088/1748-0221/13/04/P04005.

[129] J.-L. Jauberteau et al. "Langmuir probe in magnetized plasma: Determination of the electron diffusion parameter and of the electron energy distribution function". In: *Contributions to Plasma Physics* 60.2 (2020), e201900067. DOI: https://doi.org/10.1002/ctpp.201900067. eprint: https://onlinelibrary.wiley.com/doi/pdf/10.1002/ctpp.201900067. URL: https://onlinelibrary.wiley.com/doi/abs/10.1002/ctpp.201900067.

[130] J.-L. Jauberteau et al. "Langmuir probe in magnetized plasma: Study of the diffusion parameter". In: *Contributions to Plasma Physics* 62.1 (2022), e202100066. DOI: https://doi.org/10.1002/ctpp.202100066. eprint: https://onlinelibrary.wiley.com/doi/pdf/10.1002/ctpp.202100066. URL: https://onlinelibrary.wiley.com/doi/abs/10.1002/ctpp.202100066.

[131] M. Komm. *Personal communication*. July 2023.

[132] M. Greenwald et al. "20 years of research on the Alcator C-Mod tokamaka)". In: *Physics of Plasmas* 21.11 (Nov. 2014), p. 110501. ISSN: 1070-664X. DOI: 10.1063/1.4901920. eprint: https://pubs.aip.org/aip/pop/article-pdf/doi/10.1063/1.4901920/15941137/110501_1_online.pdf. URL: https://doi.org/10.1063/1.4901920.

[133] W. Dekeyser et al. "SOLPS-ITER Modeling of the Alcator C-Mod Divertor Plasma". In: *Plasma and Fusion Research* 11 (2016), pp. 1403103–1403103. DOI: 10.1585/pfr.11.1403103.

[134] R. Reksoatmodjo et al. "The role of edge fueling in determining the pedestal density in high neutral opacity Alcator C-Mod experiments". In: *Nuclear Materials and Energy* 27 (2021), p. 100971. ISSN: 2352-1791. DOI: https://doi.org/10.1016/j.nme.2021.100971. URL: https://www.sciencedirect.com/science/article/pii/S2352179121000557.

[135] J. Seidl et al. *SOLPS-postproc*. Ed. by J. Seidl. Sept. 1, 2023. URL: https://repo.tok.ipp.cas.cz/dms/solps-postproc.

[136] D. Svorc. "Validation of tokamak equilibrium reconstructions using the SOLPS-ITER edge plasma transport code simulations". MA thesis. Faculty of Nuclear Sciences and Engineering, Czech Technical University, Prague, May 10, 2024.

[137] L. C. Appel, M. K. Bevir, and M. J. Walsh. "Equilibrium reconstruction in the START tokamak". In: *Nuclear Fusion* 41.2 (Feb. 2001), pp. 169–180. DOI: 10.1088/0029-5515/41/2/303. URL: https://doi.org/10.1088/0029-5515/41/2/303.

[138] L. C. Appel et al. “A unified approach to equilibrium reconstruction”. In: *Proceedings of the 33rd EPS conference on Controlled Fusion and Plasma Physics, P-2.160*. 2006.

[139] J. Blum et al. “Problems and methods of self-consistent reconstruction of tokamak equilibrium profiles from magnetic and polarimetric measurements”. In: *Nuclear Fusion* 30.8 (Aug. 1990), p. 1475. DOI: 10.1088/0029-5515/30/8/007. URL: https://dx.doi.org/10.1088/0029-5515/30/8/007.

[140] A. Kallenbach et al. “EDGE2D modelling of edge profiles obtained in JET diagnostic optimized configuration”. In: *Plasma Physics and Controlled Fusion* 46.3 (Jan. 2004), pp. 431–446. DOI: 10.1088/0741-3335/46/3/001. URL: https://doi.org/10.1088/0741-3335/46/3/001.

[141] G. Szepesi et al. “Advanced equilibrium reconstruction for JET with EFIT++”. In: *Proceedings of the 47th EPS conference on plasma physics, Sitges, Spain*. 2021. URL: https://info.fusion.ciemat.es/OCS/EPS2021PAP/pdf/P3.1037.pdf.

[142] K. Jirakova et al. “Systematic errors in tokamak magnetic equilibrium reconstruction: a study of EFIT++ at tokamak COMPASS”. In: *Journal of Instrumentation* 14.11 (Nov. 2019), pp. C11020–C11020. DOI: 10.1088/1748-0221/14/11/c11020. URL: https://iopscience.iop.org/article/10.1088/1748-0221/14/11/C11020.

[143] J. F. Artaud et al. “Metis: a fast integrated tokamak modelling tool for scenario design”. In: *Nuclear Fusion* 58.10 (Aug. 2018), p. 105001. DOI: 10.1088/1741-4326/aad5b1. URL: https://dx.doi.org/10.1088/1741-4326/aad5b1.

[144] G. D. Porter et al. “Characterization of the separatrix plasma parameters in DIII-D”. In: *Physics of Plasmas* 5.5 (1998), pp. 1410–1422. ISSN: 1070-664X. DOI: 10.1063/1.872830. URL: http://aip.scitation.org/doi/10.1063/1.872830.

[145] P. C. Stangeby et al. “Identifying the location of the OMP separatrix in DIII-D using power accounting”. In: *Nuclear Fusion* 55.9 (Aug. 2015), p. 093014. DOI: 10.1088/0029-5515/55/9/093014. URL: https://doi.org/10.1088/0029-5515/55/9/093014.

[146] K. McCormick et al. “ITER edge database investigations of the SOL width”. In: *Journal of Nuclear Materials* 266-269 (1999), pp. 99–108. ISSN: 0022-3115. DOI: https://doi.org/10.1016/S0022-3115(98)00521-2. URL: https://www.sciencedirect.com/science/article/pii/S0022311598005212.

[147] J. D. Callen et al. “Analysis of pedestal plasma transport”. In: *Nuclear Fusion* 50.6 (May 2010), p. 064004. DOI: 10.1088/0029-5515/50/6/064004. URL: https://doi.org/10.1088/0029-5515/50/6/064004.

[148] J. Boedo et al. "A review of direct experimental measurements of detachment". In: *Plasma Physics and Controlled Fusion* 60.4 (2018), p. 044008. URL: http://stacks.iop.org/0741-3335/60/i=4/a=044008.

[149] M. Kocan and J. P. Gunn. "Comparison of scrape-off layer profiles in outboard-versus inboard-limited plasmas in Tore Supra". In: *Plasma Physics and Controlled Fusion* 52.4 (Mar. 2010), p. 045010. DOI: 10.1088/0741-3335/52/4/045010. URL: https://doi.org/10.1088/0741-3335/52/4/045010.

[150] D. L. Rudakov et al. "SOL width in limited versus diverted discharges in DIII-D". In: *Journal of Nuclear Materials* 415.1, Supplement (2011). Proceedings of the 19th International Conference on Plasma-Surface Interactions in Controlled Fusion, S387–S390. ISSN: 0022-3115. DOI: https://doi.org/10.1016/j.jnucmat.2010.10.036. URL: https://www.sciencedirect.com/science/article/pii/S0022311510006161.

[151] H. J. Sun et al. "Study of near SOL decay lengths in ASDEX Upgrade under attached and detached divertor conditions". In: *Plasma Physics and Controlled Fusion* 59.10 (2017), p. 105010. URL: http://stacks.iop.org/0741-3335/59/i=10/a=105010.

[152] J. Brotankova et al. "Measurement of sheared flows in the edge plasma of the CASTOR tokamak". In: *Plasma Physics Reports* 35.11 (2009), pp. 980–986. ISSN: 1063780x. DOI: 10.1134/S1063780X09110087. URL: http://link.springer.com/10.1134/S1063780X09110087.

[153] J. Adamek et al. "Direct Plasma Potential Measurements by Ball-Pen Probe and Self-Emitting Langmuir Probe on COMPASS and ASDEX Upgrade". In: *Contributions to Plasma Physics* 54.3 (2014), pp. 279–284. ISSN: 08631042. DOI: 10.1002/ctpp.201410072. URL: http://doi.wiley.com/10.1002/ctpp.201410072.

[154] K. Uehara et al. "Direct Identification of Magnetic Surface by a Differential Double Probe in JFT-2M". In: *Japanese Journal of Applied Physics* 45.No. 24 (June 2006), pp. L630–L633. DOI: 10.1143/jjap.45.l630. URL: https://doi.org/10.1143/jjap.45.l630.

[155] Y. Nagashima et al. "Boundary of the geodesic acoustic eigenmode in the vicinity of the magnetic separatrix". In: *Plasma Physics and Controlled Fusion* 51.6 (May 2009), p. 065019. DOI: 10.1088/0741-3335/51/6/065019. URL: https://doi.org/10.1088/0741-3335/51/6/065019.

[156] Y. Nagashima et al. "In search of zonal flows by using direct density fluctuation measurements". In: *Plasma Physics and Controlled Fusion* 49.10 (Aug. 2007), pp. 1611–1625. DOI: 10.1088/0741-3335/49/10/002. URL: https://doi.org/10.1088/0741-3335/49/10/002.

[157] R. Fischer et al. “Integrated Data Analysis of Profile Diagnostics at ASDEX Upgrade”. In: *Fusion Science and Technology* 58.2 (2010), pp. 675–684. DOI: 10.13182/FST10-110. eprint: https://doi.org/10.13182/FST10-110. URL: https://doi.org/10.13182/FST10-110.

[158] J. Svensson et al. “Modelling of JET Diagnostics Using Bayesian Graphical Models”. In: *Contributions to Plasma Physics* 51.2-3 (2011), pp. 152–157. DOI: https://doi.org/10.1002/ctpp.201000058. eprint: https://onlinelibrary.wiley.com/doi/pdf/10.1002/ctpp.201000058. URL: https://onlinelibrary.wiley.com/doi/abs/10.1002/ctpp.201000058.

[159] A. Murari et al. “Residual analysis of the equilibrium reconstruction quality on JET”. In: *Nuclear Fusion* 51.5 (Apr. 2011), p. 053012. DOI: 10.1088/0029-5515/51/5/053012. URL: https://dx.doi.org/10.1088/0029-5515/51/5/053012.

[160] J. Havlicek. “Study of Equilibrium Magnetic Configuration in Tokamak Type Devices”. PhD thesis. Faculty of Mathematics and Physics, Charles University in Prague, Sept. 1, 2015.

[161] O. Kovanda et al. “Dependence of reconstructed equilibria on input data sets using EFIT onCOMPASS and comparison with experimental observations”. In: *46th EPS conference on plasma physics proceedings*. July 8, 2019. URL: http://ocs.ciemat.es/EPS2019PAP/pdf/P4.1032.pdf.

[162] R. Coelho et al. “Plasma equilibrium reconstruction of JET discharges using the IMAS modelling infrastructure”. In: *27th IAEA Fusion Energy Conference FEC 2018*. 2018.

[163] H. Amemiya and K. Uehara. “Method for Detection of Separatrix Surface Using Differential Double Probe”. In: *Japanese Journal of Applied Physics* 45.1R (Jan. 2006), p. 247. DOI: 10.1143/JJAP.45.247. URL: https://dx.doi.org/10.1143/JJAP.45.247.

[164] J. F. Artaud and S. H. Kim. “A new free-boundary equilibrium evolution code, FREEBIE”. In: *39th EPS Conference and 16th International Congress on Plasma Physics*. 2012, P4.023.

[165] B. Faugeras et al. “2D interpolation and extrapolation of discrete magnetic measurements with toroidal harmonics for equilibrium reconstruction in a tokamak”. In: *Plasma Physics and Controlled Fusion* 56.11 (Oct. 2014), p. 114010. DOI: 10.1088/0741-3335/56/11/114010. URL: https://dx.doi.org/10.1088/0741-3335/56/11/114010.

[166] J. Urban et al. “Validation of equilibrium tools on the COMPASS tokamak”. In: *Fusion Engineering and Design* 96-97 (2015). Proceedings of the 28th Symposium On Fusion Technology (SOFT-28), pp. 998–1001. ISSN: 0920-3796. DOI: https://doi.org/10.1016/j.fusengdes.2015.06.132. URL: https://www.sciencedirect.com/science/article/pii/S0920379615301563.

[167] H. J. Sun et al. “Study of near scrape-off layer (SOL) temperature and density gradient lengths with Thomson scattering”. In: *Plasma Physics and Controlled Fusion* 57.12 (Nov. 2015), p. 125011. DOI: 10.1088/0741-3335/57/12/125011. URL: https://doi.org/10.1088/0741-3335/57/12/125011.

[168] T. Eich et al. “Correlation of the tokamak H-mode density limit with ballooning stability at the separatrix”. In: *Nuclear Fusion* 58.3 (Jan. 2018), p. 034001. DOI: 10.1088/1741-4326/aaa340. URL: https://dx.doi.org/10.1088/1741-4326/aaa340.

[169] H. W. Muller et al. “Latest investigations on fluctuations, ELM filaments and turbulent transport in the SOL of ASDEX Upgrade”. In: *Nuclear Fusion* 51.7 (June 2011), p. 073023. DOI: 10.1088/0029-5515/51/7/073023. URL: https://dx.doi.org/10.1088/0029-5515/51/7/073023.

[170] C. Hidalgo et al. “Plasma fluctuations near the shear layer in the ATF torsatron”. In: *Nuclear Fusion* 31.8 (Aug. 1991), p. 1471. DOI: 10.1088/0029-5515/31/8/004. URL: https://dx.doi.org/10.1088/0029-5515/31/8/004.

[171] A. V. Chankina et al. “Possible influence of near SOL plasma on the H-mode power threshold”. In: *Nuclear Materials and Energy* 12 (2017). Proceedings of the 22nd International Conference on Plasma Surface Interactions 2016, 22nd PSI, pp. 273–277. ISSN: 2352-1791. DOI: https://doi.org/10.1016/j.nme.2016.10.004. URL: http://www.sciencedirect.com/science/article/pii/S2352179116300382.

[172] V. Rozhansky et al. “Potentials and currents in the edge tokamak plasma: simplified approach and comparison with two-dimensional modelling”. In: *Nuclear Fusion* 43.7 (July 2003), p. 614. DOI: 10.1088/0029-5515/43/7/315. URL: https://dx.doi.org/10.1088/0029-5515/43/7/315.

[173] J. Cheng et al. “Statistical characterization of blob turbulence across the separatrix in HL-2A tokamak”. In: *Plasma Physics and Controlled Fusion* 52.5 (Mar. 2010), p. 055003. DOI: 10.1088/0741-3335/52/5/055003. URL: https://dx.doi.org/10.1088/0741-3335/52/5/055003.

[174] V. Rozhansky et al. “Modeling of electric fields in tokamak edge plasma and LH transition”. In: *28th European Physical Society Conference on Controlled Fusion and Plasma Physics, Funchal, Madeira* (Jan. 2001).

[175] G. S. Xu et al. “Blob/hole formation and zonal-flow generation in the edge plasma of the JET tokamak”. In: *Nuclear Fusion* 49.9 (Aug. 2009), p. 092002. DOI: 10.1088/0029-5515/49/9/092002. URL: https://iopscience.iop.org/article/10.1088/0029-5515/49/9/092002/meta.

[176] C. K. Tsui et al. “Poloidal asymmetry in the narrow heat flux feature in the TCV scrape-off layer”. In: *Physics of Plasmas* 24.6 (2017), p. 062508. ISSN: 1070-664X. DOI: 10.1063/1.4985075. URL: http://aip.scitation.org/doi/10.1063/1.4985075.

[177] T. D. Rognlien et al. “Two-dimensional electric fields and drifts near the magnetic separatrix in divertor tokamaks”. In: *Physics of Plasmas* 6.5 (1999), pp. 1851–1857. DOI: 10.1063/1.873488. eprint: https://doi.org/10.1063/1.873488. URL: https://doi.org/10.1063/1.873488.

[178] P. Manz et al. “Origin and turbulence spreading of plasma blobs”. In: *Physics of Plasmas* 22.2 (2015), p. 022308. DOI: 10.1063/1.4908272. eprint: https://doi.org/10.1063/1.4908272. URL: https://doi.org/10.1063/1.4908272.

[179] M. Dorf and M. Dorr. “Continuum kinetic modelling of cross-separatrix plasma transport in a tokamak edge including self-consistent electric fields”. In: *Contributions to Plasma Physics* 58.6-8 (2018), pp. 434–444. DOI: 10.1002/ctpp.201700137. eprint: https://onlinelibrary.wiley.com/doi/pdf/10.1002/ctpp.201700137. URL: https://onlinelibrary.wiley.com/doi/abs/10.1002/ctpp.201700137.

[180] B. Nold et al. “Generation of blobs and holes in the edge of the ASDEX Upgrade tokamak”. In: *Plasma Physics and Controlled Fusion* 52.6 (Apr. 2010), p. 065005. DOI: 10.1088/0741-3335/52/6/065005. URL: https://iopscience.iop.org/article/10.1088/0741-3335/52/6/065005.

[181] N. Bisai et al. “Edge and scrape-off layer tokamak plasma turbulence simulation using two-field fluid model”. In: *Physics of Plasmas* 12.7 (July 2005), p. 072520. ISSN: 1070-664X. DOI: 10.1063/1.1942427. eprint: https://pubs.aip.org/aip/pop/article-pdf/doi/10.1063/1.1942427/16090136/072520_1_online.pdf. URL: https://doi.org/10.1063/1.1942427.

[182] E. Kaveeva et al. “Speed-up of SOLPS-ITER code for tokamak edge modeling”. In: *Nuclear Fusion* 58.12 (Aug. 2018), p. 126018. DOI: 10.1088/1741-4326/aae162. URL: https://dx.doi.org/10.1088/1741-4326/aae162.

[183] F. D. Halpern et al. “The GBS code for tokamak scrape-off layer simulations”. In: *Journal of Computational Physics* 315 (2016), pp. 388–408. ISSN: 0021-9991. DOI: https://doi.org/10.1016/j.jcp.2016.03.040. URL: https://www.sciencedirect.com/science/article/pii/S0021999116001923.

[184] P. Macha et al. “Modeling of the COMPASS plasma SOL using GBS code”. In: *Book of abstracts of the Transport Task-Force EU-US joint meeting, Nancy, France*. Sept. 12, 2023. URL: https://ttf2023.sciencesconf.org/data/pages/Bookletwcover.pdf.

[185] V. Kotov, D. Reiter, and A. S. Kukushkin. *Numerical study of the ITER divertor plasma with the B2-EIRENE code package*. Research rep. Forschungszentrum Julich, Institut fur Energieforschung - Plasmaphysik, Nov. 1, 2007.

[186] S. Soldat. *Bayesian optimization for evalution of posterior distributions*. Master's thesis. May 2024.

[187] S. Wiesen et al. "On the role of finite grid extent in SOLPS-ITER edge plasma simulations for JET H-mode discharges with metallic wall". In: *Nuclear Materials and Energy* 17 (2018), pp. 174–181. ISSN: 2352-1791. DOI: https://doi.org/10.1016/j.nme.2018.10.013. URL: https://www.sciencedirect.com/science/article/pii/S2352179118301248.

[188] O. P. Ford et al. "Bayesian Combined Analysis of JET LIDAR, Edge LIDAR and Interferometry Diagnostics". In: *Proceedings of the 36th EPS Conference on Plasma Physics, Sofia*. Vol. 33E. June 29, 2009, P–2.150.

[189] V. Rozhansky et al. "Currents structure in the scrape-off layer of a tokamak". In: *Nuclear Materials and Energy* 25 (2020), p. 100840. ISSN: 2352-1791. DOI: https://doi.org/10.1016/j.nme.2020.100840. URL: http://www.sciencedirect.com/science/article/pii/S2352179120301095.

[190] V. Rozhansky et al. "Structure of the classical scrape-off layer of a tokamak". In: *Plasma Physics and Controlled Fusion* 60.3 (Jan. 2018), p. 035001. DOI: 10.1088/1361-6587/aaa11a. URL: https://dx.doi.org/10.1088/1361-6587/aaa11a.

[191] C. G. Silva et al. "SOL currents and divertor asymmetries on COMPASS-D". In: *Journal of Nuclear Materials* 266-269 (1999), pp. 679–684. ISSN: 00223115. DOI: 10.1016/S0022-3115(98)00600-X. URL: http://linkinghub.elsevier.com/retrieve/pii/S002231159800600X.

[192] M. Dimitrova et al. "Experimental observations of local plasma parameters in the COMPASS divertor in NBI-assisted L-mode plasmas". In: *Journal of Instrumentation* 16.09 (Sept. 2021), P09004. DOI: 10.1088/1748-0221/16/09/P09004. URL: https://dx.doi.org/10.1088/1748-0221/16/09/P09004.

[193] J. Hecko et al. "Drift effects in the COMPASS tokamak SOL with SOLPS-ITER". In: *Book of abstracts, 65th Annual Meeting of the APS Division of Plasma Physics, Denver, Colorado*. APS Division of Plasma Physics, 2023. URL: https://meetings.aps.org/Meeting/DPP23/Session/GP11.139.

[194] C. Silva. "Divertor physics studies on COMPASS-D". PhD thesis. Instituto Superior Tecnico, Universidade Tecnica de Lisboa, Jan. 15, 2000.

[195] L. Spitzer and R. Harm. "Transport Phenomena in a Completely Ionized Gas". In: *Physics Review* 89 (5 Mar. 1953), pp. 977–981. DOI: 10.1103/PhysRev.89.977. URL: https://link.aps.org/doi/10.1103/PhysRev.89.977.

[196] M. K. Prasad and D. S. Kershaw. "Nonviability of some nonlocal electron heat transport modeling". In: *Physics of Fluids B: Plasma Physics* 1.12 (Dec. 1989), pp. 2430–2436. ISSN: 0899-8221. DOI: 10.1063/1.859178. eprint: https://pubs.aip.org/aip/pfb/article-pdf/1/12/2430/12449442/2430_1_online.pdf. URL: https://doi.org/10.1063/1.859178.

[197] A. V. Chankin and D. P. Coster. "On the locality of parallel transport of heat carrying electrons in the SOL". In: *Journal of Nuclear Materials* 463 (2015). PLASMA-SURFACE INTERACTIONS 21, pp. 498–501. ISSN: 0022-3115. DOI: https://doi.org/10.1016/j.jnucmat.2014.10.057. URL: https://www.sciencedirect.com/science/article/pii/S0022311514007417.

[198] S. Mijin et al. "Kinetic and fluid simulations of parallel electron transport during equilibria and transients in the scrape-off layer". In: *Plasma Physics and Controlled Fusion* 62.9 (2020). ISSN: 0741-3335. DOI: 10.1088/1361-6587/ab9b39. URL: https://iopscience.iop.org/article/10.1088/1361-6587/ab9b39.

[199] Periodic Table. *Gold - Thermal Conductivity*. July 10, 2023. URL: https://www.periodic-table.org/Gold-thermal-conductivity/.

[200] G. Fugallo et al. "Thermal Conductivity of Graphene and Graphite. Collective Excitations and Mean Free Paths". In: *Nano Letters* 14.11 (2014), pp. 6109–6114. ISSN: 1530-6984. DOI: 10.1021/nl502059f. URL: https://pubs.acs.org/doi/10.1021/nl502059f.

[201] L. L. Cowie and C. F. McKee. "The evaporation of spherical clouds in a hot gas. I - Classical and saturated mass loss rates". In: *The Astrophysical Journal* 211 (1977). ISSN: 0004-637X. DOI: 10.1086/154911. URL: http://adsabs.harvard.edu/doi/10.1086/154911.

[202] P. Helander and P. J. Catto. "Two-dimensional kinetic modeling of a tokamak scrape-off layer with recycling". In: *Physics of Plasmas* 1.7 (July 1994), pp. 2213–2219. ISSN: 1070-664X. DOI: 10.1063/1.870621. eprint: https://pubs.aip.org/aip/pop/article-pdf/1/7/2213/12671247/2213_1_online.pdf. URL: https://doi.org/10.1063/1.870621.

[203] D. Tskhakaya. *Personal communication*. July 2023.

[204] A. V. Chankin, G. Corrigan, and A. E. Jarvinen. "Kinetic modelling of parallel ion transport in the scrape-off layer and divertor of inter-edge localised mode JET high radiative H-mode plasma". In: *Plasma Physics and Controlled Fusion* 62.10 (2020). ISSN: 0741-3335. DOI: 10.1088/1361-6587/abaec4. URL: https://iopscience.iop.org/article/10.1088/1361-6587/abaec4.

[205] S. Mijin et al. “Kinetic effects in parallel electron energy transport channels in the scrape-off layer”. In: *Plasma Physics and Controlled Fusion* 62.12 (2020). ISSN: 0741-3335. DOI: 10.1088/1361-6587/abbec0. URL: https://iopscience.iop.org/article/10.1088/1361-6587/abbec0.

[206] Y. Homma. “Assessment of the impact of the kinetic effect of ion parallel heat conduction on DEMO-relevant SOL plasma using integrated SOL-divertor code SONIC”. In: *Plasma Physics and Controlled Fusion* 64.4 (2022). ISSN: 0741-3335. DOI: 10.1088/1361-6587/ac48bd. URL: https://iopscience.iop.org/article/10.1088/1361-6587/ac48bd.

[207] D. Brunner et al. “An assessment of ion temperature measurements in the boundary of the Alcator C-Mod tokamak and implications for ion fluid heat flux limiters”. In: *Plasma Physics and Controlled Fusion* 55.9 (2013). ISSN: 0741-3335. DOI: 10.1088/0741-3335/55/9/095010. URL: https://iopscience.iop.org/article/10.1088/0741-3335/55/9/095010.

[208] R. C. Malone, R. L. McCrory, and R. L. Morse. “Indications of Strongly Flux-Limited Electron Thermal Conduction in Laser-Target Experiments”. In: *Physical Review Letters* 34.12 (1975), pp. 721–724. ISSN: 0031-9007. DOI: 10.1103/PhysRevLett.34.721. URL: https://link.aps.org/doi/10.1103/PhysRevLett.34.721.

[209] A. R. Bell, R. G. Evans, and D. J. Nicholas. “Elecron Energy Transport in Steep Temperature Gradients in Laser-Produced Plasmas”. In: *Physical Review Letters* 46.4 (1981), pp. 243–246. ISSN: 0031-9007. DOI: 10.1103/PhysRevLett.46.243. URL: https://link.aps.org/doi/10.1103/PhysRevLett.46.243.

[210] G. J. Radford. “The Application of Moment Equations to Scrape off Layer Plasmas”. In: *Contributions to Plasma Physics* 32.3-4 (1992), pp. 297–302. DOI: https://doi.org/10.1002/ctpp.2150320319. eprint: https://onlinelibrary.wiley.com/doi/pdf/10.1002/ctpp.2150320319. URL: https://onlinelibrary.wiley.com/doi/abs/10.1002/ctpp.2150320319.

[211] G. J. Radford et al. “The Development of Simplified Heat Flux Limiters for EDGE2D”. In: *Contributions to Plasma Physics* 38.1-2 (1998), pp. 183–188. DOI: https://doi.org/10.1002/ctpp.2150380127. eprint: https://onlinelibrary.wiley.com/doi/pdf/10.1002/ctpp.2150380127. URL: https://onlinelibrary.wiley.com/doi/abs/10.1002/ctpp.2150380127.

[212] Z. Abou-Assaleh et al. “Non-Local Transport in a Tokamak Plasma Divertor with Recycling”. In: *Contributions to Plasma Physics* 34.2-3 (1994), pp. 175–179. DOI: https://doi.org/10.1002/ctpp.2150340213. eprint: https://onlinelibrary.wiley.com/doi/pdf/

10.1002/ctpp.2150340213. URL: https://onlinelibrary.wiley.com/doi/abs/10.1002/ctpp.2150340213.

[213] S. Mijin et al. "SOL-KiT—Fully implicit code for kinetic simulation of parallel electron transport in the tokamak Scrape-Off Layer". In: *Computer Physics Communications* 258 (2021), p. 107600. ISSN: 0010-4655. DOI: https://doi.org/10.1016/j.cpc.2020.107600. URL: https://www.sciencedirect.com/science/article/pii/S0010465520302873.

[214] I. Vasileska, X. Bonnin, and L. Kos. "Kinetic-fluid coupling simulations of ITER Type I ELM". In: *Fusion Engineering and Design* 168 (2021), p. 112407. ISSN: 0920-3796. DOI: https://doi.org/10.1016/j.fusengdes.2021.112407. URL: https://www.sciencedirect.com/science/article/pii/S0920379621001836.

[215] M. Zhao, A. Chankin, and D. Coster. "SOLPS simulations with electron kinetic effects". In: *Plasma Physics and Controlled Fusion* 61.2 (2019), p. 025019.

[216] A. A. Batishcheva et al. "Fokker-Planck Simulation of Electron Transport in SOL Plasmas with ALLA Code". In: *Contributions to Plasma Physics* 36.2-3 (1996), pp. 235–239. DOI: https://doi.org/10.1002/ctpp.2150360225. eprint: https://onlinelibrary.wiley.com/doi/pdf/10.1002/ctpp.2150360225. URL: https://onlinelibrary.wiley.com/doi/abs/10.1002/ctpp.2150360225.

[217] Yu. L. Igitkhanov, A. S. Kukushkin, and A. M. Runov. "The impact of kinetic effects on the ITER divertor plasma". In: *Proceedings of the 21st EPS conference on plasma physics*. July 3, 1994.

[218] Yu. Igitkhanov, B. Bazylev, and R. Fetzer. *The quantification of the key physics parameters for the DEMO fusion power reactor and analysis of the reactor relevant physics issues*. Vol. 7661. KIT scientific reports, Jan. 1, 2015.

[219] A. Froese, T. Takizuka, and M. Yagi. "PIC Simulation Study of Heat Transport Kinetic Factors in Scrape-Off Layer Plasmas". In: *Contributions to Plasma Physics* 52.5-6 (2012), pp. 534–538. DOI: https://doi.org/10.1002/ctpp.201210045. eprint: https://onlinelibrary.wiley.com/doi/pdf/10.1002/ctpp.201210045. URL: https://onlinelibrary.wiley.com/doi/abs/10.1002/ctpp.201210045.

[220] M. Day et al. "The Effect of Heat Flux Limiting on Divertor Fluid Models". In: *Contributions to Plasma Physics* 36.2-3 (1996), pp. 419–423. DOI: https://doi.org/10.1002/ctpp.2150360259. eprint: https://onlinelibrary.wiley.com/doi/pdf/10.1002/ctpp.2150360259. URL: https://onlinelibrary.wiley.com/doi/abs/10.1002/ctpp.2150360259.

[221] D. M. Harting et al. “Intra-ELM phase modelling of a JET ITER-like wall H-mode discharge with EDGE2D-EIRENE”. In: *Journal of Nuclear Materials* 463 (2015). PLASMA-SURFACE INTERACTIONS 21, pp. 493–497. ISSN: 0022-3115. DOI: https://doi.org/10.1016/j.jnucmat.2014.12.023. URL: https://www.sciencedirect.com/science/article/pii/S0022311514009659.

[222] D. J. Sigmar et al. “Kinetic models of ELMs burst”. In: *Contributions to Plasma Physics* 36.2-3 (1996), pp. 230–234. DOI: https://doi.org/10.1002/ctpp.2150360224. eprint: https://onlinelibrary.wiley.com/doi/pdf/10.1002/ctpp.2150360224. URL: https://onlinelibrary.wiley.com/doi/abs/10.1002/ctpp.2150360224.

[223] T. D. Rognlien and M. E. Rensink. “Edge-plasma models and characteristics for magnetic fusion energy devices”. In: *Fusion Engineering and Design* 60.4 (2002), pp. 497–514. ISSN: 0920-3796. DOI: https://doi.org/10.1016/S0920-3796(02)00005-4. URL: https://www.sciencedirect.com/science/article/pii/S0920379602000054.

[224] Yu. L. Igitkhanov and A. M. Runov. “Non-Local Sheath Boundary Conditions for Fluid Equations”. In: *Contributions to Plasma Physics* 32.3-4 (1992), pp. 308–313. DOI: https://doi.org/10.1002/ctpp.2150320321. eprint: https://onlinelibrary.wiley.com/doi/pdf/10.1002/ctpp.2150320321. URL: https://onlinelibrary.wiley.com/doi/abs/10.1002/ctpp.2150320321.

[225] A. Loarte et al. “Chapter 4. Power and particle control”. In: *Nuclear Fusion* 47.6 (2007), S203–S263. ISSN: 0029-5515. DOI: 10.1088/0029-5515/47/6/S04. URL: https://iopscience.iop.org/article/10.1088/0029-5515/47/6/S04.

[226] J. F. Luciani and P. Mora. “Nonlocal heat transport due to steep temperature gradients”. In: *Physical Review Letters* 51.18 (1983), pp. 1664–1667.

[227] M. K. Prasad and D. S. Kershaw. “Stable solutions of nonlocal electron heat transport equations”. In: *Physics of Fluids B: Plasma Physics* 3.11 (Nov. 1991), pp. 3087–3091. ISSN: 0899-8221. DOI: 10.1063/1.859995. eprint: https://pubs.aip.org/aip/pfb/article-pdf/3/11/3087/12317693/3087_1_online.pdf. URL: https://doi.org/10.1063/1.859995.

[228] J. P. Brodrick et al. “Testing nonlocal models of electron thermal conduction for magnetic and inertial confinement fusion applications”. In: *Physics of Plasmas* 24.9 (Sept. 2017), p. 092309. ISSN: 1070-664X. DOI: 10.1063/1.5001079. eprint: https://pubs.aip.org/aip/pop/article-pdf/doi/10.1063/1.5001079/15654563/092309_1_online.pdf. URL: https://doi.org/10.1063/1.5001079.

[229] S. I. Krasheninnikov and O. G. Bakunin. “Electron Heat Conduction and Suprathermal Particles”. In: *Contributions to Plasma Physics* 32.3-4 (1992), pp. 255–260. DOI: https://doi.org/10.1002/ctpp.2150320313. eprint: https://onlinelibrary.wiley.com/doi/pdf/10.1002/ctpp.2150320313. URL: https://onlinelibrary.wiley.com/doi/abs/10.1002/ctpp.2150320313.

[230] A. V. Chankin and D. P. Coster. “Comparison of 2D models for the plasma edge with experimental measurements and assessment of deficiencies”. In: *Journal of Nuclear Materials* 390-391 (2009). Proceedings of the 18th International Conference on Plasma-Surface Interactions in Controlled Fusion Device, pp. 319–324. ISSN: 0022-3115. DOI: https://doi.org/10.1016/j.jnucmat.2009.01.307. URL: https://www.sciencedirect.com/science/article/pii/S0022311509001238.

[231] B. J. Braams. *A Multi-Fluid Code for Simulation of the Edge Plasma in Tokamaks," NET report NET-68*. Tech. rep. EUR-FU/XII-80/87/68, 1987.

[232] B. J. Braams. “Radiative Divertor Modelling for ITER and TPX”. In: *Contributions to Plasma Physics* 36.2-3 (1996), pp. 276–281. DOI: https://doi.org/10.1002/ctpp.2150360233. eprint: https://onlinelibrary.wiley.com/doi/pdf/10.1002/ctpp.2150360233. URL: https://onlinelibrary.wiley.com/doi/abs/10.1002/ctpp.2150360233.

[233] X. Bonnin et al. “Presentation of the New SOLPS-ITER Code Package for Tokamak Plasma Edge Modelling”. In: *Plasma and Fusion Research* 11 (2016), pp. 1403102–1403102. DOI: 10.1585/pfr.11.1403102.

[234] F. Reimold et al. “The high field side high density region in SOLPS-modeling of nitrogen-seeded H-modes in ASDEX Upgrade”. In: *Nuclear Materials and Energy* 12 (2017). Proceedings of the 22nd International Conference on Plasma Surface Interactions 2016, 22nd PSI, pp. 193–199. ISSN: 2352-1791. DOI: https://doi.org/10.1016/j.nme.2017.01.010. URL: https://www.sciencedirect.com/science/article/pii/S235217911630059X.

[235] G. M. Staebler and F.L. Hinton. “Currents in the scrape-off layer of diverted tokamaks”. In: *Nuclear Fusion* 29.10 (1989), p. 1820. URL: http://stacks.iop.org/0029-5515/29/i=10/a=017.

[236] S. Wiesen et al. “Integrated modelling of a JET type-I ELMy H-mode pulse and predictions for ITER-like wall scenarios”. In: *Plasma Physics and Controlled Fusion* 53.12 (Nov. 2011), p. 124039. DOI: 10.1088/0741-3335/53/12/124039. URL: https://dx.doi.org/10.1088/0741-3335/53/12/124039.

[237] W. Dekeyser et al. “SOLPS-ITER Study of neutral leakage and drift effects on the alcator C-Mod divertor plasma”. In: *Nuclear Materials and Energy* 12 (2017). Proceedings of the 22nd International Conference on Plasma Surface Interactions 2016, 22nd PSI, pp. 899–907. ISSN:

2352-1791. DOI: https://doi.org/10.1016/j.nme.2017.03.029. URL: https://www.sciencedirect.com/science/article/pii/S2352179116302691.

[238] A. Perek et al. "A spectroscopic inference and SOLPS-ITER comparison of flux-resolved edge plasma parameters in detachment experiments on TCV". In: *Nuclear Fusion* 62.9 (July 2022), p. 096012. DOI: 10.1088/1741-4326/ac7813. URL: https://dx.doi.org/10.1088/1741-4326/ac7813.

[239] A. Dvornova. "Characterization of the COMPASS Scrape-Off Layer by RFA Measurements and SOLEDGE2D Modelling". MA thesis. Erasmus Mundus Program on Nuclear Fusion Science and Engineering Physics, July 17, 2016.

[240] J. Adamek et al. "Ion temperature measurements in the tokamak scrape-off layer with high temporal resolution". In: *Nuclear Fusion* 61.3 (Feb. 2021), p. 036023. DOI: 10.1088/1741-4326/abd41d. URL: https://dx.doi.org/10.1088/1741-4326/abd41d.

[241] G. V. Pereverzev and P. N. Yushmanov. *ASTRA - Automated System for TRansport Analysis*. Max Planck Institut für Plasmaphysik. Feb. 2002.

[242] K. K. Kirov et al. "ECRH power deposition studies in ASDEX Upgrade". In: *Plasma Physics and Controlled Fusion* 44.12 (Nov. 2002), p. 2583. DOI: 10.1088/0741-3335/44/12/307. URL: https://dx.doi.org/10.1088/0741-3335/44/12/307.

[243] S. Wiesen et al. "Relevance of collisionality in the transport model assumptions for divertor detachment multi-fluid modelling on JET". In: *Journal of Nuclear Materials* 415.1, Supplement (2011). Proceedings of the 19th International Conference on Plasma-Surface Interactions in Controlled Fusion, S535–S539. ISSN: 0022-3115. DOI: https://doi.org/10.1016/j.jnucmat.2010.12.010. URL: https://www.sciencedirect.com/science/article/pii/S0022311510008287.

[244] F. Reimold et al. "Experimental studies and modeling of complete H-mode divertor detachment in ASDEX Upgrade". In: *Journal of Nuclear Materials* 463 (2015). PLASMA-SURFACE INTERACTIONS 21, pp. 128–134. ISSN: 0022-3115. DOI: https://doi.org/10.1016/j.jnucmat.2014.12.019. URL: http://www.sciencedirect.com/science/article/pii/S002231151400960X.

[245] D. A. D'Ippolito, J. R. Myra, and S. J. Zweben. "Convective transport by intermittent blob-filaments". In: *Physics of Plasmas* 18.6 (2011). ISSN: 1070664x. DOI: 10.1063/1.3594609. URL: http://scitation.aip.org/content/aip/journal/pop/18/6/10.1063/1.3594609.

[246] M. Hosokawa et al. "Modelling of the effects of divertor recycling conditions and toroidal field direction on divertor power and particle flux asymmetries between and during ELMs with PARASOL for COMPASS-like plasmas". In: *Proceedings of the 45th EPS conference on plasma physics, Prague*. 2018. URL: https://info.fusion.ciemat.es/OCS/EPS2018PAP/pdf/O2.110.pdf.

[247] J.-S. Park, X. Bonnin, and R. Pitts. "Assessment of ITER divertor performance during early operation phases". In: *Nuclear Fusion* 61.1 (Dec. 2020), p. 016021. DOI: 10.1088/1741-4326/abc1ce. URL: https://doi.org/10.1088/1741-4326/abc1ce.

[248] A. S. Kukushkin et al. "Scaling laws for edge plasma parameters in ITER from two-dimensional edge modelling". In: *Nuclear Fusion* 43.8 (Aug. 2003), p. 716. DOI: 10.1088/0029-5515/43/8/312. URL: https://dx.doi.org/10.1088/0029-5515/43/8/312.

[249] A. S. Kukushkin and S. I. Krasheninnikov. "Bifurcations and oscillations in divertor plasma". In: *Plasma Physics and Controlled Fusion* 61.7 (May 2019), p. 074001. DOI: 10.1088/1361-6587/ab1bba. URL: https://dx.doi.org/10.1088/1361-6587/ab1bba.

[250] P. C. Stangeby. "Two point modeling of the divertor SOL, Invited Tutorial". In: *22nd PSI conference, Rome, Italy*. May 30, 2016.

[251] P. C. Stangeby. *Strong correlation between D2 density and electron temperature at the target of divertors found in SOLPS-EIRENE and EDGE2D-EIRENE analysis*. Presented at the 24th ITPA Meeting on SOL/Divertor Physics, University of York, UK. 2017.

[252] P. C. Stangeby and C. Sang. "Strong correlation between D2 density and electron temperature at the target of divertors found in SOLPS analysis". In: *Nuclear Fusion* 57.5 (Mar. 2017), p. 056007. DOI: 10.1088/1741-4326/aa5e27. URL: https://dx.doi.org/10.1088/1741-4326/aa5e27.

[253] K. Jirakova et al. "Non-magnetic edge diagnostics for detecting the separatrix position". In: *ECPD 2019 Book of Abstracts*. Lisboa University, 2019. URL: https://www.ipfn.tecnico.ulisboa.pt/ECPD2019/pdf/ecpd2019%5C_book%5C_of%5C_abstracts.pdf.

[254] T. Eich, P. Manz, and the ASDEX Upgrade team. "The separatrix operational space of ASDEX Upgrade due to interchange-drift-Alfvén turbulence". In: *Nuclear Fusion* 61.8 (July 2021), p. 086017. DOI: 10.1088/1741-4326/ac0412. URL: https://dx.doi.org/10.1088/1741-4326/ac0412.

[255] W. Dekeyser et al. "A self-consistent K-model for anomalous transport due to electrostatic, interchange-dominated ExB drift turbulence in the scrape-off layer and implementation in SOLPS-ITER". In: *Contributions to Plasma Physics* 62.5-6 (2022), e202100190. DOI: https://doi.org/10.1002/ctpp.202100190. eprint: https://onlinelibrary.wiley.com/doi/pdf/10.1002/ctpp.202100190.

URL: https://onlinelibrary.wiley.com/doi/abs/10.1002/ctpp.202100190.

[256] J. Seidl. "Anomalous diffusion of plasma in tokamak edge region". PhD thesis. Faculty of Mathematics and Physics, Charles University, Prague, 2013.

[257] J. A. Boedo. "Edge turbulence and SOL transport in tokamaks". In: *Journal of Nuclear Materials* 390-391 (2009). Proceedings of the 18th International Conference on Plasma-Surface Interactions in Controlled Fusion Device, pp. 29–37. ISSN: 0022-3115. DOI: https://doi.org/10.1016/j.jnucmat.2009.01.040. URL: https://www.sciencedirect.com/science/article/pii/S0022311509000531.

[258] J. Horacek et al. "Scaling of L-mode heat flux for ITER and COMPASS-U divertors, based on five tokamaks". In: *Nuclear Fusion* 60.6 (May 2020), p. 066016. DOI: 10.1088/1741-4326/ab7e47. URL: https://iopscience.iop.org/article/10.1088/1741-4326/ab7e47.

[259] M. Z. Tokar. "An assessment for the erosion rate of DEMO first wall". In: *Nuclear Fusion* 58.1 (Nov. 2017), p. 016016. DOI: 10.1088/1741-4326/aa92dd. URL: https://dx.doi.org/10.1088/1741-4326/aa92dd.

[260] S. Baschetti et al. "Study of the role of the magnetic configuration in a k-e model for anomalous transport in tokamaks". In: *Journal of Physics: Conference Series* 1125.1 (Nov. 2018), p. 012001. DOI: 10.1088/1742-6596/1125/1/012001. URL: https://dx.doi.org/10.1088/1742-6596/1125/1/012001.

[261] A. Yu. Pigarov et al. "Multi-fluid code simulations including anomalous non-diffusive transport of plasma and impurities in the tokamak SOL". In: *Contributions to Plasma Physics* 44.1-3 (2004), pp. 228–234. DOI: https://doi.org/10.1002/ctpp.200410033. eprint: https://onlinelibrary.wiley.com/doi/pdf/10.1002/ctpp.200410033. URL: https://onlinelibrary.wiley.com/doi/abs/10.1002/ctpp.200410033.

[262] S. A. Zamperini et al. "Turbulent drifts of impurity ions as an explanation for anomalous radial transport in the far-SOL of DIII-D". In: *Nuclear Fusion* 64.7 (May 2024), p. 074002. DOI: 10.1088/1741-4326/ad4c78. URL: https://dx.doi.org/10.1088/1741-4326/ad4c78.

[263] A. Redl et al. "An extensive analysis of SOL properties in high-delta plasmas in ASDEX Upgrade". In: *Nuclear Fusion* (2024). URL: http://iopscience.iop.org/article/10.1088/1741-4326/ad5457.

[264] J. P. Graves et al. "Self-similar density turbulence in the TCV tokamak scrape-off layer". In: *Plasma Physics and Controlled Fusion* 47.3 (Feb. 2005), pp. L1–L9. URL: https://iopscience.iop.org/article/10.1088/0741-3335/47/3/L01.

[265] H. Wu et al. “SOLPS-ITER modeling of ASDEX Upgrade L-mode detachment states”. In: *Plasma Physics and Controlled Fusion* 63.10 (Sept. 2021), p. 105005. DOI: 10.1088/1361-6587/ac1568. URL: https://dx.doi.org/10.1088/1361-6587/ac1568.

[266] D. Carralero et al. “A study on the density shoulder formation in the SOL of H-mode plasmas”. In: *Nuclear Materials and Energy* 12 (2017). Proceedings of the 22nd International Conference on Plasma Surface Interactions 2016, 22nd PSI, pp. 1189–1193. ISSN: 2352-1791. DOI: https://doi.org/10.1016/j.nme.2016.11.016. URL: https://www.sciencedirect.com/science/article/pii/S2352179116301715.

[267] D. Mancini et al. “Investigation of the density shoulder formation by using self-consistent simulations of plasma turbulence and neutral kinetic dynamics”. In: *Nuclear Fusion* 61.12 (Nov. 2021), p. 126029. DOI: Mancini2021. URL: https://dx.doi.org/10.1088/1741-4326/ac30c9.

[268] N. Yan et al. “Dependence of upstream SOL density shoulder on divertor neutral pressure observed in L-mode and H-mode plasmas in the EAST superconducting tokamak”. In: *Nuclear Fusion* 61.7 (June 2021), p. 076018. DOI: 10.1088/1741-4326/abfe47. URL: https://dx.doi.org/10.1088/1741-4326/abfe47.

[269] A. Wynn et al. “Investigation into the formation of the scrape-off layer density shoulder in JET ITER-like wall L-mode and H-mode plasmas”. In: *Nuclear Fusion* 58.5 (Mar. 2018), p. 056001. DOI: 10.1088/1741-4326/aaad78. URL: https://dx.doi.org/10.1088/1741-4326/aaad78.

[270] I. Borodkina et al. “SOLPS-ITER predictions for power exhaust in COMPASS Upgrade tokamak”. In: *26th PSI conference, Marseille, France*. May 12, 2024.

[271] M. Giacomin et al. “Theory-based scaling laws of near and far scrape-off layer widths in single-null L-mode discharges”. In: *Nuclear Fusion* 61.7 (May 2021), p. 076002. DOI: 10.1088/1741-4326/abf8f6. URL: https://dx.doi.org/10.1088/1741-4326/abf8f6.

[272] K. Lim et al. “Effect of triangularity on plasma turbulence and the SOL-width scaling in L-mode diverted tokamak configurations”. In: *Plasma Physics and Controlled Fusion* 65.8 (June 2023), p. 085006. DOI: 10.1088/1361-6587/acdc52. URL: https://dx.doi.org/10.1088/1361-6587/acdc52.

[273] F. Militello, V. Naulin, and A. H. Nielsen. “Numerical scalings of the decay lengths in the scrape-off layer”. In: *Plasma Physics and Controlled Fusion* 55.7 (June 2013), p. 074010. DOI: 10.1088/0741-3335/55/7/074010. URL: https://dx.doi.org/10.1088/0741-3335/55/7/074010.

Appendix A

Acknowledgements and publications

A.1 Acknowledgements

I would like to thank my husband J. Hromas for supporting my PhD studies with two small sons. I would like to thank my supervisors J. Seidl, M. Komm and D.Tskhakaya for guidance, and D. Tskhakaya for the BIT1 simulations presented in section 5.7. For assistance with SOLPS-ITER modelling, I would like to thank the IPP Prague SOLPS-ITER group, I. Borodkina, J. Hecko, A. Podolnik and O. Shyshkin, and my mentors D. Coster and S. Wiesen, as well as X. Bonnin, A. Jarvinen, H. Wu, E. Tonello, S. Carli and E. Sytova. For COMPASS experimental and modelling data, I would like to thank J. Adamek, P. Bilkova, J. Cavalier, M. Dimitrova, F. Jaulmes, M. Komm, O. Kovanda, P. Macha, M. Sos, J. Varju, P. Vondracek, V. Weinzettl and the COMPASS team (see the author list of [2]).

This work was carried out within the framework of the EUROfusion Consortium, funded by the European Union via the Euratom Research and Training Programme (Grant Agreement No 101052200 - EUROfusion). Views and opinions expressed are those of the author only and do not necessarily reflect those of the European Union or the European Commission. Neither the European Union nor the European Commission can be held responsible for them.

The research presented in this work was performed under the funding from the MEYS projects LM2015045, LM2018117, LM2023045, 8D15001 and 9D22001. It was supported by the project COMPASS-U: Tokamak for cutting-edge fusion research (No. CZ.02.1.01/0.0/0.0/16_019/0000768) and projects SGS17/138/OHK4/2T/14, SGS19/180/OHK4/3T/14 and SGS22/175/OHK4/3T/14 of the Grant Agency of the Czech Technical University in Prague. It was further funded by the Czech Science foundation projects GA16-25074S, GA19-15229S, GA20-28161S and the mobility project *BAS-20-13. It was partially supported by the ENEN2plus project (HORIZON-EURATOM-2021-NRT-01-13 101061677) founded by the European Union, and by the Ministry of Education, Youth and Sports of the Czech Republic through the e-INFRA CZ (ID:90254). The results were obtained with the help of the EIRENE package (see www.eirene.de) including the related code, data and tools [32]. The work was co-funded from European structural and investment funds.

I would like to give special acknowledgement to the funds provided by the Martina Roeselová Memorial Fellowship granted by the IOCB Tech Foundation. Its mission to support young researchers pursuing both academic career and parenthood symbolises, to me, the hope that excellent science and raising children do not have to be at odds.

A.2 Publication list and authorship declaration

This section lists the journal publications and conference contributions publicizing the work presented in this thesis. The most important papers are attached in full in appendices A.3, A.4 and A.5. Note that Jiráková is my maiden name.

(Conference poster and proceedings) **K. Jiráková**, J. Seidl, J. Adámek, P. Bílková, J. Cavalier, M. Dimitrova, J. Horáček, M. Komm, *Parallel SOL transport regime in tokamak COMPASS*, 45th EPS Conference on Plasma Physics, Prague (2018)

- Summary and relevance to the thesis: The typical SOL transport regime of tokamak COMPASS is gauged based on experimental data (section 6.4). Equilibrium reconstruction inaccuracy is demonstrated on the electron temperature T_e profiles in a low- and high-collisionality discharge (section 4.2). A statistical analysis of probe data in hundreds of COMPASS discharges yields an empirical correction of the outer midplane separatrix position.
- Author contribution: experimental data processing, all figures save for figure 3, contribution text

(Conference poster) **K. Jiráková**, J. Adámek, M. Komm, O. Kovanda, P. Vondráček, J. Seidl, *Non-magnetic edge diagnostics for detecting precise separatrix position*, 3rd European Conference on Plasma Diagnostics, Lisbon, Portugal (2019)

- Summary and relevance to the thesis: Four means of direct separatrix detection are tested across hundreds of COMPASS discharges: the velocity shear layer (section 4.3) with Φ peak and with $E_r = 0$, the blob birth zone, and the near-far SOL boundary. Φ peak and $E_r = 0$ are found equivalent. Both the blob birth zone and the near-far SOL boundary lie radially outside the velocity shear layer, but the blob birth zone lies further inward for limited plasmas, suggesting the X-point acting on turbulence properties.
- Author contribution: experimental data processing, all figures save for horizontal reciprocating probe schema, contribution text

(Impacted publication) **K. Jiráková**, O. Kovanda, J. Adámek, M. Komm, J. Seidl, *Systematic errors in tokamak magnetic equilibrium reconstruction: a study of EFIT++ at tokamak COMPASS*, Journal of Instrumentation **14** (2019) C11020

- Summary and relevance to the thesis: The radial distance between the velocity shear layer and the outer midplane separatrix in hundreds of COMPASS discharges is found to depend strongly on the plasma geometry. Lower triangularity alone accounts for 77 % of the variation. Correcting the positions of inner partial Rogowski coils based on vacuum magnetic field measurements suppresses most of the dependency. The baseline EFIT equilibrium reconstruction is deemed systematically

erroneous (chapter 4).
- Author contribution: statistical analysis of the probe data, all figures, contribution text
- Attached in appendix A.3

(Impacted publication) J. Horáček et al (126 co-authors including **K. Hromasová**), *Scaling of L-mode heat flux for ITER and COMPASS-U divertors, based on five tokamaks*, Nuclear Fusion **60** (2020) 066016
- Summary and relevance to the thesis: Multi-machine scalings of the heat flux fall-off length λ_q are proposed. The COMPASS tokamak is included in the scalings, despite concerns that its typical SOL transport regime may lend itself to different transport scalings.
- Author contribution: discussion of the typical SOL transport regime of the COMPASS tokamak

(Conference poster and proceedings) **K. Hromasová**, D. Coster, M. Komm, J. Seidl, D. Tskhakaya, SOLPS-ITER simulations of the COMPASS tokamak, 47th EPS Conference on Plasma Physics, virtual conference (2021)
- Summary and relevance to the thesis: An interpretative simulation of the COMPASS discharge #17588 is presented (section 4.6). Experimental measurements are reproduced and small momentum and power losses are found. SOLPS-ITER simulations based on two magnetic equilibrium reconstructions are compared, and the reconstruction based on corrected inner partial Rogowski coils positions is proven superior (section 4.5). Several methods of predicting anomalous diffusion coefficients are found to vary to an order of magnitude (section 6.5).
- Author contribution: experimental data analysis, SOLPS-ITER modelling, all figures, contribution text
- Attached in appendix A.4

(Impacted publication) D. Tskhakaya, J. Adámek, M. Dimitrova, **K. Hromasová**, J. Seidl, M. Šos, P. Vondráček, Kinetic model of the COMPASS tokamak SOL, Nuclear Materials and Energy **26** (2021) 100893
- Summary and relevance to the thesis: Interpretative kinetic BIT1 modeling of the COMPASS discharge #16908 is presented (precursor of the BIT1 simulation shown in section 5.7).
- Author contribution: manuscript editing

(Conference poster and proceedings) **K. Hromasová**, J. Seidl, D. Tskhakaya, J. Adámek, M. Dimitrova, F. Jaulmes, M. Komm, P. Vondráček, M. Šos and the COMPASS team, *Sensitivity of COMPASS tokamak SOLPS-ITER simulations to electron and ion heat flux limiters*, 49th EPS Conference on Plasma Physics, Bordeaux, France (2023)
- Summary and relevance to the thesis: A heat flux limiter scan in an interpretative SOLPS-ITER simulation of the COMPASS discharge #16908 is presented (chapter 5). The main effects of heat flux limiting is noted to be the steepening of the parallel temperature profiles.
- Author contribution: experimental data analysis, SOLPS-ITER mod-

elling, all figures, contribution text
- Attached in appendix A.5

We, the below signed, declare that authorship declarations in the above publications, as well as in this thesis and its acknowledgements, are accurate and reflect the student's share of the work.

Mgr. Jakub Seidl, Ph.D.
Thesis supervisor (seidl@ipp.cas.cz)

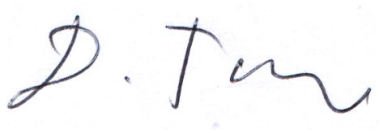

Dr. David Tskhakaya
Thesis supervisor-specialist and principal investigator of [127] (tskhakaya@ipp.cas.cz)

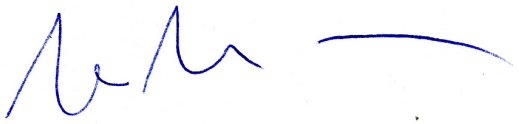

Mgr. Michael Komm, Ph.D.
Thesis supervisor-specialist (komm@ipp.cas.cz)

Mgr. Jan Horáček, DSc. dr. és sc.
Principal investigator of [258] (horacek@ipp.cas.cz)

Prohlašuji, že jsem tuto dizertaci vypracovala samostatně a použila jsem pouze podklady (literaturu, projekty, SW, atd.) uvedené v přiloženém seznamu. Nemám závažný důvod proti použití tohoto školního díla ve smyslu § 60 Zákona č. 121/2000 Sb., o právu autorském, o právech souvisejících s právem autorským a o změně některých zákonů (autorský zákon).

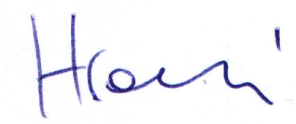

V Praze dne 26. 2. 2025
Ing. Kateřina Hromasová (hromasova@ipp.cas.cz)

A.3 Article published in the Journal of Instrumentation, 2019

Published by IOP Publishing for Sissa Medialab

Received: *June 29, 2019*
Revised: *October 27, 2019*
Accepted: *November 2, 2019*
Published: *November 20, 2019*

3rd European Conference on Plasma Diagnostics (ECPD2019)
6–10 May 2019
Lisbon, Portugal

Systematic errors in tokamak magnetic equilibrium reconstruction: a study of EFIT++ at tokamak COMPASS

K. Jirakova,[a,b,1] **O. Kovanda,**[a,c] **J. Adamek,**[a] **M. Komm**[a] **and J. Seidl**[a]

[a] *Institute of Plasma Physics, Czech Academy of Sciences, Za Slovankou 3, 182 00 Prague, Czech Republic*
[b] *Faculty of Nuclear Sciences and Physical Engineering, Czech Technical University, Brehova 7, 115 19 Prague, Czech Republic*
[c] *Faculty of Mathematics and Physics, Charles University, Ke Karlovu 3, 121 16 Prague, Czech Republic*

E-mail: jirakova@ipp.cas.cz

Abstract: Uncertainties and errors in magnetic equilibrium reconstructions are a wide-spread problem in interpreting experimental data measured in the tokamak edge. This study demonstrates errors in EFIT++ reconstructions performed on the COMPASS tokamak by comparing the outer midplane separatrix position to the Velocity Shear Layer (VSL) position. The VSL is detected as the plasma potential peak measured by a reciprocating ball-pen probe. A subsequent statistical analysis of nearly 400 discharges shows a strong systematic trend in the reconstructed separatrix position relative to the VSL, where the primary factors are plasma triangularity and the magnetic axis radial position. This dependency is significantly reduced after the measuring coils positions as recorded in EFIT input are optimised to provide a closer match between the "synthetic" coil signal calculated by the Biot-Savart law in a vacuum discharge and the actual coil signal. In conclusion, we suggest that applying this optimisation may lead to more accurate and reliable reconstructions of the COMPASS equilibrium, which would have a positive impact on the accuracy of measurement analysis performed in the edge plasma.

Keywords: Plasma diagnostics - probes; Analysis and statistical methods

Corresponding author.

https://doi.org/10.1088/1748-0221/14/11/C11020

Contents

1 Introduction

Magnetic equilibrium reconstruction is a vital component in interpreting experimental data collected in the tokamak edge region. However, many tokamak studies have reported problems in interpreting edge data caused by uncertanties in the equilibrium reconstruction (for example [1–5]). The COMPASS tokamak is no exception. One of the known issues of its EFIT++ code reconstructions is the uncertainty of separatrix position at the outer midplane (OMP), whose effect on mapping profiles to the OMP is illustrated in figure 1a. It has been attempted to correct the reconstruction errors by calibrating the edge measurement position against the velocity shear layer (VSL) position instead of the EFIT separatrix [8, 9]. However, efforts to address the issue on the reconstruction level have until recently been lacking.

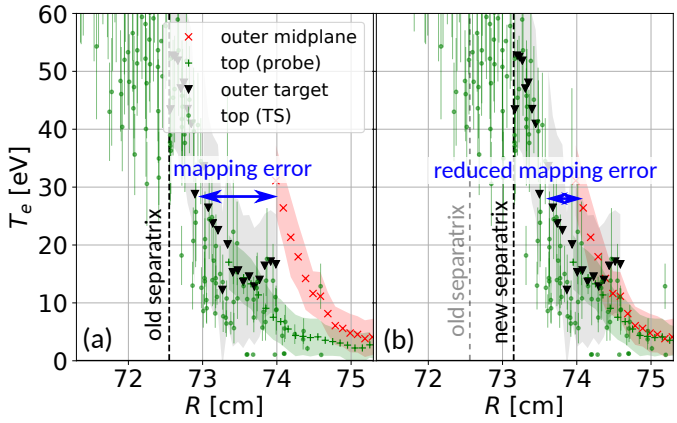

Figure 1. T_e profiles measured at the OMP (reciprocating probe), the plasma top (reciprocating probe and Thomson scattering [6]) and the outer divertor target (probe array [7]), discharge #15182. (a) Mapped to the OMP using the original EFIT reconstruction, (b) mapped to the OMP using the new reconstruction (section 2.1).

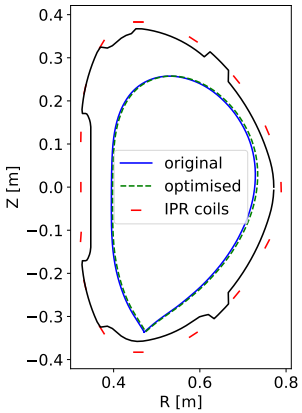

Figure 2. Location of IPR coils providing input data to EFIT, and reconstructions of discharge #15182 separatrix using original and optimised coil positions.

2019 JINST 14 C11020

In a companion work [10], Kovanda et al. put forth that reconstruction uncertainties may be affected by inaccurate records of the measuring magnetic coil positions in EFIT input, and they subsequently provide corrected coil positions (detailed in section 2.1). In this article, we systematically benchmark the resulting "corrected" reconstructions by comparing the reconstructed OMP separatrix position to the VSL position detected by electrostatic probes in L-mode. Our goal is to demonstrate systematic differences between the separatrix and the VSL position in the old reconstructions, to show that their disparity depends mainly on plasma geometry, and to corroborate that correcting for the measuring coil geometry substantially reduces the dependency. In conclusion, we recommend that equilibrium reconstructions in all previous COMPASS discharges be retroactively recalculated using the corrected measuring coil positions, as the resulting reconstructions are likely more accurate than the ones in use today.

2 Methods

2.1 EFIT++

EFIT++ is a standard solver of the Grad-Shafranov equation [11]. In reconstructing COMPASS equilibria, local magnetic fields measured by 16 inner partial Rogowski coils (IPR coils) are provided to it as minimal constraining input. The IPR coils are small measuring coils distributed poloidally around the chamber (figure 2). It was recently found that their positions recorded within the EFIT input are inaccurate. [10] Synthetic coil signals calculated by the Biot-Savart law from poloidal field coil currents in the static phase of a vacuum discharge were compared to the measured coil signals, which betrayed disagreements up to $\sim 10\%$. To infer the coil positions more accurately, their R and Z coordinates and the poloidal angle θ were varied so as to achieve a fit between the measured and the calculated coil signal in each individual coil. The match was found to be especially sensitive to coil angles, which were on average corrected by several degrees (not visible in figure 2). Providing EFIT with the corrected coil positions can alleviate the mapping problems (figure 1b).

2.2 Velocity shear layer

The VSL is a region in the edge plasma where the poloidal plasma velocity v_p varies rapidly in the radial direction. The VSL has been shown to affect the magnitude of cross-field transport by regulating the level of plasma turbulence [12] and contributing to the L-H transition [13]. The origin of a steady-state VSL may be, in the first approximation, connected to the transition between closed and open magnetic field lines. As argued in [14], the interplay between the radial force balance (closed field lines) and the sheath potential drop (open field lines) causes the plasma potential Φ to peak near the separatrix, which results in a profile in the radial electric field $E_r = -d\Phi/dr$ and in the poloidal velocity $v_p = E_r \times B_t$ — that is, a VSL. This argumentation is rather crude, but despite that a Φ peak, or the corresponding $E_r = 0$, has been observed in experiment [13, 15], gyrofluid turbulence simulations [16], fluid simulations [17] and continuum kinetic simulations [18] alike.

Refer to [10] for discussion on additional constraining input and reconstruction settings in COMPASS EFIT.

The exact relation of the separatrix and the VSL position is currently unknown — some studies suggest that the VSL forms 0.5–1 cm outside the separatrix [4, 15, 16, 18, 19] while others place it up to 1 cm inside the separatrix [17, 20]. It is likely that their relative position depends on a number of factors, including the connection length, plasma collisionality, attachement/detachment and more. However, section 3 shows that, in original COMPASS reconstructions, $R_{\text{sep}} - R_{\text{VSL}}$

2019 JINST 14 C11020

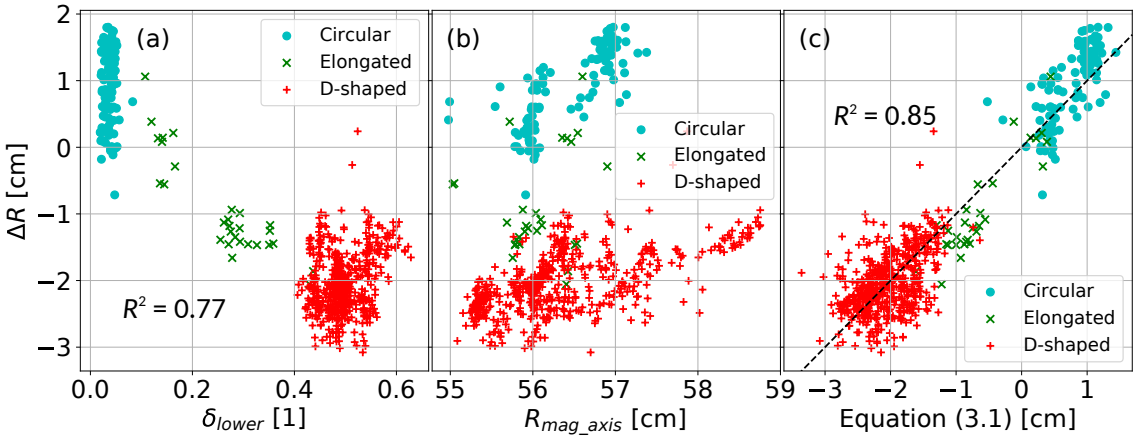

Figure 3. Dependency of $\Delta R = R_{\text{sep}} - R_{\text{VSL}}$ on (a) lower triangularity and (b) magnetic axis radial position, (c) linear regression using equation (3.1). Original EFIT reconstructions.

In this paper, we exploit the fact that COMPASS probes routinely record a Φ peak to carry out a statistical comparison of the VSL position to the magnetically reconstructed separatrix position.

2.3 Probes

The OMP reciprocating probe of the COMPASS tokamak [6] carries a ball pen probe, which is a Langmuir probe variation similar to the ion-sensitive probe both in design and measurement [22]. Its floating potential is close to the plasma potential, $V_{\text{BPP}} = \Phi - (0.6 \pm 0.3)\, T_e$, and for the purposes of this article we assume them equal. A single ball-pen probe can detect the VSL centre (Φ peak) with a spatial uncertainty ±2 mm accounting for the smoothing and the neglected T_e contribution.

3 Results

In this section we present a statistical comparison of the EFIT separatrix radial position R_{sep} to the VSL position R_{VSL}, carried out over a database of 398 COMPASS discharges (53 circular, 19 elongated and 325 D-shaped plasmas). We investigate the difference $\Delta R = R_{\text{sep}} - R_{\text{VSL}}$.

Figure 3a shows that ΔR varies considerably across the COMPASS database, from −3 cm to +2 cm, and that this variation consists of a random component and a systematic component. To find which variables affect the systematic component, we evaluated the dependence of ΔR on the variables listed in table 1 using the Principle component analysis (PCA). We found the 5 largest principle components of the phase space, responsible for 91% of its variance, and with them acting as the independent variables we performed a linear regression of ΔR. The regression matched closely with the data, $R^2 = 0.86$. Subsequently, we transformed the principle components back into the variables of table 1, obtaining the coefficients listed in table 1. In the original EFIT reconstructions, ΔR is observed to depend most strongly on the plasma lower triangularity δ_{lower} and the magnetic

is dominated by geometric factors rather than plasma parameters, reaching values from −3 to +2 cm as opposed the considerably smaller numbers found in literature. And since this systematic dependency is substantially suppressed by correcting the coil positions, which is a purely geometric adjustment, we can surmise that EFIT input inaccuracies impact the interplay between the reconstructed separatrix and VSL position significantly more than physical mechanisms.

2019 JINST 14 C11020

Table 1. Coefficients of ΔR linear fit using 5 largest principle components of the independent variable phase space: safety factor, magnetic axis radial and vertical position, elongation, upper and lower triangularity, plasma current, toroidal magnetic field, normalised beta, and the line-averaged plasma density.

EFIT	q_{95}	$R_{\text{mag\_axis}}$	$Z_{\text{mag\_axis}}$	ε	δ_{upper}	δ_{lower}	I_p	B_t	β_N	$\overline{n}_e$
original	−0.1	**0.5**	**−0.3**	0.09	**0.3**	**−1.3**	−0.03	0.03	**0.4**	0.01
new	−0.02	**0.2**	0.06	0.1	**−0.4**	−0.03	0.08	−0.07	**0.2**	−0.007

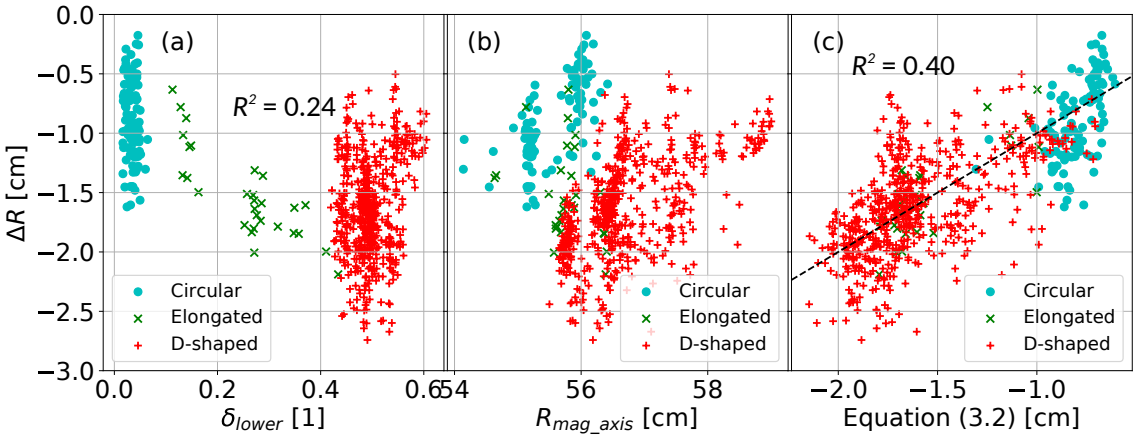

Figure 4. Dependency of $\Delta R = R_{\text{sep}} - R_{\text{VSL}}$ on (a) lower triangularity and (b) magnetic axis radial position, (c) linear regression using equation (3.2). New EFIT reconstructions.

axis radial position $R_{\text{mag\_axis}}$, which both relate to the plasma geometry. In figures 3a and 3b, one may observe both the dependencies. Finally, figure 3c shows the aforementioned linear regression with "reduced" variables — only the emboldened coefficients in table 1 were considered, that is,

$$\Delta R = -1.6 - 1.3\delta_{\text{lower}} + 0.5R_{\text{mag\_axis}} + 0.5\beta_N - 0.3Z_{\text{mag\_axis}} + 0.3\delta_{\text{upper}} \tag{3.1}$$

with an almost unchanged $R^2 = 0.85$. In figure 4, the same plots are presented for the new EFIT reconstructions. We see that purely geometrical adjustments to the EFIT input have a major impact on the reconstructed separatrix position. As observed in table 1, some dependency on triangularity and the magnetic axis position remains, but it is much less pronounced compared to the random error. The "reduced" linear regression of ΔR for the optimised EFIT is

$$\Delta R = -1.5 + 0.2\beta_N + 0.2R_{\text{mag\_axis}} - 0.4\delta_{\text{upper}}, \tag{3.2}$$

with $R^2 = 0.4$, which shows a significant suppression of the systematic component of ΔR.

4 Discussion and conclusions

We have compared the outer-midplane position of the magnetically reconstructed separatrix R_{sep} to the velocity shear layer (VSL) position R_{VSL} and drawn two conclusions: (i) current EFIT reconstructions contain a systematic error dependent on plasma geometry, and (ii) this error can be mitigated by correcting magnetic coil positions recorded in the EFIT input. It should be mentioned

2019 JINST 14 C11020

that although in previous works the VSL has been consistently associated with the separatrix, it is true that they may not coincide. In original COMPASS reconstructions, nevertheless, $R_{sep} - R_{VSL}$ is dominated by geometric factors to the point where other physical dependencies are relatively inconsequential. We thus recommend using the corrected coil positions as a solid step toward more reliable and accurate equilibrium reconstructions in COMPASS. Using this experience, similar problems can be avoided in the future COMPASS-Upgrade tokamak equilibrium reconstructions.

Acknowledgments

This work was carried out within the framework of the EUROfusion Consortium and has received funding from the Euratom research and training programme 2014–2018 and 2019–2020 under grant agreement No. 633053. The views and opinions expressed herein do not necessarily reflect those of the European Commission. This work was supported by the Grant Agency of the Czech Technical University in Prague, grant No. SGS19/180/OHK4/3T/14, project No. CZ.02.1.01/0.0/0.0/16_019/0000768, Czech Science Foundation grant No. GA19-15229S, and co-founded by MEYS projects number 8D15001 and LM2015045.

References

[1] A. Kallenbach, Y. Andrew, M. Beurskens, G. Corrigan, T. Eich, S. Jachmich et al., *EDGE2D modelling of edge profiles obtained in JET diagnostic optimized configuration*, *Plasma Phys. Control. Fusion* **46** (2004) 431.

[2] M. Kocan, R. Pitts, G. Arnoux, I. Balboa, P. de Vries, R. Dejarnac et al., *Impact of a narrow limiter SOL heat flux channel on the ITER first wall panel shaping*, *Nucl. Fusion* **55** (2015) 033019.

[3] B. LaBombard, J. Terry, J. Hughes, D. Brunner, J. Payne, M. Reinke et al., *Divertor heat flux footprints in EDA H-mode discharges on Alcator C-Mod*, *J. Nucl. Mater.* **415** (2011) S349.

[4] C.K. Tsui, J.A. Boedo, F.D. Halpern, J. Loizu, F. Nespoli, J. Horacek et al., *Poloidal asymmetry in the narrow heat flux feature in the TCV scrape-off layer*, *Phys. Plasmas* **24** (2017) 062508.

[5] G.D. Porter, J. Moller, M. Brown and C. Lasnier, *Characterization of the separatrix plasma parameters in DIII-D*, *Phys. Plasmas* **5** (1998) 1410.

[6] V. Weinzettl et al, *Progress in diagnostics of the COMPASS tokamak*, 2017 *JINST* **12** C12015.

[7] J. Adamek, J. Seidl, J. Horacek, M. Komm, T. Eich, R. Panek et al., *Electron temperature and heat load measurements in the COMPASS divertor using the new system of probes*, *Nucl. Fusion* **57** (2017) 116017.

[8] J. Seidl, J. Krbec, M. Hron, J. Adamek, C. Hidalgo, T. Markovic et al., *Electromagnetic characteristics of geodesic acoustic mode in the COMPASS tokamak*, *Nucl. Fusion* **57** (2017) 126048.

[9] J. Brotankova, J. Stockel, J. Horacek, J. Seidl, I. Duran, M. Hron et al., *Measurement of sheared flows in the edge plasma of the CASTOR tokamak*, *Plasma Phys. Rep.* **35** (2009) 980.

[10] O. Kovanda et al, *Dependence of reconstructed equilibria on input data sets using EFIT on COMPASS and comparison with experimental observations*, talk given at the 46^{th} *EPS conference on plasma physics*, Milano, Italy, 8–12 July 2019

[11] L. Appel, M. Bevir and M. Walsh, *Equilibrium reconstruction in the START tokamak*, *Nucl. Fusion* **41** (2001) 169.

2019 JINST 14 C11020

[12] S.K. Saha and R. Kumar, *Poloidal velocity shear and decorrelation of the edge fluctuations in tokamak*, in proceedings of the *30th International Conference on Plasma Science*, Jeju, South Korea, 5 June 2003, p. 469.

[13] G.R. Tynan, I. Cziegler, P.H. Diamond, M. Malkov, A. Hubbard, J.W. Hughes et al., *Recent progress towards a physics-based understanding of the H-mode transition*, *Plasma Phys. Control. Fusion* **58** (2016) 044003.

[14] K. Jirakova, *Study of edge plasma of tokamak COMPASS and its poloidal variations*, MSc thesis, Faculty of Nuclear Sciences and Physical Engineering, Czech Technical University, Czech Republic (2018), sections 3.1.2 and 3.1.5.

[15] T.D. Rognlien, D.D. Ryutov, N. Mattor and G.D. Porter, *Two-dimensional electric fields and drifts near the magnetic separatrix in divertor tokamaks*, *Phys. Plasmas* **6** (1999) 1851.

[16] P. Manz, T.T. Ribeiro, B.D. Scott, G. Birkenmeier, D. Carralero, G. Fuchert et al., *Origin and turbulence spreading of plasma blobs*, *Phys. Plasmas* **22** (2015) 022308.

[17] V. Rozhansky, S. Voskoboynikov, E. Kaveeva, D. Coster and R. Schneider, *Simulation of tokamak edge plasma including self-consistent electric fields*, *Nucl. Fusion* **41** (2001) 387.

[18] M. Dorf and M. Dorr, *Continuum kinetic modelling of cross-separatrix plasma transport in a tokamak edge including self-consistent electric fields*, *Contrib. Plasma Phys.* **58** (2018) 434.

[19] B. Nold, G.D. Conway, T. Happel, H.W. Müller, M. Ramisch, V. Rohde et al., *Generation of blobs and holes in the edge of the ASDEX upgrade tokamak*, *Plasma Phys. Control. Fusion* **52** (2010) 065005.

[20] G. Xu, V. Naulin, W. Fundamenski, C. Hidalgo, J. Alonso, C. Silva et al., *Blob/hole formation and zonal-flow generation in the edge plasma of the JET tokamak*, *Nucl. Fusion* **49** (2009) 092002.

[21] A. Field, G. Fussmann and J. Hofmann, *Measurement of the radial electric field in the ASDEX tokamak*, *Nucl. Fusion* **32** (1992) 1191.

[22] J. Adámek, J. Stöckel, M. Hron, J. Ryszawy, M. Tichý, R. Schrittwieser et al., *A novel approach to direct measurement of the plasma potential*, *Czech. J. Phys.* **54** (2004) C95.

[23] J. Adamek, H.W. Müller, C. Silva, R. Schrittwieser, C. Ionita, F. Mehlmann et al., *Profile measurements of the electron temperature on the ASDEX upgrade, COMPASS, and ISTTOK tokamak using Thomson scattering, triple, and ball-pen probes*, *Rev. Sci. Instrum.* **87** (2016) 043510.

2019 JINST 14 C11020

A.4 Proceedings contribution to the 47th EPS Conference on Plasma Physics, 2021

SOLPS-ITER simulations of the COMPASS tokamak

K. Hromasová[1,2], D. Coster[3], M. Komm[1], J. Seidl[1], D. Tskhakaya[1]

[1] *Institute of Plasma Physics, Czech Academy of Sciences, Prague, Czech Republic*

[2] *Faculty of Nuclear Sciences and Physical Engineering, Czech Technical University, Prague, Czech Republic*

[3] *Max Planck Institute for Plasma Physics, Garching, Germany*

Tokamak transport codes are an invaluable tool in assessing the edge plasma physics. SOLPS-ITER [1] is a state-of-the-art transport code, developed by the ITER Organisation. Its complex treatment of neutrals by the Monte Carlo code EIRENE allows it to accurately capture plasma recycling and neutral transport. [2] This facilitates detailed investigations of momentum and power losses in the SOL, ranging from the simple SOL to detachment. In this contribution, we present the first interpretative SOLPS-ITER simulation of the COMPASS tokamak.

The COMPASS tokamak [3] is a compact machine operated at the Institute of Plasma Physics in Prague, Czech Republic. Its extensive edge diagnostics coverage [4] synergises well with interpretative SOLPS-ITER modelling. The principal diagnostics used in this contribution are depicted in Figure 1. Upstream measurements of T_e and n_e are facilitated by the Thomson scattering diagnostic (plasma top). Target measurements are carried out by an infrared camera (total parallel heat flux density $q_{\parallel}$) and a divertor probe array of ball-pen and Langmuir probes ($q_{\parallel}$, T_e and n_e at the outer target). Bolometric diagnostics are used to determine the power radiated in the plasma core, as their divertor coverage is not suitable for gauging the divertor radiation distribution. Lastly, these diagnostics are supplemented by a magnetic equilibrium reconstruction using the EFIT++ code. [5]

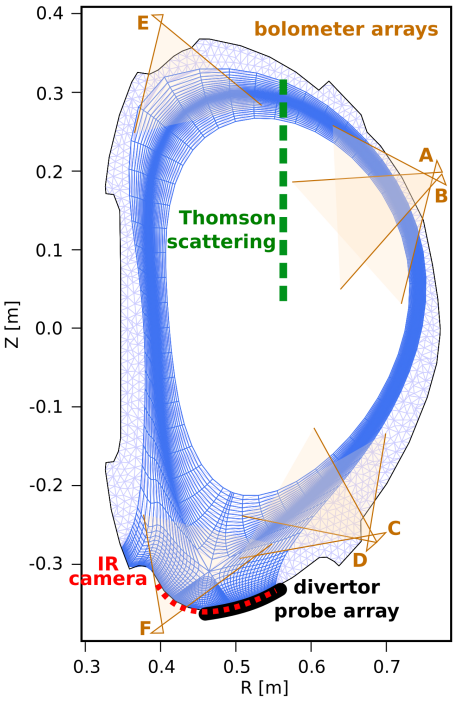

Figure 1: *Edge plasma diagnostics of the COMPASS tokamak, and B2.5 (blue) and EIRENE (lavender) grids.*

We present a simulation of the COMPASS tokamak discharge #17588 at the time $t = 1100$ ms. It is a deuterium Ohmic L-mode plasma in the divertor configuration, with the ion grad-B drift directed toward the divertor. The plasma current is $I_p = 180$ kA, the toroidal magnetic field is $B_t = 1.38$ T, the safety factor is $q_{95} = 4.2$ and the line-averaged density is $\overline{n}_e = 5 \times 10^{19}$ m^{-3}. The ohmic heating power is $P_{ohm} = 200$ kW, of which

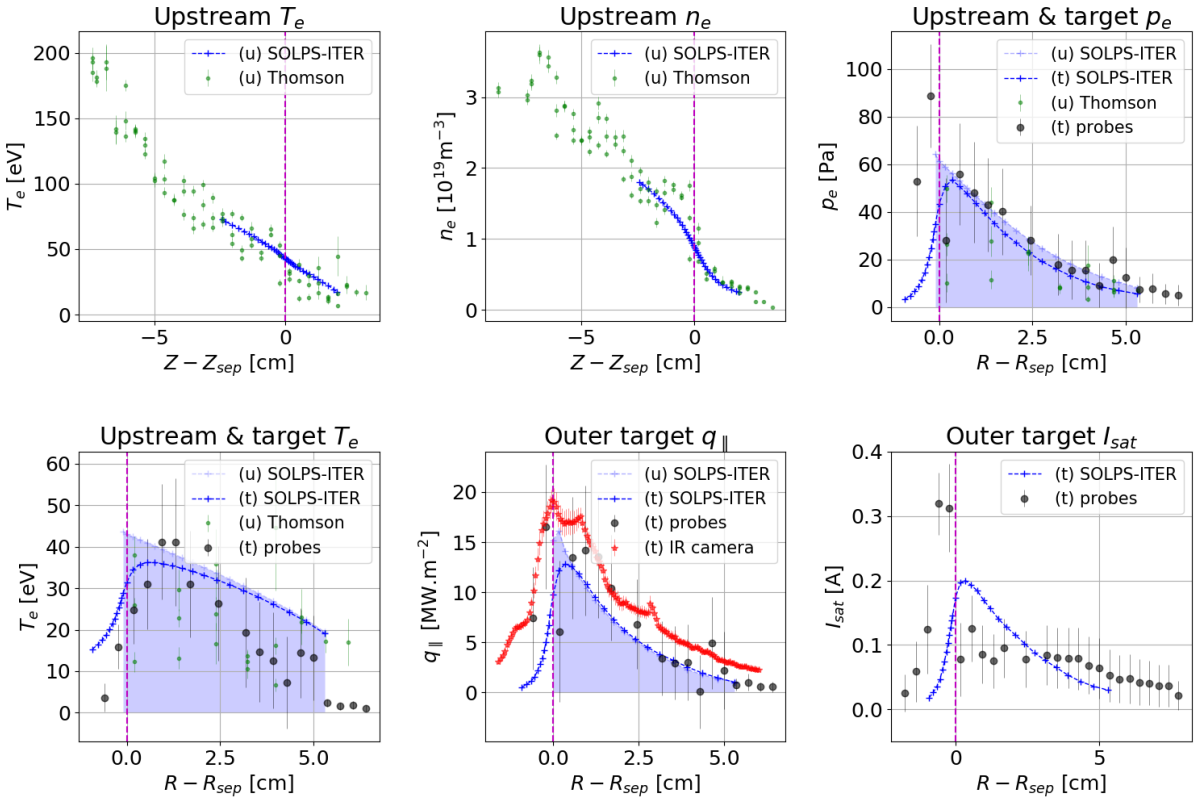

Figure 2: *Experiment-model comparison of the presented COMPASS simulation. Quantities labelled with (u) are taken from the upstream (plasma top, except for the $q_\parallel$ where the outer X-point is considered) and quantities labelled with (t) are taken from the outer target.*

$P_{rad} = 65$ kW is radiated in the core, yielding the power crossing the separatrix $P_{sep} = 135$ kW. The SOLPS-ITER simulation is coupled (B2.5+EIRENE) and drift-free. It does not account for any impurities, such as the carbon sputtered from the graphite divertor. Its resulting simplicity allows studying various simulation inputs; selected insights are discussed below.

Experiment-model comparison. Figure 2 shows that the simulation reproduces the experimental measurements with good accuracy and the profiles of T_e, n_e, $q_\parallel$ and I_{sat} match both upstream and at the outer target. The inner target heat fluxes (not shown here) are reproduced as well. This agreement may suggest that carbon impurities play a minor role in this discharge.

Magnetic equilibrium reconstruction. The equilibrium reconstruction forms the basis for building the B2.5 and EIRENE grids (figure 1). We compared two SOLPS-ITER simulations with identical inputs except for the equilibrium reconstruction used for grid construction. The two equilibrium reconstructions were constrained by magnetic measurements in the "standard" and "optimised" input configuration (more information in [6]), respectively, and their main difference was the separatrix outline ($\Delta Z = 2.1$ cm along the Thomson scattering chord). It was found that the "optimised reconstruction" (results presented herein) matched the upstream T_e

and n_e profiles automatically, while the "standard reconstruction" required an *ad hoc* upstream radial shift of 1.8 cm before it could reproduce the experimental results. This supports our previous suggestion that the "optimised" reconstructions are more accurate and illustrates the importance of high-quality equilibrium reconstructions in edge transport modelling.

Cross-field diffusion coefficient. In interpretative modelling, the diffusion coefficients associated with anomalous cross-field transport are usually determined by iteratively matching the upstream profiles. Here, this process yielded $D_n = 0.15$ m^{2}s^{-1} and $\chi_e = \chi_i = 4$ m^{2}s^{-1} (equal for lack of data). The D_n value was then compared to four D_n estimates:

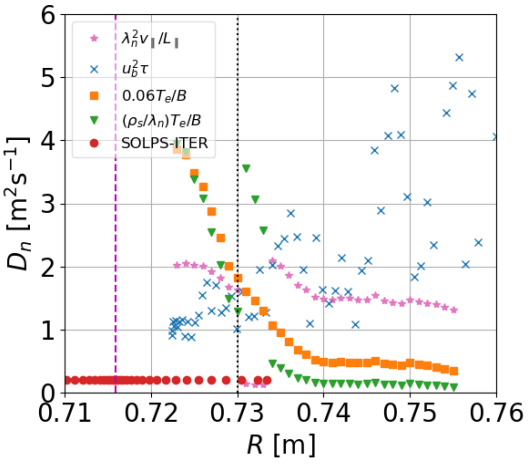

Figure 3: *Radial profiles of diffusion coefficient estimates (see text for details).*

(i) The interplay of parallel and perpendicular transport may be approximated as $D_n = \lambda_n^2 v_\parallel / L_\parallel$ [7, Eq. (2)], where λ_n is the density fall-off length, $v_\parallel = Mc_s$ is the characteristic upstream parallel velocity and $L_\parallel$ is the connection length.

(ii) [7] newly suggests calculating D_n from the edge turbulence properties, $D_n = u_b^2 \tau$, where $u_b = \mathrm{Var}(v_r)$ is the characteristic radial blob velocity and τ is the v_r autocorrelation time.

(iii) The Bohm scaling posits that $D_n = 0.06 T_e/B$.

(iv) The gyro-Bohm scaling posits $D_n = (\rho_s/\lambda_n) T_e/B$ where $\rho_s = \frac{\sqrt{m_i T_e}}{eB}$ is the Larmor radius.

The simulated discharge #17588 lacks horizontal reciprocating probe measurements needed to infer the listed plasma parameters; instead, we used the roughly similar discharge #6878. Figure 3 shows that the D_n estimates are in a bare order-of-magnitude agreement. This is a similar result to [7], but its uncertainty lends little clarification to the D_n value or physical meaning. While interpretative modelling can use the iterative matching procedure without rigorously justifying the anomalous diffusion coefficient, D_n choice in predictive modelling of future machines should be well informed. We conclude that this topic requires further inquiry.

The edge transport regime was gauged based on two criteria anchored in the two-point model [8]: the upstream-target T_e gradient and the momentum and power loss factors

$$1 - f_{mom} = \frac{p_t}{p_u} \qquad (1) \quad \text{and} \qquad 1 - f_{pow} = \frac{q_{\parallel t} R_{\parallel t}}{q_{\parallel u} R_{\parallel u}}, \qquad (2)$$

where p is the total plasma pressure and the subscripts denote upstream (outer X-point) and target (outer target). As figure 2 shows, $T_{et} \approx T_{eu}$, and figure 4 indicates only small momentum and power losses. This corresponds to the sheath-limited regime at the outer target. At the

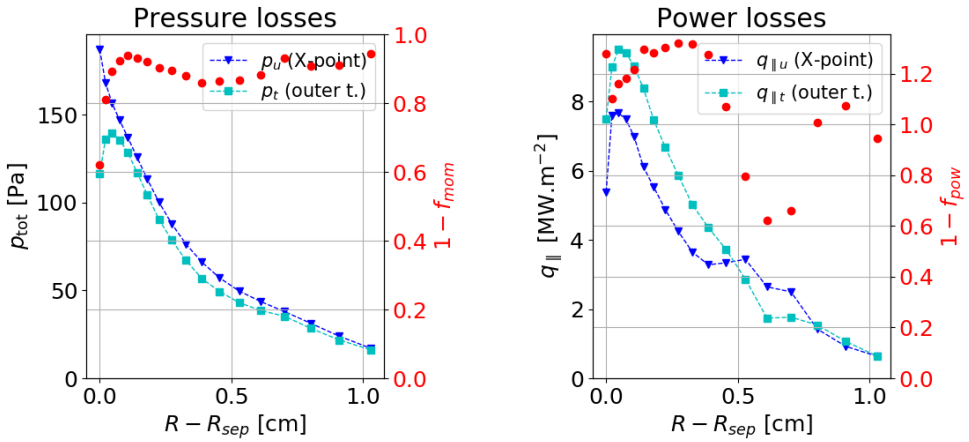

Figure 4: *Simulated profiles of the total plasma pressure p and the total parallel heat flux density $q_\parallel$. The corresponding loss factors $1 - f_{mom}$ and $1 - f_{pow}$ are plotted in red.*

inner strike point, $T_u/T_t \approx 2$ and the momentum and power losses remain small. Considering discharge #17588 is representative of a typical moderate-density COMPASS tokamak plasma, we conclude that the COMPASS tokamak typically operates in the sheath-limited regime. It is known that the transport regime can affect the spreading of turbulent structures in the SOL [9], and therefore we advise caution when using COMPASS in scaling studies together with machines operating typically in the conduction-limited regime.

Acknowledgements This work has been carried out within the framework of the EUROfusion Consortium and has received funding from the Euratom research and training programme 2014-2018 and 2019-2020 under grant agreement No 633053. The views and opinions expressed herein do not necessarily reflect those of the European Commission. The work was co-founded by the Czech Science Foundation projects GA20-28161S and GA19-15229S, the Grant Agency of the Czech Technical University in Prague, grant No. SGS19/180/OHK4/3T/14, and the MEYS projects No. 8D15001 and LM2018117.

References

[1] S. Wiesen et al, Journal of Nuclear Materials **463** (2015) 480-484

[2] R. A. Pitts et al, Nuclear Materials and Energy **20** (2019) 100696

[3] R. Pánek et al, Plasma Physics and Controlled Fusion **58** (2015) 014015

[4] V. Weinzettl et al, Journal of Instrumentation **12** (2017) C12015

[5] L. Appel et al, Nuclear Fusion **41** (2001) 169

[6] K. Jiráková et al, Journal of Instrumentation **14** (2019) C11020

[7] P. Manz et al, Physics of Plasmas **27** (2020) 022506

[8] P. C. Stangeby, Plasma Physics and Controlled Fusion **60** (2018) 044022

[9] D. A. D'Ippolito et al, Physics of Plasmas **18** (2011) 060501

s

A.5 Proceedings contribution to the 49th EPS Conference on Plasma Physics, 2023

Sensitivity of COMPASS tokamak SOLPS-ITER simulations to electron and ion heat flux limiters

K. Hromasova[1,2], J. Seidl[1], D. Tskhakaya[1], J. Adamek[1], M. Dimitrova[1], F. Jaulmes[1], M. Komm[1], P. Vondracek[1], M. Sos[1,2] and the COMPASS team[1]

[1] *Institute of Plasma Physics, Czech Academy of Sciences, Prague, Czech Republic*

[2] *Faculty of Nuclear Sciences and Physical Engineering, Czech Technical University, Prague, Czech Republic*

Heat flux limiting, like anomalous diffusion, is a remedy to an intrinsic defficiency of plasma transport codes, here the failure of the classical parallel heat flux formula in low-collisionality plasmas. The classical (or Spitzer-Härm) parallel heat flux density of species a is

$$q_{\|a}^{classical} = -\kappa_a \nabla_{\|} T_a \tag{1}$$

where κ_a is the parallel thermal conductivity of species a and $\nabla_{\|} T_a$ is the parallel gradient of its temperature. Formula (1) was derived under the assumption that the mean free path of species a is much smaller than both the parallel gradient size and the connection length. This assumption, however, is not satisfied in high-temperature, low-collisionality plasmas, and so formula (1) can drastically overestimate the physical parallel heat flux density.

A common practice in transport codes is to limit $q_{\|a}^{classical}$ by harmonically averaging it with a fraction of the free-streaming heat flux $q_{FS,a} = 0.8 e n_a T_a v_{th,a}$, where e is the electron electric charge, n_a is the species a particle density and $v_{th,a}$ is its thermal velocity. The free-streaming heat flux is the highest possible heat flux in a plasma. [1] It follows to limit the classical heat flux so it cannot exceed a fraction of the free-streaming heat flux:

$$q_{\|a}^{limited} = \left[\left(q_{\|a}^{classical} \right)^{-1} + \left(\alpha_a . q_{FS,a} \right)^{-1} \right]^{-1} \tag{2}$$

Here, $\alpha_a \sim 1$ is called the **heat flux limiter**. This is the principle of heat flux limiting.

Although heat flux limiting has been called artificial, *ad-hoc* and arbitrary [2], it can prevent unphysically high parallel heat fluxes in transport codes [1]. Consequently, optimal values of α_e and α_i are of interest. Values between 0.1 and 3 have been suggested [1], the SOLPS-ITER transport code [3] uses $\alpha_e = \alpha_i = 0.15$ by default, and $\alpha_e = \alpha_i = 0.3$ has been proposed for the COMPASS tokamak [4]. Since heat flux limiting can greatly impact the simulation [2], it is strongly recommended to perform a sensitivity analysis before settling on a particular value of α [5]. This contribution presents such a sensitivity analysis, performed by the SOLPS-ITER code in the COMPASS tokamak H-mode discharge #16908.

The COMPASS tokamak [7], operated 2009-2021 at the Institute of Plasma Physics in Prague, was a compact device focused on edge plasma physics research. The modelled discharge #16908 is an NBI-heated H-mode ($B_t = -1.15$ T, $I_p = 240$ kA, $q_{95} = 2.8$, $n_{e0} = 5 \times 10^{19}$ m^{-3}) with the ion grad-B drift pointing toward the X-point. Power balance yields the power crossing the separatrix 330 kW; this is split evenly between electrons and ions in the simulation. The plasma is modelled at $t = 1130$ ms (inter-ELM) with kinetic neutrals and carbon impurity sputtering (both physical and chemical, yield $\gamma_{chem} = 0.01$). The anomalous particle and heat diffusion coefficients were tuned by hand to achieve the best fit of upstream n_e and T_e profiles. Diagnostics used for experiment-model matching are listed in figure 1. [8]

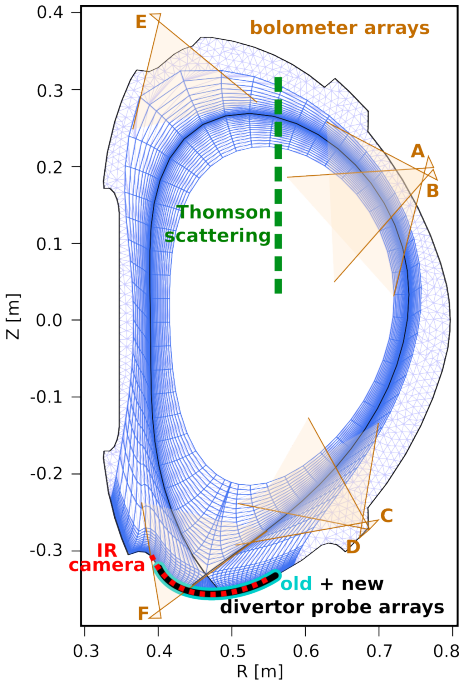

Figure 1: *Edge plasma diagnostics of the COMPASS tokamak [8], and B2.5 (blue) and EIRENE (lavender) grids.*

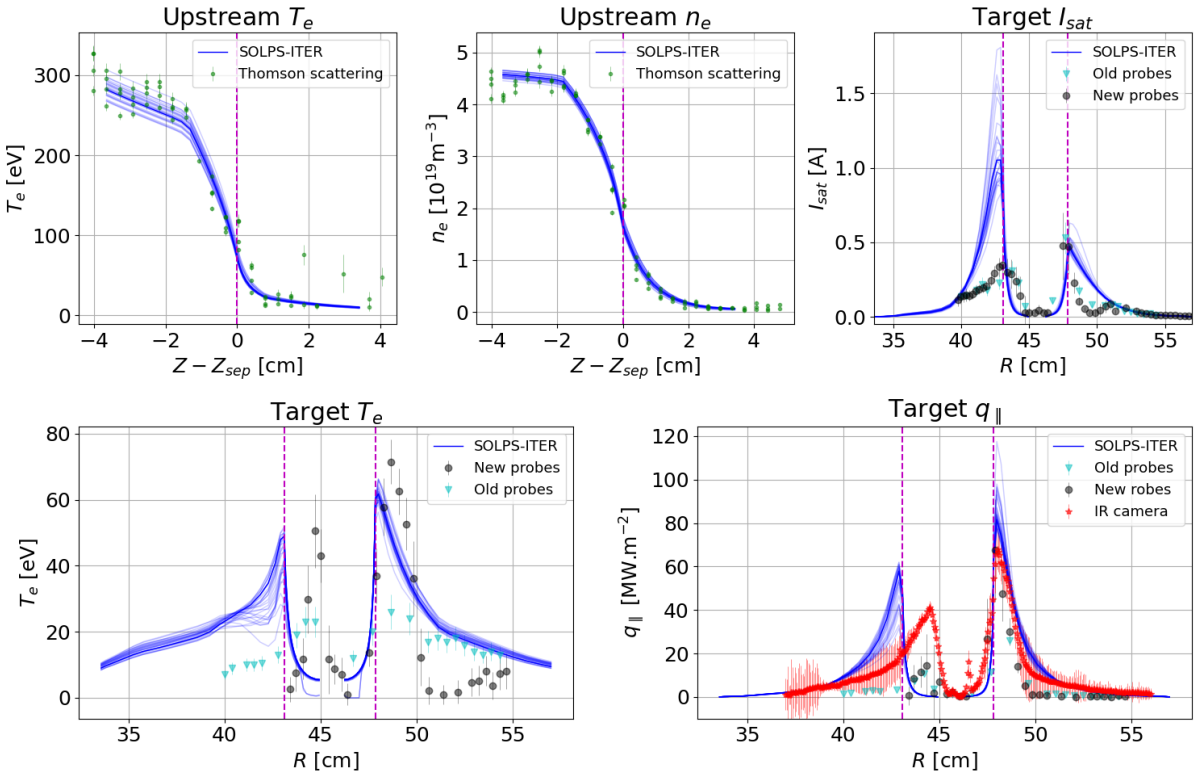

Figure 2: *Comparison of experimental data to all simulations within the parameter scan. The central simulation $\alpha_e = \alpha_i = 0.3$ is plotted with a saturated blue line. The inner strike point is displaced due to equilibrium reconstruction inaccuracy.*

To gauge the sensitivity of COMPASS tokamak simulations to heat flux limiting, we performed a 5x5 parameter scan for $\alpha_{e,i} \in \{0.1, 0.2, 0.3, 0.5, 1.0\}$ with four additional simulations for $[\alpha_e, \alpha_i] = [0.06, 0.3], [\infty, 0.3], [0.3, 0.01], [0.3, \infty]$, where ∞ corresponds to no heat flux limiting (classical heat flux). As figure 2 shows, the variation caused by heat flux limiting generally does not exceed diagnostics uncertainties, rendering experimental determination of α difficult.

To identify the effects of heat flux limiting, we reduced the 2D variation of plasma parameters to single numbers, such as "parallel gradient of T_i in the 4th SOL flux tube". This is possible as heat flux limiting typically does not change the radial profile shape, and the 4th SOL flux tube is representative of the entire SOL. Heat flux limiting was found to affect all plasma parameters, but the strongest effect, corroborated in figure 3, is this: **Heat flux limiting steepens the parallel temperature gradient.** Mind that this effect is not strong enough to counter the reduction in thermal conductivity in equation (1), so the conductive heat flux is still reduced. The steepening is sharper in ions (decreasing α_i from 1.0 to 0.1 decreses $q_{\parallel i,cond}$ fivefold while increasing T_{iu}/T_{it} tenfold), but it also pertains to electrons (decreasing α_e from 1.0 to 0.1 decreses $q_{\parallel e,cond}$ twofold while increasing T_{eu}/T_{et} twofold). The effect is more pronounced on the inner target.

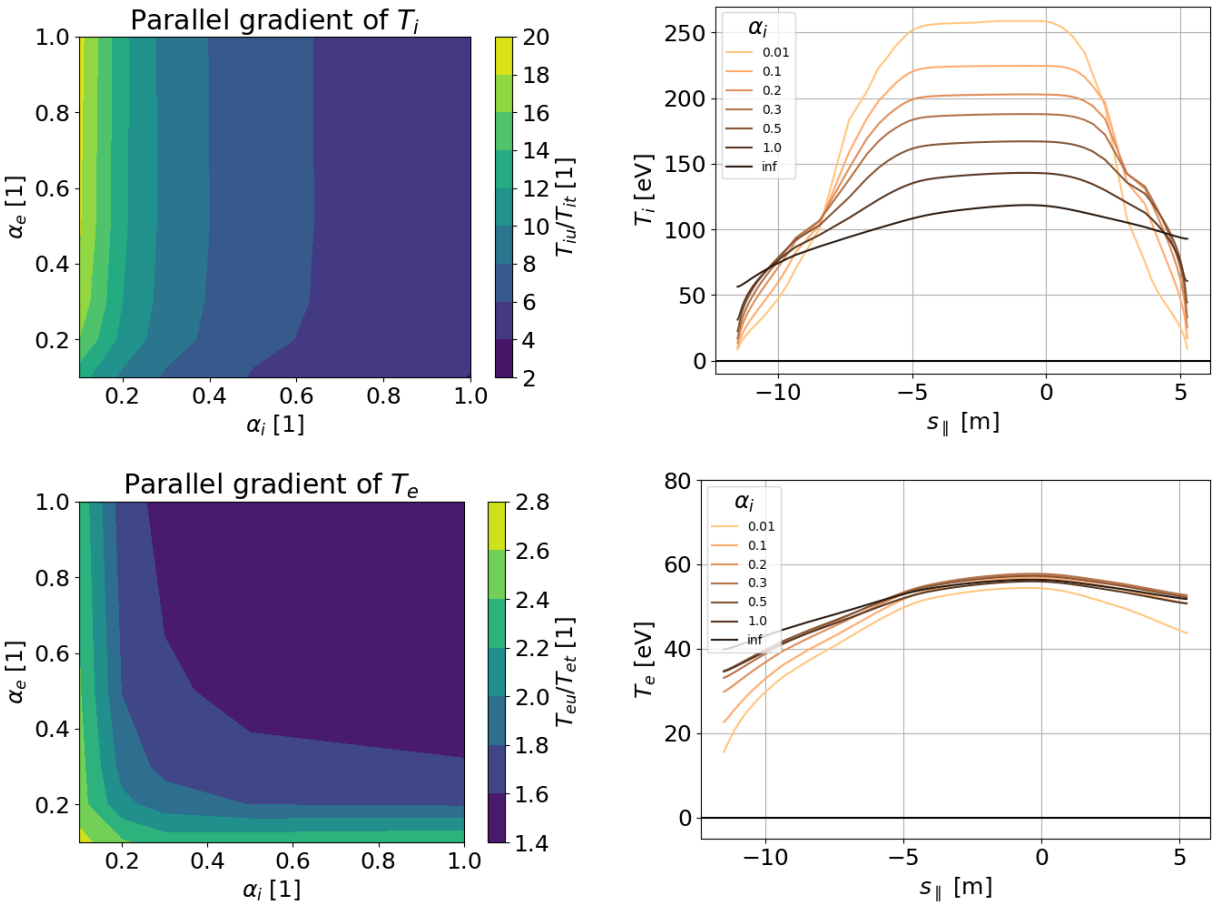

Figure 3: The strongest effect of heat flux limiting: temperature parallel gradient steepens.

Gradient steepening is a robust, previously reported effect [5, 9], but it does not immediately follow from the principle of heat flux limiting. Our interpretation is the following. Since we fix the input power P_{SOL} and leave T free to evolve, $\nabla_{\|}T$ builds up in response to the magnitude of heat flux to be conducted. Heat flux limiting "strangulates" the conduction channel. Some of the energy is transferred to another transport channel (typically $q_{\|i,cond} \rightarrow q_{\|e,cond}$), while $\nabla_{\|}T$ steepens to allow more energy to be conducted. Power transfer from electrons to ions explains why $\nabla_{\|}T_e$ steepens in response to both electron and ion heat flux limiting.

Seeing that SOLPS-ITER simulations of tokamak COMPASS are quite sensitive to heat flux limiting, the next step is to determine the best value of α_e and α_i. This is complicated by the lack of T_i measurements and reservations toward inner target T_e measurements. We plan to assemble several indirect measurements (inner/outer heat flux distribution from the IR camera, radiation patterns, T_i measurement [10]) as well as simulations (core transport code METIS, kinetic SOL code BIT1) and optimise the heat flux limiter value against all the available data.

Acknowledgements This work has been carried out within the framework of the EUROfusion Consortium, funded by the European Union via the Euratom Research and Training Programme (Grant Agreement No 101052200 - EUROfusion). Views and opinions expressed are however those of the author(s) only and do not necessarily reflect those of the European Union or the European Commission. Neither the European Union nor the European Commission can be held responsible for them. The work was co-founded by the Czech Science Foundation projects GA20-28161S and GA19-15229S, the Grant Agency of the Czech Technical University in Prague grant SGS22/175/OHK4/3T/14, and the MEYS projects 9D22001 and LM2023045. It was supported by the Martina Roeselová Memorial Fellowship granted by the IOCB Tech Foundation and by the project COMPASS-U: Tokamak for cutting-edge fusion research (No. CZ.02.1.01/0.0/0.0/16_019/0000768), and co-funded from European structural and investment funds.

References

[1] W. Fundamenski, Plasma Physics and Controlled Fusion **47** (2005) R163

[2] M. Day et al, Contributions to Plasma Physics **36** (1996) 419-423

[3] S. Wiesen et al, Journal of Nuclear Materials **463** (2015) 480-484

[4] D. Tskhakaya et al, Nuclear Materials and Energy **26** (2021) 100893

[5] D. Coster et al, Physica Scripta **T108** (2004) 7-13

[6] M. Hron et al, Nuclear Fusion **62**(4) (2022) 042021

[7] V. Weinzettl et al, Journal of Instrumentation **12** (2017) C12015

[8] Y. Homma, Plasma Physics and Controlled Fusion **64** (2022) 045020

[9] A. Dvornova, *Characterization of the COMPASS Scrape-Off Layer by RFA Measurements and SOLEDGE2D Modelling*, Master thesis (2016), figures 4.11 and 4.12